IMPROVED CHARACTERIZATION OF THIN BED AND LOW-RESISTIVITY/LOW-CONTRAST HYDROCARBON RESERVOIRS

HIJAZ KAMAL BIN HASNAN

FACULTY OF SCIENCE
UNIVERSITI MALAYA
KUALA LUMPUR
2020

IMPROVED CHARACTERIZATION OF THIN BED AND LOW-RESISTIVITY/LOW-CONTRAST HYDROCARBON RESERVOIRS

HIJAZ KAMAL BIN HASNAN

THESIS SUBMITTED IN FULFILMENT OF THE REQUIREMENTS FOR THE DEGREE OF DOCTOR OF PHILOSOPHY

DEPARTMENT OF GEOLOGY
FACULTY OF SCIENCE
UNIVERSITI MALAYA
KUALA LUMPUR

2020

UNIVERSITI MALAYA

ORIGINAL LITERARY WORK DECLARATION

Name of Candidate: **HIJAZ KAMAL BIN HASNAN**

Matric No: **HHS150001**

Name of Degree: **DOCTOR OF PHILOSOPHY**

Title of Thesis ("this Work"):

IMPROVED CHARACTERIZATION OF THIN BED AND LOW-RESISTIVITY/LOW-CONTRAST HYDROCARBON RESERVOIRS

Field of Study:
GEOLOGY

I do solemnly and sincerely declare that:

(1) I am the sole author/writer of this Work;
(2) This Work is original;
(3) Any use of any work in which copyright exists was done by way of fair dealing and for permitted purposes and any excerpt or extract from, or reference to or reproduction of any copyright work has been disclosed expressly and sufficiently and the title of the Work and its authorship have been acknowledged in this Work;
(4) I do not have any actual knowledge nor do I ought reasonably to know that the making of this work constitutes an infringement of any copyright work;
(5) I hereby assign all and every rights in the copyright to this Work to the University of Malaya ("UM"), who henceforth shall be owner of the copyright in this Work and that any reproduction or use in any form or by any means whatsoever is prohibited without the written consent of UM having been first had and obtained;
(6) I am fully aware that if in the course of making this Work, I have infringed any copyright whether intentionally or otherwise, I may be subject to legal action or any other action as may be determined by UM.

Candidate's Signature Date:

Subscribed and solemnly declared before,

Witness's Signature Date:

Name:

Designation:

IMPROVED CHARACTERIZATION OF THIN BED AND LOW-RESISTIVITY/LOW-CONTRAST HYDROCARBON RESERVOIRS

ABSTRACT

Thin-bed and low-resistivity/low-contrast (LRLC) reservoirs such tidal heterolithic deposits contain a significant amount of the global hydrocarbon reserves. However, due to millimetre-to-centimetre thin sandstone, forecasting hydrocarbon reserves and production are challenging. Producing hydrocarbon economically from heterolithic deposits in thin-bed reservoirs requires the characterisation of flow properties in thin beds for improved hydrocarbon reserves and production estimates. Sedimentology interpretation of the study area and reservoir in Malaysia shows that heterolithic deposits are part of tidal bars in a shallow marine environment with a large areal extent that suggests the substantial volume of heterolithic deposits which represent potential hydrocarbon reserves. Conventional Well Logs and Experimental Core Analysis cannot resolve and represent the flow properties in millimetre-to-centimetre scale sandstone layers in heterolithic deposits, which resulted in underestimated hydrocarbon reserves estimates. Characterisation of flow properties in thin sandstone layers is the first step in a multiscale workflow in reservoir modelling that could improve hydrocarbon reserves estimates in heterolithic deposits.

This thesis applied X-Ray Micro-CT Imaging and Analysis, Digital Core Analysis, gas permeability analysis and 3D Visualisation on five mini-plugs from the sand dominated regions of two muddy heterolithic core plugs, two laminated rock core plugs and one sandy heterolithic core plug that represent sandstone units in the reservoir. The main objectives are to characterise the porosity, permeability and connectivity of the thin sandstone layers in the heterolithic samples and investigate the multi-scale impact of

small-scale heterogeneities such as average grain size and carbonate laminates on permeability.

Computed porosities of the five mini-plugs are consistent with the experimental results that validated the computed porosity using digital core analysis. The computed permeability of a mini plug from one heterolithic core plug is similar to the results of the laminated sandstone mini-plugs which are benchmark reservoir sandstones. 3D visualisation of the heterolithic core plug reveals laterally continuous thin sandstone layers that are well connected and represent potential hidden sand pay and additional hydrocarbon reserves in heterolithic deposits. Permeability gas probe measurements of the surfaces of the core plugs validated the computed results of all samples. The results verified the presence of permeable thin sandstone layers in the heterolithic core plug. Also, 3D visualisation of the sandstone core plugs reveals carbonate minerals. The carbonate causes lower core plug permeability compared to their more homogeneous mini-plugs. This result highlights the multi-scale effects of small-scale heterogeneities on permeability at larger scales. Grain size analysis of all samples indicated that permeability increases with smaller average grain sizes and is the main factor in permeability difference between similar rock types.

To sum up, the methodology used in this thesis characterised the permeability of well-connected millimetre-to-centimetre scale reservoir sandstone layers in heterolithic deposits that represent additional net sand pay and potential hydrocarbon reserves in heterolithic deposits. Our methodology and results contribute to the first stages of a multi-scale workflow for reservoir modelling of heterolithic deposits in thin-bed LRLC reservoirs. Our methods can incorporate the properties millimetre-to-centimetre scale sandstone layers and other small-scale heterogeneities into reservoir models for improved the hydrocarbon reserves and production forecasts.

Keywords: Thin Beds, Heterolithic, Low-Resistivity/Low-Contrast Pay, X-Ray Micro-CT, Digital Core Analysis, 3-D Visualization

PENAMBAHBAIKAN PENCIRIAN RESERVOIR LAPISAN ENNAPAN NIPIS DAN KEBERINTANGAN-RENDAH/KONTRAS-RENDAH

ABSTRAK

Deposit heterolitik di dari reservoir keberintangan-rendah/kontras-rendah mengandungi hingga 30% daripada simpanan hidrokarbon global. Walau bagaimanapun, kerana lapisan pasir nipis dengan ketebalan milimeter hingga sentimeter yang banyak dalam reservoir jenis ini, meramal rizab takungan dan pengeluaran hidrokarbon sangat mencabar. Menghasilkan hidrokarbon secara ekonomi dari deposit heterolitik memerlukan pencirian sifat aliran di lapisan pasir enapan yang nipis untuk meramal rizabtakungan hidrokarbon dan anggaran pengeluaran yang lebih tepat. Tafsiran sedimentologi di kawasan kajian dan rizab takungan di Malaysia menunjukkan bahawa deposit heterolitik adalah sebahagian daripada perkitaran air laut pasang surut dan laut yang cetek yang luas dengan jumlah deposit heterolitik yang besar dengan potensi rizab hidrokarbon yang menguntungkan . Analisis pengelog telaga Konvensional dan dan kaedah makmal iaitu Routine Core Analysia (RCA) tidak dapat menyelesaikan dan mewakili sifat aliran dalam lapisan batu enapan pasir berskala milimeter hingga sentimeter dalam deposit heterolitik. Kekurangan ini yang perkiraan rizab hidrokarbon yang tidak meyakinkan. Pencirian sifat aliran pada lapisan batu enapan pasir tipis adalah langkah pertama dalam aliran kerja multiskala dalam pemodelan reservoir yang dapat meningkatkan anggaran rizab hidrokarbon dalam deposit heterolitik. Tesis ini mengaplikasikan Pengimejan dan Analisis X-Ray Mikro-CT, Analisis Teras Digital, analisis kebolehtelapan gas dan Visualisasi 3D pada lima palam mini . Dua palam mini adalah batuan enapan heterolitik berlumpur, dua palam enapan batu laminasi pasir dan satu batuan enapan heterolitik berpasir. Satu palam mini batu laminasi berpasir yang mewakili unit utama batu pasir reservoir. Objektif utama adalah untuk mencirikan nilai keporosan, kebolehtelapan dan ciri penyambungan lapisan batu enapan pasir nipis dalam

sampel heterolitik dan menyiasat kesan pelbagai skala heterogen skala kecil seperti saiz butiran batuan enapan dan laminasi karbonat pada ciri kebolehtelapan.

Keporosan yang dikira dari lima plug mini adalah selaras dengan perkiraan keporosan melalui eksperimen Routine Core Analysis mengesahkan keporosan yang dikira menggunakan analisis teras digital. Kebolehtelapan yang dikira dari palam mini dari satu palam teras heterolitik adalah sama dengan kebolehtelapan hasil palam mini batu pasir berlamina yang dijadikan rujukan bagi batu pasir reservoir .Visualisasi 3D pada palam teras heterolitik menunjukkan kehadiran lapisan batu pasir nipis berterusan dan bersambung dengan baik yang berkemungkinan mengandungi rizab hidrokarbon tambahan dalam deposit heterolitik. Pengukuran kebolehtelapan dengan prob gas pada permukaan palam teras adalah sama dengan kebolehtelapan palam mini yang dikira sampel melalui kaedah Analisis Teras Digital . Persamaan dua perkiraan ini mengesahkan adanya lapisan batu pasir nipis yang telap dalam palam teras heterolitik yang mempunyai ciri aliran yang sama dengan batu pasir reservoir .Visualisasi 3D palam batu pasir menunjukkan mineral karbonat yang mengurangkan kebolehtelapan palam teras berbanding dengan palam mini yang lebih homogen. Hasil ini menunjukkan kesan multi-skala heterogenitas skala kecil pada kebolehtelapan pada skala yang lebih besar. Analisis saiz butiran batuan enapan dari semua palam mini menunjukkan bahawa kebolehtelapan meningkat dengan ukuran saiz butiran yang lebih besar. Saiz purata butiran enapan batu merupakan faktor utama perbezaan kebolehtelapan antara jenis batuan yang serupa.

Secara Ringkasnya, metodologi yang digunakan dalam tesis ini mencirikan kebolehtelapan lapisan batu pasir reservoir skala milimeter-ke-sentimeter yang bersambung dengan baik dalam deposit heterolitik. Lapisan nipis batu yang ipis dengan ciri aliran yang tinggi adalah sebahagian dari tambahan batuan pasir bersih reservoir dalam deposit heterolitik. Batuan pasir tambahan ini menyimoan rizab hidrokarbon

tambahan dalam deposit heterolitik. Metodologi dan hasil kerja kami menyumbang kepada peringkat pertama aliran kerja pelbagai skala untuk pemodelan reservoir dan rizab hidrokarbon dalam deposit heterolitik yang terdiri daripada batuan enapan nipis di dalam reservoir keberintangan-rendah/kontras-rendah. Kaedah kami boleh mencirikan sifat lapisan aliran pada enaman nipis batuan pasir dengan ketebalan pada skala milimeter hingga sentimeter. Kajian kami juga dapat mencerapkan kesan heterogen skala kecil ke atas ciri aliran ke dalam model reservoir untuk penambahbaikan ramalan rizab dan pengeluaran hidrokarbon dari reservoir keberintangan-rendah/kontras-rendah.

Kata Kunci: Enapan nipis, keberintangan-rendah/kontras-rendah: , Pengimejan X-Ray Mikro-CT, Analisa Batu Digital, Visualisasi 3-Dimensi

ACKNOWLEDGMENTS

First and foremost, I would like to express my gratitude to my supervisors and panel review members:

- Profesor Dr. Adrian Sheppard, Department of Applied Mathematics, Research School of Physics and Engineering, Australian National University
- Profesor Dr. Mark Knackstedt, Department of Applied Mathematics, Research School of Physics and Engineering, Australian National University
- Profesor Dr. Wan Hasiah Abdullah, Department of Geology, Universiti Malaya
- Dr. Meor Ahmad Hakif, Department of Geology, Universiti Malaya

The invaluable contributions by the following individuals are also acknowledged for their support of this study in terms of providing access to the core materials and data used in this PhD study.

- Mr Kamal Embong, Principal Reservoir Geologist, Petronas Reserves and resources, PETRONAS, Kuala Lumpur, Malaysia
- Mr Grant Heavysege, Principal Petrophysicist, PETRONAS, Kuala Lumpur, Malaysia

I would also like to express my gratitude to Dr Jill Middleton for her technical assistance in using MANGO and MORPHY, Dr Michael Turner for his technical assistance in preparing the samples for X-Ray Micro-CT Imaging and Dr Levi Beeching for his assistance in using Drishti. I would also like to acknowledge Dr Ralph Kugler. He was my supervisor at Universiti Malaya in 2015 until his retirement in 2016 for providing the opportunity to be part of this PhD studies. His enthusiasm and energy in geology remain a motivation for me.

TABLE OF CONTENTS

LIST OF FIGURES

LIST OF TABLES

LIST OF EQUATIONS

LIST OF SYMBOLS AND ABBREVIATIONS

3-D	: 3-Dimensional
ANU	: Australian National University
BV	: Bulk Volume
DCA	: Digital Core Analysis
LRLC	: Low-Resistivity/Low-Contrast
MICP	: Mercury Injection Capillary Pressure
NER	: Acronym for 'New England Research' mini-permeameter tool
NMR	: Nuclear Magnetic Resonance
OOIP	: Original Oil in Place
PV	: Pore Volume
SBED	: Name of software used for modelling bedform scale rock models.
SEM	: Scanning Electron Microscopy
SEM-EDS	: Energy Dispersive X-Ray Spectroscopy
XMCT	: X-Ray Micro-Tomography

CHAPTER 1 : INTRODUCTION

This PhD study proposes to use XMCT Imaging and Analysis and Digital Core Analysis (DCA) as part of a methodology to characterize porosity and permeability of core plugs from a heterolithic thin bed reservoir in Malaysia. Chapter 1 provides an overview of Thin Bed as a source of hydrocarbon and the associated general challenges in characterizing the hydrocarbon resources in thin-bed reservoirs. This chapter is followed by Chapter 2, which provides the literature review of low-resistivity/low-contrast (LRLC) issues in thin-bed reservoirs. Chapter 2 discusses the limitation of current reservoir characterization methods in appraising thin-bed reservoirs and the challenges posed by thin-bed reservoirs in terms of geology and estimating the hydrocarbon reserves in place. Chapter 3 of this thesis provides a review and discussion of XMCT and DCA methods used in this study and significance to this PhD study. Chapter 4 provides the methodology in this study that includes other methods such as NER gas probe for permeability measurement and mineralogical analyses. Chapter 5 and 6 provide the geological and sedimentological description of heterolithic deposits in the study area and reservoir. Chapter 7 provides the mineralogical framework of the sandstone samples from two core plugs used in this study. Chapter 8 provides the results and discussion for XMCT Imaging, Digital Core Analysis, 3D Visualization and Gas Probe Analysis. We conclude this thesis with Chapter 9 that summarises and discusses the results of this thesis and their impact on the reservoir characterization of thin-bed LRLC reservoirs and future work.

1.1 Background

Large and thick sandstone dominated hydrocarbon reservoirs around the world that were targeted for easy hydrocarbon production are facing depletion. As a result, countries with modest hydrocarbon reserves such as Malaysia are turning their focus to thin-bed and low-resistivity/low-contrast reservoirs such as heterolithic tidal deposits which are proven to hold a sizable portion of the world's hydrocarbon reserves (Jackson et al., 1999; Snyder et al., 2016); Sun et al. (2014). It is estimated that a significant portion of the world's hydrocarbon reserves is contained within thin-bed and LRLC reservoirs (Passey et al., 2006). However, forecasting hydrocarbon reserves in heterolithic deposits is difficult due to multiscale heterogeneity. This multi-scale heterogeneity takes the form of thin beddings and low resistivity pay that affect water saturation measurements. Also, some heterolithic deposits are affected by freshwater formation such as in Malaysia, which cause poor contrast between the hydrocarbon and fresh water-bearing interval, causing additional uncertainty is hydrocarbon reserves estimates.

The multi-scale heterogeneity in thin-bed reservoirs affects pore structures, rock-fluid and fluid-fluid interaction which have a significant impact on hydrocarbon reserves estimation and production. An example is the Archie equation that establishes the relationship between fluid saturation and the resistivity of the reservoir and formation fluid (Kumar et al., 2010). Fluid saturations of water and hydrocarbon are essential variables in determining the amount of hydrocarbon in place.

Many thin-bed reservoirs are described as low-resistivity/low-contrast (LRLC) pay as they exhibit averaged low resistivity measurements in the well logs' due effects of alternating layers of mudstone and sandstone beds as a significant factor. Low resistivity affects the Resistivity Index and Archie Equation which is used to determine the water saturation from the well logs. Equation 1 shows that low average resistivity reading affects the R_t value in the Resistivity Index. Similarly, Equation 2 shows that low R_t in low resistivity pay leads to high water saturation. Equation 3 merely shows the formation factor.

In low resistivity pay intervals, the R_t value approaches the value of the brine water (R_0). This causes the Resistivity Index (Equation 1) to approach the value of 1.0, which indicates the reservoir is saturated with water (Tiab et al., 2012). The Resistivity Index is used in the Archie equation (Equation 2) used to calculate saturation. As a result, a low R_t value in thin-bed and LRLC reservoirs will cause the Archie equation to calculate a higher water saturation. Therefore, resistivity well logs that use the Archie equation to measure water saturation would interpret most LRLC intervals with interpreted high water saturation as non-reservoir. As a result, well logs analysis would interpret thin-bed and LRLC reservoirs as having low net sand pay and hydrocarbon reserves potential.

Equation 1: Resistivity Index (R.I.)

$$\textbf{Resistivity Index}\ (\mathbf{R.I.}) = A = \frac{\mathrm{R_t}}{\mathrm{FR_w}} = \frac{\mathrm{R_t}}{\mathrm{R_0}}$$

Equation 2: The Archie Equation used for measuring water saturation

$$\textbf{Archie Equation} = (S_w)^{-n} = \frac{\mathrm{R_t}}{\mathrm{FR_w}} = \frac{\mathrm{R_t}}{\mathrm{R_0}}$$

Equation 3: Formation Factor used in Archie Equation

$$\textbf{Formation Factor}\ (\mathbf{F}) = \frac{a}{\emptyset^m}$$

F = Formation Factor which is defined by porosity (Ø) and tortuosity (a)

S_w = Water Saturation = proportion of pore filled with water

m = cementation exponent

n =saturation exponent

$R_0 = F^*R_w$= Resistivity of Brine Water

R_t = True Resistivity

R_w=Water Resistivity

A = Tortuosity Factor

Low-resistivity in reservoirs is caused by the averaging effect of the thin beds where the conductive mudstone layers lower the averaged resistivity measurements in thin-bed reservoirs. Low-contrast refers to the low conductivity contrast between the mudstone and sandstone layers which is exacerbated in freshwater formations which creates poor contrast between the hydrocarbon and fresh water-bearing interval, which exhibit low resistivity contrast. The combination of low-resistivity and low-contrast creates significant issues in terms of measuring the water saturation from resistivity logs and measuring the net hydrocarbon-bearing, which are crucial for hydrocarbon reserves and production forecasts.

Thin bed and LRLC reservoir intervals are present in many existing and developed hydrocarbon fields but were often neglected due to perceived reduced commercial viability and low recovery factor (Elfenbein et al., 2005). However, oil and gas companies target these low resistivity intervals development as a means to extend the life cycle of mature reservoirs (Kantaatmadja et al., 2014). Also, new technologies and improved computing capabilities enabled multi-scale modelling of complex and heterogeneous reservoirs for improved petrophysical properties and hydrocarbon reserves forecast (Hurley et al., 2012; Ringrose et al., 2008). Multi-scale modelling provides opportunities to unlock the commercial value of thin-bed LRLC reservoirs around the world in the form of additional hydrocarbon reserves.

Historically, thin-bed and LRLC hydrocarbon reservoirs are not recognizable using conventional well logs analysis reservoirs and therefore overlooked (Worthington, 2000). The resolution limit of the well logs cannot resolve and detect most of sub-meter thin beds and laminations. As a result, net sand pays in LRLC intervals are underestimated, which lowers the commercial viability of LRLC intervals.

Core analysis data which include porosity, permeability, petrography and mercury injection and capillary pressure data most often indicate thin reservoirs are of generally of poorer quality compared to conventional sandstone reservoirs (Carney et al., 2008). Also, the under-sampling and wide range of experimental analysis result in uncertainty in core plug data which do not represent the properties of millimetre-to-centimetre scale beddings. As a result, permeability data based on experimental results of heterogeneous core plugs have a broad range of values that are not accurate for representing any single rock type that makes up the heterogeneous rock (Ringrose et al., 2014). The uncertainty occurs because, up to 80% of thin sandstone layers in a thin bed reservoir are below the thickness of a standard core plug diameter of 25 mm (Passey et al., 2006). As a result, current well log analysis and conventional core analysis underestimate net sand pay, hydrocarbon saturation and hydrocarbon reserves in LRLC reservoirs (Kantaatmadja et al., 2014).

1.2 Challenges In developing thin-bed and LRLC reservoirs

This section summarizes the challenges faced when describing reservoir properties and forecasting hydrocarbon reserves in thin-bed and LRLC pay. These challenges include resolution limitations of well logs, inadequate petrophysical models, low resistivity pay, and complex geology.

1.2.1 Well Log Resolution Limitations

The difficulties encountered in developing thin bed LRLC reservoirs are attributed to the thin sandstone and mudstone layers that are below the resolution limits of conventional well logs. Resistivity well logs cannot detect beddings that are below one meter in thickness (Passey et al., 2006). As a result, well logs cannot resolve and detect beddings and laminations with thickness in the millimetre-to-centimetre range (Passey et al., 2006). Well logs measure petrophysical properties such as resistivity that is converted into water saturation using petrophysical models such as the Archie equation. The Archie equation has derivatives such as the Shaly Sand Model which are typically used in heterogeneous reservoirs. The well logging tools are constrained by their limited resolution where they can only resolve and detect rock layers that are at least 1 meter thick (Manescu et al., 2010). As the well logging tools are unable to detect very thin beds, the measured resistivity is averaged and biased towards the lower end(Eshimokhai et al., 2011). Well logs indicating high water saturation in these low resistivity pay which also translates into low hydrocarbon reserves estimates. Also, this causes heterolithic intervals with thin sand beddings are often excluded as net pay by the well logs analysis cut-off method (Passey et al., 2006).

1.2.2 Incompatible Petrophysical Models

A significant challenge in characterizing LRLC reservoirs is that current petrophysical models developed to correlate well log measurements to reservoir rock and fluid properties are only applicable in specific geology. Petrophysical models such as Archie Equation and its derivatives such as the Simandoux, Shaly Sand and Timur Equations for water saturation interpretation are currently not appropriate for thinly bedded formations (Passey et al., 2006). Therefore, there is a need for models to improve the interpretation of LRLC pay to determine the reservoir properties more accurately. However, improving current models require well log tool with an improved resolution that can resolve and measure the petrophysical properties of very thin beds common in LRLC reservoirs. This limitation remains a significant obstacle.

1.2.3 Low Resistivity Pay

Thin bed LRLC reservoirs exhibit lower than usual resistivity measurements by that indicate high water saturation levels and low hydrocarbon saturation(Jackson et al., 1999; Nordahl, 2004; Ringrose,Nordahl, et al., 2005). The low resistivity in LRLC pay is attributed to other small-scale heterogeneities. These small scale heterogeneities include millimetre-to-centimetres scale mud drapes, and layers of varying angles, geometries and high-resolution cyclicity (Gupta et al., 2001). These small scale heterogeneity non-uniform porosity and permeability distribution at different volume sizes (Carney et al., 2008). Also, the conductive minerals in mudstone layer tends to retain water and reduces the resistivity contrast between hydrocarbon and water-bearing intervals. The high content of conductive minerals such as pyrite, mica and iron can also contribute to low resistivity pay (Kantaatmadja et al., 2014; Worthington, 2000). As a result, the net pay potential of the thins sandstone are masked by adjacent mudstones and are often overlooked.

1.2.4 Complex Geology of Thinly Bedded LRLC reservoirs

Thin bed and LRLC reservoirs such as heterolithic tidal deposits are developed in coastal environments such as wave or tidal dominated estuaries and deltas (Martinius et al., 2005). These environments include external levees, depositional terraces and during the stages of channel abandonment(Hansen et al., 2015). These depositional processes create alternating layers of sandstone and clay and mudstone. These heterogeneous layered rocks have variable sedimentary structure and varying bioturbation intensity. The dimensions of these sedimentary features occur at millimetres to meter scales. The multi-scale heterogeneity in thin-bed LRLC reservoirs causes petrophysical properties variations that have a significant impact on the hydrocarbon reserves and production forecasts (Massart et al., 2016).

Thin bed and LRLC reservoirs often consist of several rock types which include rippled bioturbated heterolithic rock and bioturbated muddy sandstone (Carney et al., 2008). The rock type diversity results in significant variations in terms of petrophysical properties. In addition, rocks of the same type may also exhibit petrophysical properties variations that depend on factors such as the geometry of the mud drapes and the thickness of the laminations (Massart,Jackson,Hampson, & Jackson, 2016) and the bioturbation intensity (Chai et al., 2008). These factors can affect the flow properties of rocks at different length scales and volumes sizes which makes forecasting reservoir properties challenging. The thin beddings in thin-bed LRLC reservoirs also grade vertically and laterally into sand reservoirs or clay dominated non-reservoirs which causes difficulty in recognizing identifying net sand pay for volumetric analysis (Carney et al., 2008; Chai et al., 2008). These complexities associated with thin bed formations have a significant impact on hydrocarbon reserves and production forecast uncertainty as they affect flow properties such as permeability differently at different volumes scale (Massart et al., 2016; Nordahl, 2004).

Besides, thin-bed LRLC reservoirs that consist of tidal deposits have very complex reservoir architecture where the tidal sands bars that make up the reservoir may not be vertically or horizontally connected. As a result, extracting the hydrocarbon in place is very difficult resulting in average 60% of the resources in tidal sand reservoirs to be overlooked and remain unexploited due to the complex reservoir architecture and connectivity (Oifoghe, 2014; Wood, 2004).

1.3 Opportunities

Despite the challenges faced in characterizing and developing LRLC reservoirs, thin-bedded LRLC reservoirs are increasingly important to countries like Norway, Alaska, Canada, Venezuela and Russia where such reservoirs are conventional and in abundant. (Martinius et al., 2005). There are LRLC reservoirs that produced a commercially viable amount of despite the well logs interpreting high water saturation in LRLC intervals (Kantaatmadja et al., 2014; Worthington, 2000). Hence there is keen commercial interest to improve the evaluation of these reservoirs to improve the prediction of hydrocarbon reserves and production from heterolithic deposits. Besides, there is a good potential that LRLC intervals in existing fields can contribute to the production and extend the life cycle of mature reservoirs (Kantaatmadja et al., 2014).

Experience in Malaysia has demonstrated that low net to gross LRLC reservoirs has produced commercial amounts of hydrocarbon despite interpreted water saturations of 70% from the well logs (Chai et al., 2008). Similarly, another well in Malaysia produced up to 3000 barrels of oil per day for several years from an LRLC interval despite perceived high water saturation measurements from the well logs (Kantaatmadja et al., 2014). These cases support the perception that current reservoir characterizations methods still overlooked the substantial amount of hydrocarbon reserves in existing thin bed LRLC reservoirs. Studies in Malaysia also estimate that LRLC reservoirs may contain tens of millions of barrels of untapped hydrocarbon reserves in Malaysian oil and gas fields (Kantaatmadja et al., 2014).

In Norway, small scale centimetre-to-meter reservoir modelling and description of thinly bedded heterolithic hydrocarbon reservoirs have resulted in improved reserves estimates and recovery by up to 55% for one heterolithic reservoir compared to preliminary estimates using conventional coarse gridded reservoir modelling with meter scale resolutions (Elfenbein et al., 2005; Martinius et al., 2005). This experience in Norway demonstrates the value of improving the reservoir models of heterogeneous reservoirs for improved reserves and production estimates.

Despite the lucrative opportunities in thin-bed LRLC reservoirs, current reservoir model workflows exclude flow properties of sub-meter beddings that are below the resolution of well logging tools including. Also, Routine Core Analysis of core plugs does not represent the flow properties of thin sandstone layers below the thickness of standard core plugs (Passey et al., 2006). Routine Core Analysis data are used the Representative Elementary Volume in current reservoir models. Therefore, reservoir models that are based on well logs and core plug data are unreliable in predicting hydrocarbon reserves in thin-bed and LRLC reservoirs.

This thesis proposes using X-Ray Micro-CT (XMCT) Imaging and Digital Core Analysis (DCA) to characterize reservoir properties at the millimetre-to-centimetre scale. The flow properties such as porosity and permeability of thin sandstone layers contribute to a multi-scale workflow in reservoir model, which could unlock additional net sand pay and hydrocarbon reserves with more certainty. Multi-scale modelling of thin-bed reservoirs has increased hydrocarbon recovery forecast by 10% to 20% compared to conventional coarse grid modelling (Ringrose et al., 2008). Multi-scale modelling additional hydrocarbon reserves by up to 16 million barrels in a large oilfield in Norway which uses the meter scale bedform model to incorporate small scale heterogeneity in its reservoir model (Elfenbein et al., 2005).

1.4 Research Questions

The research question listed below addresses the complex geology of thinly bed LRLC reservoirs and its impact on hydrocarbon reserves in place.

- How can computation of porosity and permeability small rock samples representative of small-scale thin beddings sandstone in heterolithic deposits improve estimates of effective flow properties and hydrocarbon reserves estimates?
- How reliable and valid are X-Ray Micro-CT Imaging (XMCT)and DCA in calculating porosity and permeability of samples from a thin bed LRLC reservoir compared to experimental Core Analysis results?
- How do small scale flow properties characterizations and Image Analysis and DCA contribute to multiscale workflow in reservoir modelling and improve hydrocarbon reserves estimates in thinly bed LRLC reservoirs?
- How does the geometry of small-scale heterogeneities such as thin sandstone layers, carbonate laminates and mud drapes affect the effective permeability performance of core plugs examined in this thesis and their potential impact at a larger scale?

1.5 Objectives of the Research

Our main objective is to improve the characterization of thin-bed and low-resistivity/low-contrast reservoirs at millimetre-to-centimetre scale by using XMCT imaging and Digital Core Analysis. We use these methods to compute porosity and permeability of small-scale samples that represent millimetre-to-centimetre thin sandstone layers and other small scale heterogeneity such as low permeability laminates. This small-scale heterogeneity affects reservoir properties at different length scales. The following methods listed below are applied to achieve the objective.

- Apply sedimentology to characterize the lithofacies and facies association to interpret the depositional environment that makes up the geological framework of the reservoir. Sedimentology also describes the reservoir in terms of the abundance of the heterolithic deposits and their lateral and vertical connectivity that affect reserves and production forecasts.
- Apply X-Ray Micro-CT (XMCT) Imaging Analysis, 3D Visualization Image Analysis and Digital Core Analysis
  - o to compute porosity and permeability of very small rock samples (core plugs and mini plugs) representing thin sandstone layers in heterogeneous rocks.
  - o We validate the computed porosity and permeability of the mini-plugs using Digital Core Analysis with experimental core plug and the NER permeameter measurements.
  - o Determine if the porosity and permeability of thin sandstone layers in heterolithic rock types are comparable to reservoir sandstone reference samples.
  - o Determine if the connectivity and continuity of the thin sandstone layers are a key factor to the reservoir quality of the heterolithic core plugs.

1.6 Data

This study has requested the following data and samples from an LRLC reservoir in Malaysian from PETRONAS, the national oil company of Malaysia. The most relevant resource to this study is the core plugs from the reservoir for pore network modelling and digital core analysis. Other data that are also crucial to this study are the well logs, sedimentological description and core analysis reports.

Table 1.1: List of data requested from PETRONAS for this study.

No.	Data Type	Details
1	**Well Logs**	Final Well Logs/Digital Laser files Conventional Suite Gamma Ray Shallow and Medium Resistivity Logs Neutron Density
2	**Petrographic Reports**	Petrographic reports on thin section
3	**X-Ray Diffraction**	X-Ray Diffraction Report Clay Analysis
4	**Geological Reports**	Sedimentology
5	**Routine Core Analysis**	Routine Core Analysis Reports on core plugs
6	**Special Core Analysis**	Special Core Analysis reports on core plugs Vertical plugs from thin beds for kV Capillary Pressure Pc Relative Permeability kr

CHAPTER 2 : LITERATURE REVIEW

This chapter reviews the causes of LRLC pay in thin-bed reservoirs, the limitations of well log resolution and analysis in characterizing thin beds and the availability of current methods and technology for characterizing the flow and reservoir properties in thin-bed reservoirs.

2.1 Causes of low-resistivity/low-contrast pay

The oil and gas industry acknowledged thin-bed and LRLC reservoirs as being a significant source for the world's hydrocarbon reserves. Still, these reservoirs are mainly overlooked due to perceived reduced commercial viability and technical challenges in hydrocarbon volumetric analysis of the hydrocarbon reserves potential (Passey et al., 2006). Also, the previously abundance of conventional and easy to produce sandstone reservoirs puts less emphasis on the study of thin-bed and LRLC reservoirs, which are considered to be financially risky.

LRLC reservoirs generally have low resistivity measurements based on the well logging tools measurements. However, there is no reference or absolute value of a low resistivity pay. This lack of reference is because LRLC reservoirs around the world exhibit a wide range of low resistivity values (Worthington, 2000). Instead, the low resistivity characteristic of LRLC pay is due to the relatively low conductivity difference and contrast between the adjacent reservoir sandstone and non-reservoir mudstone beddings (Oifoghe, 2014).

Worthington (2000) reviewed low-resistivity/low-contrast reservoirs around the world and identified six leading causes of low resistivity nature in these reservoirs, which are:

- Laminated Shale sequence
- Fresh Water Formation
- Conductive Minerals
- Fine-Grained Sands
- Internal Microporosity
- Superficial Microporosity

Worthington (2000) also reviewed conventional well log analysis limitations such as Archie's equation in evaluating properties of LRLC reservoir. Also, Passey (2006) reviewed current methodologies and technologies used for appraising low resistivity thin-bedded reservoirs. Besides, Passeey (2006) also discussed the limitations of current well logs and petrophysical models in appraising thin bed geology. These limitations will each are discussed in the following sections.

2.1.1 Laminated Shale Sequence

One of the first causes of low resistivity pay is the occurrence of a laminated sequence that consists of thin sandstone and mudstone layers. The thickness and geometry of these laminates are usually below the resolution of conventional well logs. As a result, these well logs cannot detect and resolve these thin laminates. Besides, the well logs average the resistivity of the thin-bed intervals, which is biased to lower values (Passey et al., 2006; Worthington, 2000). The low average resistivity values in LRLC reservoirs result in underestimated net sand pay and hydrocarbon reserves (Manescu et al., 2010). The effects of thin beds and laminations are discussed extensively in section 2.3.

2.1.2 Fresh Water Formation

Freshwater is present in some thinly bedded reservoirs contributes to poor resistivity contrast in the well logs. Freshwater intervals between hydrocarbon-bearing zones create poor contrast between freshwater and hydrocarbon-bearing layers which makes differentiating hydrocarbon and water-bearing intervals difficult as both fluids have similar resistivity range. (Heavysege, 2002).

Also, freshwater formation causes poor resistivity contrast between adjacent sandstone and freshwater-bearing mudstone layers. The mudstone containing conductive minerals results in low resistivity pay (Heavysege, 2002). Poor contrast occurs between these zones because water saturation is indirectly measured from resistivity measurement using the Archie equation or its derivative such as Shaly Sand models. Due to low resistivity values in low contrast intervals, well logs interpret high water saturation (Oifoghe, 2014). These issues highlight that conventional petrophysical evaluation of clean and shaly formations cannot interpret LRLC reservoir intervals for accurate hydrocarbon reserves and net sand pay estimates (Worthington, 2000). Resolution limitation of well logs that cannot resolve thin sand beds in thinly bedded LRLC reservoirs is the leading cause to these issues.

2.1.3 Conductive Minerals

Conductive minerals contribute to low resistivity readings in reservoirs but are rarely cited as the leading factor to low resistivity phenomena (Heavysege, 2002). However, studies have shown that there are mineral types that contribute to low resistivity pay. For example, large concentrations of iron-bearing minerals such as pyrite have been identified as factors to low resistivity pay (Worthington, 2000). Another example shows that content of 7% pyrite of the total solid by volume has been quantified as the critical level that would induce low resistivity pay (Worthington, 2000). Other minerals of the same category include glauconite and iron-bearing mica which exhibit a high level of conductivity. These conductive minerals skew the reservoir resistivity to the lower end of the spectrum (Worthington, 2000). Figure 2.1 below shows a reservoir affected by conductive iron-rich minerals.

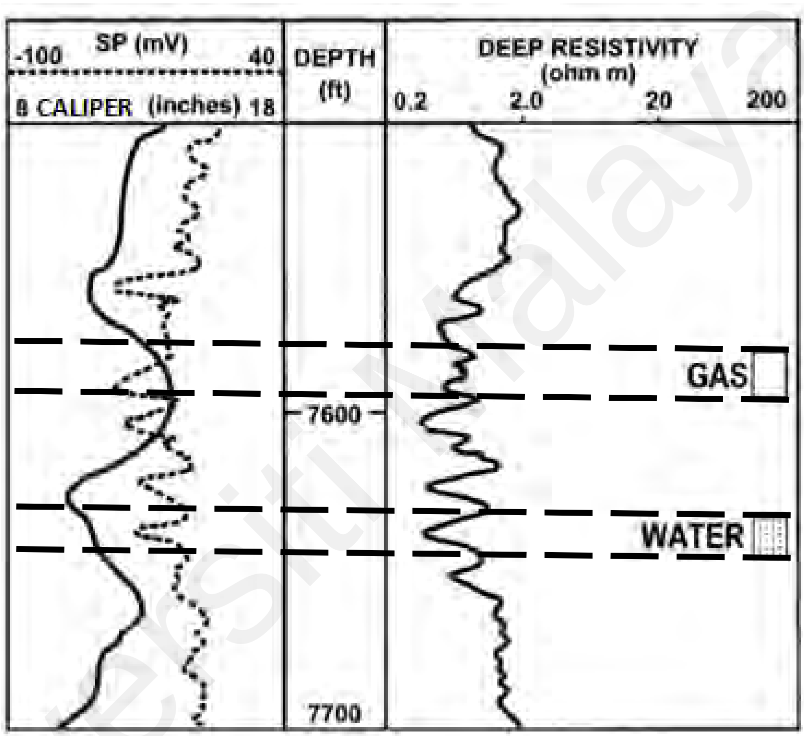

Figure 2.1: An example of a low resistivity reservoir in the Eutaw play, Mississippi. Conductive minerals cause poor resistivity contrast between the gas and water-bearing intervals (Worthington, 2000).

2.1.4 Fine-Grained Sands

Fine to very fine grains sands with a particle diameter range between 2mm to 4mm (Tiab et al., 2012) can affect LRLC reservoirs in two ways. LRLC reservoirs in Malaysia have also been described as being fine-grained (Chai et al., 2008).

2.1.4.1 Fine sands acting as minerals

The very fine sands behave like minerals such as quartz which has high conductivity due to large surface pore area which allows water in the reservoir to exist as a continuous phase resulting in high conductivity and low resistivity measurements (Rink et al., 1974). Also, very fine grain sands restrict the capillary pressure, which causes high initial irreducible water saturation and low resistivity values (Vajnar et al., 1977). The impact of this excess conductivity will have to be addressed in the water saturation algorithm if it is identified as a cause of low resistivity pay.

2.1.4.2 High Irreducible water saturation

Very fine grains cause high irreducible water saturation which exists as a continuous phase and increases the conductivity within the formation. This impact is more significant than the first. Therefore, the water saturation must be evaluated and thoroughly understood before it is designated as immobile or free fluid (Worthington, 2000).

Firstly, to address high irreducible water saturation in low resistivity pay, we need to use an appropriate water saturation algorithm. This approach is a similar approach when addressing freshwater reservoirs. For example, Shaly-Sand analysis is not appropriate if there is a significant silt component which tends to be incorrectly identified as a distinct mineral despite its principally consisting of quartz with traces amount of dolomite. The study on fresh to brackish water reservoirs highlights the significance of the water saturation model and the relationship between different factors that cause low resistivity pay (Worthington, 2000).

The second action is to assess the proportion of free fluid present in the pore space. The is typically achieved by determining the number of movable hydrocarbons on a level by level approach or correlating the interpreted water saturation to the irreducible water saturation for a particular group of sands. Spontaneous Potential Logs which are used to differentiate between permeable and impermeable formation by measuring the spontaneous potential difference between the borehole and the surface are typically used to evaluate movable hydrocarbons by studying the characteristics of the flushed (permeable) and undisturbed impermeable zones. Magnetic resonance logging is also used to evaluate movable hydrocarbons or free fluid under irreducible water saturation (Worthington, 2000).

Figure 2.2 illustrates an example of a fine-grained sands reservoir in the Gulf of Mexico. The deep induction log can resolve the hydrocarbon-bearing intervals that have resistivity as low as 0.3 ohms which indicate a water saturation of 80%. Yet, it produced 470 barrels of dry oil per day. The water zone has a resistivity of 0.2 ohms. High irreducible water saturation and large pore surface area in fine-grain sediments cause a low contrast between the water and hydrocarbon intervals (Worthington, 2000).

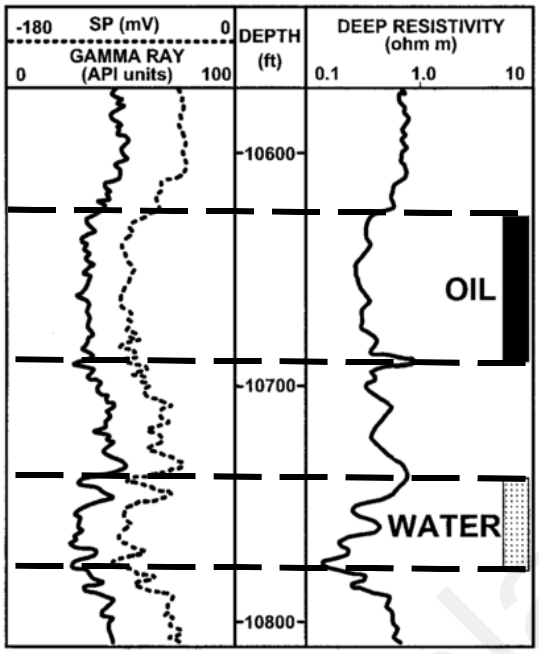

Figure 2.2: A wireline log from a clean and fine sands reservoir in Tertiary Sands, Gulf of Mexico. High capillarity in the fine-grain sediments causes low resistivity and low contrast issues between the water and oil intervals (Worthington, 2000).

2.1.5 Internal Microporosity

Microporosity is pore spaces that are less than 1 micron in diameter, exists in the rock matrix. Also, microporosity is not associated with clay induced microporosity which can be distinguished as overgrowth microporosity. Microporous reservoirs are principally associated with carbonates and granular chert reservoirs in which the microporosity level can be as high as 50%. In microporous reservoirs, during the resistivity measurement, the conductivity is assumed to be uniformly ionic without considering the effects of surface conduction effect. This assumption requires a correction on the resistivity measurement. In reservoirs consisting primarily of chalk, the conductance is associated with the high pore surface area. The strategies for addressing microporosity are similar to the ones used for freshwater formation and fine-grained reservoirs. These strategies include applying the appropriate water saturation method which divides the water into immobile microporosity or movable microporosity (Worthington, 2000).

Another right approach in studying microporosity is by studying the pore size distribution. High capillarity is usually not associated with unimodal distribution with pore diameters between 5 to 10 microns. Meanwhile, a bimodal distribution of micropores and macropores indicate a microporosity problem most likely associated with internal microporosity. If a reservoir is largely microporous, magnetic resonance logging can be appropriate in evaluating the flow potential (Worthington, 2000).

After having identified microporosity as the main factor in LRLC behaviour, its effect on the saturation exponent is studied by using strategies such as controlled-flow continuous injection. This strategy includes water saturation near the irreducible level (Worthington, 2000).

Figure 2.3 illustrates a wireline log in a microporous limestone reservoir in Texas. The bottom part of the wireline log is less than 1.0 ohm which translates to water saturation of 66%. The resistivity on the upper part is one order higher in magnitude, which leads to the producing gas interval being interpreted as water-bearing. The high-water saturation in the gas interval is caused by immobile water present within and around the grains, which is validated by mercury injection and scanning electron microscopy. The conclusion is that the intergranular porosity and microporosity within the upper and lower intervals have different fluid phases (liquid or gas).

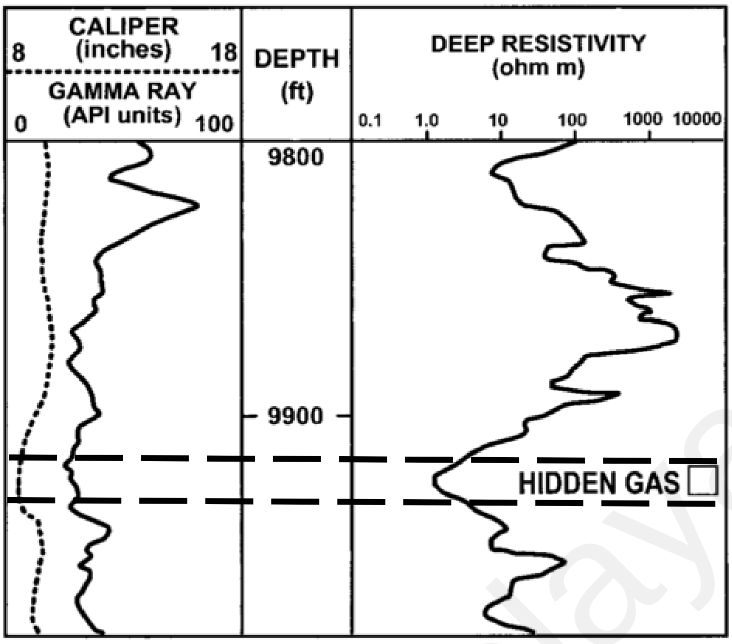

Figure 2.3: A wireline log from a microporous reservoir in the Rodessa Limestone, Texas. The gas interval has low resistivity due to immobile water in intragranular pores (Worthington, 2000). Due to its low resistivity, the gas interval was interpreted as water.

2.1.6 Superficial Microporosity

Superficial microporosity refers to situations where the micropores are associated with minerals overgrowth which developed externally from the original granular matrix. This category of microporosity, like internal microporosity, can be distinguished petrophysically. Superficial microporosity include issues associated with Internal Microporosity and Fine-Grained Sands. Figure 2.4 shows low resistivity intervals caused by superficial microporosity in a well log from an Indonesian field (Worthington, 2000).

Superficial microporosity occurs as clay minerals that coat quartz matrix The conductivity of these clay minerals causes excess conductivity and low resistivity characteristics which cannot be addressed and corrected using the shaly-sands algorithms.

The widely used Waxman-Smiths model used in well logs analysis is not appropriate for addressing superficial microporosity (Worthington, 2000).

As explained in the previous sections, strategies to address superficial microporosity can be divided into two parts which are evaluating the water saturation and dividing the water into free fluid and immobile fluid (Worthington, 2000).

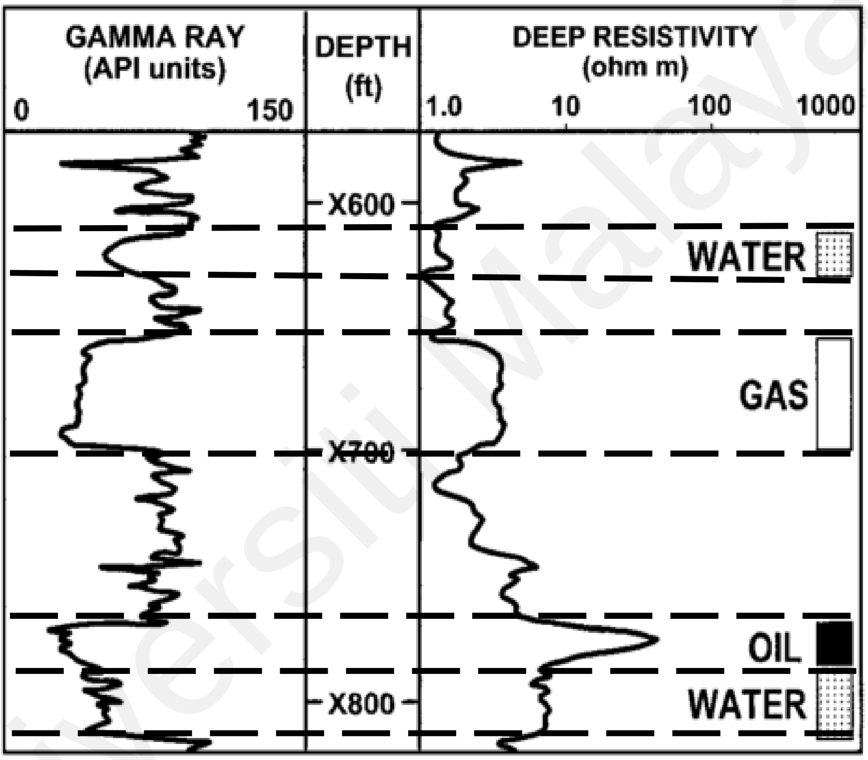

Figure 2.4: Wireline log from a superficially microporous reservoir in the Attaka field, Indonesia. The 'low resistivity' upper section gas interval is microporous compared to the 'high resistivity' oil interval in the bottom (Worthington, 2000).

2.2 Well Log Resolution Limitation

A significant amount of hydrocarbon is potentially stored in thin beds and laminae within thinly bedded reservoirs (Figure 2.5) that are below the resolution limits of conventional well logging tools (Jackson et al., 1999; Passey et al., 2006; Sun et al., 2014). Thin beddings and their associated anisotropy affect pore structure, fluid distribution, mechanical properties, thermal and hydraulic behaviours(Yun et al., 2013). As a result, evaluating the petrophysical properties in thinly bedded reservoirs using conventional well logging methods is challenging (Oifoghe, 2014; Sun et al., 2014). Current well logging tools have resolution constraints in which could not be resolve beddings that are below one meter. As a result, well log s cannot accurately measure petrophysical properties required to estimate the amount of hydrocarbon in place.

Figure 2.5: An example of a thin bed outcrop. Deep-water Turbidites, Permian Collingham Formation, Baviaans Syncline, Laingsburg Karoo, South Africa. Picture by Anthony Spragues (Passey et al., 2006)

2.3 Thin Beds and Laminations

Thin-bed and LRLC reservoirs such as the heterolithic deposits encountered in Norway are categorized as marginal reservoirs(Brandsæter et al., 2001) due to the interpreted low hydrocarbon reserves and low recovery factors that can be as low as 30% (Elfenbein et al., 2005). This type of reservoir is also common in Alaska, Canada, Venezuela and Russia. (Martinius et al., 2005) . Thin-bed and LRLC reservoirs consist of sedimentary facies that have bi-modal and multi-modal grain size distribution with frequently occurring alternating layers of coarser sandstone and very fine mudstone/siltstone. The sandstone and mudstone layers thickness range from decimetre to centimetre scale ranging from laminae that are below 0.05m, sets of 0.05m to 2m to sequences of 5-100m or more (Wen et al., 1998). Due to the presence of varying types of facies and sedimentary structure with length scales ranging from small bedform scale to reservoir scale, representing heterogeneous facies or rock types with different geometries in a reservoir model is challenging (Jackson et al., 1999; Wen et al., 1998). The net ratio of sand thickness relative to the gross thickness of the reservoir in thin-bed reservoirs ranges between 0.3 to 0.9 with recovery factors between 15% to 40% (Brandsæter et al., 2001; Martinius et al., 2005). The thickness of the lamina, permeability variability, and flow direction relative to the laminae orientation are also significant factors on the reservoir quality and fluid flow behaviour (Massart et al., 2016; Ringrose et al., 1993). The Norwegian experience emphasizes the importance of both small scale and large scale heterogeneities on reservoir quality and performance (Brandsæter et al., 2001; Jones et al., 1995). Their experience demonstrated that hydrocarbon recovery could be improved if we take a multi-scale approach in reservoir characterization, which leads to improved development and hydrocarbon recovery strategies (Elfenbein et al., 2005). However, describing these reservoirs at different scales is still very challenging.

Figure 2.6 from Passey et al. (2006) illustrates a significant problem with thinly bedded reservoirs with relation to the resolution of the well logs and scale of the thin beddings. The plot of cumulative per cent reservoir versus bed thickness indicates the reservoir is from a 'tidal environment' which shows that all the bed thickness in the tidal reservoir are below the resolution of the Gamma Ray (GR) and the image logs. In this reservoir, 80% of the net reservoir consists of beddings with thickness below the diameter of a standard core plug.

The following list below provides the rank of well log tools with the lowest resolution at the top to the highest resolution at the bottom. It is noted that the absolute resolution of the tool depends on other factors besides vertical resolution such as the sampling rate, logging speed and processing methods.

1. Spontaneous Potential (SP)
2. Deep resistivity
3. Gamma Ray (GR)
4. Bulk density, neutron porosity, and acoustic
5. Very shallow resistivity
6. Dip meter and electric borehole image (EBI)

Increasing resolution from 1 to 6

One the of most crucial well log tools used to determine the hydrocarbon capacity of a reservoir is the deep resistivity tool. Therefore, the resolution of the deep resistivity tool defines the lower limit of bed thickness that can be detected. The deep resistivity tool has a vertical resolution of 2 feet or 0.6 meters. However, they still cannot resolve beddings and laminae with thickness at millimetre-to-centimetre scale. This limitation highlights the disadvantages of current well logging tools in characterizing thin-bed and LRLC reservoirs.

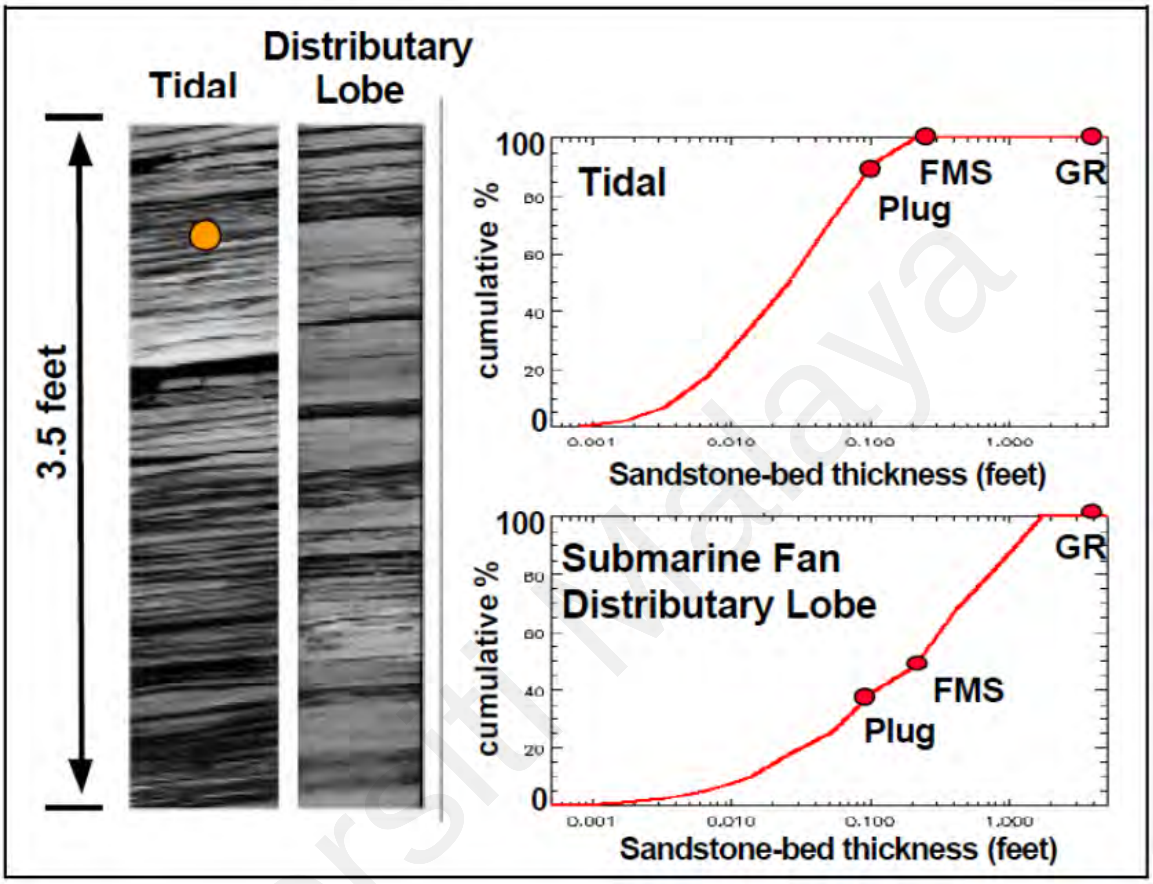

Figure 2.6: Core images from two thin-bed reservoirs and their bed thickness distribution plots showing the approximate resolution of core plugs and Gamma Ray(GR) and borehole image logs (Passey et al., 2006)

2.4 Rock Type Identification

Another challenge in characterizing thin-bed and LRLC reservoirs is the identification of rock type or facies which are categorized based on sand and mud proportions, the geometry of the mud drapes and bioturbation intensity (Gupta et al., 2001). The facies identification process is crucial to identify LRLC pay and characterize the effects of heterogeneity on flow potential between different rock types (Chai et al., 2008). We identified the identification of rock types and characterizing the petrophysical properties as an essential part of a multi-scale workflow for reservoir simulation (Hurley et al., 2012).

Due to the variety of facies in the heterolithic tidal sandstone reservoir encountered in Norway, differentiating these different facies and reservoir from non-reservoir facies or rock types has been challenging (Martinius et al., 2005). The limitation of current well logging technology which has a vertical well log resolution of between 0.5 meters to 1 meter constrains the identification of these rock types. The resistivity of the thin beds is averaged and biased to low resistivity values. These low resistivity values do not comply to the conventional shale volume cut-offs for hydrocarbon bearing pay(Anyiam et al., 2016) which causes underestimated net sand pay and overestimates high water saturation based on the Archie Model(Mode et al., 2015; Worthington, 2000).

Due to the averaging effect, thin mudstone and sandstone layers have the same gamma-ray and resistivity reaction and are presumed to be a single rock type. Despite the availability of tools with improved vertical resolution such as micro-resistivity tools, borehole imaging tools and electromagnetic propagation tool, these devices remain scarce (Gupta et al., 2001) and expensive. As a result, without access to the actual core data from the LRLC interval, most well logs may have incorrectly interpreted sand pay in heterolithic intervals as non-reservoir shaly sand or mud dominated facies (Chai et al., 2008).

To sum up, we can categorize the different rock types in a thin bed LRLC reservoir by grain size, mud-to-sand ratios, and bioturbation intensity. This categorization is one of the first steps in modelling the impact of small-scale heterogeneities on effective flow properties which we often overlooked in reservoir models.

2.5 Hydrocarbon Pore Thickness

To assess the amount of hydrocarbon in a reservoir, determining the original hydrocarbons in place (OHIP) is a crucial factor. The following volumetric Equations 4 calculates the original oil-in-place (Passey et al., 2006):

Equation 4: Original Oil in Place equation

$$\mathbf{OOIP} = \mathrm{A.h.}(1 - \mathrm{S_{wi}}).7758.\left(\frac{1}{\mathrm{B_{oi}}}\right) = \mathrm{A.HPT.}7758.\left(\frac{1}{\mathrm{B_{oi}}}\right)$$

Where OOIP is Original Oil in Place (stock tank barrels, STB)

A= gross reservoir area (acres)

h= Average oil-bearing rock thickness (feet)

ø= average total porosity of oil-bearing rock (fraction)

S_{wi}=average total initial water saturation of oil-bearing rock (fraction)

B_{oi} = the average initial oil formation volume factor (reservoir barrels/stock tank barrels or RB/STB)

HPT=h.ø. (1 -Swi) = hydrocarbon pore thickness (feet)

In standard well log analysis, the summation for HPT only include intervals that are assessed as a net reservoir or net pay. Geologists and petrophysicists apply cut-offs to parameters such as porosity, shale volume, water saturation etc. to differentiate net pay from non-net pay. For example, intervals with less than 12%, porosity, shale volume exceeding 50% and water saturation exceeding 80% are categorized as non-reservoir. These cut-offs can have significant implications in thin-bed and LRLC reservoirs where resolution limits of well logs overestimate water saturation readings. Cut-offs may also affect hydrocarbon pore thickness and net sand thickness measurements which could lead to inadequate hydrocarbon reserves and production forecast. (Passey et al., 2006).

For a thinly bedded reservoir, the net error for calculating the hydrocarbon pore thickness is due to the three main factors (h, ø and (1 -Swi)) in the HPT equation. The findings below are based on a comparison between the actual net to the gross and cut-off method by Passey et al. (2006):

- Conventional cut-off methods estimate sand thickness as higher if actual net sand is more than 50%.
- Measured sand porosity is an average of fine-scale sand and shale beds within the sand interval that are below the porosity-tool resolution.
- Measured and averaged resistivity readings in a sand interval containing embedded shale laminae is reduced by a low fraction of the low-resistivity shale layers. Reservoirs that exhibit this characteristic are called low-resistivity/low-contrast pay due to the difficulty in differentiating reservoir and non-reservoir intervals due to poor resistivity contrast.

Figure 2.7 shows that well logs underestimate net to gross values compared to the actual value due to resolution limitation. The net to gross underestimation causes low hydrocarbon reserves forecasts in thin-bed and low-resistivity/low-contrast hydrocarbon reservoirs.

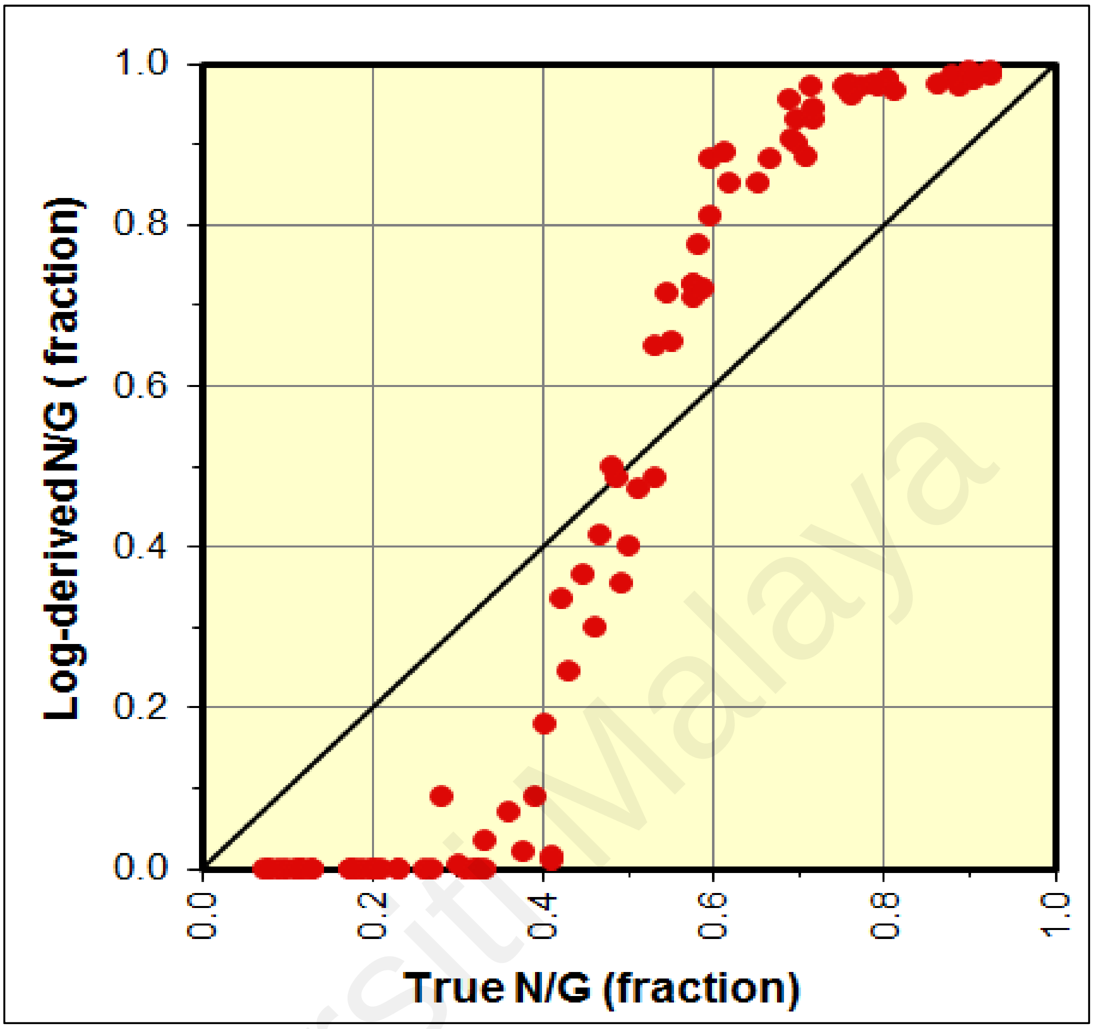

Figure 2.7: Actual Gamma Ray and Well log derived net sand fraction or Net to Gross (N/G) for a 130 feet thin bed-bed reservoir simulation (Passey et al., 2006). This figure shows that log derived net-to-gross is lower compared to actual net-to-gross.

2.5.1 Shaly Sand Analysis

Well log measurements require mathematical models to convert the measurements into their equivalent petrophysical properties such as porosity and water saturation. For example, Neutron-Density logs interpret porosity and resistivity measurements to interpret water saturation.

Some of the mathematical models used to interpret petrophysical properties are Shaly Sand Analysis which is based on the Archie Water Saturation Equation. However, these methods do not incorporate the effects of thin beds on the well log measurements as they specifically target the effects of dispersed clay on well-log measurements for resistivity and not the effects of alternating sand and shale. The effects of dispersed clay and interbedded shale in sandstone on resistivity measurements are also different. Consequently, the correction used in these two analyses is not appropriate for resistivity measurements in thin-bedded reservoirs. (Passey et al., 2006).

2.5.2 Archie and Dual Water Examples

This section examines the outcomes of using Archie and Dual Water Analyses in determining reservoir properties and the net to gross in a thin bed reservoir. Passey (2006) uses a thin bed simulator to create a synthetic dataset using Archie and Dual Waters analyses summarized below.

Summary of the comparison between the Archie and Dual Water analyses with actual values shown in Table 2.1.

- Applying cut-off derived net sand to Archie and Dual Water analyses reduce the HPT by up to 1/3 from the actual value. This error is a combination of the three factors in the HPT equation - h, ø and (1 -S_{wi})
- Dual Water with cut-offs has better results in terms of water saturation, but the HPT value is still 1/3 of the actual true value.
- The cumulative HPT are very low for the Archie and Dual Waters analyses.

- The Archie and Dual Waters analyses produce higher water saturation values compared to the actual value. Consequently, the calculated hydrocarbon saturation and volume estimates will be as lower.

Table 2.1: Archie and Dual Water Analyses (Passey et al., 2006)

Reservoir Property	**Model Values**	**Archie with cut-off**	**D-W with cut-off**	**Archie, no cut-off**	**D-W, no cut-off**
Net to Gross %	50	39	39	100	100
Sand porosity(frac)	0.3	0.24	0.24	0.22	0.22
Sand Sw (frac)	0.1	0.57	0.47	0.64	0.51
HPT (feet)	2.71	0.79	0.98	1.6	2.18
% of actual HPT	100	29	36	59	80

Passey et al. (2006) simulated the Hydrocarbon Pore Thickness values in Figure 2.8 to acquire the same results as seen in Table 2.1 but for 130 thin bed models. The horizontal axis shows the true HPT value while the vertical axis shows the HPT as a % of the true value for four methods which are Archie and Dual Waters with and without cut-offs. The following observations are derived from Figure 2.8:

- Conventional Archie and Dual Water analyses approach actual value when the ratio of net sand thickness to the gross reservoir thickness (sand-to-reservoir ratio) approaches 90%. Both models are less accurate in reservoirs with a sand-to-reservoir ratio lower than 90%.
- The cut-off method reduces the calculated HPT results for both Archie and Dual Water methods.

- Dual Water produces HPT and water saturation results that are closer to the real values, especially at the lower net to gross values. However, HPT is generally still 20% lower compared to the true value.

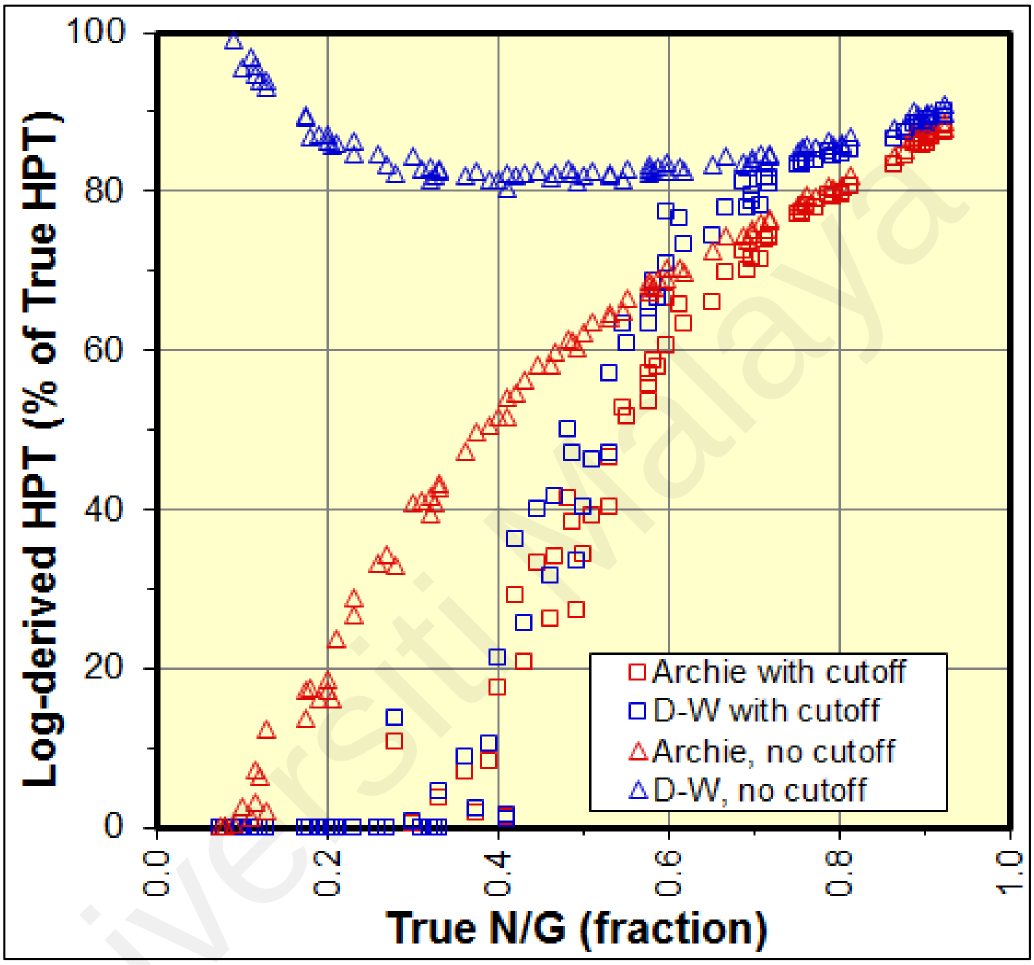

Figure 2.8: Log derived HPT for 130 simulated thin-bed reservoirs

Passey et al. (2006) have demonstrated that the use of cut-offs to differentiate reservoir and non-reservoir intervals are not appropriate in calculating OOIP. It is shown that using standard cut-offs in Archie and Dual Water underestimate the HPT and Water Saturation in thin-bedded reservoirs. Passey et al. (2006) demonstrated that conventional shaly sand methods used interpret well log measurements to underestimate parameters such as the hydrocarbon pore thickness (HPT) and water saturation which may lead to lower OOIP values.

2.6 Other challenges in characterizing thin-bed and LRLC reservoirs

The review on current cut off methods and shaly sand analyses used to interpret well logs discussed in previous sections shows that conventional well log analysis underestimates important petrophysical properties such as permeability. Resolution limitations of current well logging tools underestimate reservoir properties such as hydrocarbon saturation and sand porosity. As a result, well log measurements are biased towards low pay reserves. Besides, well logs analysis methods such as Shaly Sands method are incompatible with thinly bedded geology.

Other studies also identified other challenges encountered when appraising thinly bedded LRLC reservoirs around the world. These challenges are related to well logging tools resolution limitation, complex multi-scale heterogeneity and varying sedimentary structures. These complexities create difficulties in estimating primary petrophysical properties such as porosity, water saturation and net-to-gross. Also, these issues affect the measurement of other reservoir properties such as relative permeability and capillary pressure, which are essential for calculating the hydrocarbon capacity in the reservoir: We summarise thee challenges below:

- Variable and multiscale sedimentary properties cause difficulties in determining the effective reservoir and flow properties such as permeability, fluid saturations and capillary pressure (Elfenbein et al., 2005; Martinius et al., 2005; Tyagi et al., 2008)

- Upscaling the reservoir properties from a small scale such as the size of a plug progressively to the reservoir scale remains a challenge in reservoir modelling (Bastia et al., 2007). This problem is also described as a scale transition issue for upscaling reservoir properties in reservoir modelling (Nordahl, 2004).
- Determination of the lateral and vertical distribution and connectivity of the LRLC deposits is difficult (Bastia et al., 2007; Chai et al., 2008).
- Evaluation of the effects of bioturbation in thin-bed reservoirs that could destroy or enhance porosity by either increasing or decreasing the isotropy of the sediment structure is difficult with current tools and methods (Ben-Awuah et al., 2015; Tonkin et al., 2010)
- Heterogeneity causes permeability anisotropy which makes it challenging to determine the effective permeability that affects hydrocarbon reserves and production forecast from thin-bedded reservoirs. (Elfenbein et al., 2005; Massart et al., 2016; Nordahl, 2004).
- Freshwater in some thin-bedded reservoirs causes low resistivity contrast which makes differentiating adjacent reservoir and non-reservoir rocks more difficult. (Heavysege, 2002). This poor contrast causes low resistivity and high water saturation measurements in LRLC pay (Worthington, 2000).
- Impact of mud drapes and geometries and its distribution of effective permeability in heterolithic and cross-bedded tidal sandstones (Massart et al., 2016; Massart et al., 2016)

Also, the deposition environments of thin-bed and LRLC reservoir may pose a challenge at the reservoir or regional scale. Thin-bed and LRLC reservoirs are interpreted to be part of tidal and deltaic deposits pose difficulties in terms of hydrocarbon recovery due to reservoir lateral and vertical connectivity. Commonly, 60% of the resources characterized in tidal/deltaic deposits are not extracted due to challenges such as poor connectivity between the sand deposits within the reservoir and lateral and vertical connectivity (Wood, 2004). As a result, the development of tidal/deltaic reservoirs requires a secondary recovery method, which can be financially risky. To mitigate the risks, detailed and multiscale 3-D fluid flow reservoir model of heterogeneous and complex tidal influenced reservoirs are essential for planning the hydrocarbon extraction and secondary recovery plans required for the field development process (Ringrose et al., 2008).

2.7 Overview of Thin Bed Technology

Thin bed LRLC reservoirs have always been a contentious issue in the oil and gas industry for decades due to the limitations of current well log technology. The main issues in appraising thinly bedded LRLC reservoirs are the limitation in characterizing its petrophysical properties for hydrocarbon estimates. New technology and improved methods have been continuously developed to address these issues to appraise and develop LRLC reservoirs economically.

2.7.1 High-Resolution Logs or Borehole Image

An effective tool described by Passey et al. (2006) to address thin-bed reservoirs is high-resolution logs or borehole image, which is used to distinguish thin beds in the reservoir at high resolution. After the thin beds are resolved, defined sets of boundaries called earth models from high resolution bore imaging is used in conjunction with forwarding models. These models were used for the logging tools to perform inversion, which creates improved measurement of the net pay in the thinly bedded interval (Oifoghe, 2014). As there are beddings that are thinner even for the high-resolution borehole image, the forward modelling inversion method using Borehole Image logs may have limitations in the application when encountering thin beds below the borehole image resolution.

2.7.2 Nuclear Magnetic Resonance (NMR)

Another emerging technology that is effective in appraising thin-bed reservoirs is the nuclear magnetic resonance (NMR) tool that has good potential to improve the measurement of hydrocarbon pore thickness (HPT) in thinly bedded formations. The NMR is useful in evaluating the producibility of hydrocarbon from shale dominated intervals in the well-logs. The NMR also qualitatively identifies the amount of free fluids of hydrocarbons in the reservoirs. Worthington (2000) has suggested that nuclear magnetic resonance be used to evaluate movable hydrocarbons and free fluids in an LRLC reservoir under irreducible water conditions. Categorizing the water in the reservoir into immobile(irreducible) and free fluids is a crucial strategy for evaluating the hydrocarbon reserves in LRLC reservoirs which can be achieved using nuclear magnetic resonance technology. However, nuclear magnetic resonance cannot identify thin beds directly but is a useful tool for measuring the cumulative hydrocarbon pore thickness in thin-bed reservoirs.

2.7.3 Bed-form Modelling

Bed-form modelling method as described by Ringrose et al. (2005) uses bed-form model blocks (0.1m x 0.5m x 0.5m) which contain the geometries and structures in the actual beddings and preserves the sedimentary structures such as ripple laminations. Each block contains several types of facies that represent a facies assemblage unique to a depositional environment, for example, a heterolithic facies assemblage in a tidal environment. Different bed-form model blocks are created with a range of sand and mud proportions and stratigraphic surfaces (wavy, laminae, lenticular, etc.) for every type of facies assemblage. The facies within the models are assigned petrophysical properties such as permeability and porosity integrated from well logs, actual core analysis data or simulated measurements (Theting et al., 2005). Fluid flow simulation using numerical calculation is applied to the bed-form models to calculate upscaled effective petrophysical properties such as permeability and capillary pressure in a larger reservoir. This method is also described by Elfenbein et al. (2005) as Process-Based Modelling. Bedform models can be used to investigate the impact of variable sandstone and mudstone structures and geometries in heterogeneous formations such as tidal heterolithic deposits. Bedform modelling simulates petrophysical properties such as relative permeability that is an essential factor in hydrocarbon reserves estimates and recovery strategies (Ringrose,Skjetne, et al., 2005). Bedform Modelling and Simulation (Figure 2.9) can be integrated with well logs analysis and upscaled to predict reservoir properties in intervals that have no core sample (Alam et al., 2014).

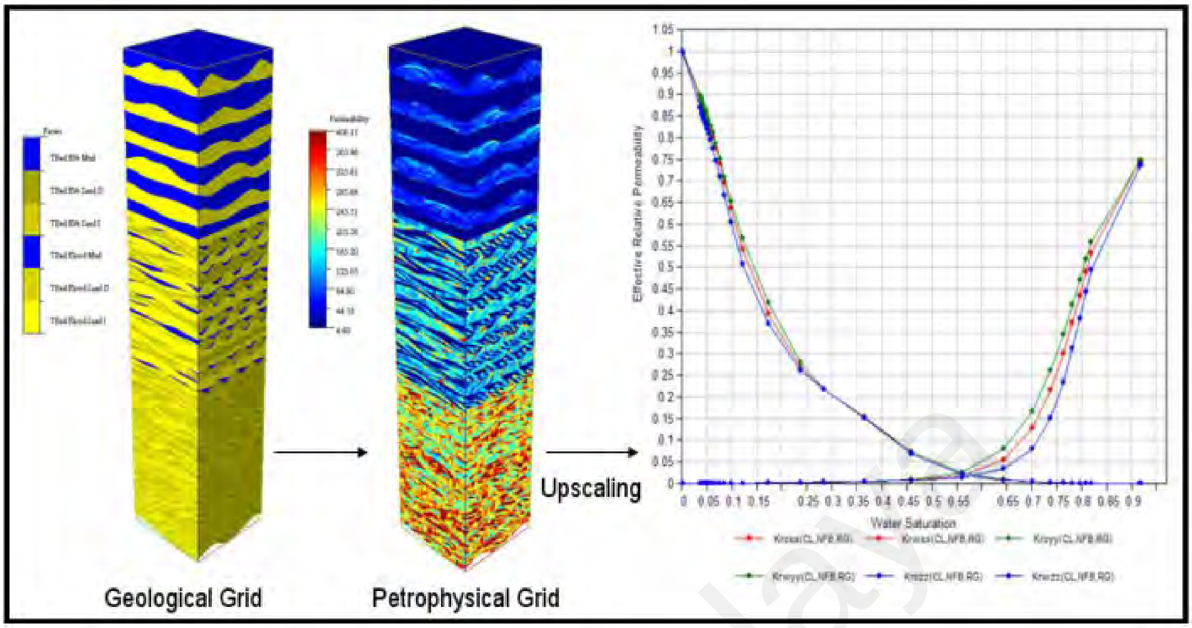

Figure 2.9: Metre scale bedform model of a wellbore above shows the upscaling process from the wellbore scale to reservoir scale (Alam, 2012).

2.7.4 Digital Core Analysis

An increasingly critical technology that is utilized in this study is Digital Core Analysis (DCA) that uses X-Ray Micro Computer Tomography (XMCT) Imaging for analysing and computing petrophysical properties such as porosity and permeability of rock samples. Chapter 3 of this thesis provides an extensive overview of Digital Core Analysis and application in the geoscience and this thesis.

2.8 Opportunities for Improved Reservoir Characterization

Reservoir modelling constructs an often-simplified digital representation of a reservoir called a static model. The static model represents the reservoir characteristics and properties such as the boundary layers of the reservoir formation, fluid contacts and spatial distribution of the reservoir and petrophysical properties such as porosity and water saturation (Ringrose et al., 2014). These properties are acquired from tools such as seismic data, well log data, experimental core analysis data and other tools (Figure 2.10). The resolution of the tools ranges from hundreds of meters using seismic to meter-scale of well logs measurements. The reservoir model integrates this information to form the static model, which is used for volumetric and flow analysis. These analyses allow geologists and petroleum engineers to estimate the amount of hydrocarbon in place and identify optimal hydrocarbon recovery strategies. These objectives are achieved using reservoir modelling and simulation software such as PETREL and ECLIPSE and other software for static modelling analysis and flow analysis, respectively.

Estimating the amount of hydrocarbon in a heterogeneous reservoir becomes more complex and uncertain as current methods are unable to provide information at scales representative of small scale heterogeneity such as thin beds (Bentley, 2015). Characterizing the hydrocarbon resources in thin-bed reservoirs require the spatial distribution of reservoir and petrophysical properties such as porosity, permeability, fluid saturations and capillary pressure properties. These properties are samples at the representative elementary volumes (REV) of the geology and are upscaled for volumetric analyses of the hydrocarbon resources in place. However, in thin-bed reservoirs where the representative elementary volumes(REV) are at the millimetre-to-centimetre scale, well logs and core analysis data are not appropriate due to the resolution of these two methods which cannot resolve millimetre-to-centimetre beddings. This limitation causes uncertainty in hydrocarbon reserves and production forecasts (Elfenbein et al., 2015).

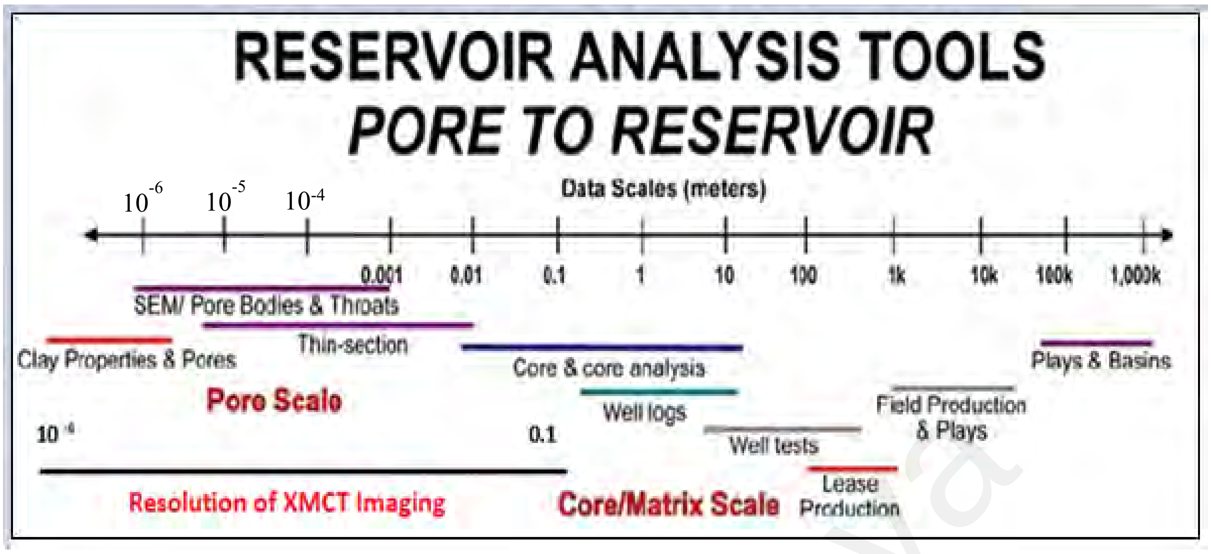

Figure 2.10: Reservoir characterization and modelling incorporate observations ranging in a scale of at least nine orders of magnitude. (Watney et al.). Current X-Ray Micro-CT imaging extends from nanoscale to millimetre scale.

Currently, geoscientists in Norway have developed process-based modelling methods such as the SBED modelling method that incorporate small scale sedimentary features such as the complex intercalating sandstone and mudstone beddings in heterolithic reservoirs at a centimetre-to-meter scale. The thin beddings of different rock types are assigned petrophysical properties from experimental core analysis. By integrating the effects of sedimentary details and small scale beddings on the reservoir properties via SBED modelling, we can create synthetic well logs to estimate crucial petrophysical properties that have control on hydrocarbon reserves estimates and production behaviour (Elfenbein et al., 2005).

However, it must be noted that the SBED models simulate the deposition process using a sign curve. The model use sign curves create approximated models of sedimentary structures such as the intercalating structured of the thin beddings in some rocks. These approximations do not reflect the actual complex structure of the heterogeneous rocks being modelled (Nordahl, 2004). Therefore, even though SBED can simulate the general shape of the observed geological structures, it still cannot accurately model the observed natural variability. Some of the natural variable structures that SBED cannot simulate accurately are 1) isolated ripples (formsets) 2) rippled crests that split and rejoin 3) ripples with migration vector under or parallel the horizontal plane and 4) depositional rate and length of the silt and sand lamina types but only for the flood or ebb migrating stages. To sum up, SBED tends to oversimplify the structures of the actual geology, which may result in inaccurate simulated reservoir properties (Nordahl, 2004).

Despite the progress in modelling complex geology with tools such as SBEDS modelling, the current benchmark for small scale properties in reservoir models are still experimental core analysis data. Core plug data cannot resolve the flow properties of millimetre-to-centimetre scale beddings that are prevalent in thin-bed and LRLC pay. According to Passey (2006), up to 80 per cent of the net sand pay in LRLC reservoirs exist as thin beds with the thickness that is below the dimension of core plugs (one inch in diameter and height) which are used in experimental core analysis. Characterizing these thin beds is vital to investigate effects on reservoir quality. Hence, there is an opportunity to improve the reservoir characterization of thinly bed LRLC reservoir by characterizing the properties of thin beds in the millimetre-to-centimetre scale. These small-scale properties can then be upscaled either numerically or integrated into other upscaling methods such as SBED modelling to predict and estimate the effective reservoir properties at the wellbore and inter-well scale for improved hydrocarbon reserves and production forecasts.

To provide reservoir properties at millimetre-to-centimetre scale in a reservoir model, this thesis focuses on using XMCT imaging and DCA to compute porosity and permeability of small samples representative of the millimetre-to-centimetre scale sandstone layers in heterogeneous rocks in thin-bed reservoirs. XMCT technology application in the geosciences has become significant due to the availability of computing resources to process the large amount of data involved in 3D datasets reconstruction and numerical calculation for calculating petrophysical properties. Properties derived from pore-scale can be integrated into a multi-scale workflow for reservoir model of thin-bed reservoirs that can convert and upscale the properties of small scale volumes to coarse grids while preserving key rock properties at all scale (Hurley et al., 2012).

CHAPTER 3 : AN OVERVIEW OF DIGITAL CORE ANALYSIS

3.1 Introduction to XMCT Technology

X-Ray Micro-CT (XMCT) Imaging technology is increasingly applied in the geosciences due to its inherent ability to visualize the interior of rock samples at high resolution which enable the rock fabric to be accurately represented in a 3D volume dataset. Application of XMCT imaging in the geosciences initially started with the imaging of rocks samples to scout the interior of core plugs using low-resolution X-Ray Imaging to select suitable undamaged core plugs for laboratory-based core analysis. Currently, XMCT imaging creates detailed 3D digital models of rock samples at the pore scale for detailed image-based analysis and to predict petrophysical properties (Cnudde et al., 2013). Digital Core Analysis (DCA) uses mathematical models such as the Lattice Boltzmann method to calculate petrophysical properties such as permeability directly on the 3D images and volumes of the rock samples (Arrufat et al., 2014). The high-resolution imaging recreates the flow limiting microstructures of the rocks accurately. Geologists use this technology to study and probe the interior of the rock for fossils or meteorites, conduct a textural analysis of metamorphic rocks, and derive properties such as permeability and porosity (Arns et al., 2005; Ketcham et al., 2001; Krakowska et al., 2016). These technologies have brought the geosciences into new frontiers of cutting-edge research. This thesis demonstrates that these technologies can be used to investigate the impact of geological heterogeneity on hydrocarbon reserves and production estimates (Golab et al., 2013).

XMCT Imaging and DCA have significant advantages over conventional laboratory-based methods such as Routine Core Analysis (RCA) and Special Core Analysis (SCAL) for measuring petrophysical properties of core samples. Two significant advantage of

Digital Core Analysis is that it consumes less time and is non-destructive compared to experimental core analysis. Experimental core analyses consume a significant amount of time to process in addition to destroying the rock samples or core plugs which are difficult and expensive to recover. XMCT Imaging and DCA use less time to calculate petrophysical properties of rock samples, and its non-destructive analysis provides results that are comparable and reliable as the experimental results using RCA and SCAL (Arns et al., 2003; Cnudde et al., 2013; Ketcham et al., 2014; Knackstedt et al., 2007; Knackstedt et al., 2009; Riepe et al., 2011; Turner et al., 2004).

XMCT imaging and DCA software have undergone significant advancement in terms of high-resolution imaging and improved DCA software thanks to the availability of faster computing capabilities (Cnudde et al., 2013). As such, they can be new standalone analytical methods or integrated with other workflows such as multi-scale reservoir modelling to provide input of flow properties of rocks at smaller and finer scales. Previous studies have shown that the computed petrophysical properties are easier in sandstone which has predictable properties such as pore size. In contrast, complex rock types such as carbonates have multi-modal pore size distribution and have complex diagenesis that affects (Sheppard et al., 2006). Despite the challenges, geoscientists use Digital Core Analysis to study carbonates such as investigating heterogeneity permeability and permeability anisotropy of carbonate reservoirs that causes difficulties in predicting hydrocarbon reserves and production (Sun et al., 2017).

Similarly, predicting hydrocarbon reserves and production is a challenge in thin-bed and LRLC reservoirs due to the inability of well in resolving millimetre-to-centimetre sand beddings that potentially represent additional hydrocarbon reserves (Passey et al., 2006; Worthington, 2000). Meanwhile, experimental core plug data are unable to sample the flow properties of millimetre-to-centimetre beddings that dominate heterolithic reservoirs (Ringrose et al., 2014). A previous study using surface models show that that connectivity and continuity of thin sandstone layers in low resistivity heterolithic reservoirs are a key factor to improved effective permeability data that can lead to better hydrocarbon reserves and production estimates (Massart et al., 2016; Massart et al., 2016)).

In this thesis, we use XMCT imaging and DCA to characterize the permeability, connectivity and continuity of thin sandstone layers in heterolithic rocks. We use Digital Core Analysis software method compute porosity and permeability of small mini-plugs extracted from sand regions of the core plug. We use segmented high-resolution XMCT images of these mini-plugs in Lattice Boltzmann solver to compute permeability. Also, image analysis software extracts information such as porosity and grain size from the segmented XMCT images of the mini-plugs. Also, we used 3D volume visualization to characterize the connectivity and continuity of the sandstone layers in the heterolithic core plugs. Our findings show that the permeability, connectivity and the continuity of the thin sandstone layers are key to identifying reservoir heterolithic rocks that represent additional net sand pay and potential hydrocarbon reserves in low net to gross and low resistivity heterolithic intervals. Our results are consistent and further validates the findings by a previous study (Massart et al., 2016) that highlight the connectivity and continuity of thins sandstone layers as a key factor to improved effective permeability information in heterolithic rocks. In addition to providing the ability to show connectivity and continuity of thin sandstone layers in 3D, we show that DCA can compute the permeability of these millimetre-to-centimetre sandstone layers. Our results provide information at very small scales that are not accessible from well logs and core plug data/

3.2 Introduction to Digital Core Analysis

DCA uses computational suites to extract petrophysical properties from segmented XMCT images of rock samples. DCA is an increasingly efficient method in evaluating and predicting the transport properties of porous rock over a wide range of reservoir conditions, flow regimes and fluid compositions through numerical calculation and simulation on a 3D volume dataset of a rock sample. In this thesis, we used a DCA software that uses the Lattice Boltzmann method to calculate petrophysical properties such as permeability (Arns et al., 2004; Arrufat et al., 2014). Previous studies demonstrated that calculated properties using DCA have good accuracy compared to laboratory-based Special Core Analysis (SCAL) and Routine Core Analysis results (Grader et al., 2010; Karoteev et al., 2014; Øren et al., 2006). This method is more efficient due to the shorter data processing time and the high quality of the analysis and data (Grader et al., 2010).

Most importantly, XMCT imaging can resolve most of the flow limiting microstructures (Kalam et al., 2012). DCA uses high-resolution XMCT images and volumes of small scale rock samples to compute petrophysical and flow properties such as porosity and permeability. Well, logs and core plug analysis cannot resolve and measure the reservoir properties of rock volumes that are below one meter and smaller than a standard one-inch diameter core plug. As a result, XMCT imaging and DCA provide the capability to accurately measure the reservoir properties of very thin sandstone beddings that make up thin-bed and LRLC reservoirs.

Consequently, DCA is advantageous over laboratory-based measurements and its associated rudimentary rock physics models which oversimplify the geometry of the rocks. As a result, experimental results are unable to correlate measured properties with different types of rocks with varying microstructures. DCA, on the other hand, provides the ability to investigate and study rock property relations such as transport properties and the pore-scale processes (Andrä et al., 2013).

Most importantly, DCA calculations are accurate. Previous studies have shown that calculated flow properties using DCA are relatively similar to the results of experimental methods such as RCA and SCAL (Grader et al., 2010; Lopez et al., 2010; Riepe et al., 2011). Another essential benefit of DCA is that it avoids the alteration and destruction of scanned objects and core samples and can be a risk reduction tool for studies in areas such as Enhanced Oil Recovery by avoiding the shortcoming of conventional core flood methods. (Cnudde et al., 2013; Karoteev et al., 2014; Long et al., 2009). The non-destructive of nature of DCA enables multiple analysis to be conducted on the same core sample for further studies. The application of DCA in the calculation of flow properties in complex geology such has enabled reservoir characterization to include small scale heterogeneities and flow-limiting microstructures which were previously not possible due to technological and computational limitations. (Bultreys et al., 2015)

3.3 XMCT image acquisition and Image Processing

We used an XMCT machine such as the Helical XMCT scanner at the CTLab facility at the ANU (Turner et al., 2004) to image and re-create 3D datasets of core samples used in this PhD study. DCA analysis uses the MANGO software at the Department of Applied Maths, ANU to calculate properties such as porosity. A second software used in this thesis is MORPHY, which uses the Lattice-Boltzmann method to calculate the permeability on the 3D datasets of the rock samples.

3.3.1 Image Acquisition

The XMCT machine uses a source that emits polychromatic X-Rays that irradiates a sample placed on a holder. During the imaging process, we rotated the sample 360 degrees, and the detector captures two-dimensional images of the object. The 2-dimensional images of the object are called CT slices or a tomogram. After the imaging process is concluded, several thousands of tomograms would have been imaged. A software would compile the tomograms into a 3D volume dataset of the object and eliminates image artefacts. We controlled other variable factors during the imaging are the resolution stated as dimension per voxel, which affects the smallest feature or dimensions that can be captured by the imaging. For example, a resolution of 10 microns/voxel would not be able to resolve a pore that is 2 microns. The tomograms are in a greyscale coloured scheme. The variation of the greyscale shades corresponds to varying levels of X-Ray attenuation, which indicate the number of X-Rays that are scattered and absorbed as they pass through the scanned object(Krassakopoulos, 2013). The level of X-Ray attenuation depends on the density and the atomic number of the materials of the scanned object(Al-Raoush et al., 2005a; Kyle et al., 2015).

3.3.2 Imaging Techniques

When a material is irradiated with X-Ray, photons are absorbed, which causes the solid material to eject electrons. The ionized atoms in the material that lose the electrons will revert to its neutral state, emitting X-Rays which are specific to the atoms of the material.

Lambert-Beer's law describes the attenuation of X-Rays in Equation 6 below as it passes through a solid material (Ketcham et al., 2014; Krakowska et al., 2016; Wildenschild et al., 2013).

Equation 5: X-Ray Attenuation Equation

$$I = I_0 e^{-\mu x}$$

I= Attenuated intensity after the X-Ray passes through the solid material

x= thickness of the object

I_o= incident radiation intensity

μ = linear attenuation coefficient

XMCT machine emits polychromatic X-Ray beams which consist of a broad spectrum of energies.

3.3.2.1 Beam Hardening and Artefacts

When a polychromatic beam passes through a material with a specific thickness, such as a cylinder of rock, cylinder's outer regions absorb and scatter the lower energies in the X-Ray spectrum, leaving only higher energy rays passing through the centre. As a result, the interior of the cylinder will be darker than the outer regions, which seem to be more attenuating than the inner region. As a result, the rims of the cylinder will appear brighter than the middle of the cylinder after reconstruction. This darkening of the inner region is called beam hardening and can cause streaking and other artefacts with irregular shapes. (Ketcham et al., 2014). Beam Hardening causes misinterpretation during the analysis of 3D images.

3.3.2.2 Beam Hardening Correction

We applied beam correction methods to reduce or eliminate the effects of beam hardening that may lead to misinterpretation of 3D image analysis,

One method used is to pre-filter the X-Ray beams to remove the low energy spectrum. However, this method only reduces the effects instead of removing it entirely and can be time-consuming. We achieve this by using a filter or putting the object in a material that can absorb the low energy spectrum (Ketcham et al., 2014).

The more popular method is to post-process the tomograms before reconstruction to eliminate the beam hardening effects. This method is called linearization, that transforms the polychromatic attenuation curve into a monochromatic curve. However, the process can be time-consuming, and the determination of the correction coefficient requires trial and errors and are subjective. (Wildenschild et al., 2013)

Another method to reduce beam hardening artefacts is to use dual-energy scanning method. This method scans an object at high and energy levels to differentiate the different attenuations caused by photoelectric absorption, which is dependent on the composition of the material and Compton scattering that changes linearly with the material density. (Ketcham et al., 2014). However, this method is very time-consuming as it requires at least two separate scans.

3.3.3 Pore Network Modelling

Pore network models are not explicitly used in this thesis as we can directly compute permeability on the segmented 3D volumes of rocks. However, we provide an overview of pore network models as highlight its usefulness in the geosciences for predicting petrophysical properties.

Pore network models are a simplified network of pore volumes connected by channels that represent the more complex pore space geometry in rock and soil. We generated the pore network models from XMCT imaging, and numerical calculation is applied using software to calculate and simulate petrophysical properties and transport behaviour (Sakellariou et al., 2007). Flow properties in complex reservoirs occur at the pore scale, and there is a strong focus on pore-scale flow simulation to describe the transport and flow behaviour and their effects at a larger scale (Bultreys et al., 2015). The physics used to describe transport behaviour through a pore network model are simple and uses computerized and conservation-based mathematical models. A widely used mathematical model is the Lattice Boltzmann method which is used to compute permeability and simulate and study phenomena such as dissolution precipitation (Meakin et al., 2009) and carbon dioxide sequestration (Bultreys et al., 2015). These pore-scale models are also used to study multiphase flow in complex reservoirs which could lead to improved capability in predicting bulk parametric relationships (Al-Raoush et al., 2005b). In this thesis, we use a Lattice-Boltzmann solver that directly uses the segmented pores and grains in the 3D models of rock sample to compute permeability. However, the pore network model remains an option for future work in studying petrophysical properties in thin-bed and LRLC reservoirs.

3.4 Digital Core Analysis

3.4.1 Image Processing and Segmentation

We used the Image Analysis Software called MANGO (**M**edial **A**xis and **N**etwork **G**enerati**O**n) at the Australian National University (Sheppard et al., 2014) to segment the

3D digital rocks into distinct phases. These phases include the grain(rock matrix), pores and intermediate phases. The segmentation process is tedious and user subjective and requires attention to detail to extract a pore network model that best describes the actual physical rock (Sheppard et al., 2004).

3.4.2 Petrophysical Properties computation

After we segmented the 3-D datasets of the rock samples, we use the petrophysical calculator software MORPHY to calculate the porosity and permeability from the segmented 3D datasets. We use MORPHY to compute petrophysical properties such as permeability and conductivity based on the Lattice Boltzmann method (Arns et al., 2004; Golab et al., 2013).

3.4.2.1 Lattice Boltzmann Method for Absolute Permeability Calculation

The Lattice Boltzmann Method (LBM) solver used by MORPHY, which is based on kinetic theory is optimal for fluid simulation in complex porous media due to its ability to solve complex boundary conditions problems. The underlying theory of the Lattice-Boltzmann method is to use simplified kinetic models that include the physics of microscopic and mesoscopic processes that would result in averaged macroscopic properties that are governed by the desired macroscopic equations(Sun et al., 2017). This thesis uses the MORPHY petrophysical package, which uses a Lattice Boltzmann solver to compute absolute permeability of 3D datasets of rock samples (Arns et al., 2004; Arrufat et al., 2014).

3.4.2.2 3D Volume Visualization

We rendered the 3D volume datasets of rock samples using visualization software such as Drishti that allows 3D datasets from XMCT imaging to be interactively explored using tools such as volume sculpting, animation and mesh generation for various applications (Limaye, 2012; Sakellariou et al., 2007). Also, we can use Drishti, and other commercial visualization software to explore specific features of the 3D rock sample such as identifying sand beddings, fossils and signs of biogenic traces such as funnels. We used 3D volume rendering to provide qualitative information to model and characterize small scale heterogeneities such as the connectivity and continuity of sand beddings in heterogeneous rocks for potential flow evaluation.

3.4.3 Advantages of Digital Core Analysis

This section summarises the advantages of High-Resolution Computer Tomography Imaging in the field of geosciences. We also discussed the limitations of the technology.

3.4.3.1 Detailed 3-Dimensional Imaging

The main advantage that is highlighted by proponents of X-Ray Micro-CT (XMCT) technology is its ability to create highly detailed 3-dimensional imaging of flow-limiting microstructures of rock samples. CT imaging created 3-dimensional models of rocks by creating a distribution of the local linear attenuation coefficient in 3-D. Using specialized 3D model rendering software such as Drishti and Pergeos, it is possible to visually review and inspect the interior of the 3D volume using the local attenuation coefficient. (Cnudde et al., 2013)

3.4.3.2 Non-destructive technique

Another main advantage of 3D imaging using CT technology that has made this technology highly relevant and attractive is its non-destructive nature. This valuable characteristic of CT imaging allows investigation into areas such as

- Investigation of structural properties within the same sample that undergo environmental changes such as temperature or mechanical stress(Saadatfar et al., 2012; Sheppard et al., 2006)
- Documenting changes in the sample using time-lapse (Mokso et al., 2012)
- Characterize petrographic and petrophysical properties of porous media for pore-scale simulation (Alyafei et al., 2016; Munawar et al., 2018)
- Multi-phase flow analysis in porous media which allows the prediction of phase transport properties (Turner et al., 2004)

3.4.3.3 Limitation of Digital Core Analysis

However, current DCA still have deficiencies that limit its effectiveness.

- In this thesis, we show that high-resolution XMCT imaging requires small samples which requires the extraction of smaller sub-plugs or mini-plugs from a large core plug. Therefore, in some cases, DCA requires the original sample to be partially destroyed.
- In complex rocks such as carbonates, where multi-scale heterogeneity is the main issue, there is a poor match between computed and experimental results with some computed properties such as elastic moduli diverges significantly from experimental results (Jouini et al., 2015).

- DCA can use pore network models used for studying multi-phase flow in porous media still cannot capture all of the pore-scale characteristics such as aspect ratio and pore-pore correlation that essential for understanding the multiphase fluid systems (Al-Raoush et al., 2005b). Also, DCA is still unable to compute many petrophysical properties that still requires experimental approaches which are generally still favoured over the numerical and simulated result (Schepp et al., 2020).

CHAPTER 4 : METHODOLOGY

We achieve the objectives of this study is to through the following components which are

- Apply sedimentology description to interpret the depositional environment of low resistivity heterolithic reservoirs. The aim is to determine the spatial distribution of heterolithic deposits and their impact on hydrocarbon reserves potential.
- Calculate Porosity and Absolute Permeability at micron-to-centimetre scale using 6 mm and 8 mm mini-plugs from five core plugs of varying rock types using Digital Core Analysis software.
- Apply Image-based Analysis and Image Registration Techniques on the mini-plugs 3D datasets using 3D-to-3D volume registration and 3D Volume Visualization.
- Measure permeability of thin beddings on the core plug surface using the New England Research (NER) gas permeability probe for millimetre-to-centimetre scale permeability measurement.
- Use a QEMSCAN machine to map the mineralogy on two sandstone mini-plug samples. The aim is to identify conductive minerals that cause low resistivity.

4.1 Sedimentology Analysis

We identify the facies types and facies assemblage and interpreting the depositional environment and processes. This information provides the geological input and underlying reservoir architecture by

4.1.1 Facies Analysis

This task involves the characterization of the rocks and basic geologic units observed in the core in terms of

- Types of facies identification and facies assemblage
- depositional fabric
- sedimentary structure,
- bioturbation

4.1.2 Depositional Environment Interpretation

We used facies types and assemblages identified to interpret the depositional environments and processes which results in the deposition of the sequence of sediments. Interpreted depositional environments conceptualize the reservoir architecture in terms of the facies types and their distribution and connectivity. For example, a shallow marine environment consist of tidal sand bars are laterally extensive but may not be vertically connected. The depositional environment also affects the character of the various deposits such as the sand-to-mud ratio, sedimentary structures and bioturbation intensity. The reservoir architecture is essential for providing insight into estimating the number of reservoir deposits and connectivity that affect hydrocarbon reserves and production forecast.

4.2 X-Ray Micro-CT (XMCT) Imaging

In this thesis, XMCT imaging created 3D volume datasets of the core plugs and mini plugs from a thin bed LRLC reservoir in Malaysia. The MANGO and MORPHY software use these datasets to compute porosity and absolute permeability. The main goal is to identify thin sandstone layers within heterolithic rocks and evaluate their potential as hidden net sand pay. A secondary objective is to characterize the carbonate minerals observed in the sandstone core plugs and their impact on permeability. 3D volume visualization software, Drishti was used to visualize the core plugs and mini-plugs to visualize sandstone layers in mud dominated heterolithic core plugs (Sample 64 and 245) and carbonate minerals in the sandstone core plugs (Sample 127, 148 and 210). We discussed the shape, thickness, connectivity and location of the sandstone layers heterolithic core plugs (Sample 64 and 245) and carbonate minerals in the sandstone core plugs (127, 148 and 210) and their effects on the permeability of the samples in Chapter 8.

We divided the XMCT imaging into two stages which are the low-resolution scoping scan using the 37 mm diameter core plugs and the high-resolution imaging of the 6mm or 8 mm mini plugs extracted from the sand dominated regions of the core plugs. The core plugs received for this project have a height and diameter of 38mm or 1.5 inches.

We scanned the core plug at a low-resolution resolution of between 16 microns/voxel (Table 4.1). The low resolution is sufficient for us to scope the interior of the core plugs for sandstone dominated regions. We will extract a mini plug from the sands dominated regions from each core plug. We note, however, that some mini-plugs also sample mudstone due to heterogeneity. We show the approximated location of the mini-plugs relative within the core plugs in section 8.3.

The mini plugs extracted from the core plugs have diameters of 6mm and 8mm with a height of 38mm. However, we only imaged 20 mm of the mini-plugs' length at high resolution. The resolution of the scan is 2.8 or 3.8 microns per voxels depending on the diameters (Table 4.2). These resolutions are sufficient to resolve many of the grains, pores and flow-limiting microstructures.

Table 4.1: CT Imaging parameters used on the core plugs (stacked in threes)

Core Plugs	Power(kV)	Current(μA)	Filter	Projections	Voxel Size	Acquisition Time (hours)
64-81-127	120	140	5mm Stainless Steel	17028	16.4	19
245-148-210	120	140	5mm Stainless Steel	16719	16.4	19

Table 4.2: Imaging parameters used on the mini-plugs.

Core Plug	Power (kV)	Current(μA)	Filter	Projections	Voxel Size (μm/voxel)	Acquisition Time (hours)
64	100	55	2mm Aluminium	23444	2.87	18
127	100	55	2mm Aluminium	25218	2.85	20
148	100	55	2.5mm Aluminium	26323	3.87	19
210	100	55	2.5mm Aluminium	19052	3.87	19
245	100	55	2mm Aluminium	24210	2.82	19

4.2.1 Workflow for core plug analysis using X-ray Micro-CT Imaging and Digital Core Analysis

The project received nine core plugs from X-4 for the initial analysis. The plugs were selected base on the permeability measurement and represent the length of the X-4 core. However, only five core plugs out of the nine were in useable and suitable condition for XMCT Imaging. We did not select the other samples for further analysis due to fractures and poor condition.

This study will use a modified version of a workflow adopted by Kumar et al. (2013) in Figure 4.1 at the ANU Micro-CT Centre when analysing samples using XMCT Imaging and processing the XMCT datasets for Image Analysis and Digital Core Analysis.

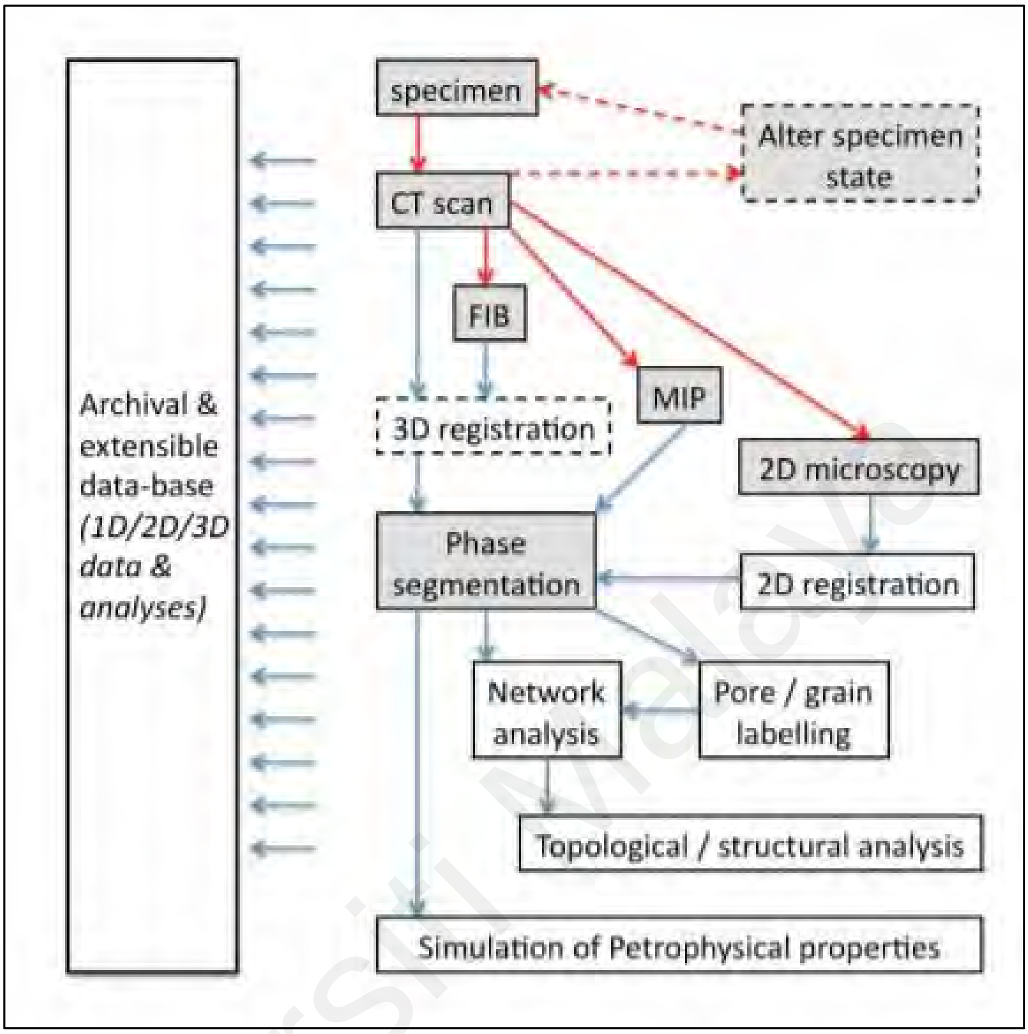

Figure 4.1: A proposed workflow used for specimen analysed using Computer Tomography Imaging at the Australian National University (Kumar et al., 2013). MIP= Mercury Intrusion Porosimetry.

4.2.1.1 The selected five core plugs from Well X-4, Field X

Table 4.3 and 4.4 show the information about the five core plugs from Well X-4 that were selected for this thesis. The core plugs were selected base on several criteria

- They represent the different rock types in a well within Field X, such as sandstone and heterolithic rocks. Non-reservoir mudstone and coal are excluded.
- The core samples are from a different depth of the total core length.

- The core plugs have different permeability values ranging from hundreds of millidarcy to below one millidarcy.

Table 4.3: Details of the rock types, sedimentary structure, and bioturbation intensity in the five core plugs from well X-4.

Depth (m)	**Sample**	**Rock Type**	**Main Sedimentary Structure**	**Bioturbation**	**2nd Sedimentary Structure**	**Remark**
1476	64	Heterolithic	Lenticular	Low	Muddy	Well bioturbated
1495	127	Sandstone	Silt Laminae	Low	Laminated	Well bioturbated
1501	148	Sandstone	Silt Laminae	Low	Well laminated	**Main reservoir unit**
1520	210	Heterolithic	Lenticular	Low	Rippled-Laminated	Sparsely bioturbated
1530	245	Heterolithic	Lenticular	High	Muddy	Intensely bioturbated

Table 4.4: Petrophysical properties of the nine core plugs from well X-4 provided by the Routine Core Analysis report from Petronas.

Sample	**Rock Type**	**Ambient He porosity**	**Corrected porosity (%)**	**Gas Horizontal Permeability (mD)**	**Empirical. Klinkenberg (mD)**	**Grain Density (g/ml)**
64	Heterolithic	19.19	18.86	41.84	35.98	2.70
127	Sandstone	28.90	28.41	603.00	633.00	2.69
148	Sandstone	28.03	27.55	414.00	394.16	2.70
210	Heterolithic	29.20	28.70	287.00	276.00	2.73
245	Heterolithic	15.95	15.68	1.29	0.90	2.66

4.2.1.2 The workflow of the Micro-CT scan of the core plugs

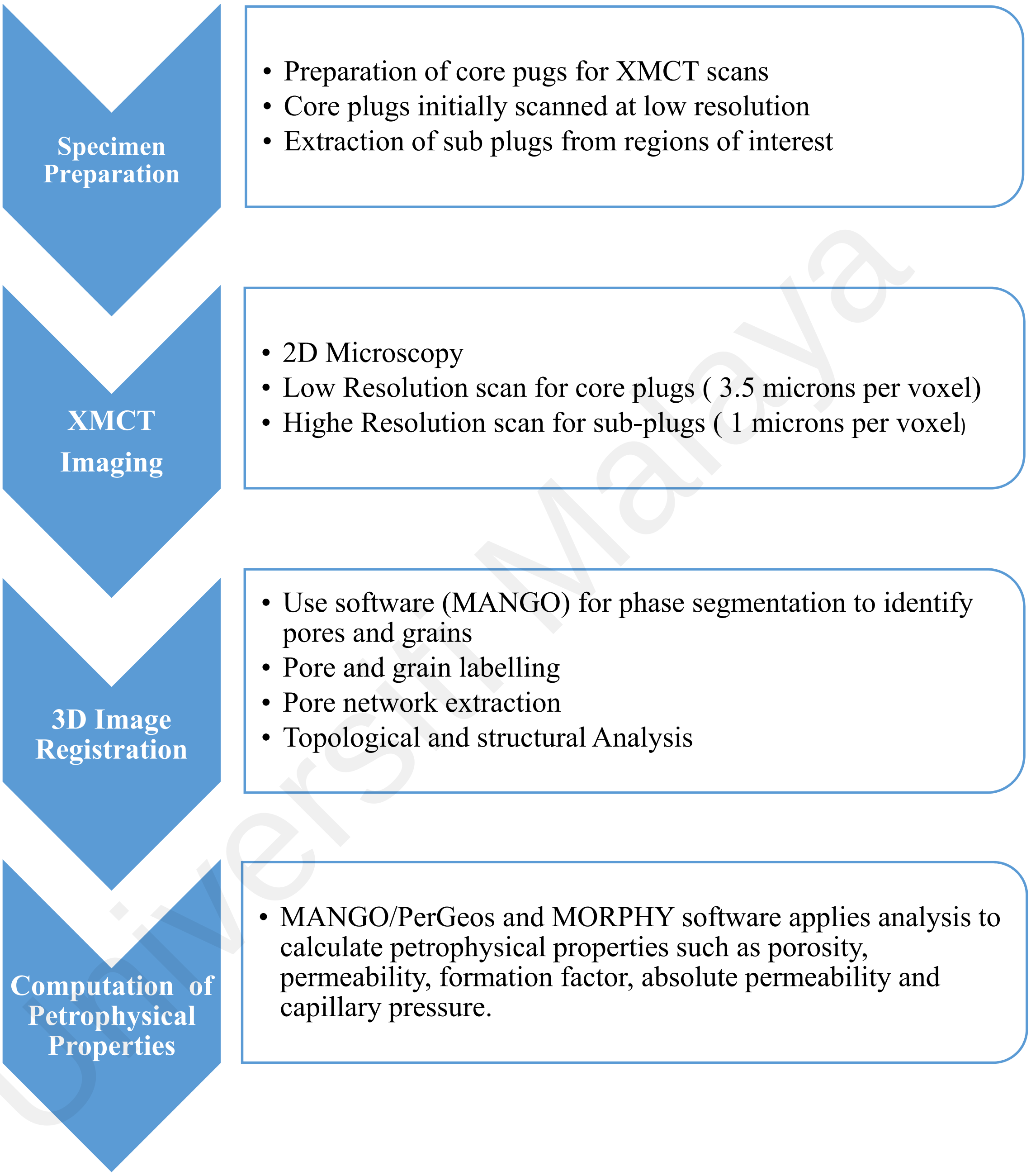

4.2.1.3 The workflow of the Digital Core Analysis using MANGO

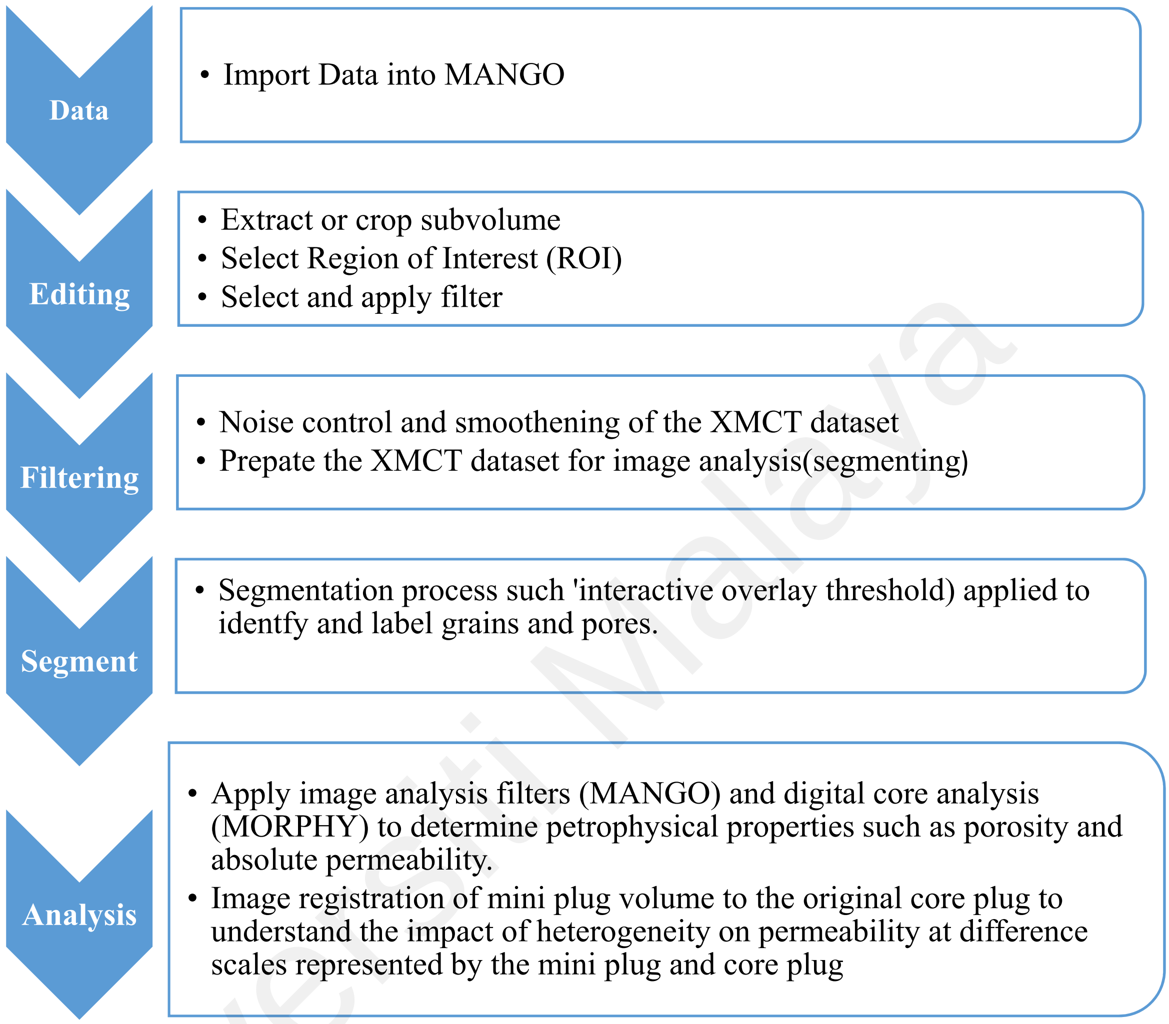

4.2.2 Core Plug Preparation for Low-Resolution Imaging

We put three core plugs into a cylindrical sleeve made of Aluminium and placed inside the ANU CT machine and scanned for almost 24 hours. The cylindrical sleeve was inserted into a holder within the CT machine and locked in place to prevent movements that can spoil the CT imaging. The CT machine X-Ray source and sample distance were adjusted to provide a voxel size of 16 microns per voxel (Table 4.5).

To save cost and time, three core plugs were stacked on top of each other and inserted into a single sleeve made of aluminium. The core plugs are also separated by a thin piece of foam which will make it easier to differentiate the core plugs from one another. A single low-resolution imaging scan at the ANU costs at least AU$600, hence by stacking the core plugs, we only required three scanning sessions for all the core plugs which were cost-effective and saved time.

Table 4.5: The volume by voxels and a voxel size of the reconstructed core plugs. Three core plugs were stacked together and imaged at the same time to save time and cost. Each image contains three core plugs.

Core Plugs	**Volume (voxels)**	**Volume (diameter x height)**	**Voxel Size (µm/voxels)**
64-81-127	2800 x 2800 x 7400	37mm x 111 mm	16.32
245-148-127	2800 x 2800 x 7400	37mm x 111 mm	16.33

4.2.3 Region of Interest Selection

We reconstructed and compiled the 20,000 projections collected from a single XMCT imaging session into a 3D volume dataset by using the Raijin computing facility at the ANU. We used the ANU CT Image viewer software, called the NCViewer to scout the interior of the core plug slice by slice in different perspectives such as from the top (Z-direction) and the sides (X and Y directions). We reviewed the 3D volume datasets for sandstone dominated regions in each core plug. Later, we extracted 6mm, or 8mm mini-plugs were extracted from the sandstone regions of the core plugs. For heterolithic core plugs which consist of mudstone and sandstone, we extracted mini-plugs from regions with the most amount of sandstone.

Some of the core plugs (127, 148 and 210) are predominantly sandstone interbedded with carbonate thin and thick laminates which we show in section 8.2, Chapter 8. The sandstone regions within the core plugs feature distinct grains of sand with pores between the grain boundaries. Some pores are filled with cement, minerals or clay that are generally more attenuating than the grey sand grains, as shown in Figure 4.2.

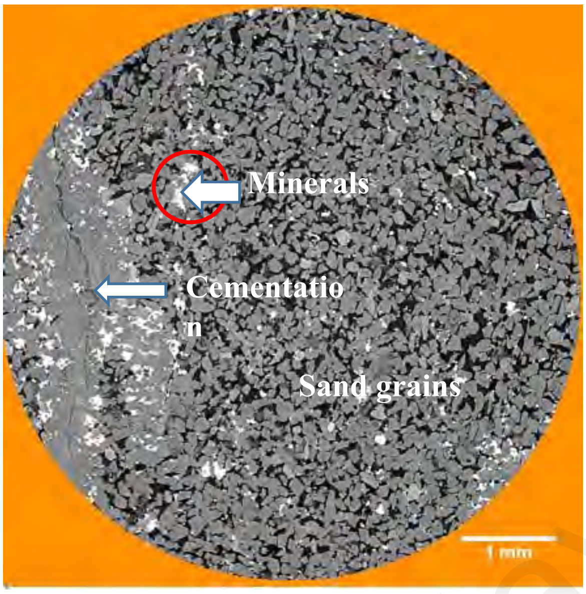

Figure 4.2: A single greyscale tomogram of a mini plug.

Based on these observations, we decided that the regions of interest will be the sand dominated regions that are least affected by mudstone and cementation. For heterolithic core plugs which are mud dominated, we targeted regions that contain the most sandstone. One objective is to determine if the sandstone in the heterolithic plugs from the are similar in terms of porosity and permeability.

4.2.4 Mini Plug extraction

We drilled and extracted he mini-plugs using a modified milling machine which uses specially manufactured hollow drilling bits with 6 mm and 8 mm inner diameters that are drilled into core samples to retrieve mini plugs.

The core plugs were held in place by a clamp while the rotating drilling penetrates the core plug from end to end. The mini plug extraction process takes 10 to 15 minutes and does not cause further damage to the core plugs. Dr Michael Turner, the Technical Officer at the Department of Applied Mathematics ANU, conducted the mini-plugs extraction process.

4.2.5 High-Resolution XMCT Scan of Mini Plugs

We inserted the mini-plugs into aluminium tubes with the corresponding diameters which were then capped by a piece of foam and rubber on the top to prevent micron level sample movement. Table 4.6 shows the dimensions and volume in voxels of the mini-plugs.

We inserted the aluminium cylinder into a drilling bit clamp within the CT machine and the X-Ray source and detector adjusted accordingly to achieve a resolution of 2 to 3 microns per voxel. The XMCT scans of the mini plug were prepared and run by the Department of Applied Mathematics Technical Officer, Dr Michael Turner

The duration of the scan was 20 hours, and the ANU Raijin Supercomputer reconstructed the collected tomograms numbering 20,000 to 24000 projections for several hours. The reconstructed 3D volume datasets of core plugs and mini-plugs of the five mini-plugs were processed using the MANGO software and segmented to separate pore, grains and intermediate phases which we show in Chapter 8.

Table 4.6: The volume by voxels and a voxel size of the reconstructed and cropped mini plugs.

Mini Plug	Volume (voxels)	Volume (diameter x height)	Voxel Size (µm/voxels)
64	1809 x 1837 x 7401	6 mm x 20 mm	2.74
127	1809 x 1837 x 7400	6 mm x 20 mm	2.72
148	1803 x 1807 x 5560	8 mm x 20 mm	3.74
210	1969 x 2009 x 5520	8 mm x 20 mm	3.76
245	1809 x 1837 x 7400	6 mm x 20 mm	2.73

4.2.6 Image Analysis

We used several image analysis techniques using the MANGO software to acquire qualitative and quantitative information from the segmented XMCT images of the core plugs and mini plugs. These techniques are listed below, and the results summarized in Chapter 8.

- Segmentation
- Median Grain Size Distribution
- Microporosity Analysis
- Image Registration of mini-plug dataset to core plug dataset.
- Spanning Cluster Analysis
- 3D Volume Visualization

4.2.7 3D Volume Visualization

Another software used in this study for image-based analysis is the Drishti software at the ANU, which we used to visualize tomography and electron-microscopy data (Limaye, 2012). The software enables image-based visualisation of the different constituent rock types in a core plug due to the different rock types having a different level of attenuation to x-rays. Other information that can be derived using Drishti is to identify indicators of bioturbation such as funnels, burrows and fossils that affect permeability from the structure and arrangements of the sediments in the core plug. In this thesis, Drishti rendered thin sandstone layers in the heterolithic core plugs to characterize the connectivity and structure of the sandstone that can be correlated to measured permeability of the core sample. We noted the presence of bioturbation in one of the heterolithic core plugs that changed the structured of the sandstone layers significantly, resulting in lower permeability. The impact of bioturbation on the sample's permeability is discussed later in section 8.2, Chapter 8.

4.3 Digital Core Analysis

This thesis uses DCA software to simulate petrophysical properties directly from 3D datasets generated from XMCT images of rock samples (Sakellariou et al., 2007). We use Image Analysis software MANGO to segment the 3D datasets of the mini-plugs into the pore, grain and intermediate phases (Figure 4.3) and simulate petrophysical properties such as porosity (Sheppard et al., 2006). Also, we use a Lattice-Boltzmann software called MORPHY to simulate permeability directly on the 3D datasets of each mini plug which we segmented into grain and pore phases (Arns et al., 2003). However, some phases cannot be segmented into pore and grain as the greyscale value is between the threshold limits of either phase. We used Additional Segmentation to combine these outlier phases into the intermediate phase, which can potentially be clay: minerals and silt.

MANGO segmented the 3D volume datasets of the mini-plugs into the pore (Phase 0), grain (Phase 1) and intermediate phases (Phase 2) phases. The phase volume fraction of the pore is the porosity of the 3D volume of the mini plug. Initially, we segmented the greyscale tomogram into grain and pores. The segmentation is not complete as there are phases that cannot be segmented into pore and grain as the greyscale value is outside the threshold limits of either phase. We use Additional Segmentation filter in MANGO to combine these phases into a third phase which we called intermediate phase. A second DCA software MORPHY calculates the absolute permeability directly on the segmented 3D datasets of the mini-plugs. We compared the porosity and permeability of the miniplugs to their corresponding core plug permeability measured using RCA.

We used the image registration techniques in the MANGO software to overlay the mini plug dataset onto the core plug dataset using a 3D-to-3D volume registration method. We used the technique to position the 3D datasets of the mini-plugs to their original location within their respective core plugs. This method helps us to understand as to why the computed permeability of the smaller mini-plug using DCA is significantly different from the permeability of the core plug measured experimentally. Also, we use this comparison to correlate permeability difference between the two-volume scales to the different rock composition. For example, a sandstone dominated mini-plugs from thin sandstone layers in a heterolithic core plugs has higher computed permeability than the entire heterogeneous core plug, which consist of mudstone layers that can affect fluid flow. We summarized the results of the image registration technique in section 8.2, Chapter 8.

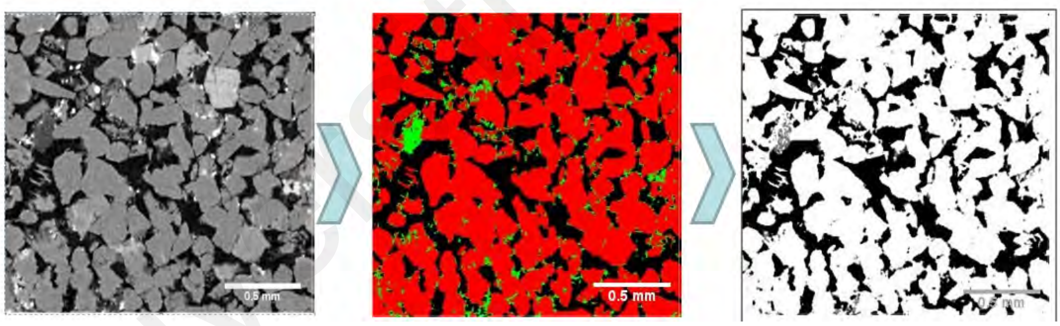

Original greyscale tomogram

3 Phase Segmentation into

- Black: Pore
- Red: Grain
- Green: Intermediate phases

Binarized image

Figure 4.3: Segmented XMCT image of mini plugs using MANGO. Resolution is 2.74 microns/voxel. (Images were taken at Australian National University CTLab and processed using the MANGO software)

4.3.1 Computing Permeability using MORPHY

MORPHY calculated the absolute permeability of the segmented 3D dataset of the rock samples using the Lattice-Boltzmann method (Alyafei et al., 2016; Bernaschi et al., 2009) (Arns et al., 2004; Arrufat et al., 2014).

The Digital Core Analysis software MORPHY, a scripting program, calculates the absolute permeability of the segmented 3D volume datasets within the framework of the Lattice-Boltzmann method (Alyafei et al., 2016; Arns et al., 2004; Bernaschi et al., 2009). A highlighted advantage of this method is that permeability computations are performed on multiple small sub-volumes of the segmented XMCT datasets, thereby generating statistically significant and useful numbers of data points (Botha, 2017). In this thesis, we divided the datasets of the mini-plugs into sub-volumes with side lengths of 300 voxels and 400 voxels (Table 4.7) to determine the impact of heterogeneity of the computed permeabilities at these two sub-volumes. A relatively homogeneous rock will have similarly computed permeabilities at these two volume sizes.

The computed permeability is sensitive to the porosity of the segmented dataset of the rock samples as a small range of porosity values may result in a large variation of permeability values (Hommel et al., 2018). We compared the computed porosity of the segmented mini-plugs to the experimentally measured permeability of the original core plugs in section 8.2, Chapter 8. Our results show that the difference between the computed and measured values are marginal and acceptable.

Also, previous studies using the same Lattice-Boltzmann solver as this thesis show good agreement between the computed permeability of sandstone was in good agreement for all porosity values. Also, the variation of the computed permeability is the same as the experimental permeability data (Arns et al., 2004). Therefore, we are confident that the Lattice-Boltzmann solver (MORPHY) can provide reliable and accurate permeability data of the sandstone in the mini-plugs.

Table 4.7: Summary of the sub-volume sizes in mm at 300 voxels and 400 voxels side lengths

Mini Plug	Resolution µm/voxel	Volume with 300 voxels side length (mm^3)	Volume with 400 voxels side length (mm^3)
64	2.87	0.63	1.51
127	2.85	0.62	1.48
148	3.87	1.56	3.71
210	3.87	1.56	3.71
245	2.82	0.61	1.44

Figure 4.4 shows the workflow for computing permeability using the Lattice-Boltzmann solver (Arns et al., 2004). In the workflow, we divided the segmented 3-D dataset of a mini plug into cubic sub-volumes with 300 voxels and 400 voxels side lengths. The Lattice-Boltzmann solver simulates fluid flow in each cubic sub-volume in the mini-plug to compute permeability data. The computed permeability is comparable to experimental results (Alyafei et al., 2016; Evans et al., 2010; Knackstedt et al., 2006; Sakellariou et al., 2007). Table 4.9 shows the parameters of the sub-volume sizes of each mini-plug used by the Lattice-Boltzmann solver to compute permeability and porosity.

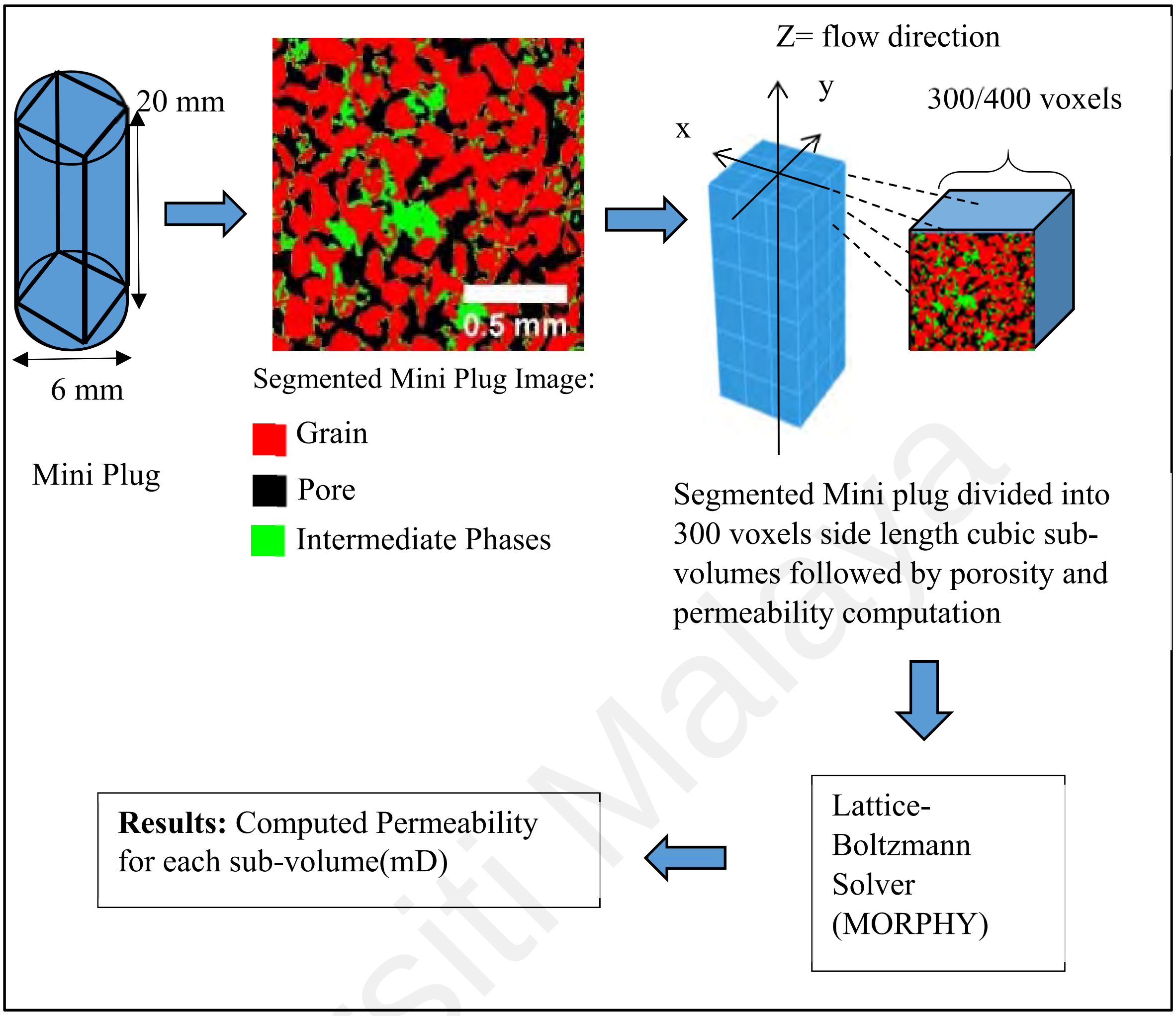

Figure 4.4: Workflow for computing permeability and porosity using a Lattice-Boltzmann method. The direction of simulated flow in the z-direction, which is the same as the direction of the injected fluid in core plug analysis.

Table 4.8 shows the total volume of the sub-volumes or the 'Sample size', grid spacing (resolution) and the side lengths of the sub-volumes. Figure 4.8 shows the side lengths of the sub-volume are limited by the actual dimension of the mini plug datasets. We selected 300 voxels and 400 voxels side length for the sub-volumes as the total volume sizes are within the mini plug.

The millimetre-scale of the cubic sub-volumes shown in Table 4.5 is similar to the thickness of the mm-to-cm sandstone layers common in heterolithic rocks. Hence, the Lattice-Boltzmann solver can measure the permeability of the millimetre-to-centimetre sandstone layers in the mini plug samples and provide a large number of data points from the sub-volumes that are useful for statistical analysis.

We note that only computed permeability in the axial direction (z-direction) is presented as to be consistent with the fluid flow direction through the core plug in the experimental Routine Core Analysis used to measure the permeability of the core plugs.

Table 4.8: Used parameters of the sub-volumes of the mini plugs for the computation of permeability and porosity using the Lattice-Boltzmann solver. The figure below Table 8.12 illustrates the partitioning of the mini plug into cubic sub-volumes.

Parameters		**A**	**B**	**C**
Mini plug diameter x height (mm)		8 x 20	6 x 20	6 x 20
Number of voxels (x, y, z)		: <1200><1200><5400>	: <1200><1200><7200>	<1200><1200><7200>
Grid spacing Δh (μm)		3.87	2.87	2.87
300 voxels^3	**Side length (mm)**	1.16	0.86	0.86
	No. of sub-volumes	162	216	216
400 voxels^3	**Side length (mm)**	1.55	1.15	1.15
	No. of sub-volumes	117	162	162

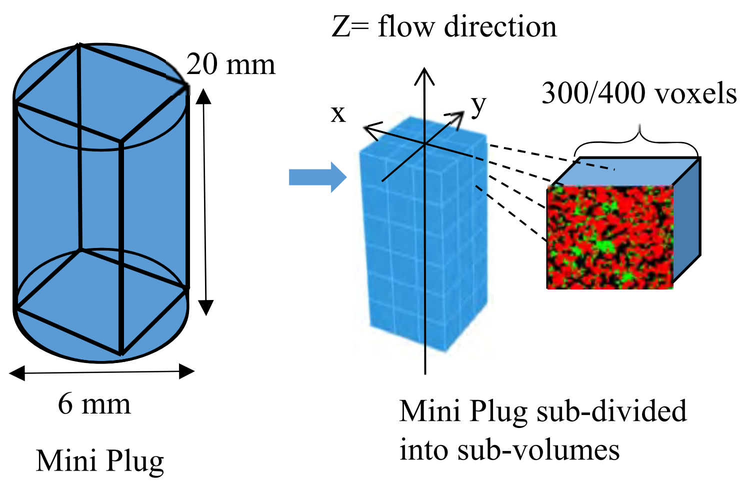

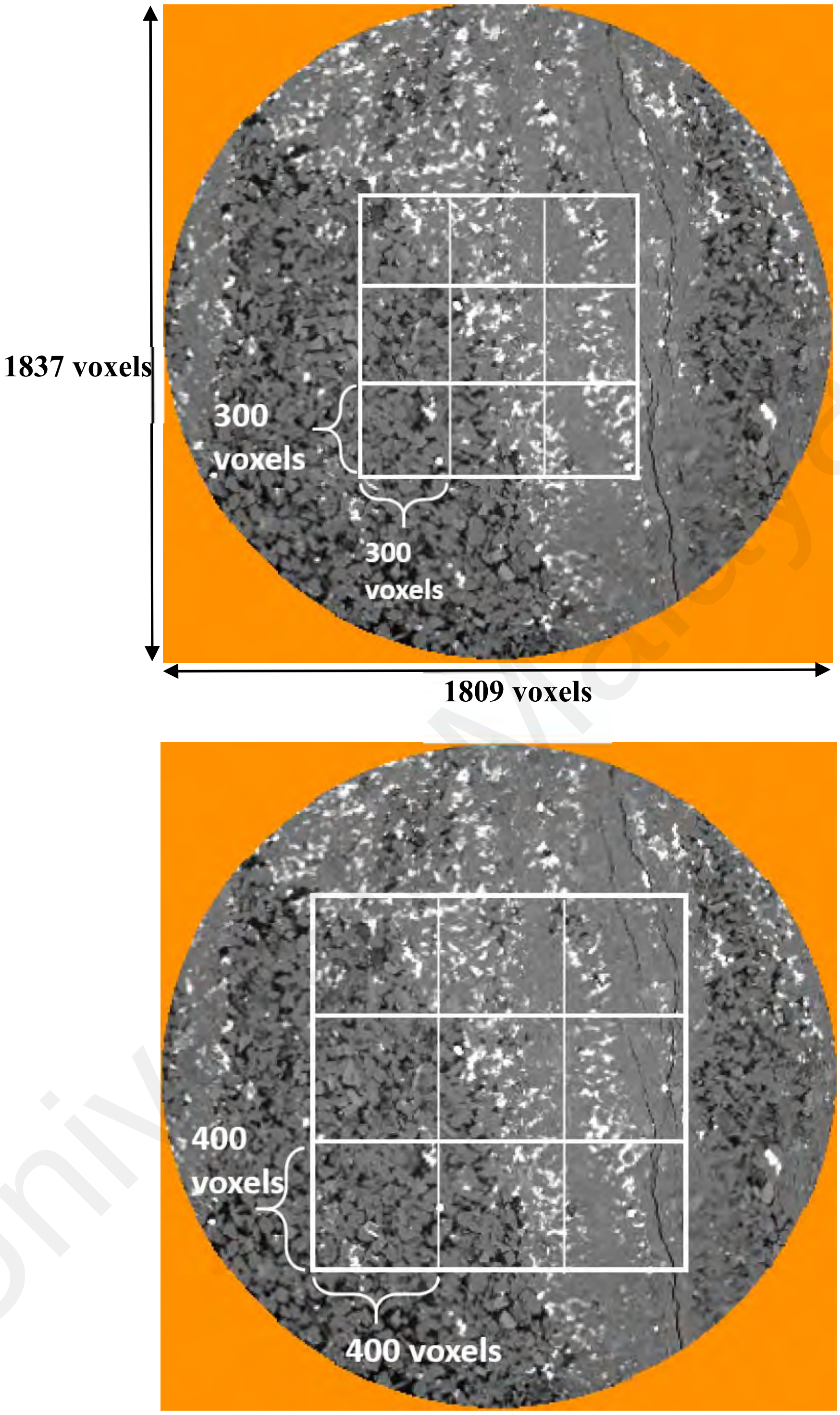

Figure 4.5: An image of the core plug B. The side length of the sub-volumes is constrained within the dimensions of the mini plug diameter. The dimensions of the mini-plugs allow sub-volumes with 300 voxels and 400 voxels side lengths.

4.4 New England Research (NER) Permeameter Measurement

This study uses the New England Research (NER) permeability gas probe or permeameter at the CTLab, ANU. Figure 4.6 illustrates the NER permeameter utilizing gas injecting probes that directly measures permeability on the surface of core slabs and core plugs (Grover et al., 2016). In this thesis, we used the NER permeameter to measure the permeability on the flat surfaces of the five core plugs of this study. The permeameter measures the permeability by using a steady-state injection technique with one-millimetre steps between each measured point. Also, the measured permeability is presented visually in the form of a permeability map with the permeability contrast indicated by colour, which we show later in section 8.2, Chapter 8.

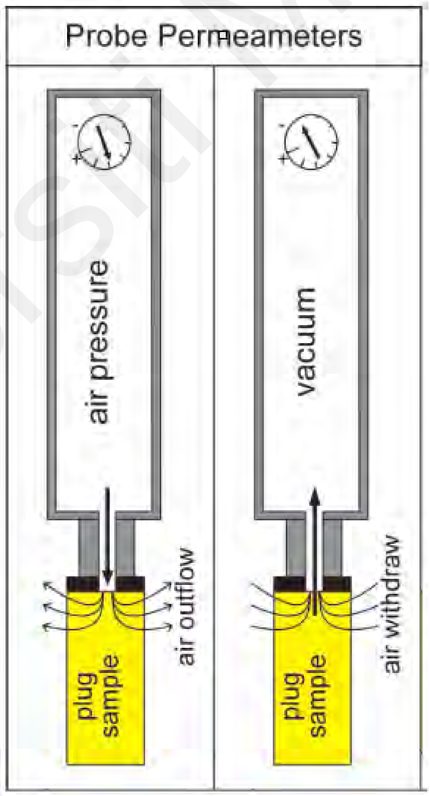

Figure 4.6: Permeability measurement using a New England Research mini-permeameter using air injection principle (Filomena et al., 2013)

The permeameter is useful in this thesis as it measures the permeability of millimetre-to-centimetres beddings or layers directly on the core slab or core plugs. The permeability map produced from the measurements provides both qualitative and quantitative information with regards to the permeability variations between adjacent layers of different types of rock. We used the permeameter to verify the calculated permeability using MORPHY. The Lattice-Boltzmann solver we use computes permeability on sub-volumes that make up the 3D datasets of the mini-plugs. These sub-volumes have dimensions in the millimetre scale that is similar to the amount of volume of rock measured by the NER permeameter. The NER permeameter and MORPHY provides a substantial amount of useful data points that reflect the permeability variation at millimetre-to-centimetre scale on the surfaces and within 3D volumes of geological samples such as the core plugs and mini plugs.

4.5 Mineralogical Analysis

The Mineralogical Analysis in this study employs Thin Section Analysis, and Scanning Electron Microscopy (SEM) provides the mineralogical framework in the samples. SEM analysis provides qualitative analyses on the impact of facies, pore type, and pore connectivity on flow properties such as permeability (Al-Marzouq et al., 2014). In this study, SEM is used to identify the presence and quantity of conductive minerals such as iron minerals and pyrite that can result in low resistivity pay in the sandstone sediments within some of the core plugs. This study employs an SEM facility at the ANU Centre of Advanced Microscopy called QEMSCAN.

Quantitative Evaluation of Minerals using a Scanning Electron Microscopy (QEMSCAN) can generate images of the organic material and minerals by scanning the sample (Tang et al., 2016). The instrument can provide the element analysis on each measurement point according to the X-ray energy spectrum. Based on the grey value of the back-scattered electron image and the intensity of the X-ray, the mineral phase can be determined. We used the QEMSCAN equipment at the Centre for Advanced Microscopy at the ANU to analyse the Organic Material and minerals of the core samples and generate high-resolution mineralogy map of the surface of the mini-plugs. The pixel resolution of the map images is 1 mm. The QEMSCAN tool provides quantitative and qualitative content of the organic materials and minerals on an exposed surface of the core plug samples.

We used the QEMSCAN tool to characterize the mineralogical framework, such as the clay content and conductive minerals. Also, we determine the percentage weight of iron minerals and pyrite in the sand mini-plugs from sample 210 and 148. We quantify the number of conductive minerals such as Pyrite, Iron minerals such as Siderite because they are one of the leading factors to low resistivity pay besides laminated structures (Pratama et al., 2017; Worthington, 2000).

4.5.1 Sample Preparation for QEMSCAN analysis

The Mini plug was cut to a length of 13 mm and placed in resin and later grounded to below 12 mm in length. A 5 mm by 5 mm region of interest on the mini plug was analyzed using QEMSCAN to produce a mineral map The QEMSCAN analysis parameter is 2-micron resolution, 2000 counts per pixel and a field area of 5 mm^2 which we divided into nine sub-areas. The length of the scan was 10 hours. Post-processing using Nanomin identifies the minerals and elements by percentage weight. Dr Michael Turner prepared the mini plugs for the QEMSCAN analysis at the Department of Applied Maths Rock Lab. Later, Dr Frank Bink conducted the QEMSCAN analysis on 14th December 2017, and the results were post-processed on 19th and 20th December 2017 using the Nanomin software.

CHAPTER 5 : REGIONAL GEOLOGY OF STUDY AREA

This chapter reviews the reservoir from which the samples used in the thesis came. The overview covers the tectonic framework, stratigraphic and paleo-environment framework, hydrocarbon occurrence and geological description. We provided most of the information in this chapter from the Pre-drilling report of a well in Field X and the Malaysian basin geological description (Madon et al., 1999) by PETRONAS, the Malaysian national oil company. Due to confidentiality, we censored the name and identification of the well and field.

5.1 Introduction to the Reservoir

The reservoir that provided the core plugs for this study were from field X in Malaysia that is located within a hydrocarbon-rich basin offshore Malaysia (Figure 5.1). This field's location is within the PX XXX block that is several hundred kilometres offshore Malaysia. The reservoir consists of an elongated east-west anticline. The reservoir is isolated from a westward field by north-south trending normal fault.

The primary hydrocarbon product from the X field is mainly gas that is contained within the Middle Miocene D and E groups. The nearest gas field is the eastward A field and westward B field both located 10km and 5 km respectively from the X field.

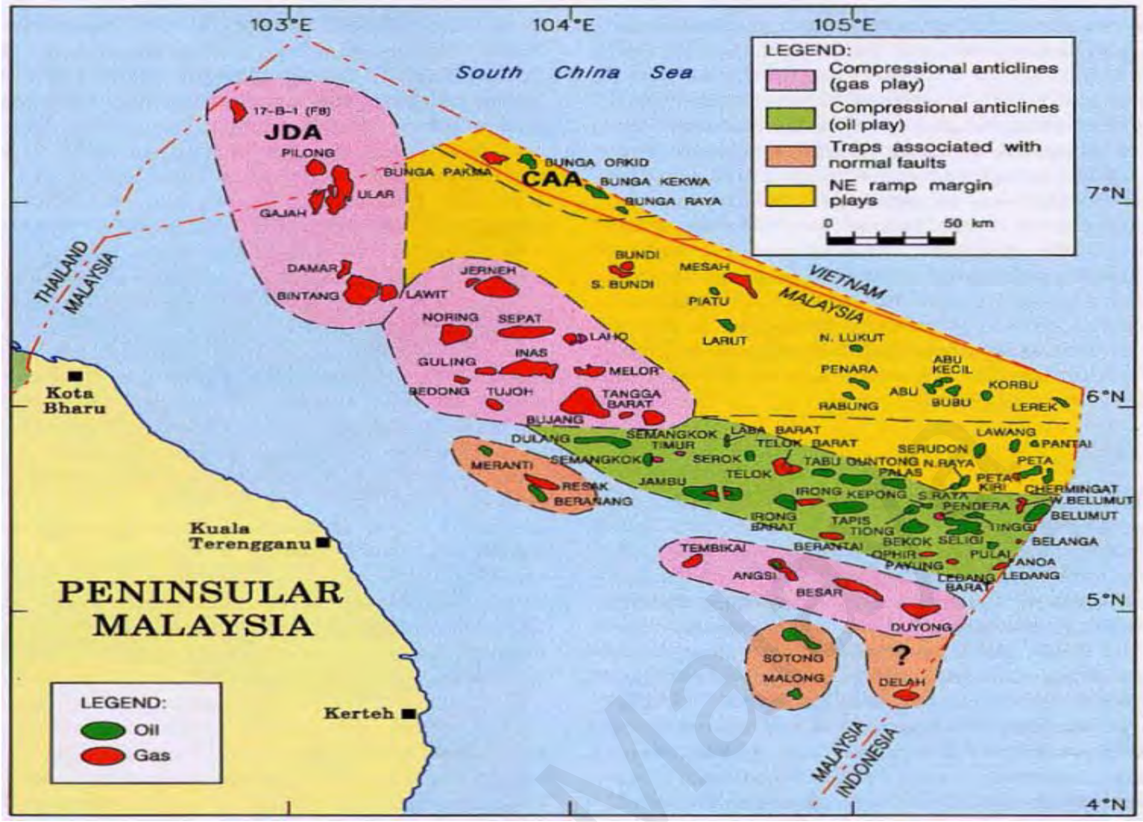

Figure 5.1: A map indicating the general location of the X field offshore Malaysia. (Madon et al., 1999)

5.2 Tectonic Framework

The basin is a complex rift basin with an East-West trending network of numerous grabens and half grabens. Towards the South-East, the basement of basin becomes shallow due to tectonic deformation during the Late Middle Miocene. Tectonic deformation has also caused the creation of compression anticlines. Also, The southern flank of the anticlines is bounded by reactivated reverse faults. (Madon et al., 1999)

From the North-West to the South-East, the intensity of the deformation becomes lesser. The basin is described as a rift sag basin caused by lithospheric stretching which consists of preliminary periods of rifting, then followed by a phase of sagging caused by thermal-induced subsidence. (Madon et al., 1999)

The location of the basin is within the middle area of Sundaland, which is the cratonic core of South East Asia. The basin is the deepest continental extensional basin in the region and was conceived during the early periods of the Tertiary era. The trend of the basin is from North-West to South-East and overlies a basement which consists of a late Mesozoic continental landmass. (Madon et al., 1999)

The pre-Tertiary basement becomes shallower as the basin trends South-East due to deformation and uplift during the late Miocene. Thie trend resulted in compressional anticlines and reactivation of normal faults. The faults in the Malay basin generally strike from East to West with 35 degrees oblique to its Northwest-Southeast trend.

With regards to the kinematic development, regional dextral mega shear occurs due to indentation of India to Asia in the early Tertiary era (Madon et al., 1999). Consequently, this local shear caused east-trending faults within the fault zone to turn and form half grabens that underwent transgression due to changes in the regional stress field. (Madon et al., 1999)

Finally, a wrench development causes the basin to experience an inversion between the Middle and Late Miocene. This inversion resulted in the development of compressional anticlines within the axial region of the basin. The timing and growth of the inversion anticlines are essential elements for hydrocarbon entrapment. A study discovered this inversion phenomena and causes of the thickness of the syn-inversion stratigraphic unit to decrease towards the coastal region. The erosion and deformation of the depositional surfaces cause a decrease in thickness. (Madon et al., 1999)

5.3 Stratigraphy and Paleo-environment

The stratigraphic development of the Malay Basin is correlated to its structural evolution which consists of three phases (Madon et al., 1999):

- Pre-Miocene extensional syn-rift phase
- Early to Middle Miocene thermal/tectonic subsidence phase accompanied by basin inversion
- Late Miocene to Quaternary subsidence phase

5.4 Hydrocarbon Occurrences

Figure 5.2 illustrates the general stratigraphy of a well in the Malay Basin and the depth where oil and gas occurrences were identified. Previous studies by PETRONAS show that most of the oil and gas occurrences are in the lower and middle Miocene.

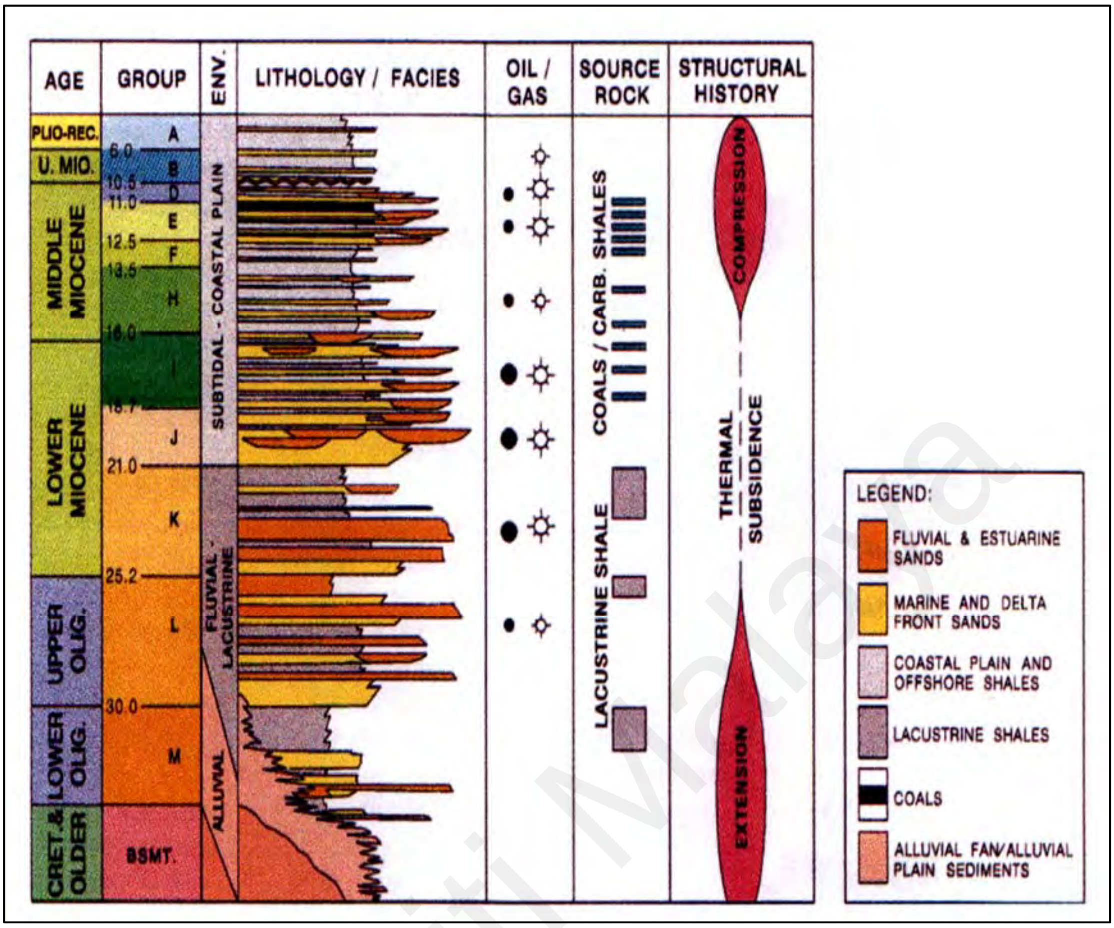

Figure 5.2: Generalized stratigraphy of the reservoir from which the samples in this study came. The samples in this study were extracted from the lower Miocene where most of the hydrocarbon in the basin are produced (Madon et al., 1999)

5.5 Geological Description

5.5.1 Trap Style

The hydrocarbon trap in the X field consists of a three-way gentle dip closure that is confined to the North by faults. Stratigraphic traps by shale-out deposition are possible but have not been encountered (CariGali, 2008).

5.5.2 Vertical Relief

At the shallowest mapped geological surface, the vertical relief is 100 m. There is an interval called D-55 that has a vertical relief of 140 m. Another interval D60 has a relief of 150m (CariGali, 2008).

5.5.3 Structure

The structure of field X is an elongated, East-West trending anticline that forms a field with a size that is approximately 30 km by 12 km. Two major normal faults are present at the eastern and western side of the field. At the central part of the field, there are northeast-southwest trending normal faults that could create compartmentalization. The structure of the field dips gently to the west and then rises across a saddle, forming the South West structure. The field dips moderately to the north and south. The age of D and E groups in Field X was dated to between the Middle and Late Miocene. These groups are related to the North-West trending dextral shear transpressional movements along basement faults such as the Axial Malay Fault Zone (CariGali, 2008).

5.5.4 Seal

Hydrocarbons have been detected in multiple reservoirs within different sands in groups-B, D and E. Layers of mudstone from the top seal of the reservoirs. Mudstone in the upper D and B group form the top regional seal. Lateral seals are dependent on the fault's effectiveness determined by the juxtaposition of sands, lithofacies and the shale gouge ratio. Core analysis from field X indicates that the reservoirs are dominated by heterolithic rock types that could act as seals, as some heterolithic rock types such as lenticular heteroliths are impermeable (CariGali, 2008).

5.5.5 Stratigraphy

Field X stratigraphy (Figure 5.3) consists of the younger Group B, D and E and the older Group F and H. The youngest interval is Group B which is dated to Early Miocene to Pliocene in age. The B group deposition occurred on a prominent erosional surface (Pliocene/Miocene Unconformity) during relative sea rise (CariGali, 2008).

Group D deposition occurred during the Middle Miocene and marked by an unconformity. This group consists of facies described as interbedded sand and shale. Group D also consists of a series of progradational successions composed of marine-influenced deposits interpreted as representing deposition in shallow marine, tidal channel, and lower coastal plain depositional environments. The D group also consists of several zonal boundaries which include D34, D50, D55 and D60 zones which are characterized as being deposited in a high-energy environment. D35 is a gas reservoir while D50, D55 and D60 are oil and gas containing reservoirs (CariGali, 2008).

Group E strata were deposited in distributary channel and crevasse splay sand environments and were deposited during a regional regression. During Group D deposition, the shoreline was encroaching landward to a small degree (CariGali, 2008).

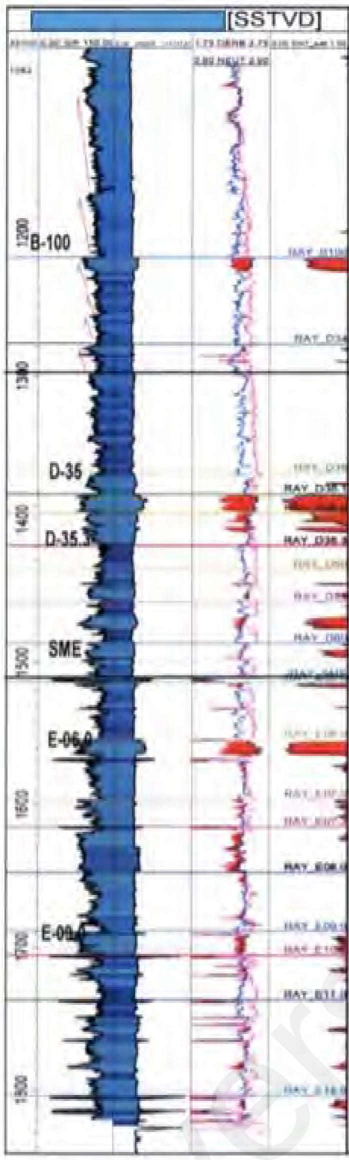

Group	Age	Remarks
A and B Group	Late Miocene to Pliocene	A and B Group is a series of progradational sequence. Sediments comprise shallow, marine, fluvial channel deposits and lower coastal plain deposit in the B Group. The base of this group is marked by regional uncomformity/hiatus recognized from the seismic and nannofossile interpretations.
D Group	Middle Miocene	The top D group is associated with uncomformity/Hiatus. These groups consists of interbedded sand and shale. Coal was not deposited during the deposition of D group.D group shows an overall increase in marine influence. This group is a series of a progradational sequence consist of deltaic deposits with marine influence, fluvial channel deposits and lower coastal plain deposits. Sediments in the D-lower was deposited in a higher energy environment characterized by sand deposition. No coal deposition in the D Group.
E Group		E Group is a series of retrogradational sequence. Sediments deposits with some marine influence, fluvial channel deposits. Sediments are dominated by sands deposited in fluvial channels. Coal deposition is abundant within E groups.

Figure 5.3: Stratigraphy of field X Field (CariGali, 2008)

CHAPTER 6 : SEDIMENTOLOGY OF THIN-BED AND LOW-RESISTIVITY/LOW-CONTRAST RESERVOIRS

This chapter reviews the definitions and occurrence of thin beds and LRLC pay. This chapter focuses on the depositional environment and rock types such as rhythmites and heterolithic rocks that are abundant in thin-bed LRLC reservoirs. This chapter also focuses on occurrences of heterolithic reservoirs due to its large abundance in well X-4 in Field X. An essential part of this chapter is the Facies Analysis of Well X-4, which interprets the types of facies, facies association and depositional environment. Lastly, we discussed the impact of the interpreted depositional environments of Well X-4 and Field X to evaluate their impact on the reservoir in terms of the reservoir architecture, the aerial extent of the reservoir, reservoir and hydrocarbon accumulation and production.

6.1 Definitions and Geologic Occurrence of Thin Beds in Clastic Reservoirs

Based on geological literature, beds are distinct layers of a sedimentary body which form the basic units of geological bodies. Beds have sedimentary surfaces as boundaries which are also called bedding surfaces. These surfaces are synchronous, and a bed is considered an informal time-stratigraphic unit of an area that represents a brief period. By order from smallest to largest, beds of a sedimentary body are categorized into (Campbell, 1967):

- laminae,
- laminae-sets,
- beds and
- bed-sets

Thin beds are interpreted differently by different people, even within the field of geology. By one definition, thin beds have a thickness ranging between 5 to 60cm (Bates et al., 1984) while another defines thin beds ad beds with a thickness between 3 and 10cm (Campbell, 1967). In thinly bedded LRLC reservoirs, we defined thin beds as beddings that are below the resolution of well logs which is limited to 60cm (Passey et al., 2006).

6.2 Petrophysical Beds

In Petrophysics well log analysis, the bed terminology refers to an interval within a formation that has constant reservoir properties such as clay volume, porosity and water saturation. These beds with same geological genetic material, provide consistent, well log readings such as Gamma Ray and Resistivity measurement which can infer lithology and water saturation indirectly. In Petrophysics, thin beds refer to units of constant petrophysical properties that have thicknesses that are below the vertical resolution of well logging equipment. The vertical resolution of well log equipment is the smallest bed thickness in which we can acquire measurements. (Passey et al., 2006)

We defined a petrophysical bed as any contiguous unit of rock with a narrow distribution of petrophysical characteristics (which include porosity, grain density, permeability, capillary pressure behaviour) that is bounded above and below by units with significantly different petrophysical characteristics' (Passey et al., 2006)

Also, we defined a petrophysical thin bed as a petrophysical bed with a thickness between 2.5 cm and 60 cm. (Passey et al., 2006). We identified 60 cm as the cut off for thin-bed as it is the vertical resolution for porosity logs and high-resolution resistivity logs.

Also, we defined a petrophysical very thin as a petrophysical bed with thickness less than 2.5 cm' (Passey et al., 2006) which are below the resolution of electrical borehole image (EBI) logs and conventional core plugs (Passey et al., 2006).

6.3 Low-Resistivity Reservoirs

In thin-bed and LRLC reservoirs such as tidal heterolithic deposits, sand and mineral-rich mudstone beddings are interbedded with each other. The presence of clay minerals alongside sandstone impacts the well log measurements in terms of water saturation measurements using resistivity logs. Adjacent clay beddings reduce the resistivity measurements in shaly sands and heterolithic formations which makes it challenging to distinguish reservoir from non-reservoir pay (Chen et al., 2009; Mode et al., 2015) and hydrocarbon and water (Heavysege, 2002). As a result, we tend to underestimate hydrocarbon reserves in LRLC pay due to interpreted high water saturation caused by averaging and thin bed effects (Cerepi et al., 2002; Worthington, 2000). LRLC intervals which cannot be evaluated using conventional petrophysical evaluation, cut-off methods and well log analysis which tend to contribute to low reserves estimate. These issues are discussed extensively in Chapter 2.

The reservoir interval examined in well X-4 examined in this study consists of laminated shaly sands that consist of alternating sand and mudstone rhythmites and heterolithic lenticular structures where mudstone and sandstone layers are intercalated. Some of the heterolithic intervals in X-4 are also affected by bioturbation that has significant implications on flow properties interpretation. Also, the reservoir is a freshwater formation which contributes to poor contrast that causes difficulties in differentiating hydrocarbon and water-bearing intervals. These factors contribute to the

LRLC pay that causes challenges in appraising the reservoir quality of thin-bedded reservoirs.

6.4 Depositional Environments of Thinly Bedded Sandstone Reservoirs

6.4.1 Tidal Deposits

The reservoir in this study involves tidal deposit in a shallow marine setting rich in shaly sands and heterolithic rocks. The intricate heterogeneity in tidal heterolithic reservoirs is due to the depositional process and environment. The shallow marine environment created a variety of rock types with different sand-to-mud ratio, thin beddings with variable thickness and bioturbation intensity. The heterogeneity in tidal heterolithic deposits causes complexity in terms of varying petrophysical responses on the well logs and large flow properties contrast between adjacent rock types. Depending on the depositional environment such as tidal bars and deltaic deposits, the lateral and vertical connectivity of the sand and heterolithic deposits would differ. As a consequence of complex 3-Dimensional architecture with variable lateral and vertical connectivity, modelling for flow analysis is difficult (Gupta et al., 2001; Massart et al., 2016).

Tidal deposit facies such as tidal rhythmites, tidal bundles and heterolithic deposits are associated with tide-influenced deposits. These deposits are influenced by the tidal cycle, which creates alternating sand and mud layer found in rhythmites and heterolithic facies. Also, different periods of ebb and tide deposit different thickness of mud. For example, a more extended period between the tide and ebb cycle deposit thicker layers of mud and silt with a two hour low tide period typically depositing millimetre -to-centimetre layers of mud depending on other factors such as the supply of sediment and wave conditions (Reineck et al., 1980).

Heterolithic facies encountered in well X-4 used in this study show convincing evidence of tide and wave influences. Variations of the strength of the tidal cycles have an impact on creating heterolithic facies with varying bedding thickness and ripple structures which are sum effects of tide and wave actions. The different rock types in heterolithic reservoir include flaser, wavy and lenticular heterolith. These rock types have varying sand to mud ratio, ripples structures and bioturbation intensity that affect reservoir properties. Therefore, understanding the petrophysical effects of this spectrum of heterolithic rocks are crucial to model the impact of heterogeneity on the reservoir quality in terms of flow potential and hydrocarbon reserves estimates.

6.4.2 Impact of Tidal Cycle on Sedimentological Records

The tidal cycle causes variation in sea level caused by the interaction between the gravities of the Earth, the Sun and The Moon. The difference between the maximum sea level and its minimum is called the tidal range. The maximum sea level achieves during flooding and falls to its minimum during ebbing. The flood and ebb cycle induces a horizontal current. A tidal cycle with a higher tidal range will create a higher speed tidal current. Within the tidal range, there are several classifications described below (Nordahl,2004):

- Micro-tidal: less than 2-m tidal range
- Meso-tidal: 2 to 4 m
- Macro-tidal: More than 4 m

Meanwhile, the deposition environment affected by the tidal cycle may also be sub-categorized into different zones:

- Sub-tidal: below the mean low water level and submerged during low tide.
- Supra-tidal: above the mean water level that arises during spring tides.
- Intertidal zone: between the supra-tidal and sub-tidal zones

Tide influenced deposits are present in a wide range of deposition environments which include shelf barrier, lagoons, delta and estuaries (Nordahl, 2004).

6.4.3 Flood and Ebb four-stage cycle

Within the sub-tidal, there exists a period between the ebb and flood period where the water would be standstill called the 'slack water' period. The sediment transport during slack water is more extended, which is related to the entrainment velocity on the bed and current strength. The ebb-flood cycle can be resolved into four different stages (Nordahl, 2004):

- The dominant current stage
- The slack water stage after dominant current stage
- The subordinate current stage
- The slack water stage after the subordinate current

This cyclic variation in current speed due to the ebb, slack water and flood cycle affects the depositional process of tidally influenced deposits. For example, variation in current speed can have some effects on the ripple morphology of the tidal deposits. The result of the four-stage ebb-flood cycle is observed in bars and dunes and planar and ripple cross-laminated beddings. Ripple laminated sand and mudstone commonly found and observed in tidal deposits have been described and categorized according to sand and mudstone ratio shown in Figure 6.1 (Nordahl, 2004).

One important deposition process that should be studied in the tidally influenced environment is the deposition of mud which is a function of mud concentration in the water and the settling velocity. Characteristics of mud deposition can be correlated with the water salinity, the mud particles electrical conductivity, and turbulent shear. For example, a concentration of mud at 1gm/cm^3 and a settling velocity of 0.04 cm/s would deposit 0.3cm of mud layer (Nordahl, 2004).

A type of sedimentary structure common and specific to tidal deposits are tidal rhythmites. Tidal rhythmites are horizontal beddings that consist of alternating beddings of sand and mudstone/silt. Figure 6.1 shows that the alternating layers strongly indicate cyclicity in the thickness of the sand and mudstone beddings caused by diurnal and neap spring changes in tidal speed. The low tide, which is the weaker of the tidal cycle is too weak to deposit sediment. Consequently, each couple of coarse and fine sediment bedding is representative of a single tide cycle. The coarse beddings in a pair of tide cycle have no internal structure due to deposition by suspension, however, where the current of the tide is at its peak, ripple cross laminations are evident (Dalrymple et al., 2010).

6.4.3.1 Tidal Rhythmites/Tidal Bundles

The occurrence of tidal rhythmites shown in Figure 6.1 requires several factors. Firstly, the supply of sediment must be high as to deposit layers of sediment several millimetres every 12 hours. These conditions only occur in specific deposition systems such as at the margins of channels and within delta-front and pro-delta conditions. Secondly, the presence of strong tidal is required to flocculate the sediments into suspension and cause them to settle on the surface of the beddings to form the rhythmites. Due to these two factors, tidal rhythmite is most commonly deposited in macrotidal (>4 meters) environments, although they are also common in areas with a tidal range of only two meters. The deposition of tidal rhythmites must also be in a sheltered setting without string waves or wind-induced tides that could alter the tidally influenced deposition process. Due to this, tidal rhythmites are common in the landward parts of estuarine and deltas that predominantly tidal influenced (Dalrymple et al., 2010).

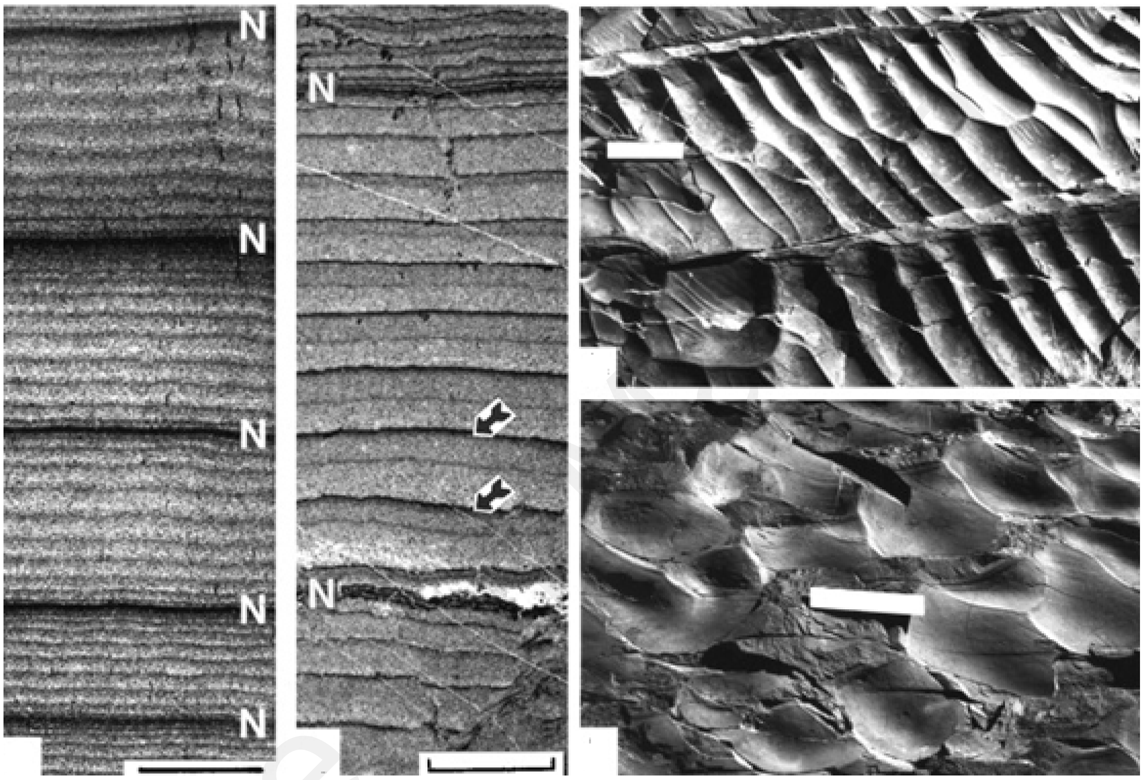

Figure 6.1: Tidal rhythmites from the Elatina Formation in South Australia (Williams et al., 2008)

Figure 6.2 below illustrates tidal rhythmites formations during a tidal cycle. Different periods of low tides, high tides, rising and falling tides create different configurations of equal and unequal couplet formations of sandstone and mudstone layers with different thicknesses (McLean & Wilson, 2016).

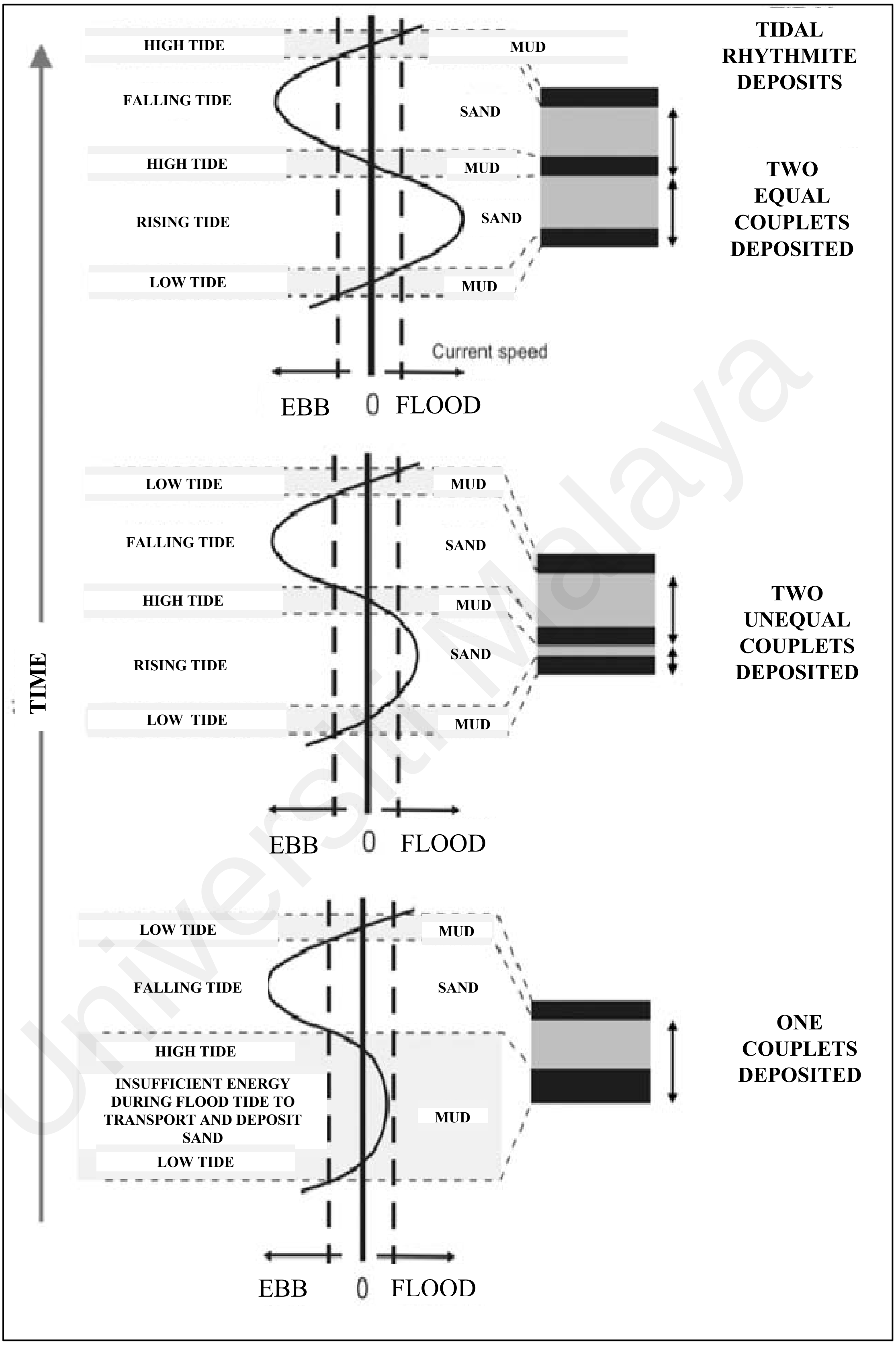

Figure 6.2: Pairs of sand and mud deposition during the tidal cycle (McLean & Wilson, 2016). Note the vertical dashed lines refer to the ebb and flood part of the tidal cycle.

6.4.3.2 Flaser, Wavy and Lenticular Beddings

The heterolithic facies in tidal deposits are generally categorized based on the different sand and mudstone ratio with rippled and intercalated sand and mud structures. Figure There are three types of heterolithic beddings described by Nordahl (2004). Figure 6.3 shows the three main types of heterolithic beddings. Also, different sand and mud content create different sedimentary structures in the heterolithic beddings.

- Flaser or Sandy Heterolithic: Sand dominant (more than 50% sand content)
- Wavy: Equal amount of sand and mudstone
- Lenticular or Muddy Heterolithic: Mudstone dominant (more than 50% mudstone content)

Identifying the type of heterolithic facies provides information such as the energy level of the current during deposition, sediment supply that indicate the depositional process and environments. Also, heterolithic rock types features such as the thickness of the sand and shale bedding, the inclination of the beddings, ripple structure and bioturbation intensities are correlated to depositional processes such as the current strength. Characterizing the depositional settings of heterolithic deposits provides a geological framework to the reservoir architecture that affects lateral and vertical connectivity and the distribution of reservoir sand and heterolithic deposits.

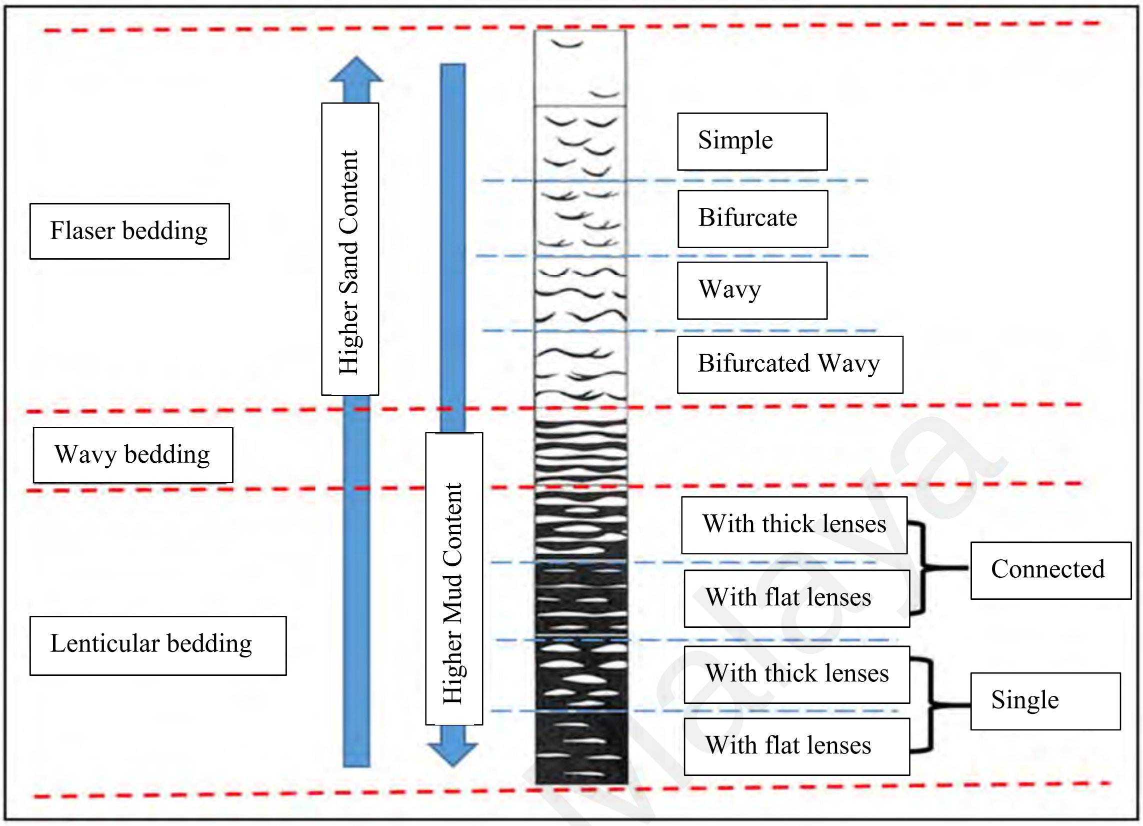

Figure 6.3: Categorization of heterolithic facies into flaser, wavy and lenticular beddings. The white rocks represent sand while mudstone is black in the figure (Reineck & Wunderlich, 1968).

6.4.3.3 Impact and significance of Heterolithic facies

Heterolithic facies which include flaser, wavy and lenticular rocks are also described as Low-Resistivity and Low-Contrast pay. LRLC pay consists of millimetre-to-centimetre beddings with varying sand and mud contents with fine-scale reservoir connectivity and bioturbated facies that cause an extensive range of pore throat profiles (Carney et al., 2008). Heterolithic rocks that consist of intercalated thin sandstone and mudstone laminates are common in mudflats, tidal point bars, and tidal sand bars (Jackson et al., 1999). Figure 6.4 and Table 6.1 provide a visual and general description and actual images respectively of the flaser, wavy and lenticular facies typical in heterolithic deposits that we can use as a reference for categorizing heterolithic rocks in the field.

Sand dominated heterolithic facies like flaser heteroliths, or Sandy Heterolithic has low entry pressure and low irreducible water saturation and high sandstone connectivity and continuity. In contrast, mud dominated heteroliths such as wavy and lenticular heterolithic rock (or muddy heterolithic rock) have high entry pressure, high irreducible water saturation and low sandstone connectivity and continuity. (Carney et al., 2008) which demonstrates that these varied rock types have different flow characteristics correlated to their thin bed structure and sand-to-mud ratio. Once we identified the reservoir heterolith rocks based on initial information such as initial saturations, other consideration such as the continuity of the sand layers, the ratio of sand and areal extent are additional are evaluated for further appraisal before committing to full production (Vajnar et al., 1977).

Therefore, different heterolithic rock types have different properties such as different capillary pressure profiles and different wettability that can have an impact of the reservoir's quality in terms of hydrocarbon reserves estimates and flow potential during production. The complex geometry and distribution of mud and mineral drapes and lamination can also impact the effective properties at larger reservoir scale in a reservoir model of heterolithic deposits (Massart et al., 2016; Massart et al., 2016).

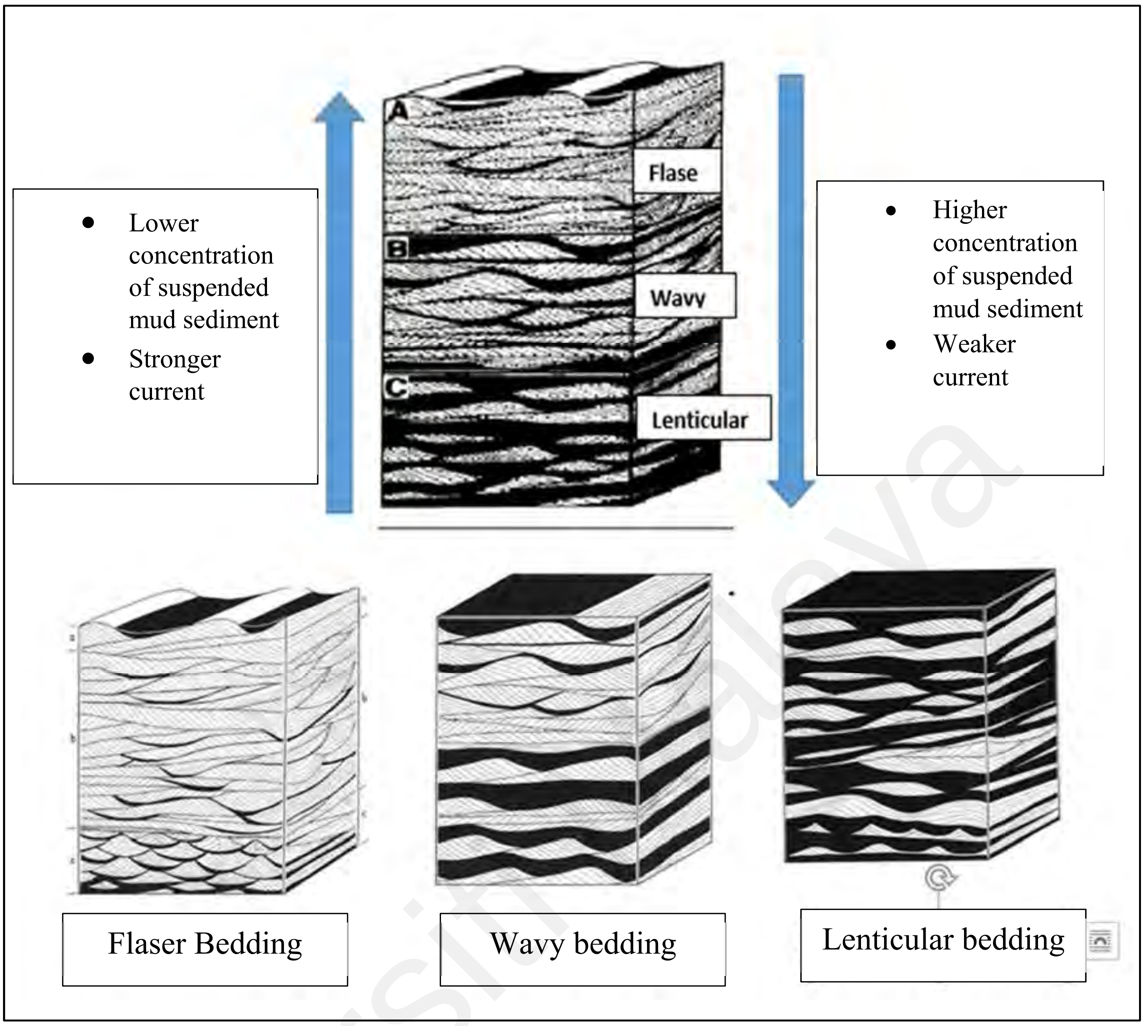

Figure 6.4: Flaser bedding (A), wavy bedding (B) and lenticular bedding (C) (Reineck & Singh, 1980)

Table 6.1: Picture and description of flaser, wavy and lenticular beddings (Bellile, 2003)

<table>
<tr><th colspan="2">Flaser Bedding</th></tr>
<tr><td></td><td>

- Indication of fluctuating flows with start/stop currents
- Sand ripples intercalated with troughs filled with mud
- Environment setting that favours sand deposits which have relatively strong currents that deposit more sand than mud and erode mud deposits from the ripple crests
- Predominantly sand

</td></tr>
<tr><th colspan="2">Wavy Bedding</th></tr>
<tr><td></td><td>

- Indication of fluctuating flows with start/stop currents
- Alternating layers of sand ripples and mud-filled ripple troughs that thinly covers the crest
- Environment setting does not require favour sand or mud deposits with currents alternating between strong current followed by a calm period
- Equal amounts of sand and mud deposits

</td></tr>
<tr><th colspan="2">Wavy Bedding</th></tr>
<tr><td></td><td>

- Indication of fluctuating flows with start/stop currents
- Sand ripples intercalated within predominantly mud deposits
- Environment setting of calm periods with weak current favours mud deposits
- Predominantly mud

</td></tr>
</table>

6.4.3.4 Bioturbation

Bioturbation is signs of disturbance by living organisms which include plants and animals in the sediments such as signs of burrowings, tunnels and fossils. Signs of Bioturbation provides important clues of the environment of deposition. Information such as sediment supply, the salinity of the water, the coherency of the substrate, oxygen level, turbidity, abundance of food and its type, subaerial exposure, we may infer the depth of the water, temperature and deposition energy and surface colonization may occur from the bioturbation structures. (McLean et al., 2016) The intensity of bioturbation traces within the formation provides information about the condition of the environment. We correlated the trace fossils, and ichnofacies to the paleoenvironment at the point of their existence.

In tidal environments, the conditions are described as stressed or inhospitable to living organisms due to variations in salinity, changing water levels, concentrations of sediment in suspension, and other variable conditions. (Dalrymple et al., 2010) This stressed environment is typically present in brackish water where freshwater and marine environment meet. In sediments where such environment is evident, we used the study of fossils and their traces (or ichnofacies) to interpret the fluvial-tidal transition regions. Conditions upstream are more fluvially dominated compared to the tidally influenced downstream. Changing conditions from tidal (downstream) to fluvial(upstream) conditions cause a decrease in the intensity of bioturbation as there is a decrease in size and diversity of the associated biogenic structures (McLean et al., 2016). Burrow fills that are rhythmic or cyclic indicate tidal influence which we can correlate to organisms feeding patterns, simple burrow structures, lining and materials and regular occurrences and the abundance of trace fossils types.

6.4.3.5 Impact and Significance of Bioturbation

According to Tonkin (2010), a sizable portion of the world's clastic reservoirs is affected by intense levels of bioturbation. Lucrative hydrocarbon productive reservoirs such as the Lower Cretaceous Ben Navis formation, Jeanne d' Arc Basin, offshore Newfoundland, Canada; Upper Jurassic Fulmar Formation and Middle Jurassic Ile Formation, Halten Terrace, offshore mid-Norway; and Lower Cretaceous McMurray Formation, Alberta, Canada are bioturbated reservoirs. Bioturbation modified the flow and reservoir properties in these reservoirs.

Bioturbated sandstone has an extensive range of pore throat profiles which affect different properties. For example, the varying pore throat profiles causes high irreducible water saturation in sand dominated facies and low irreducible water saturation in mud dominated facies. (Carney et al., 2008). As a result, laboratory-based measurement of the capillary pressure in the study of bioturbated facies is technically challenging(Heavysege, 2002). The effects of bioturbation on heterogeneous facies such as thin bedding are more complicated due to the presence of mudstone and sand beddings that may be modified by biogenic activities. As a result of the modified beddings, properties such as porosity and permeability may be enhanced or reduced depending on the type biogenic activities (Ben-Awuah et al., 2015).

According to Tonkin (2010), porosity and permeability in the reservoirs are controlled by these factors

- Sedimentary processes
- Biogenic processes
- Diagenetic processes.

Organisms burrowing through the sediment creates biogenic structures that consist of trails, tracks, burrows while reworking lithic clast, mineral grains and organic material which changes the main physical sedimentary fabrics. The organism that creates bioturbation is classified into mixers, cleaners, packers and pipe builders who have a different impact on the permeability of the sediments. These bioturbators change the sorting of the grains and create networks of open burrow systems and filling them with fine or coarse material. These changes affect fluid flow or permeability through the sediment.

6.4.3.6 Classification of Ichnofabric and Bioturbation

This study uses a semi-quantitative classification method of bioturbation which classifies fossils and their traces based on the pattern of the proportion of the sediment that has been disturbed by burrowing organisms. (Droser et al., 1986) We used this method with the ichnology description to determine the intensity of the bioturbation observed in the sediment. Figure 6.5 shows the Ichnofabric index described by Droser et al. (1986) which we can use as a reference for categorizing bioturbation intensity in the field.

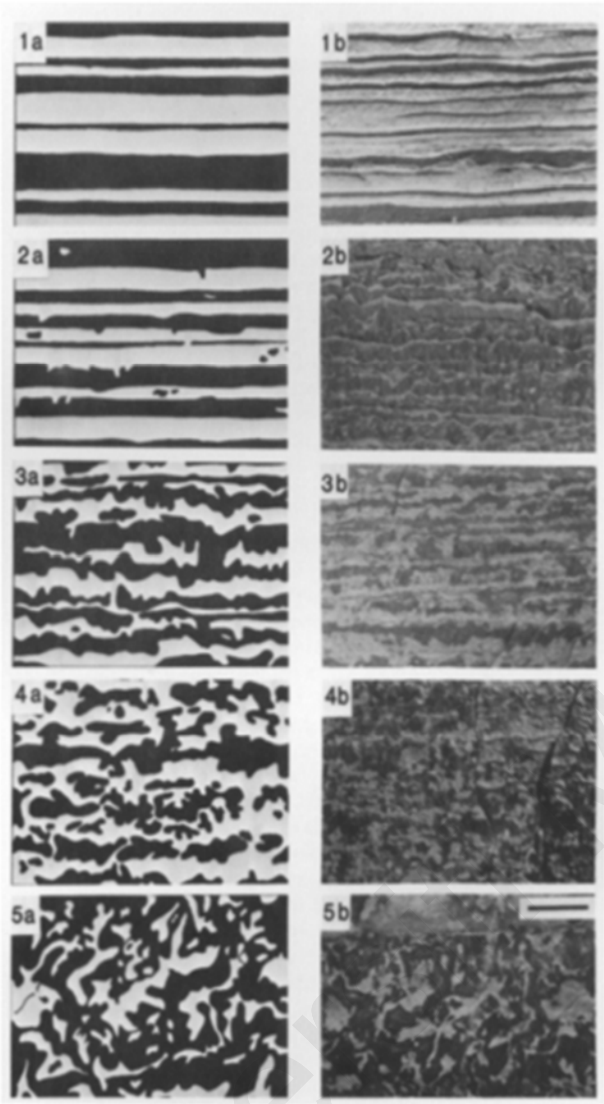

1a. Ichnofabric Index 1

1b. Example of Ichnofabric Index 1 from the Middle Ordovician Badger, Flat Limestone, Mazourka Canyon, White-Inyo Mountains, California.

2a. Ichnofabric Index 2

2b. Example of Ichnofabric Index 2 from the Upper Cambrian Nopah Formation, Nopah Range, California.

3a. Ichnofabric Index 3

3b. Example of Ichnofabric Index 3 from the Lower Cambrian Poleta Formation White-Inyo Mountains, California.

4a. Ichnofabric Index 4

4b. Example of Ichnofabric Index 4 from the Middle Cambrian Bonanza King Formation, SouthWestern Nevada.

5a. Ichnofabric Index 4

5b. Example of Ichnofabric Index 5 from the Bonanza King Formation, SouthWestern Nevada.

Figure 6.5: Schematic Diagram of Ichnofabric index (Droser & Bottjer, 1986)

Ichnofabric Index 1: No Bioturbation observed with the original beddings such as laminae still fully intact

Ichnofabric Index 2: Distinct trace fossil that is isolated. 10% of original beddings disturbed

Ichnofabric Index 3: Between 10 to 40% of the beddings in place restructured by trace fossils or biogenic structures such as overlapping burrows.

Ichnofabric Index 4: Biogenic structures and fossils restructured. Between 40 to 60% of the original beddings. The beddings are barely recognizable.

Ichnofabric Index 5: The original beddings wholly restructured. Burrows are still isolated, and the fabric of the sediments are not mixed.

Ichnofabric Index 6: Beddings are entirely restructured and homogeneously mixed.

6.5 Facies Analysis

An initial description of well X- 4 facies was conducted using high-resolution photos of the core supplied by Petronas. The length of well X-4 core is 42 meters. A visit to the Petronas Core Storage Facility in Kuala Lumpur, Malaysia was conducted on 4th June 2016 to identify the cores suitable for this study. Tables 6.2 shows the length of core and quantity of core plugs from well X-4 that we selected for this thesis. We selected this interval of the core because of their excellent condition. Also, this interval of core contains a substantial amount of heterolithic rocks that are of significant interest in this study. Another crucial factor for selecting well X-4 is that Petronas has extracted a substantial amount of vertical and horizontal core plugs from the well. The core plugs from this interval represent different rock types with different sedimentary structures and varying levels of bioturbation. These core samples were analysed using XMCT imaging, Image Analysis, and digital core analysis to compute porosity and permeability.

Table 6.2: Length of core and number of plugs selected from well X-4.

Field	Well	Length. of cores selected(meters)	No. of plugs accessed
X	**4**	42	40

The resolution of the photo of the core interval was sufficient to resolve millimetre-to-centimetre scale bedding layers, the sedimentary structure, sign of trace fossils and bioturbation. The core description involves categorizing the facies into basic rock types such as sandstone, mudstone, heterolithic rocks and coal. Each rock type is also categorized based on its sedimentary structure. For example, we divided the sandstone in X-4 into cross-bedded sandstone or sandstone with silty laminae.

We recorded the thickness of each rock type and its sedimentary structure in detail. This information allows the percentage of the total length by rock type and its sedimentary structure to be recorded and categorized. Because of this method, we observed that most of the rock in X-4 is heterolithic. Figure 6.6 below shows some parts of the core from well X-4 that are heterolithic rocks.

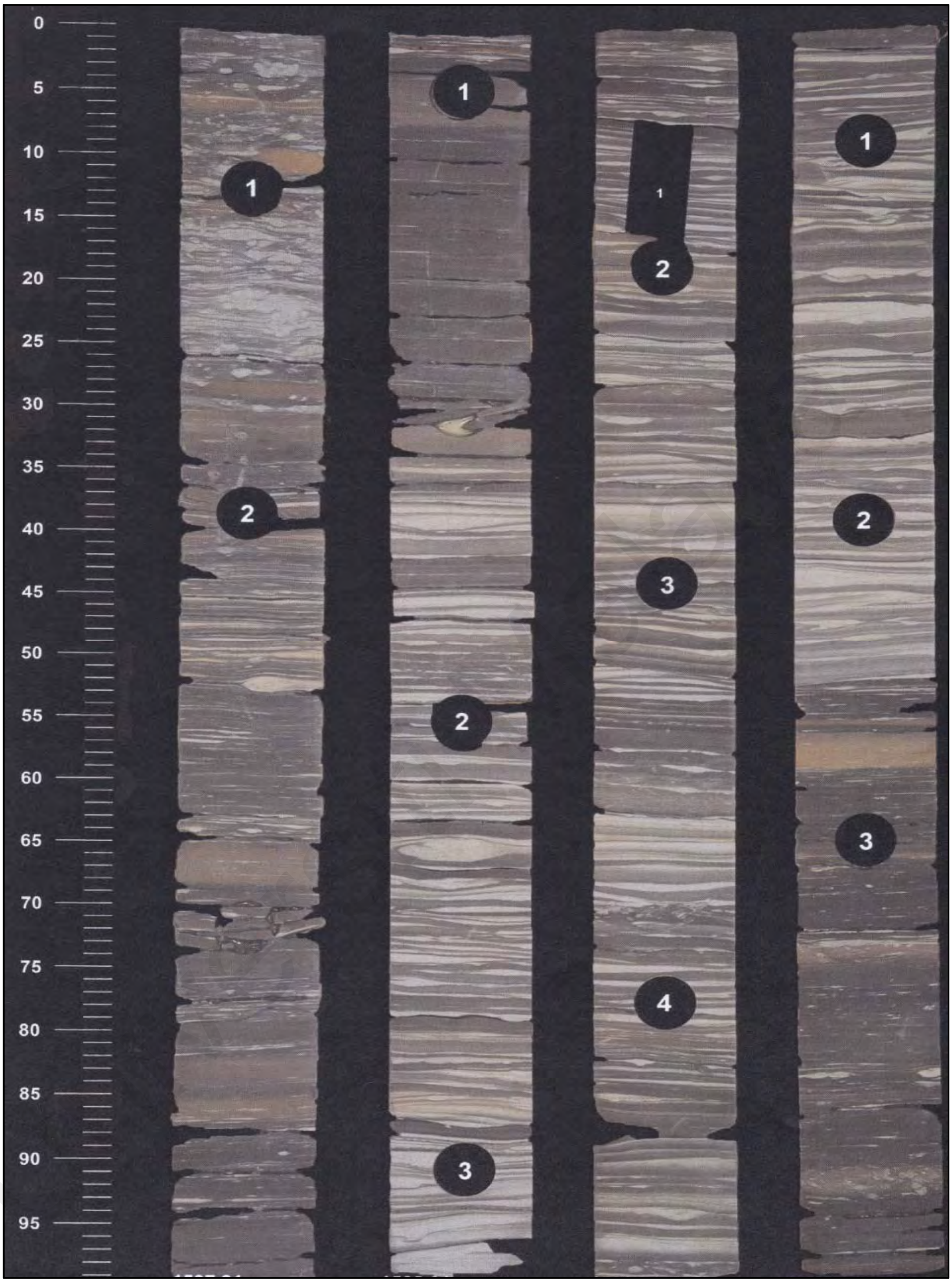

Figure 6.6: A picture showing four sets of one-meter core slab from X- 4 that consists of tidal rhythmites and heterolithic rocks which include wavy and lenticular sedimentary structures. (Petronas, n.d). The scales at the side are in cm, and the number in holes are the order of the core plug extracted from each slab.

6.5.1 X- 4 Facies Analysis

We categorized Well X-4 into four major rock types which consist of heterolithic, sandstone, mudstone and coal. As summarised in Table 6.3, 58.7% of X-4 vertical succession consists of heterolithic rocks, followed by sandstone (25.97%), mudstone (11.57%) and coal (3.8%). Each rock type is subdivided based on different sedimentary structures and mudstone contents. For example, the heterolithic rocks in X-4 are categorized into flaser, wavy or lenticular facies which is dependent on the sandstone to mudstone ratio. Table 6.3 summarizes the four major types of rocks and their subcategories or facies types. In total, there were 13 types of facies or rock types identified.

Table 6.3: We categorized the rock types in well X-4 core photos and the percentage of each rock type and sedimentary structure of total core length.

Row Labels	Sum of Interval(m)	Percentage of total interval
Heterolithic Rocks	**46.34**	**58.67%**
Flaser	1.26	1.60%
Lenticular	42.17	53.39%
Wavy	2.91	3.68%
Sandstone	**20.51**	**25.97%**
Clean	1.44	1.82%
Interbedded Mudstone	6.28	7.95%
Mudstone Streaks	4.37	5.53%
Silt Laminae	8.42	10.66%
Mudstone	**9.14**	**11.57%**
Graded	3.34	4.23%
Interbedded Sandstone	1.38	1.75%
Laminar	1.88	2.38%
Sandstone Laminae	0.55	0.70%
Sandstone Streaks	1.99	2.52%
Coal	**2.99**	**3.79%**
Coal	2.99	3.79%
Grand Total	**78.98**	**100.00%**

6.6 Lithofacies

This section summarizes the lithofacies or rock types that make up Well X-4, a gas-producing well in Malaysia. We categorize well X-4 as a thin bed and LRLC reservoir due to a large amount of lithofacies that consist of alternating layers of thin sandstone and mudstone beddings Well X-4 is dominated by rhythmites and and heterolithic rocks with several types of sandstone and mudstone.

6.6.1 Identified Lithofacies in well X-4

Figure 6.7 shows that we divided the interval within well X-4 into 13 types of lithofacies or rock types. Heterolithics that make up 59% consist of Lenticular Beds, Graded Beds and Wavy Flaser Beds. Sandstone is the second largest group of lithofacies that make up 26% of well X-4. We divided the sandstone into bioturbated sandstone, crossbedded, laminated and cross-bedded laminated sandstones. The third group of prevalent lithofacies is mudstone. Table 6.7 provides a detailed description and core photos of the rock types in well X-4. The information in Table 6.4 was provided by PETRONAS, which we used as a reference for categorizing the different rock types in Figure 6.7.

Despite the apparent low net to gross (due to the low sandstone proportion) of well X-4, Well X-$ was a productive gas producing field in Malaysia. The pre-drilling report by PETRONAS indicates the evaluation of the hydrocarbon in place of well X-4 requires 30% additional hydrocarbon reserves or a reduction of development cost by 30% (CariGali, 2008). The discrepancy between the pre-drilling report and the commercial amount of gas suggests that a significant amount of hydrocarbon was produced from the low-resistivity heterolithic lithofacies that make up almost 60% pf well X-4. Geoscientists in Malaysia are characterizing LRLC pay using a multidisciplinary approach to measure reservoir properties more accurately that will be incorporated into reservoir models to improve reserves estimates improve field development and management (Chai et al., 2008).

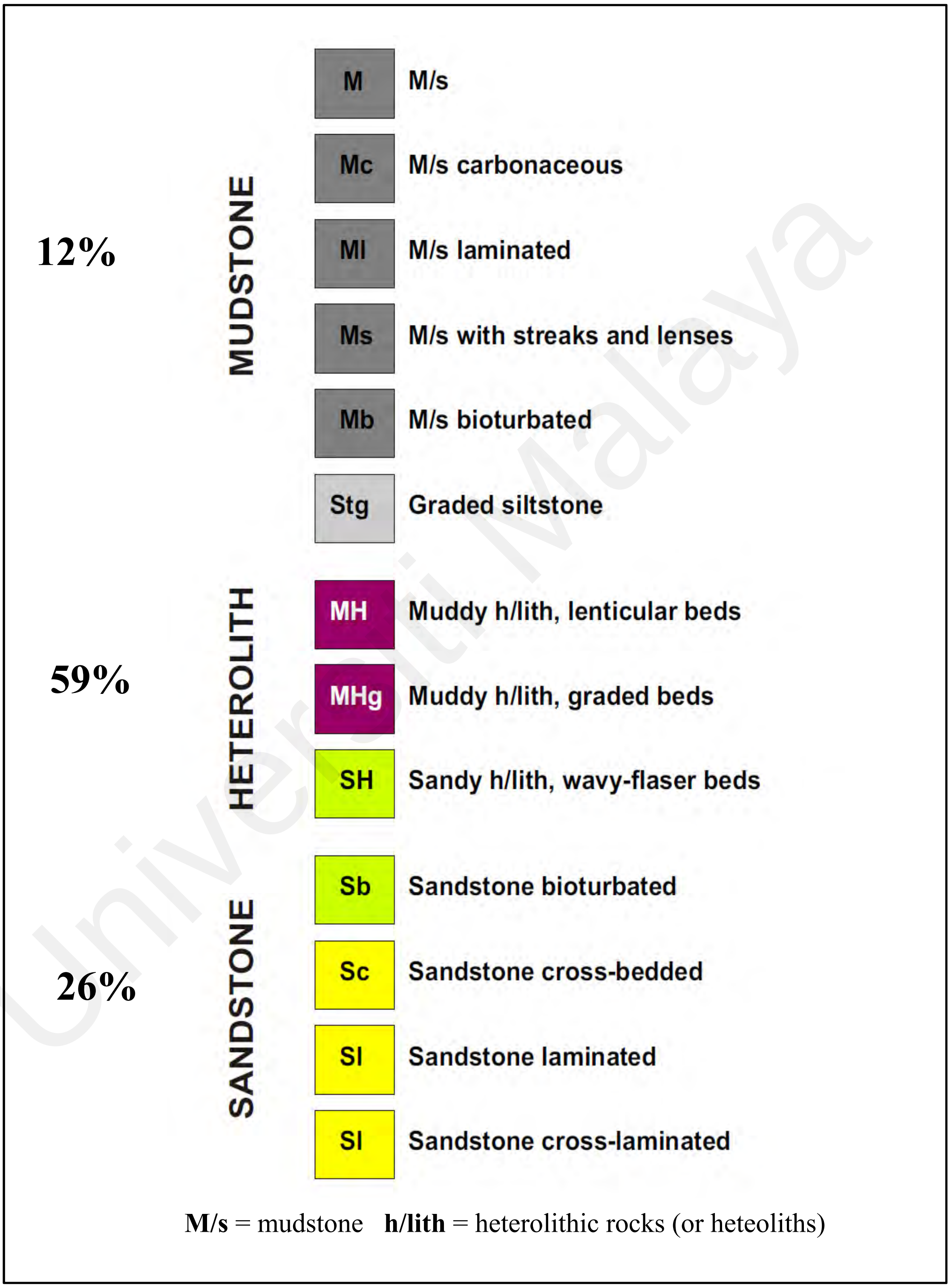

Figure 6.7: Identified lithofacies or rock types in well X-4.

Table 6.4: Description of rock types observed in well X-4 from top to bottom. PETRONAS geologists described the rock type in well X-4. Please note the holes on some cores are locations where a core plug extracted.

Plug no.	Depth (m)	Rock Type	Description	Core Photo
11V 11	1459.96 1460.02	Mudstone	Claystone: medium-dark grey to dark brownish grey, occasionally greenish grey to dark greenish grey, medium-hard, sub-platy to sub-blocky, trace carbonaceous material, non to slightly calcareous, silty in part.	 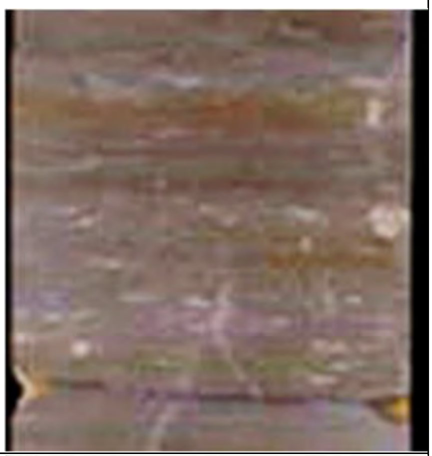
21V	1462.95	Sandstone	Claystone: medium grey to medium-dark grey, moderately hard, sub-platy, occasionally sub-blocky, trace carbonaceous material, slightly calcareous, silty in part.	

Table 6.4 continued

Plug no.	Depth (m)	Rock Type	Description	Core Photo
21 31V	1463.02 1465.95	Sandstone	Sandstone: light grey to light brownish grey, occasionally very light grey, translucent to transparent, firm to moderately hard, very fine to fine grain, sub-rounded to sub-angular, moderate sorted, argillaceous matrix, silica cement, predominantly Quartz, trace Feldspar, trace Glauconite, trace carbonaceous material, non to slightly calcareous, very poor visible porosity, no oil show.	 

Table 6.4 continued

Plug no.	Depth (m)	Rock Type	Description	Core Photo
33	1466.35	Heterolithic	Sandstone: very light grey, occasionally light yellowish-grey, clear, translucent to transparent, fragile, fine to medium-fine grain, occasionally very fine to fine grain, sub-rounded to sub-angular, moderate sorted, predominantly Quartz, trace Feldspar, trace Glauconite, trace Mica, trace carbonaceous material, non to slightly calcareous, fair visible porosity, no oil show.	

Table 6.4 continued

Plug no.	Depth (m)	Rock Type	Description	Core Photo
46	1470.55	Sandstone	Sandstone interlamination with Claystone; Sandstone: very light grey to light grey, translucent to transparent, firm, very fine grain, sub-rounded to sub-angular, moderate sorted, argillaceous matrix, silica cement, trace Glauconite, trace carbonaceous material, Quartz, non to slightly calcareous, reduced visible porosity, dull yellowish to yellowish-white direct fluorescent (20 %), slow yellowish-white streaming cut, no oil stain, weak odour, trace oil show. Claystone: medium-dark grey to dark grey, hard to medium-hard, sub-platy, occasionally subblocks, trace carbonaceous material, non to slightly calcareous.	

Table 6.4 continued

Plug no.	Depth (m)	Rock Type	Description	Core Photo
54	1472.89	Mudstone	Claystone with intermittent of thin Sandstone; Sandstone: very light grey to light grey, translucent to transparent, friable to a firm, very fine to fine grain, subrounded to rounded, moderate sorted, argillaceous matrix, silica cement, predominantly Quartz, trace Glauconite, trace carbonaceous material, non to slightly calcareous, reduced visible porosity, dull yellowish direct fluorescent (10 %), yellowish-white slow streaming cut, no oil stain, weak odour, trace oil show. Claystone: dark brownish grey, occasionally brownish grey, hard to medium-hard, sub-platy to sub-blocky, trace carbonaceous material, non to slightly calcareous, silty in part.	

Table 6.4 continued

Plug no.	Depth (m)	Rock Type	Description	Core Photo
57	1473.8	Mudstone Bioturbated	Claystone: medium-dark grey, hard to medium-hard, sub-platy, occasionally sub-blocky, trace carbonaceous material, non to slightly calcareous, silty in part.	

Table 6.4 continued

Plug no.	Depth (m)	Rock Type	Description	Core Photo
58	1474.07	Heterolithic	Sandstone interlamination with Claystone; Sandstone: very light grey to light brownish grey, translucent to transparent, firm, very fine grain, sub-rounded to sub-angular, moderate sorted, argillaceous matrix, predominantly Quartz, trace Feldspar, trace Glauconite, trace Mica, trace carbonaceous material, non to slightly calcareous, poor to good visible porosity, pale yellowish to yellowish-white direct fluorescent (15 %), slow yellowish-white streaming cut, very light yellowish residual oil ring, fair odour, trace oil show. Claystone: dark grey, hard to medium-hard, sub-blocky to sub-platy, trace carbonaceous material, non to slightly calcareous.	

Table 6.4 continued

Plug no.	Depth (m)	Rock Type	Description	Core Photo
59 60 64	1474.39 1474.69 1475.96	Heterolithic Bioturbated	Sandstone interlamination with Claystone; Sandstone: very light grey to light brownish grey, translucent to transparent, firm, very fine grain, sub-rounded to sub-angular, moderate sorted, argillaceous matrix, predominantly Quartz, trace Feldspar, trace Glauconite, trace Mica, trace carbonaceous material, non to slightly calcareous, poor to good visible porosity, pale yellowish to yellowish-white direct fluorescent (15 %), slow yellowish-white streaming cut, very light yellowish residual oil ring, good odour, trace oil show. Claystone: dark grey, hard to medium-hard, sub-blocky to sub-platy, trace carbonaceous material, non to slightly calcareous.	  

Table 6.4 continued

Plug no.	Depth (m)	Rock Type	Description	Core Photo
66	1476.57	Heterolithic Bioturbated	Siltstone: medium grey to medium brownish grey, medium-hard, sub-blocky to sub-platy, trace carbonaceous material, non to slightly calcareous, shaly, locally grading to very fine Sandstone, poorly visible porosity, no show.	

Table 6.4 continued

Plug no.	Depth (m)	Rock Type	Description	Core Photo
71 71V	1478.14 1478.22	Heterolithic Bioturbated	Sandstone interlamination with Claystone; Sandstone: light yellowish-grey to light brownish grey, clear, translucent to transparent, moderately hard to friable, very fine grain, sub-rounded to sub-angular, reduced to the moderate sorted, argillaceous matrix, silica cement, predominantly Quartz, trace Feldspar, trace Glauconite, trace Mica, trace carbonaceous material, slightly calcareous, poor to fair visible porosity, dull yellowish direct fluorescent (10 %), yellowish-white slow streaming cut, no oil stain, weak odour, trace oil show. Claystone: medium grey to medium brownish grey, medium-hard, sub-blocky to sub-platy, trace carbonaceous material, slightly calcareous, silty.	 

Table 6.4 continued

Plug no.	Depth (m)	Rock Type	Description	Core Photo
72 81	1478.45 1481.09	Heterolithic Bioturbated	Sandstone interlamination with Claystone; Sandstone: light yellowish-grey to light brownish grey, clear, translucent to transparent, moderately hard to friable, very fine grain, sub-rounded to sub-angular, reduced to a moderate sorted, argillaceous matrix, silica cement, predominantly Quartz, trace Feldspar, trace Glauconite, trace Mica, trace carbonaceous material, slightly calcareous, poor to fair visible porosity, dull yellowish direct fluorescent (10 %), yellowish-white slow streaming cut, no oil stain, weak odour, trace oil show. Claystone: medium grey to medium brownish grey, medium-hard, sub-blocky to sub-platy, trace carbonaceous material, non to slightly calcareous, silty.	 

Table 6.4 continued

Plug no.	Depth (m)	Rock Type	Description	Core Photo
81V	1481.2	Sandstone Bioturbated	Sandstone interlamination with Claystone; Sandstone: light brownish-grey to light yellowish-grey, clear, translucent to transparent, fragile, very fine grain to fine grain, sub-rounded to sub-angular, moderate sorted, argillaceous matrix, predominantly Quartz, trace Feldspar, trace Glauconite, trace Mica, trace carbonaceous material, slightly calcareous, fair visible porosity, bright yellow to gold, direct yellow fluorescent (40 %), yellowish-white slow streaming cut, very light brown residual oil ring, fair to strong odour, very light brown oil stain, trace to fair oil show. Claystone: medium grey to medium brownish grey, medium-hard, sub-blocky to sub-platy, trace carbonaceous material, calcareous, silty.	

Table 6.4 continued

Plug no.	Depth (m)	Rock Type	Description	Core Photo
82	1481.41	Heterolithic Bioturbated	Sandstone interlamination with Claystone; Sandstone: light brownish-grey to light yellowish-grey, clear, translucent to transparent, fragile, very fine grain to fine grain, sub-rounded to sub-angular, moderate sorted, argillaceous matrix, predominantly Quartz, trace Feldspar, trace Glauconite, trace Mica, trace carbonaceous material, slightly calcareous, fair visible porosity, bright yellow to gold, direct yellow fluorescent (40 %), yellowish-white slow streaming cut, very light brown residual oil ring, fair to strong odour, very light brown oil stain, trace to fair oil show. Claystone: medium grey to medium brownish grey, medium-hard, sub-blocky to sub-platy, trace carbonaceous	

Table 6.4 continued

Plug no.	Depth (m)	Rock Type	Description	Core Photo
89	1483.5	Mudstone	Claystone: medium grey, medium-hard, sub-blocky to sub-platy, trace carbonaceous material, slightly calcareous, silty in part.	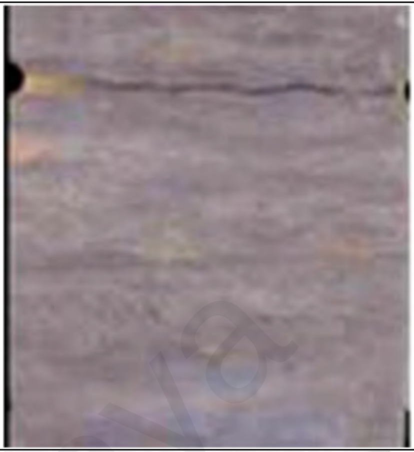
127	1494.75	Mudstone	Claystone: medium brownish-grey to dark grey, moderately hard, sub-platy, trace carbonaceous material, non to slightly calcareous, silty in part.	

Table 6.4 continued

Plug no.	Depth (m)	Rock Type	Description	Core Photo
129 148	1495.39 1501.11	Sandstone	Sandstone: light brownish-grey to very light grey, clear, translucent to transparent, firm, brittle, very fine grain to fine grain, sub-rounded to sub-angular, moderate to well-sorted, predominantly Quartz, trace Feldspar, trace Glauconite, trace Mica, trace carbonaceous material, non to slightly calcareous, fair visible porosity, yellowish-white direct fluorescent (80 %), milky white fast streaming cut, very light brown residual oil ring, fair to strong odour, very light brown oil stain, fair to good oil show.	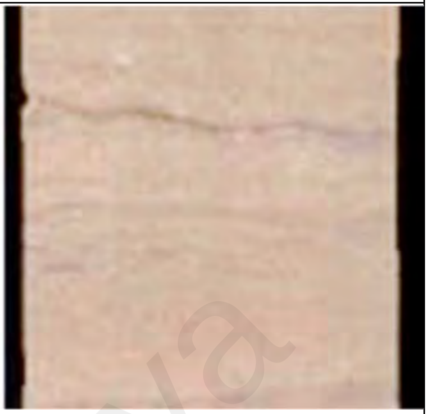 

Table 6.4 continued

Plug no.	Depth (m)	Rock Type	Description	Core Photo
159	1504.41	Sandstone	Sandstone interlamination with Claystone; Sandstone: light brownish-grey to very light yellowish-grey, clear, translucent to transparent, firm, brittle, very fine grain to fine grain, sub-rounded to sub-angular, moderate to well-sorted, predominantly Quartz, trace Feldspar, trace Glauconite, trace Mica, trace carbonaceous material, non to slightly calcareous, fair visible porosity, yellowish-white direct fluorescent (80 %), milky white fast streaming cut, very light brown residual oil ring, good odour, very light brown oil stain, good oil show. Claystone: medium brownish-grey to dark grey, moderate hard, sub-platy to sub-blocky, trace carbonaceous material, slightly calcareous, silty	

Table 6.4 continued

Plug no.	Depth (m)	Rock Type	Description	Core Photo
198 199	1516.11 1516.41	Heterolithic Bioturbated	Sandstone interlamination with Claystone; Sandstone: light yellowish-grey to light brownish grey, clear, translucent to transparent, moderately hard to friable, very fine grain, sub-rounded to sub-angular, reduced to a moderate sorted, argillaceous matrix, silica cement, predominantly Quartz, trace Feldspar, trace Glauconite, trace Mica, trace carbonaceous material, slightly calcareous, poor to good visible porosity, dull yellowish direct fluorescent (10 %), yellowish-white slow streaming cut, no oil stain, weak odour, trace oil show. Claystone: medium grey to medium brownish grey, medium-hard, sub-blocky to sub-platy, trace carbonaceous material, non to slightly calcareous, silty.	 

Table 6.4 continued

Plug no.	Depth (m)	Rock Type	Description	Core Photo
209	1519.3	Heterolithic	Sandstone interlamination with Claystone; Sandstone: light yellowish-grey to light brownish grey, clear, translucent to transparent, moderately hard to friable, very fine grain, sub-rounded to sub-angular, poor to a moderate sorted, argillaceous matrix, silica cement, predominantly Quartz, trace Feldspar, trace Glauconite, trace Mica, trace carbonaceous material, slightly calcareous, poor to fair visible porosity, dull yellowish direct fluorescent (10 %), yellowish-white slow streaming cut, no oil stain, weak odour, trace oil show. Claystone: medium grey to medium brownish grey, medium-hard, sub-blocky to sub-platy, trace carbonaceous material, non to slightly calcareous, silty.	

Table 6.4 continued

Plug no.	Depth (m)	Rock Type	Description	Core Photo
210	1519.7	Sandstone	Sandstone: light brownish-grey to very light grey, clear, translucent to transparent, firm, brittle, very fine grain to fine grain, sub-rounded to sub-angular, moderate to well-sorted, predominantly Quartz, trace Feldspar, trace Glauconite, trace Mica, trace carbonaceous material, non to slightly calcareous, fair visible porosity, yellowish-white direct fluorescent (80 %), milky white fast streaming cut, very light brown residual oil ring, fair to strong odour, very light brown oil stain, fair to good oil show.	

Table 6.4 continued

Plug no.	Depth (m)	Rock Type	Description	Core Photo
236	1527.48	Mudstone	Claystone: dark grey, occasionally medium-dark grey, moderately hard, sub-blocky to sub-platy, trace carbonaceous material, slightly calcareous, silty in part.	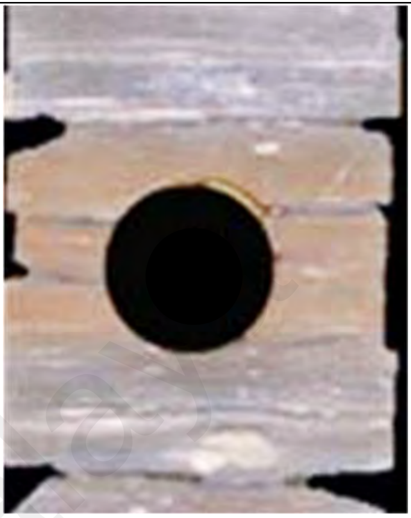

Table 6.4 continued

Plug no.	Depth (m)	Rock Type	Description	Core Photo
239 240	1528.39 1528.69	Sandstone Bioturbated	Sandstone interlamination with Claystone; Sandstone: light brownish-grey to light yellowish-grey, clear, translucent to transparent, friable, very fine grain to fine grain, sub-rounded to sub-angular, moderate sorted, argillaceous matrix, predominantly Quartz, trace Feldspar, trace Glauconite, trace Mica, trace carbonaceous material, slightly calcareous, fair visible porosity, bright yellow to gold, direct yellow fluorescent (40 %), yellowish-white slow streaming cut, very light brown residual oil ring, fair to strong odour, very light brown oil stain, trace to fair oil show. Claystone: medium grey to medium brownish grey, medium-hard, sub-blocky to sub-platy, trace carbonaceous material, slightly calcareous, silty.	 

Table 6.4 continued

Plug no.	Depth (m)	Rock Type	Description	Core Photo
245 245V	1530.08 1530.17	Heterolithic Bioturbated	Sandstone interlamination with Claystone; Sandstone: light yellowish-grey to light brownish grey, clear, translucent to transparent, moderately hard to friable, very fine grain, sub-rounded to sub-angular, poor to a moderate sorted, argillaceous matrix, silica cement, predominantly Quartz, trace Feldspar, trace Glauconite, trace Mica, trace carbonaceous material, slightly calcareous, poor to fair visible porosity, dull yellowish direct fluorescent (10 %), yellowish-white slow streaming cut, no oil stain, weak odour, trace oil show. Claystone: medium grey to medium brownish grey, medium-hard, sub-blocky to sub-platy, trace carbonaceous material,	 

Table 6.4 continued

Plug no.	Depth (m)	Rock Type	Description	Core Photo
247	1530.38	Heterolithic Bioturbated	Sandstone interlamination with Claystone; Sandstone: light yellowish-grey to light brownish grey, clear, translucent to transparent, moderately hard to friable, very fine grain, sub-rounded to sub-angular, poor to the moderate sorted, argillaceous matrix, silica cement, predominantly Quartz, trace Feldspar, trace Glauconite, trace Mica, trace carbonaceous material, slightly calcareous, poor to fair visible porosity, dull yellowish direct fluorescent (10 %), yellowish-white slow streaming cut, no oil stain, weak odour, trace oil show. Claystone: medium grey to medium brownish grey, medium-hard, sub-blocky to sub-platy, trace carbonaceous material, non to slightly calcareous, silty.	

Table 6.4 continued

Plug no.	Depth (m)	Rock Type	Description	Core Photo
275V 275	1539.03 1539.1	Heterolithic	Sandstone interlamination with Claystone; Sandstone: light brownish-grey to very light yellowish-grey, clear, translucent to transparent, firm, brittle, very fine grain to fine grain, sub-rounded to sub-angular, moderate to well-sorted, predominantly Quartz, trace Feldspar, trace Glauconite, trace Mica, trace carbonaceous material, non to slightly calcareous, fair visible porosity, yellowish-white direct fluorescent (90 %), milky white fast streaming cut, very light brown residual oil ring, strong odour, very light brown oil stain, good oil show. Claystone: medium brownish grey, moderately hard, sub-platy to sub-blocky, trace carbonaceous material, non to slightly calcareous, silty in part.	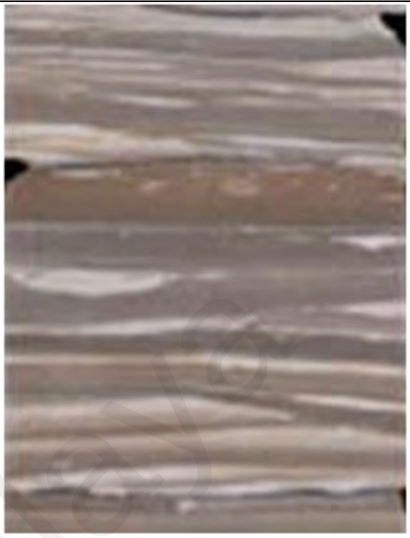 

Table 6.4 continued

Plug no.	Depth (m)	Rock Type	Description	Core Photo
311 312	1549.94 1550.25	Mudstone	Sandstone interlamination with Claystone; Sandstone: light brownish-grey to very light yellowish-grey, clear, translucent to transparent, firm, brittle, very fine grain to fine grain, sub-rounded to sub-angular, moderate to well-sorted, predominantly Quartz, trace Feldspar, trace Glauconite, trace Mica, trace carbonaceous material, non to slightly calcareous, fair visible porosity, yellowish-white direct fluorescent (90 %), milky white fast streaming cut, very light brown residual oil ring, strong odour, very light brown oil stain, good oil show. Claystone: medium brownish grey, moderately hard, sub-platy to sub-blocky, trace carbonaceous material, non to slightly calcareous, silty in part.	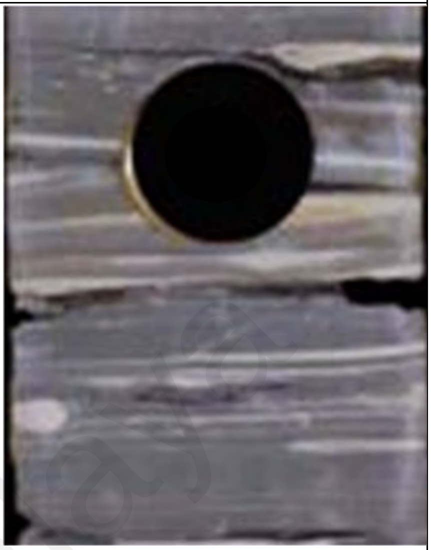 

Table 6.4 continued

Plug no.	Depth (m)	Rock Type	Description	Core Photo
313	1550.54	Heterolithic	Sandstone interlamination with Claystone; Sandstone: light brownish-grey to very light yellowish-grey, clear, translucent to transparent, firm, brittle, very fine grain to fine grain, sub-rounded to sub-angular, moderate to well-sorted, predominantly Quartz, trace Feldspar, trace Glauconite, trace Mica, trace carbonaceous material, non to slightly calcareous, fair visible porosity, yellowish-white direct fluorescent (90 %), milky white fast streaming cut, very light brown residual oil ring, strong odour, very light brown oil stain, good oil show. Claystone: medium brownish grey, moderately hard, sub-platy to sub-blocky, trace carbonaceous material, non to slightly calcareous, silty in part.	

6.7 Key Stratigraphic Surfaces

This section summarizes and interprets identified key surfaces and depositional environments within well X-4 based on facies association description and modelling.

6.7.1 Facies Association and Stratigraphic Sequences

We interpreted three facies association in well X-4 stratigraphy in Figure 6.8, which are:

- Offshore/Pro-delta
- Tidal Bar/ Delta Front
- Offshore/Pro Delta Outer Bay

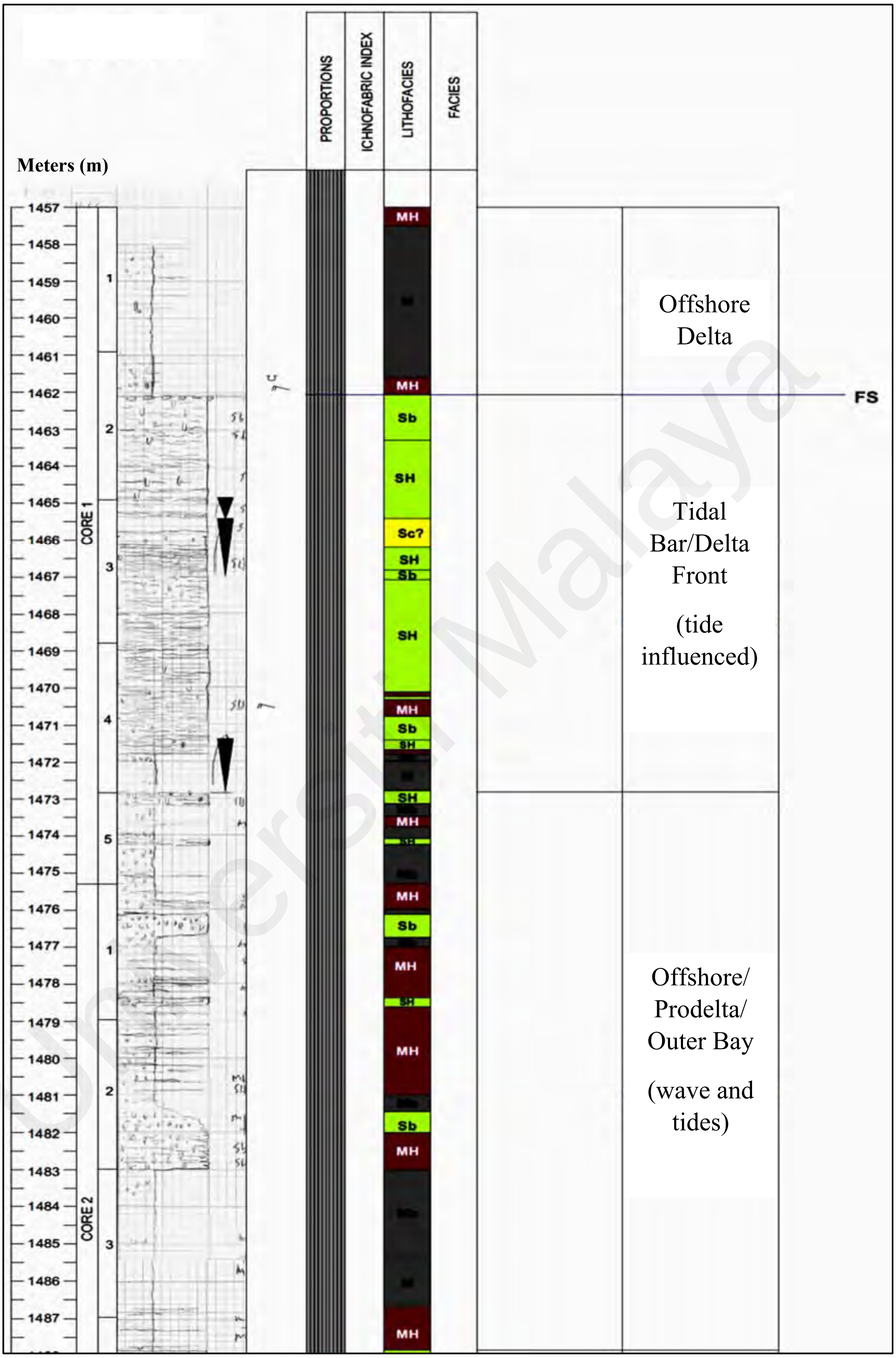

Figure 6.8: Facies association for well X-4 formation.

6.7.1.1 Offshore/Pro Delta

This facies association is well X-4 consist predominantly of mudstone capped at the top and bottom by muddy heterolithic facies. The facies have a coarsening upward trend where facies are trending from fine at the bottom and gradually becoming coarser towards the top of the interval indicating a shallowing effect or sea-level drop upwards.

Offshore/Pro Delta environment is considered distal or further from land in the shallow marine coastal environment. This environment deposits fine-grained materials such as silt and mudstone due to the extended distance from the sediment source inland to the point of deposition. This significant distance results in the weathering of sediments into finer grains as they travel downstream. Meanwhile, the fluvial and tidal influenced offshore environment deposits muddy heterolithic facies that consist of coarser grain sand intercalated with fine mudstone and silt. These facies are reconstituted by tidal and wave actions into heterolithic intercalating structures.

The thick interval of mudstone between the muddy heterolithic section in the Offshore/Pro-Delta facies association indicates a period of low energy where the fine mudstone can settle. This thick mudstone column may indicate a period of high sea level to result in higher sea depth or accommodation space which are ideal for the deposition of fine silt.

The muddy heterolithic facies at the bottom and top of the facies association indicated an influx on coarser grain sediments possibly from a river. This facies arrangement indicates an environment more proximal or closer to a river mouth. It indicates a period of low sea level at which the point of deposition of the sediments becomes closer to land due to receding coastline. Also, the low sea-level deposits the sediments in shallow depth water.

The arrangements of the muddy heterolithic and mudstone column indicate a cyclic event that indicates of a regressive and transgressive cycle. This cycle deposits muddy heterolithic facies followed by a rise in sea level which deposited the thick column of fine-grained mudstone and silt followed by a fall in sea level which deposits the muddy heterolithic facies in a shallower environment. The muddy heteroliths at the bottom are also the flooding surface of the well X-4 interval, indicating the highest landward position reached by the sediment.

6.7.1.2 Tidal Bar/Delta Front

This facies association shown previously in Figure 6.8 underlies the Offshore/Pro-delta facies association and consist of sand dominated facies. The facies include

- sandy heterolithic
- facies such as flaser and wavy heteroliths,
- bioturbated sand,
- clean sand and
- a single muddy heterolithic bed of facies.

The facies strongly indicate a depositional environment that is more proximal or closer landward that is indicative of a shallow marine environment that is fluvial and wave-influenced. The sand dominated facies indicates fluvial influenced deposition process that coarse-grained deposit sandstone. Meanwhile, the presence of cross-bedded and laminated sandstone indicate wave-influenced environment. The presence of sparsely bioturbated sandstone in some of the intervals facies also indicates a stressed environment that is indicative of a shallow marine environment such as an estuarine or delta front that indicates a transition zone between marine and freshwater environments.

The bottom of the facies association consists of a thin interval of mudstone which is indicative of a low energy environment and possibly high sea level that allows the settlement of fine-grained mudstone and silt. Above the mudstone is a thin interval of sandstone followed by a thin layer of muddy heterolithic rocks followed by thick layers of sandstone dominated heterolithic rocks (wave and flaser beds) and cross-bedded and laminated sandstone. The coarsening upwards trend from mudstone at the bottom to sandstone dominated facies at the top are indicative of a falling sea level or a period of regression.

6.7.1.3 Offshore/Pro Delta Outer Bay

This facies association is situated at the bottom of the X-4 interval and consist mostly of mudstone dominated facies such as heterolithic facies such as lenticular and wavy beddings intersected by two thin intervals of bioturbated sandstone and a single isolated flaser bedding at the upper section.

The nature of the facies association is indicative of a pro-delta environment that is influenced by waves and tides. The pro-delta environment is sufficiently distal to allow the settlement of fine-grained mudstone during the sea-level rise, and during sea-level drop can be proximal to receive fluvial deposited sandstone facies. The presence of the wavy and muddy heterolithic beddings are indicative of a tidally influenced environment. The presence of bioturbated sandstone indicates a shallow marine environment and a period of low sea level to allow biogenic activities for a brief period.

The large alternating layers of mudstone and heteroliths interjected by thin bioturbated sandstones indicate a cycle of rising and falling sea level. This pattern indicates a transgressive-regressive cycle of the sea level.

6.8 Discussion

Several factors influence the heterogeneity and diversity of the facies of the X-4 interval used in this study

- Eustasy and sea-level change
- Tide influence
- Wave influence
- Proximity to source of fluvial sediment

The change in sea level in a cyclical manner creates a transgressive-regressive sequence or a rising and falling sea level sequence. Alternating intervals of coarse sediments such as sand dominated facies deposited during sea-level fall and mud dominated facies such as heterolithic facies during sea-level rise indicate this rising and falling sea level sequence. The boundaries between the transgressive and regressive are indicated by flooding surfaces indicating the highest sea level during the sequence where the sand dominated facies grade into mudstone dominated facies.

High sea levels create an ample accommodation space and are more distal from the source of fluvial sediment. As a result, fine sediments such as mudstone and silt are deposited during periods of transgression through current turbidity mechanism. At the transgression cycle ends, the deposits during the highest level achieved are called the flooding surfaces. The maximum flooding surface is deposited at the highest sea level achieved during the transgressive cycle. We can observe Underlying facies affected by bioturbation features such as tunnels and fossil accommodation indicate the transgressive cycle within the X-4 interval.

The regression period reduced the accommodation space, and the environment is more proximal to the source of fluvial sediments which result in the deposition of coarser grain sediments typically coarse-grained sandstone. The smaller accommodation also exposes the facies to external influences such as waves and tides that change the sorting and composition of the facies. These changes result in facies or rock types with cross-bedded and laminated sandstone from wave action and heterolithic facies that result from both wave and tidal action.

The X-4 interval indicates a complex vertical heterogeneity due to the cyclic transgressive-regressive cycle that consists of about 14 types of facies with varying sedimentary structure and sand/mud ratio. The rock types consist of multiscale heterogeneity where the sand and mud layers can range from millimetres to meter thickness and overlie each other in an alternating sequence called thin beds. The thin beds also undergo further re-sorting from the effects of bioturbation from biogenic activities and wave and tidal effects that alter the beddings into structures such as cross lamination and heterolithic structures.

As discussed previously in Section 6.4.3.2, heteroliths consist of layers of sand and mud facies intercalated or folded into each other due to tidal and wave influences. The strength of the tidal action during high tides and low tides create different categories of heteroliths with different sand/mud ratio. High energy tidal action creates sand dominated flaser heteroliths. In contrast, low energy tidal action tends to form mud dominated lenticular facies, in between there is also wavy heteroliths which consist of an equal proportion of sand mud. The mud and sand layers in the heteroliths are not continuous and exist in the form of lenses that are wavy in structure and have varying thicknesses.

6.9 Depositional Models

We interpreted the deposition environments of well X-4 as a shallow marine environment with is influenced by the tidal cycle, oceanic waves and the river flow. We illustrated the environments that comply with this description in Figure 6.9, which include tide-dominated estuaries, wave-dominated estuary, lagoons, delta plains, tidal flats, strand plains and alluvial plains. Figure 6.10 shows additional schematics of 15 types of coastal environments created by varying factors such as sediment input and wave influence.

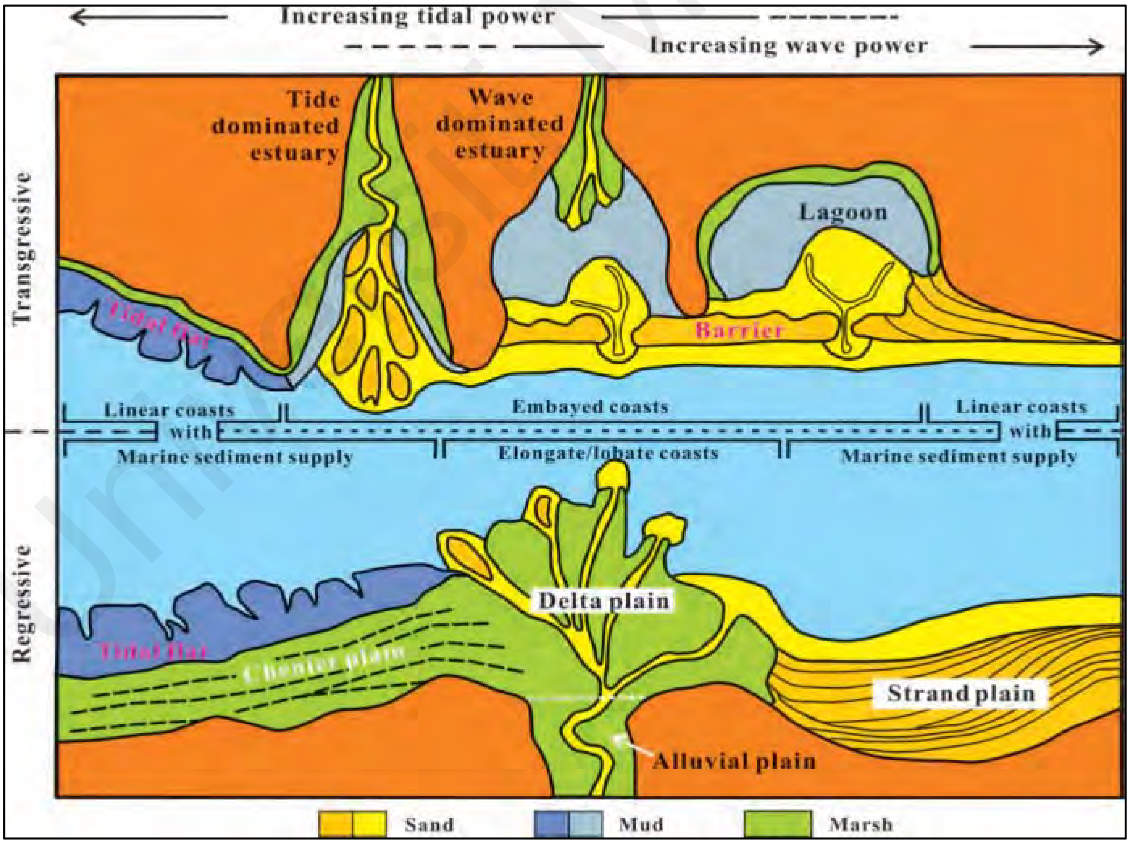

Figure 6.9: The primary distribution of coastal depositional settings and environments (Boyd, Dalrymple, & Zaitlin, 1992)

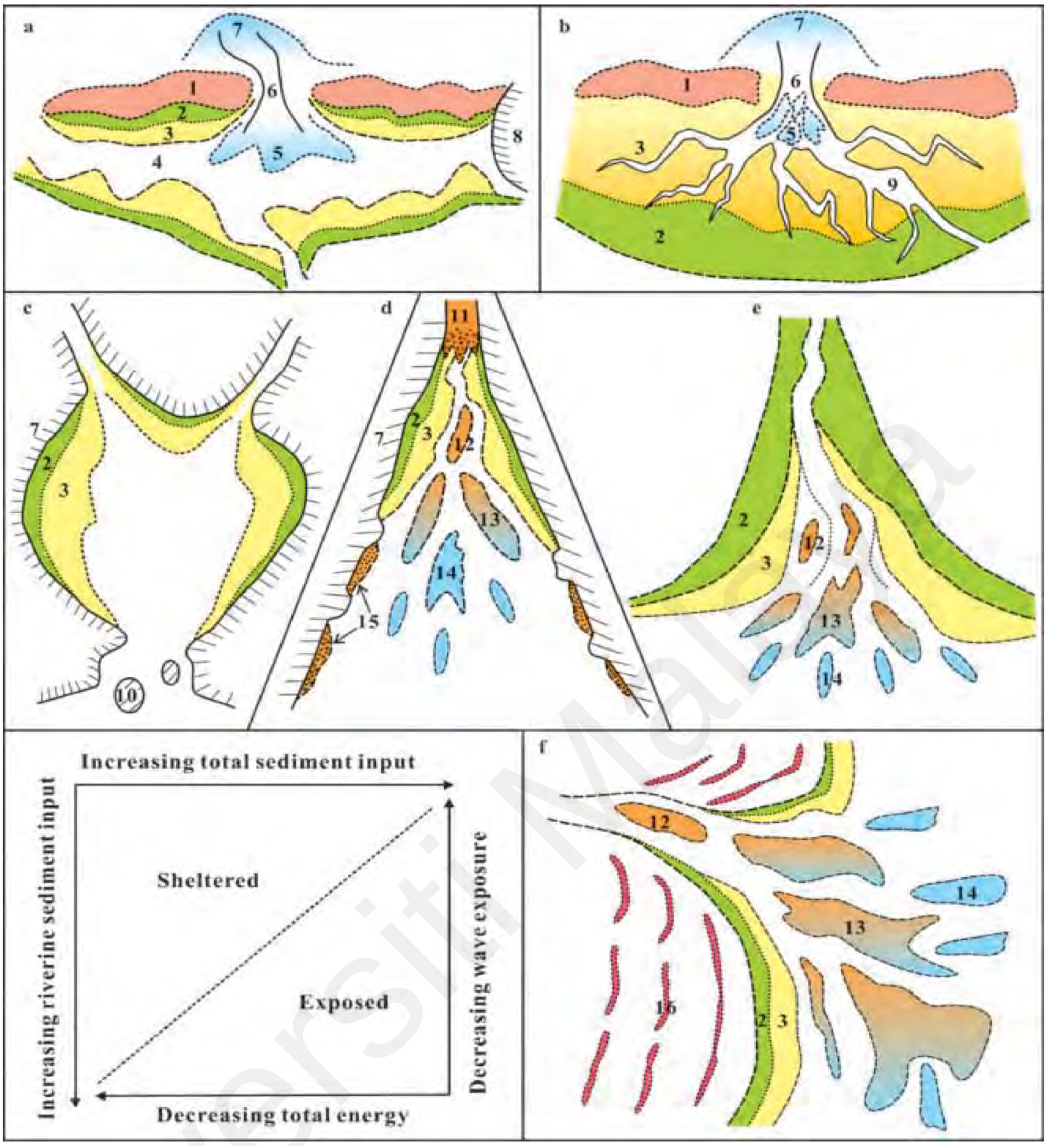

Figure 6.10: Schematic plots of tidal flats in the different coastal environments with varying sediment input and wave exposure. A– Barrier-lagoon to the wave-dominated-estuary system; b–Barrier-flat system (e.g., Wadden Sea); c–Poorly filled gourd-shaped estuary; d– Partly filled open-mouth estuary; e–Highly filled open-mouth estuary; f–tide-dominated delta and adjacent Chenier plain. 1–Barrier island, 2–Saltmarsh, 3–Bare intertidal flat, 4–Lagoon, 5–Flood tidal delta, 6–Tidal inlet, 7–Ebb tidal delta, 8–Rocky coast, 9–Tidal channel/creek, 10–Rocky island, 11–Bay-head delta, 12 ~ 13–Tidal sand bar/island, 14–Subtidal sand bar/ridge, 15–Gravel/sand beach, 16–Chenier ridge. (Daidu et al., 2013)

The varying levels of bioturbation in well X-4 indicate a brackish water environment where freshwater and marine environment intersect. The varying levels of bioturbation are an indication of an environment transitioning from fluvial to the marine that is characteristic of a swampy and brackish water environment. Such stressed environment best fits a tide-dominated estuary. Figure 6.11 illustrates a facies association of a shallow marine and fluvial setting with high sands deposition, which include brackish marsh and sandflat. The facies association in Figure 6.11 fines upward and transitions into marine environments such as tidal bar and mixed flats. These environments deposited laminated sandstone and mudstone. The facies transitions back into by shallow swampy mudflats in a shallow marine setting rich with very fine mudstone.

Other sedimentary structures in X-4 such as the lenticular beddings indicate a flat tidal environment which is heavily influenced by the tides and waves that induce the formation of heterolithic beddings and facies. The tidal cycles create the rhythmite structures followed by the action of the oceanic waves that reconstitute the rhythmites structures into lenticular or muddy heterolithic beddings, sand-rich flaser or sandy heterolithic beddings or the equally or wavy beddings which are differentiated by sandstone-to-mudstone ratios.

Other possible environments are fluvial plains which form alternating sand and mud structures at overflow channel levees at some sections of the river. However, the presence of bioturbation and tidal and wave-influenced heterolithic facies in X-4 strongly indicate a marine-influenced environment, hence reducing the notion of a fluvial dominated environment.

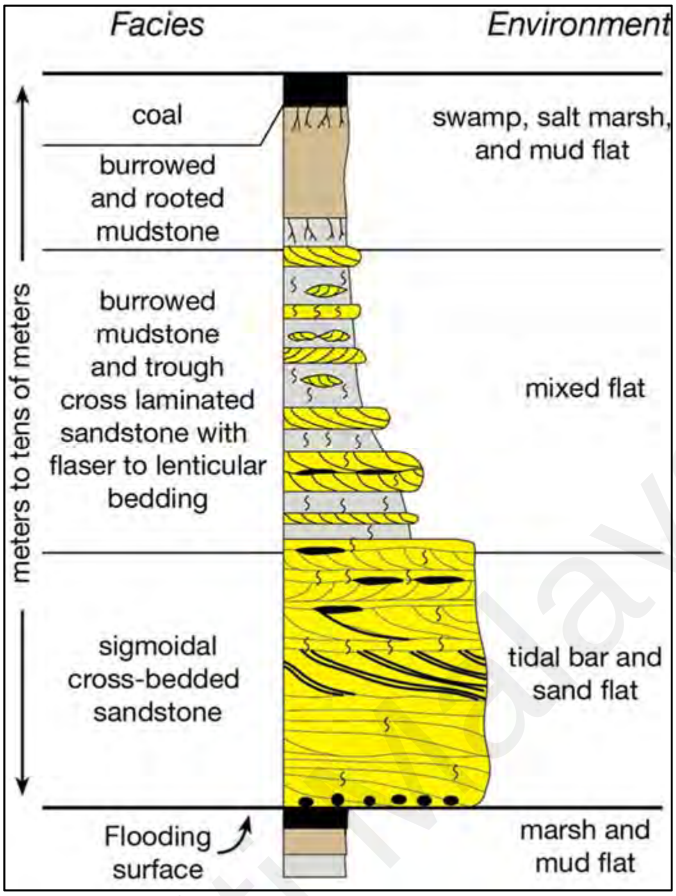

Figure 6.11: Facies association and interpreted depositional environment for the tidal bar, mixed flats and swamp, salt marsh and mudflat (Van Wagoner, 1990).This facies association is a good model for the shallow marine environment that is the depositional environment of well X-4.

6.10 Impact of Shallow Marine Depositional Environment on Hydrocarbon Reserves Potential

The interpretation of the core photos and sedimentology reports strongly indicate that the sediments in well X- 4 facies are deposited in a shallow marine environment. Facies association of the core indicate a shallow marine setting such as pro-delta, tidal bars and delta fronts with strong signs wave and tidal influences such as tidal heterolithic deposits.

The tidal bars and pro-delta facies association in well X-4 are sand dominated with and abundance of heterolithic and rhythmites that are deposited due to tidal and wave influences. Most tidal influenced deposits have the following sedimentary features such as heterolithic facies, and rhythmites (Boyd et al., 1992; Hassan, 2013; Reineck et al., 1968) are abundant in well X-4 and strongly associated with tidal bar deposits. Figure 6.12 illustrates an excellent example of a flat tidal environment as it transitions seaward. These environments are profoundly influenced by tidal and wave actions.

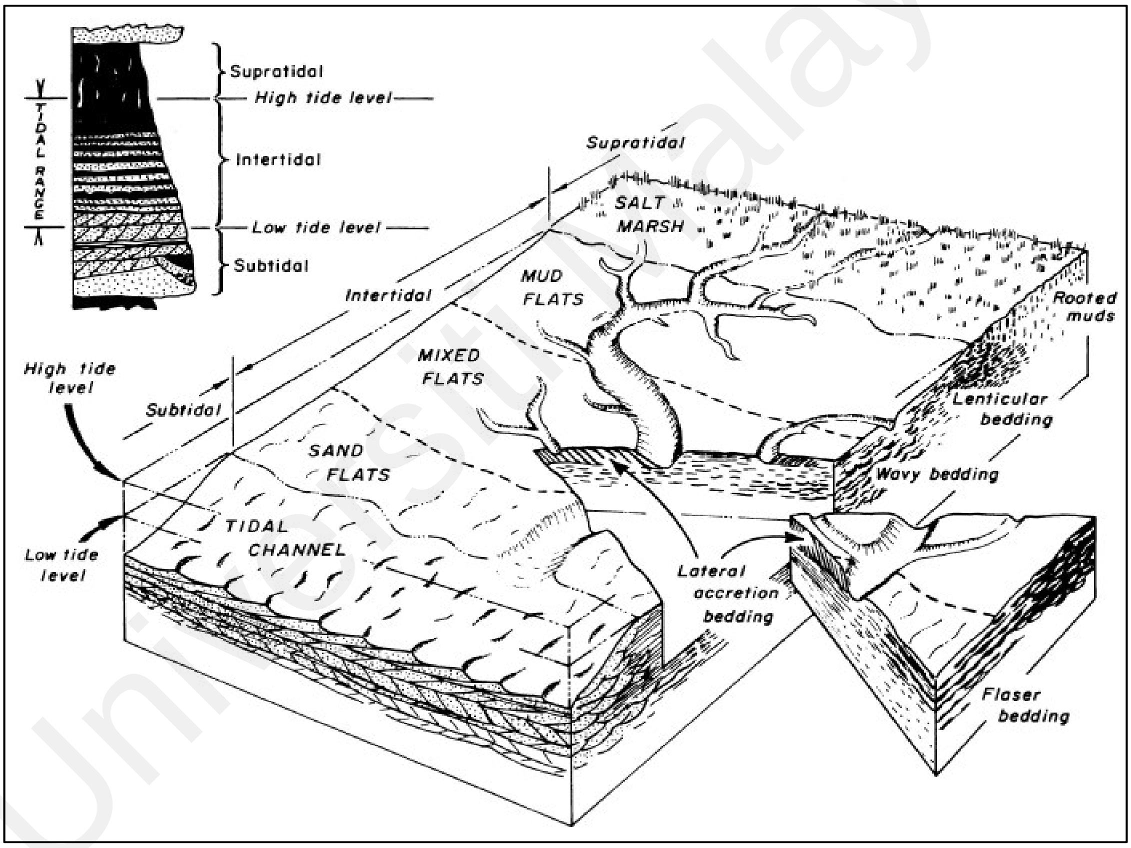

Figure 6.12: Block diagram of a channel associated tidal flat. The tidal flats sediments become finer as it moves further from the channel towards the high tide level, passing gradationally from sand flats to mixed flats and mudflats and salt marshes (Dalrymple et al., 2010).

The pro-delta and tidal bar intervals can potentially be hydrocarbon-bearing reservoirs due to high net to the gross ratio. These intervals consist of thick sandstone beddings, and heterolithic deposits with thin sandstone beddings such as in well X-4 that produced hydrocarbon, mainly gas (Kantaatmadja et al., 2014). Also, the shallow marine environment creates elongated sand bodies that form from merged tidal bars and pro-delta deposits that can have lengths in kilometres (Ringrose et al., 2014). However, such deposition may also create stacked reservoir bodies such as deltaic, tidal and sand bars. These stacked reservoirs may not connect vertically and laterally due to complex dimensions of the sand bars. The deposition of these sand bards depends on the river and oceanic currents, as shown previously in Figure 6.10. Depending on the type of tidal setting, either deltaic or estuarine settings, deltaic bars tend to have progradational stacking patterns versus retrogradation stacking pattern for the estuarine setting. Well X-4 facies and facies association are interpreted to be associated mainly with deltaic tidal bars which typically provide a progradational stacking pattern (Hassan, 2013). that refers to the growth of the delta towards the sea due to high sediment input and falling sea level, which result in the coastline moving seaward.

Tidally influenced shoreline and deltaic deposits are one of the most common hydrocarbons bearing deposits and also the most architecturally complicated. Producing hydrocarbon from these deposits are complicated and challenging due to the complex architecture of the reservoirs that typically consist of tidal bars that have varying dimensions and limited lateral and vertical connectivity, as a result, by average about 40% of the resources were extracted with the remaining 60% left behind (Wood, 2004). However, recent advances in 3D modelling backed by available computing resources allow geologists and engineers to create improved fine-scale reservoir models and secondary recovery programs to improve hydrocarbon reserves estimates and extraction from these marginal reservoirs. Characterizing the hydrocarbon reserves and flow potential of complex tidal influenced reservoirs requires modelling of small scale heterogeneity and sandstone beddings in heterolithic deposits. Also, describing reservoir deposits geometries and their effects on effective reservoir properties in large scale reservoir model is crucial for improved hydrocarbon reserves (Wood, 2004).

Another interpreted environment in X-4 is a lacustrine-delta environment. This environment forms elongated sheets of sand formed by the merging of mouth bars and sub delta deposits. Similar in tidal bar deposits, the width of the elongated sand sheets in this deposited in this system can be in kilometres. Rapid progradation causes sediment deposition that create large volumes of heterolith. These heteroliths include thin sandstone beddings that contribute to high net gross in heterolithic deposits. Within the stratigraphy sequence, the reservoir would be stratified with interbedded sandstone and mudstone with the mudstone and silt dominated lobes and layers in the vertical sequence acting as potential traps and seal. The potential for hydrocarbon storage in each genetic sequence may not have the same fluid contact. It may pose some challenges in terms of estimating the amount of recoverable hydrocarbon resources and applying appropriate primary and secondary recovery strategies.

CHAPTER 7 : RESULTS OF MINERALOGICAL ANALYSIS

In this chapter, we summarize the mineralogical analysis results of a thin section from mini-plugs 148 and 210. The thin section of mini plug 148 represents the reference reservoir sandstone while the sandstone in mini plug 210 is finer and have lower permeability than the reference reservoir sandstone. Mineralogically, both mini-plugs have a similar amount of quartz and clay content by weight percentage, which is indicative that the sandstone is similar. Although further analysis in Section 8.2.1.2 indicates that the sandstone in mini plug 210 is significantly finer than in mini plug 148, which cause a difference in permeability between the two mini-plugs.

7.1.1 Mini Plug 148 QEMSCAN Results

The post-processing of the QEMSCAM images of mini plug 148 using the Nanomin software in Figure 7.1 involved stitching the nine sub-areas. We used a uses a recipe with the mineral list/library in Nanomin to identify the minerals by matching the spectrum in the library with the spectrums in mini plug 148. We based the mineral identification on the XRD report provided by PETRONAS, which identified many of the minerals in the mini-plugs. We added additional minerals that are not on the list/library where appropriate based on the element compositions.e identified 26 minerals in the mineral map of mini plug 210 with 2.6% of the area in the mineral map are unclassified.

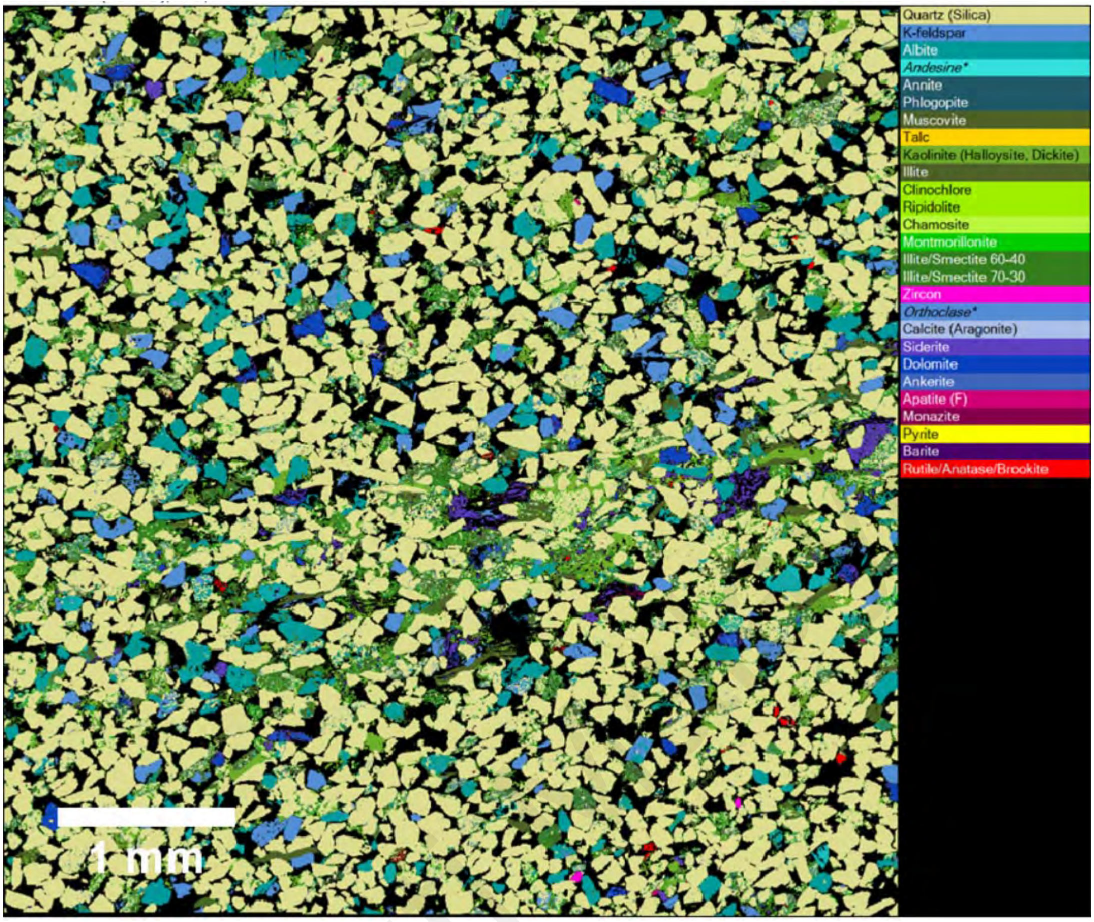

Figure 7.1: Mineral map of a single slice from mini plug 148 (5 mm x 5 mm)

Figure 7.2 shows that 67.75% of the minerals in mini plug 148 are quartz, followed by Alkali feldspar and' 'plagioclase that makes up 13.22%. Clay makes up 15.81% and mainly consists of Illite (5.54%), Illite/Smectite Interstratified (5.98%), Kaolinite (3.03%), Smectites (1.98%) and Chlorite (0.35%) Other minerals/clay such as siderite (1.54%) and muscovites occur in trace quantities.

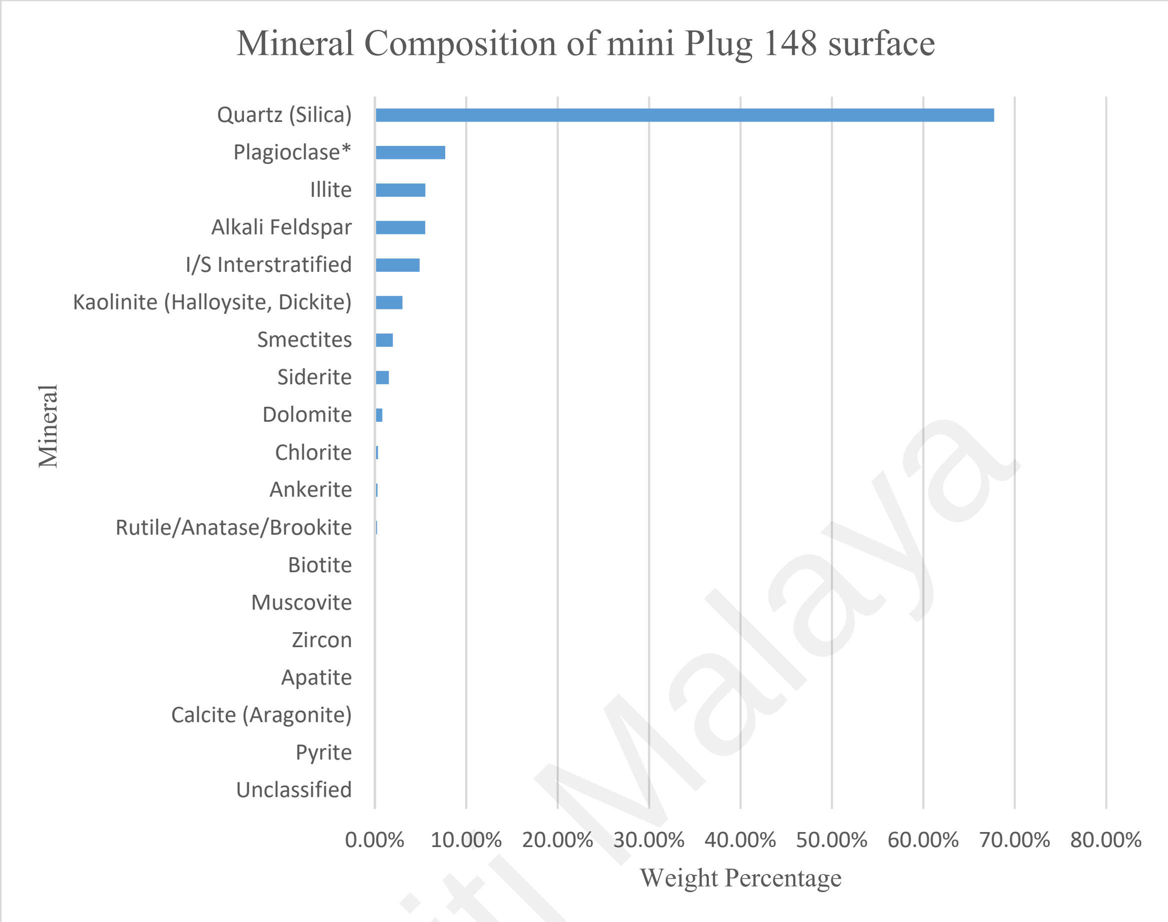

Figure 7.2: Mineral Composition by weight percentage of Mini Plug 148 surface. We excluded minerals that are less than 0.1%. Unclassified minerals make up 2.6% of total weight.

The mineral composition is similar to another mineralogical analysis of mini-plug 210 (stratified sandstone rock) with similar quartz and clay percentage. This similarity strongly supports that the sandstone in both core plugs is mineralogically similar despite being of different rock types and different depths.

Figure 7.3 shows that clay makes up almost 16% of the %area. Based on the results, we described mini plug 148 as sand dominated rock with thin interbedded mudstone laminates.

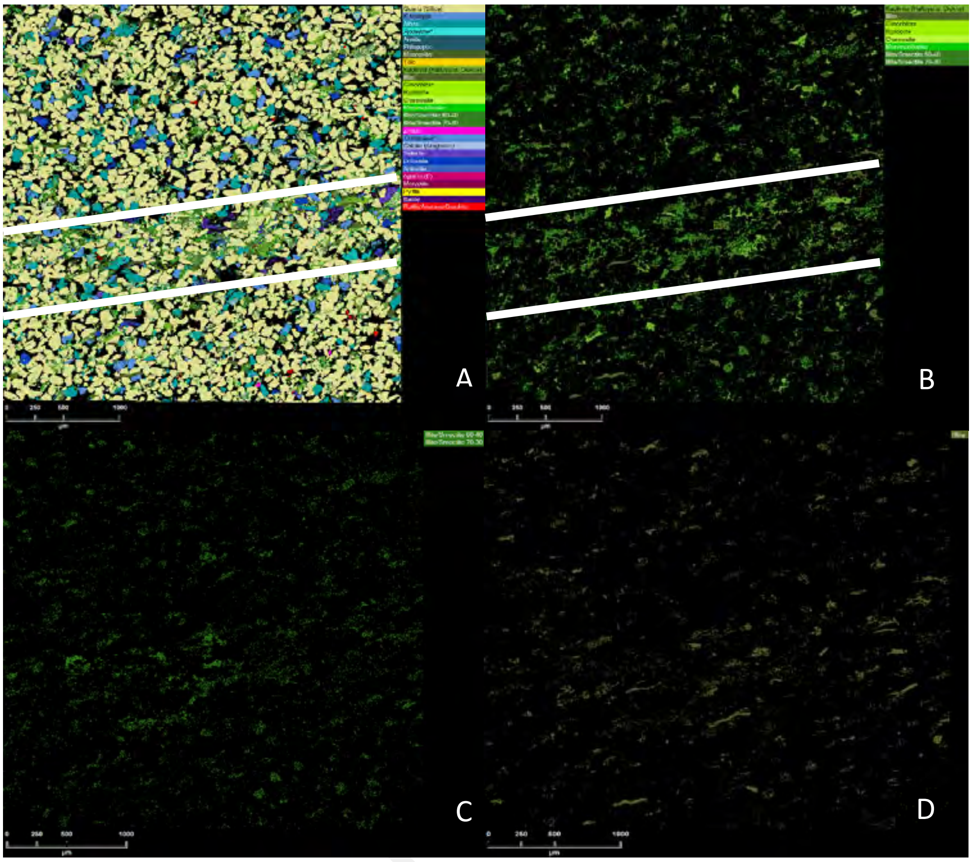

A: Original Mineral Map
B: Distribution map of All Clay: 14% of Area
C: Distribution map of Illite-Smectite clay: 5.58% of Area
D: Distribution map of Illite clay: 3.28% of Area

Figure 7.3: Distribution map of clay, illite and illite-smectite clay on Mini Plug 148.

7.1.2 Mini plug 210 QEMSCAM Results

The post-processing of the QEMSCAN images of mini plug 210 using Nanomin software in Figure 7.4 involved stitching the nine sub-areas into a single image. We used a uses a recipe with the mineral list/library in Nanomin to identify the minerals by matching the spectrum in the library with the spectrums in mini-plug 210. Mineral identification was based on the XRD report provided by Petronas. Additional minerals that are not on the list/library are added where appropriate based on the element compositions. Twenty-three minerals were identified in mini plug 210 mineral map.3.29% of the area in the mineral map are unclassified.

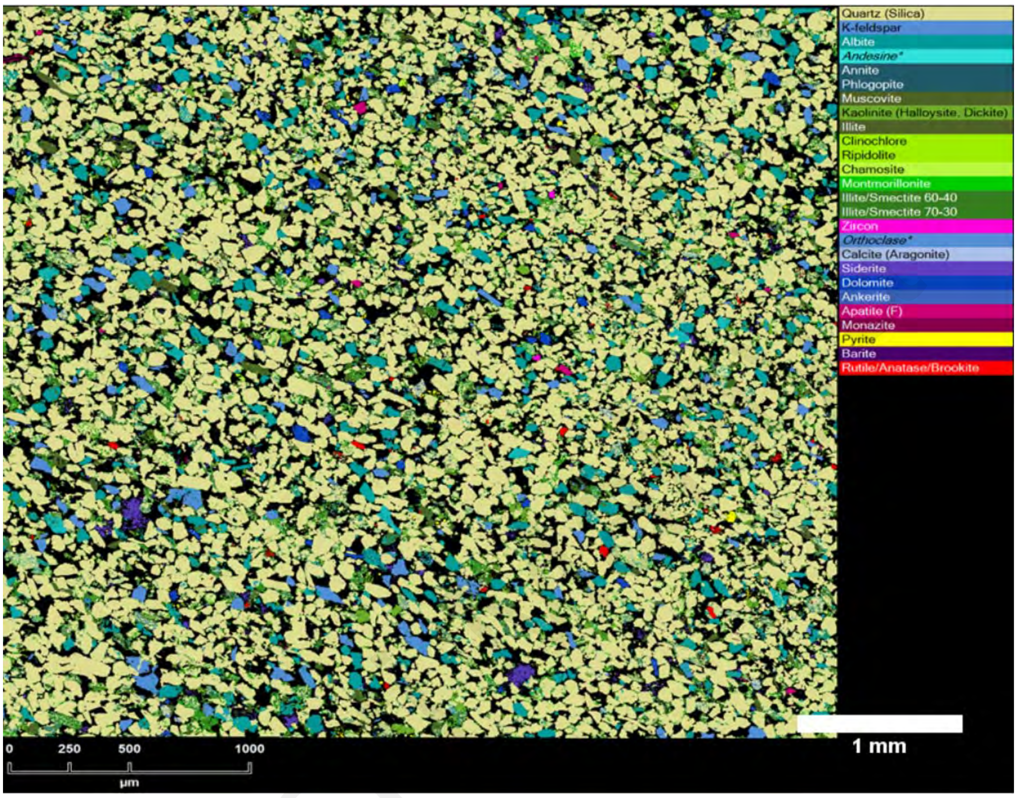

Figure 7.4: Mineral map of a single slice of mini plug 210 (5 mm x 5 mm)

Figure 7.5 shows that 68% of the minerals in mini plug 210 are quartz, followed by 'plagioclase and feldspar' that makes up 12.13%. Clay makes up 13.91% and mainly consists of Illite/Smectite Interstratified (5.58%), Illite (3.28%), Smectites (2.89%) and Kaolinite(1.94%) Other minerals/clay such as siderite and muscovites occur in trace quantities. Low clay content is consistent with the facies description of mini- plug 210 as sandstone dominated Sandy Heterolithic or Flaser rock.

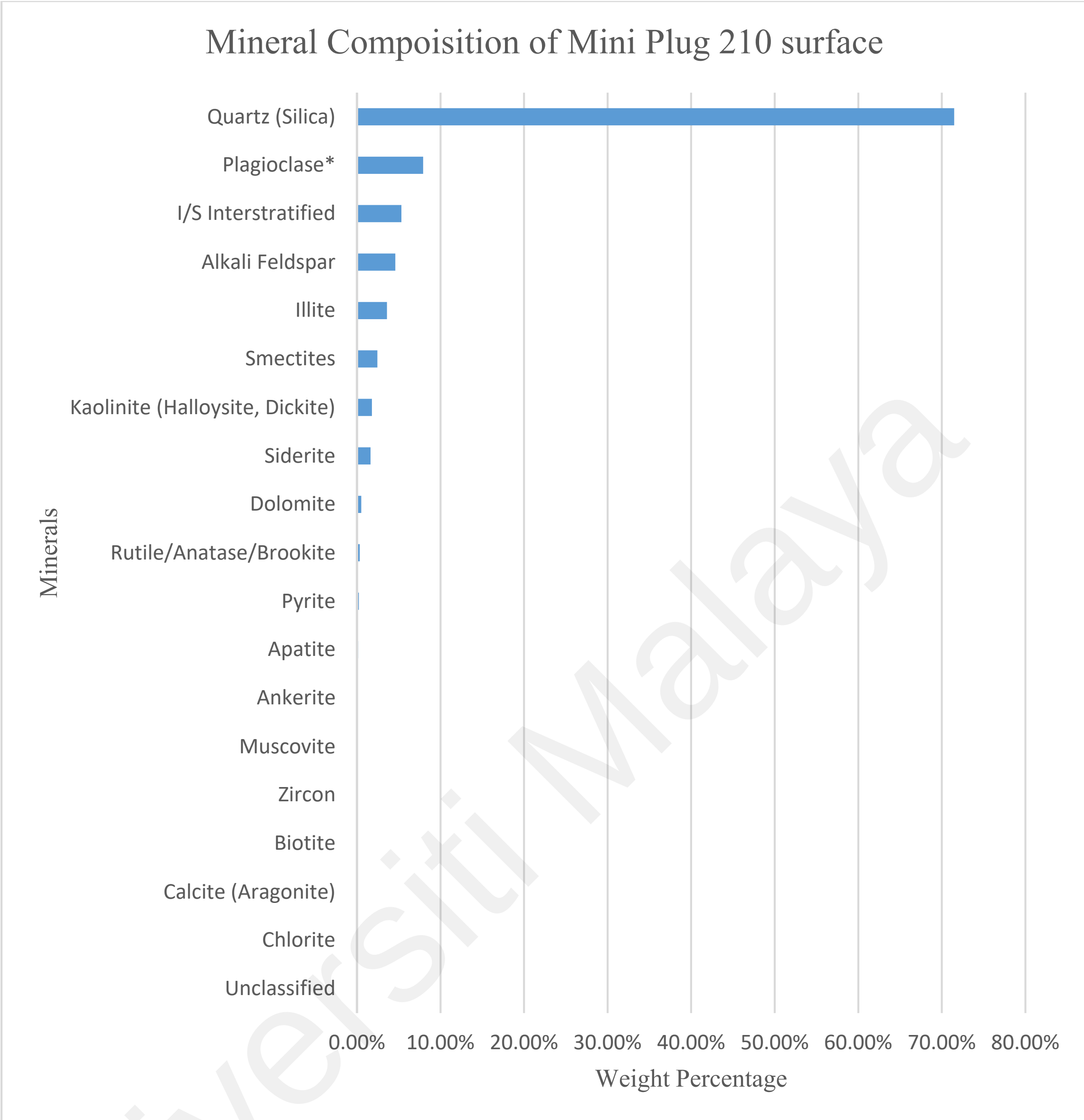

Figure 7.5: Mineral Composition by weight percentage of Mini Plug 210. Minerals that are less than 0.1% are not listed. Unclassified minerals make up 3.29% of the total weight.

Figure 7.6 shows that clay makes up 13.91% and mainly consists of Illite/Smectite Interstratified (5.58%), Illite (3.28%), Smectites (2.89%) and Kaolinite(1.94%) Other minerals/clay such as siderite and muscovites occur in trace quantities. Low clay content is consistent with the facies description of mini-plug 210 as sandstone dominated Sandy Heterolithic or Flaser rock.

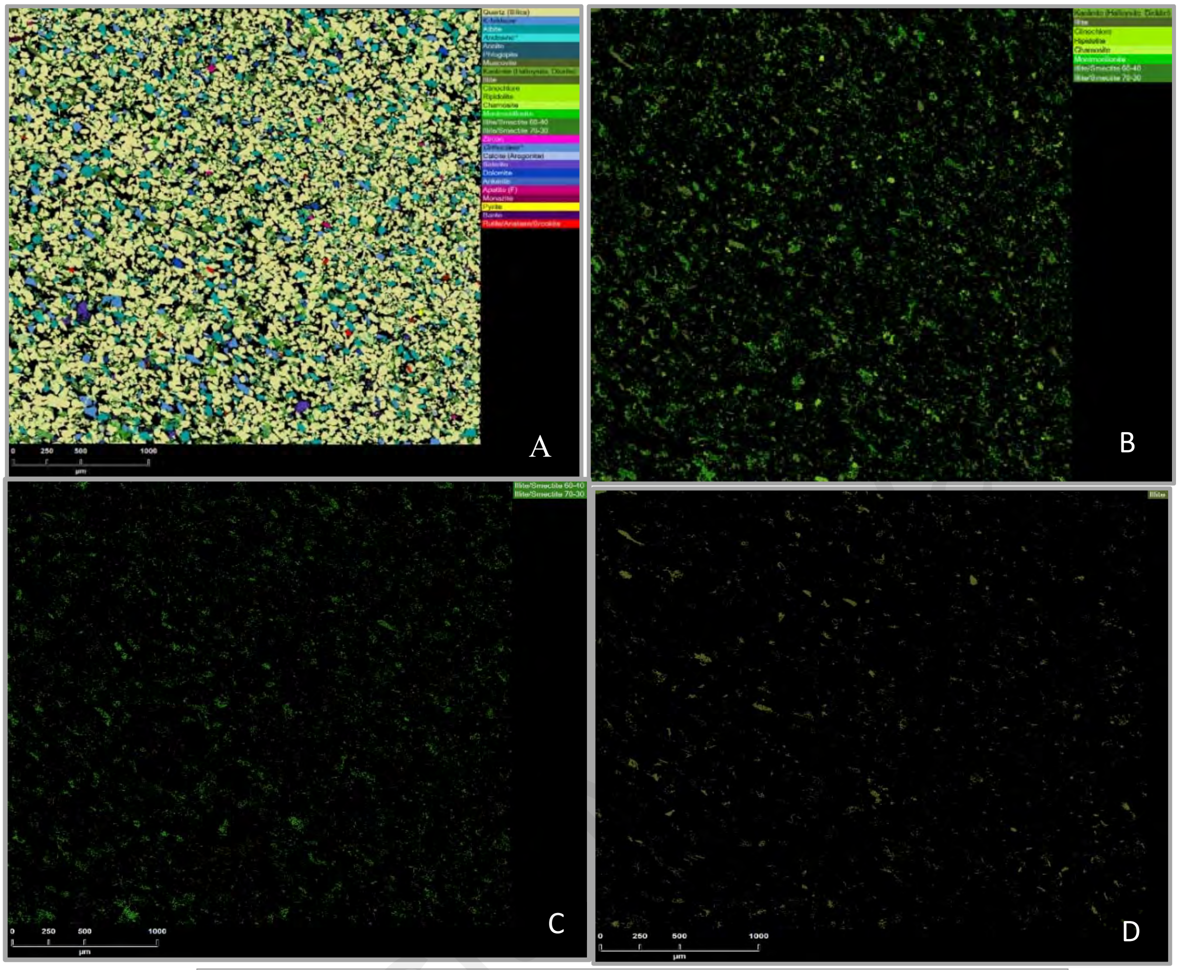

A: Original Mineral Map
B: Distribution map of All Clay: 14% of Area
C: Distribution map of Illite-Smectite clay: 5.58% of Area
D: Distribution map of Illite clay: 3.28% of Area

Figure 7.6: Distribution map of clay, illite and illite-smectite clay on Mini Plug 210. The clays are generally uniformly dispersed on the surface of mini plug 210.

7.1.3 Comparison between mini-plug 148 and 210 Mineralogy

Figure 7.7 shows that the mineral composition of the sandstone in mini plug 148 is similar to mini 210 in terms of quartz and clay percentage. However, the percentage of types of clay differ. For example, illite percentage is highest in 148 instead of illite/smectite in 210. However, the differences are not significant.

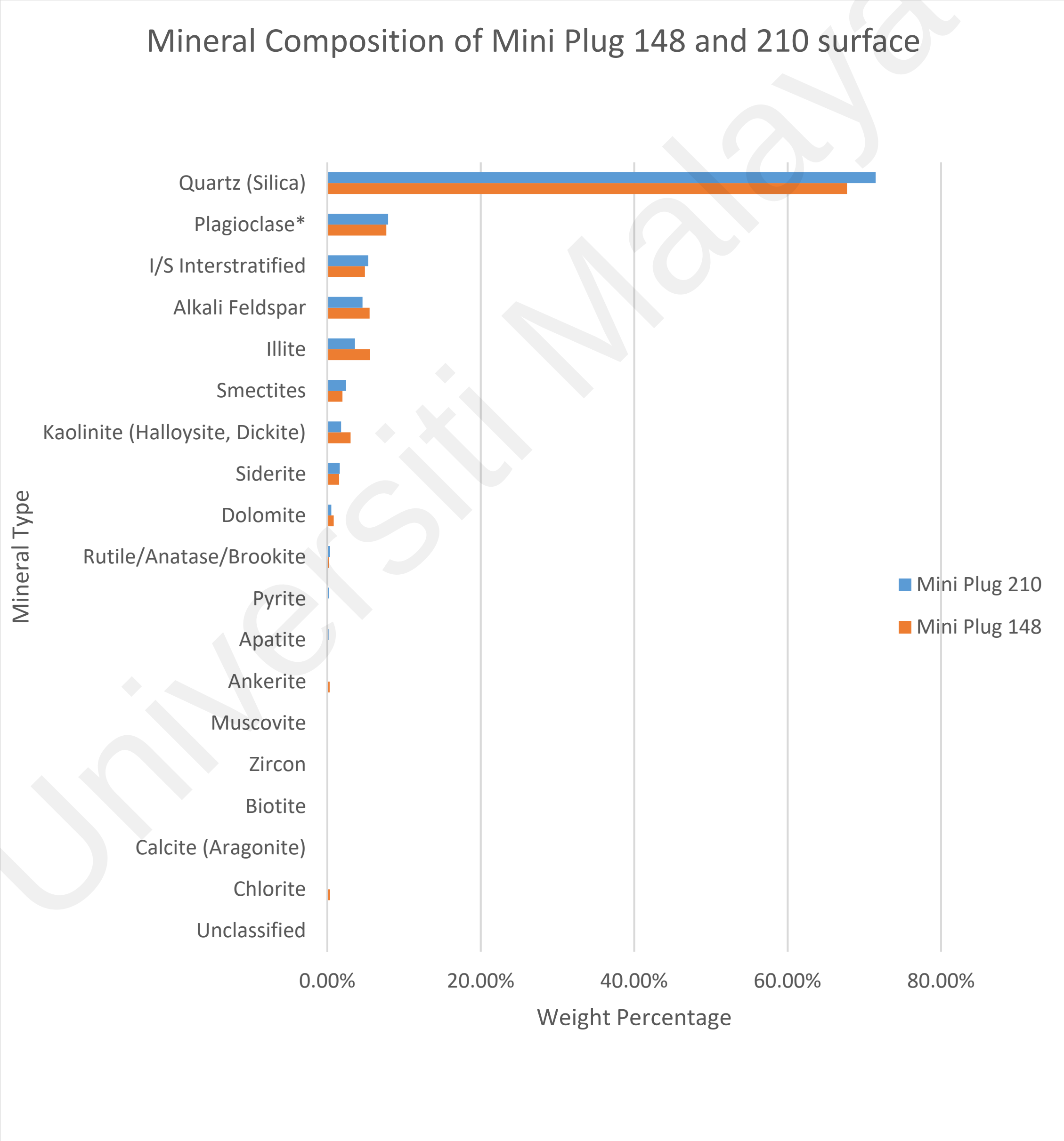

Figure 7.7: Mineral Composition comparison between mini plug 148 and 210 surfaces. The weight percentages of the minerals are almost similar.

The mineralogical analysis of mini plugs 148 and 210 strongly indicate that the sandstone (we extracted the mini-plugs from sand dominated regions in core plugs148 and 210) in both mini-plugs are mineralogically similar. This similarity indicates that the sediments could come from the same source, which is likely as they are only 18 meters apart. Base on this premise, Mini-Plug 127 should have the same mineral composition as mini plug 148 as core plug 127 and 148 are only six meters apart.

Table 7.1 shows that clay makes up 14% and 16% by weight percentage in mini plug 210 and 148 respectively. Both mini-plugs are generally sandstone dominated. The presence of diagenetic clay in these two mini-plugs such as illite, smectite and kaolinite can have an impact on the permeability of the rock due to their pore filling nature. Also, Illite and smectite lines and bridge the pore throats and act as barriers and baffles to fluid flow which affects permeability (Nadeau, 1998). These clays are water-sensitive and may swell in different salinity that can affect permeability and fluid flow. (Baptist et al., 1954). Kaolinite, when present in significant quantities, has been observed and documented to cause a significant drop in rock permeability (Aksu et al., 2015). However, these clays exist in minimal quantities to cause any significant impact on the permeability of the mini-plugs.

Table 7.1: Clay content in the sandstone in mini-plugs 210 and 148

Mini Plug	**148**	**210**
Illite	5.54%	3.28%
Illite/Smectite Interstratified	5.98%	5.58%
Smectites	1.98%	2.89%
Kaolinite	(3.03%	1.94%
Muscovite/Chlorite	0.35%	0.22%
Total Clay	15.81%	13.91%

An interesting result in mini 148 is that there is a distinct layer of clay minerals (highlighted between the white lines in Figure 7.6). This layer does not seem to be dominated by any particular clay mineral and is visible when all clay minerals in the mineral map are selected. This indicates that the clay minerals in mini-plug 148 are not evenly distributed and form thin beds of clay. These thin beds can have an implication on effective permeability at the core plug scale by acting as baffles and barriers to fluid flow (Massart et al., 2016)

Two minerals of interest in low resistivity pay are pyrite (Kantaatmadja et al., 2014) and siderite (Pratama et al., 2017), which can cause excess conductivity (Worthington, 2000). These minerals exist in very trace amounts in both mini plugs. Other conductive minerals, such as iron and mica, were not detected in both mini-plugs. Hence, our results show no significant mineralogical factors that contribute to low resistivity pay in the sandstone of mini plug 210 and 148.

CHAPTER 8 : RESULTS OF XMCT IMAGING AND DIGITAL CORE ANALYSIS.

This chapter summarises and discusses the significant findings and results of this thesis. We divided this chapter into two sections. The first section summarises and discusses the porosity and permeability results for each sample using XMCT Image Analysis, Digital Core Analysis and NER permeability probe analysis and their correlation with the effects of heterogeneity. The second section summarises and discusses the results of the XMCT imaging and Digital Core Analysis of the five mini-plugs and core plugs that we used. The section also compares the computed results based Digital Core Analysis to the NER measured surface permeabilities. Also, we discussed the significance of the results of the five mini-plugs and core plugs we used in this thesis.

8.1 Summary of Image Analysis, DCA and Surface Permeability Analysis.

This section summarizes the methods used in this thesis and its results. The methods are categorized based on the software and tools used. Under Image Analysis which used the MANGO software, results include First Stage Segmentation, Median Grain Size Distribution, Microporosity Analysis, Image Registration Technique and the Spanning Cluster Analysis. Under the digital core analysis software, MORPHY, computed porosity and permeabilities are presented. These methods are followed by 3D Volume Visualization that present images of the rendered 3D volumes of each core plug and the results from the NER permeability gas probe measurements.

8.1.1 MANGO Image Analysis

We used image segmentation that converts multiphase dataset from XMCT datasets into one, two or more phases. We used Image Analysis Software at the Australian

National University (ANU) MANGO (**M**edial **A**xis and **N**etwork **G**enerati**O**n) for parallel segmentation and network generation and pre- and post-processing and analysis of XMCT datasets used in this thesis. (Sheppard et al., 2014; Sheppard et al., 2004)

Generally, we segmented a grey level image into low and high phase object. This seemingly simple but manual process proves to be quite challenging as it requires human input in thresholding the grey levels for the phase segmentation procedure and additional processing of the images to achieve a satisfactory segmentation result (Sheppard et al., 2014; Sheppard et al., 2004). To achieve a satisfactory result, we compared the computed porosity of the segmented dataset of rock samples to experimental results if available.

In this section, we also present a microporosity analysis of the wet images of mini plug 148. The objective is to determine if microporosity causes low resistivity in the sandstone. We also present the results of 3D-to-3D registration of mini plug 64 to core plug 64 to investigate the effects of multi-scale heterogeneity on permeability.

8.1.1.1 Segmentation

The first stage segmentation using the MANGO involved partitioning the XMCT image into phases based on their voxel intensity. Firstly, we segmented the XMCT datasets of the mini-plugs into the pore and grain phases. Additional Segmentation was applied on the segmented dataset twice that created 4 phases. We merged the two phases that are not part of the pore and grain phases into a third 'Intermediate phase'. The intermediate phase is part of the solid grain and not pore. The 'intermediate phase' in the mini-plugs represents phases with different density and attenuation than the solid grains and represent clay and minerals. The threshold values applied for the segmentation and Addition Segmentation are shown in Table 8.1. Also, in Lattice-Boltzmann solver

(MORPHY), we specify that the segmented 3D datasets have three phases. If we do not create the third phase, the Lattice-Boltzmann solver will identify multiple numbers of phases that are neither grain nor pores and will not be able to compute permeability.

Figures 8.1, 8.2, 8.3, 8.4 and 8.5 shows the voxel intensity histograms generated from XMCT images of the mini-plugs using MANGO. Figure 8.6 shows all the voxel intensity histograms, and they greyscale and segmented images of the five mini plugs. Each histogram shows three curves that represent the pore, grain and intermediate phases. The histograms of mini plugs 64, 127, 148 and 210 show a bimodal distribution with two curves, with curves to the left, represent pore phase and the curve to the right represents the grain phase. The small curve in the middle represents the intermediate phase. Datasets with bi-modal profiles with the pore and grain curves having the same shape indicate a well-balanced pore and grain system in a relatively homogeneous rock with well-sorted grains such as the histogram of Mini Plug 127 and 148 which represent relatively homogeneous sandstone. These relatively balanced profiles have a higher certainty in terms of segmenting the pore and the grains. Therefore, the segmented phase should be relatively accurate. In more the heterogeneous mini plug 64 and 245, there are a more considerable amount of grain phases than the pores resulting in the curve of the grains to be substantially larger than the curve of the pores, indicating a poorly sorted rock. Also, these poorly sorted rock profiles have a large number of voxels that lie within the intersection area between the pore and grain curves. As a result, segmenting the pore and grain is delicate that may lead to inaccurate porosity values. This inaccurate porosity values can have implication when using the dataset to compute permeability, where poor porosity estimates may lead to inaccurate computed permeabilities. Therefore, in heterogeneous rocks, it would be good practice to compute absolute permeabilities using segmented datasets with slightly different segmentation thresholds.

The segmentation process is manual and subjected to human error and bias. Therefore, we benchmarked the computed porosity of the mini-plugs to the measured permeability of their corresponding core plugs. We clarify that we do not deliberately segment target to match the experimental results which we only use as a benchmark. Our results show that the computed and measured results are very similar with a marginal difference which is acceptable. We attribute the marginal difference to the difference of heterogeneity between the core plug and mini plugs. We also clarify that the Routine Core Analysis method used to measure the permeability of the core plugs cannot measure samples that are smaller than standard core plugs with a diameter and height of one inch. Therefore, the experimentally measured permeability of the core plugs is the best reference for validating the computed porosity of the mini-plugs. Previous studies also use experimentally measured core plug porosity and permeability as benchmarks for validating computed results which relatively good match between the results of the two methods with some marginal difference (Arns et al., 2005).

Table 8.1: The threshold ranges for the first stage Segmentation (CAC), Additional Segmentation on grain phase (ASC1) and Additional Segmentation 2 (ASC2) on pore phase using MANGO. Intermediate phases are nether pore nor grain.

Mini Plug		64	127	148	210	245
CAC	Lower Threshold	11100	10950	10850	10900	11210
	Upper Threshold	11250	11000	10950	10950	11250
ASC1	Lower Threshold	10950	10850	10950	10900	11050
	Upper Threshold	11120	11300	11120	11100	11200
ASC2	Lower Threshold	10640	10500	10640	10650	11050
	Upper Threshold	11000	11050	11000	10980	11230
Computed Porosity		17.00%	25.40%	26.70%	25.20%	15.20%
Measured Core Plug Permeability		18.9%	29.0%	28.0%%	28.0%	15.0%
Grain		80.00%	71.50%	69.60%	69.95%	77.0%
Intermediate Phase		2.00%	3.10%	3.70%	4.85%	7.00%

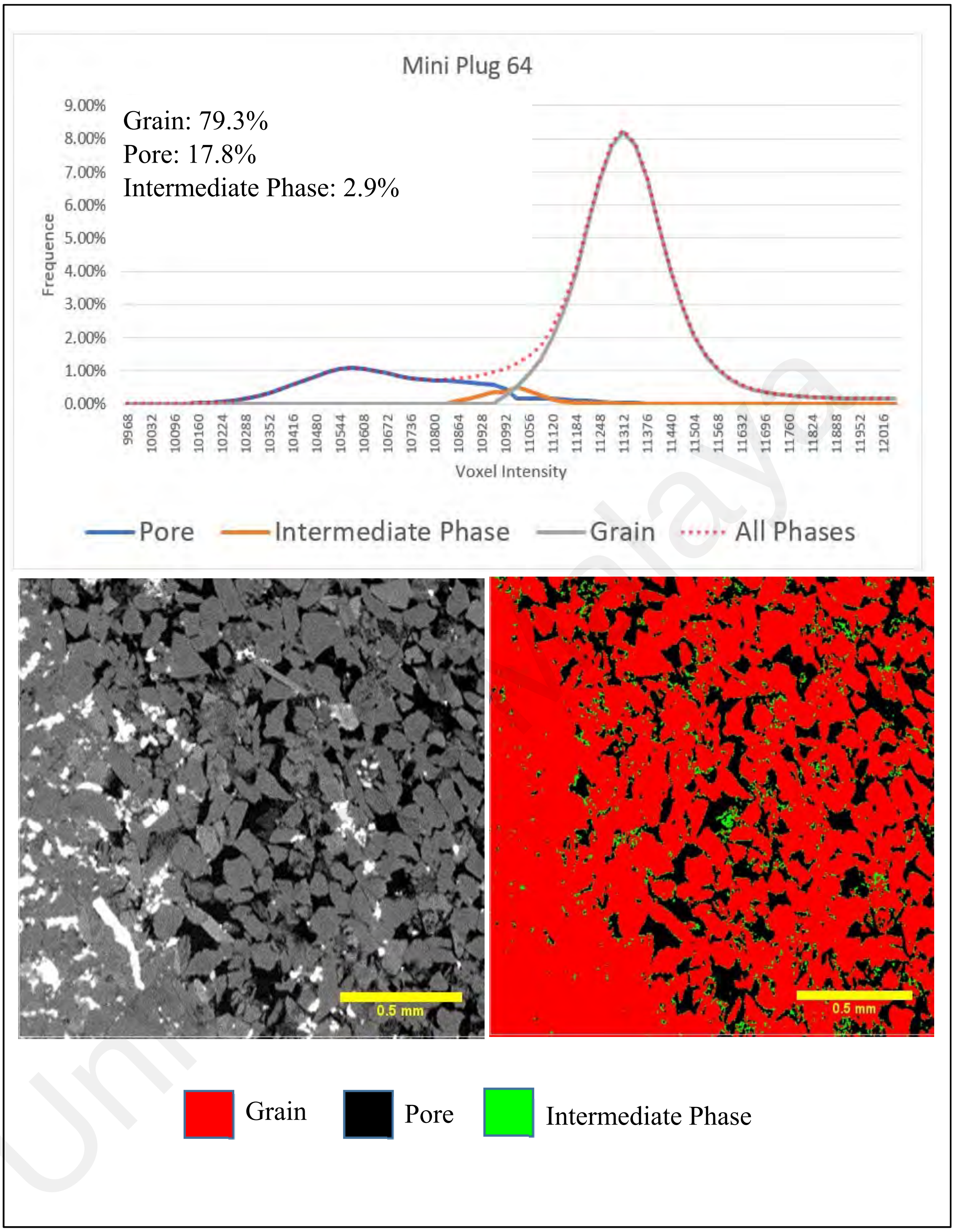

Figure 8.1: Top: Voxel Intensity Histograms of mini plug 64. Bottom: Greyscale and segmented images the mini plug 64

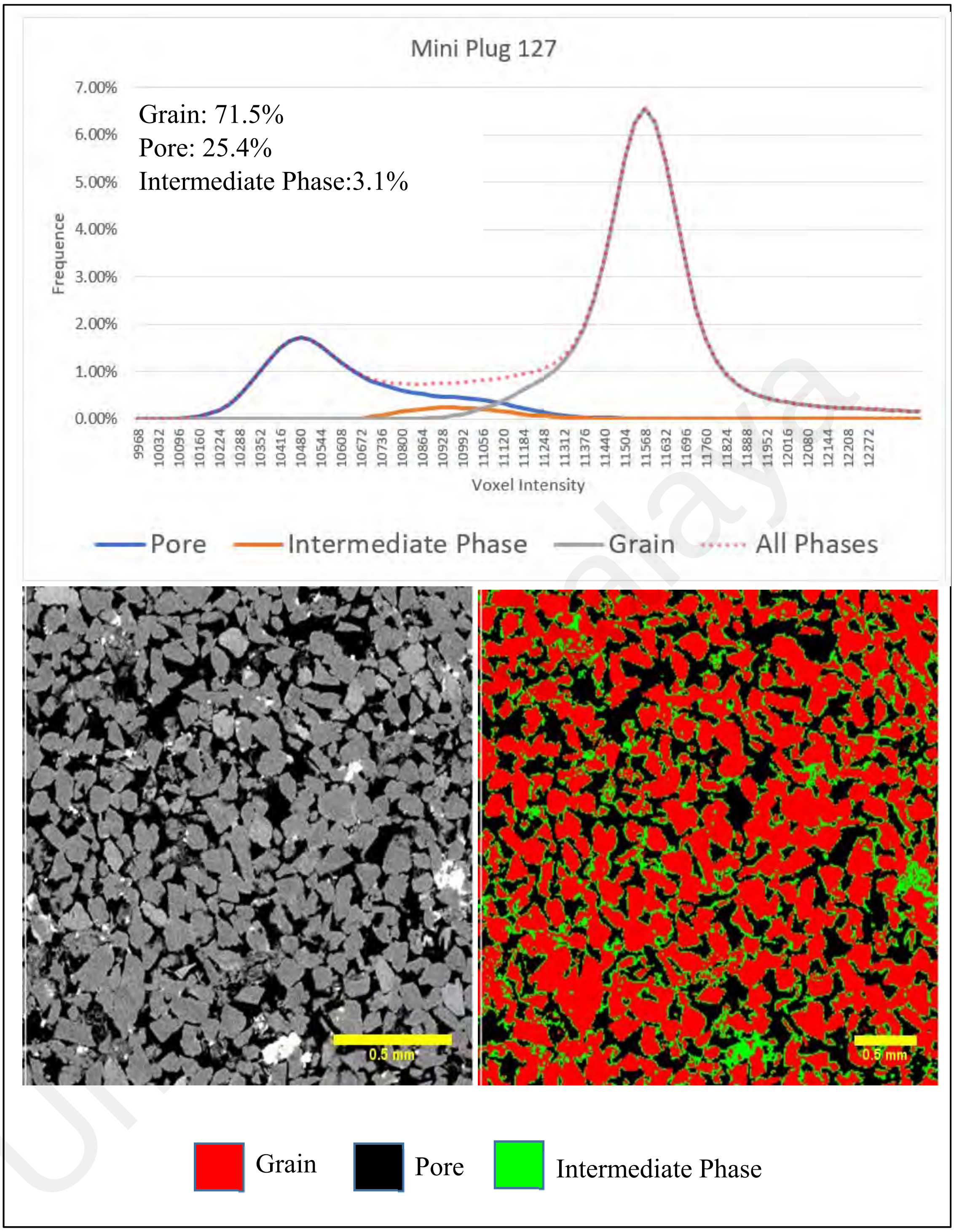

Figure 8.2: Top: Voxel Intensity Histograms of mini plug 127. Bottom: Greyscale and segmented images the mini plug 127.

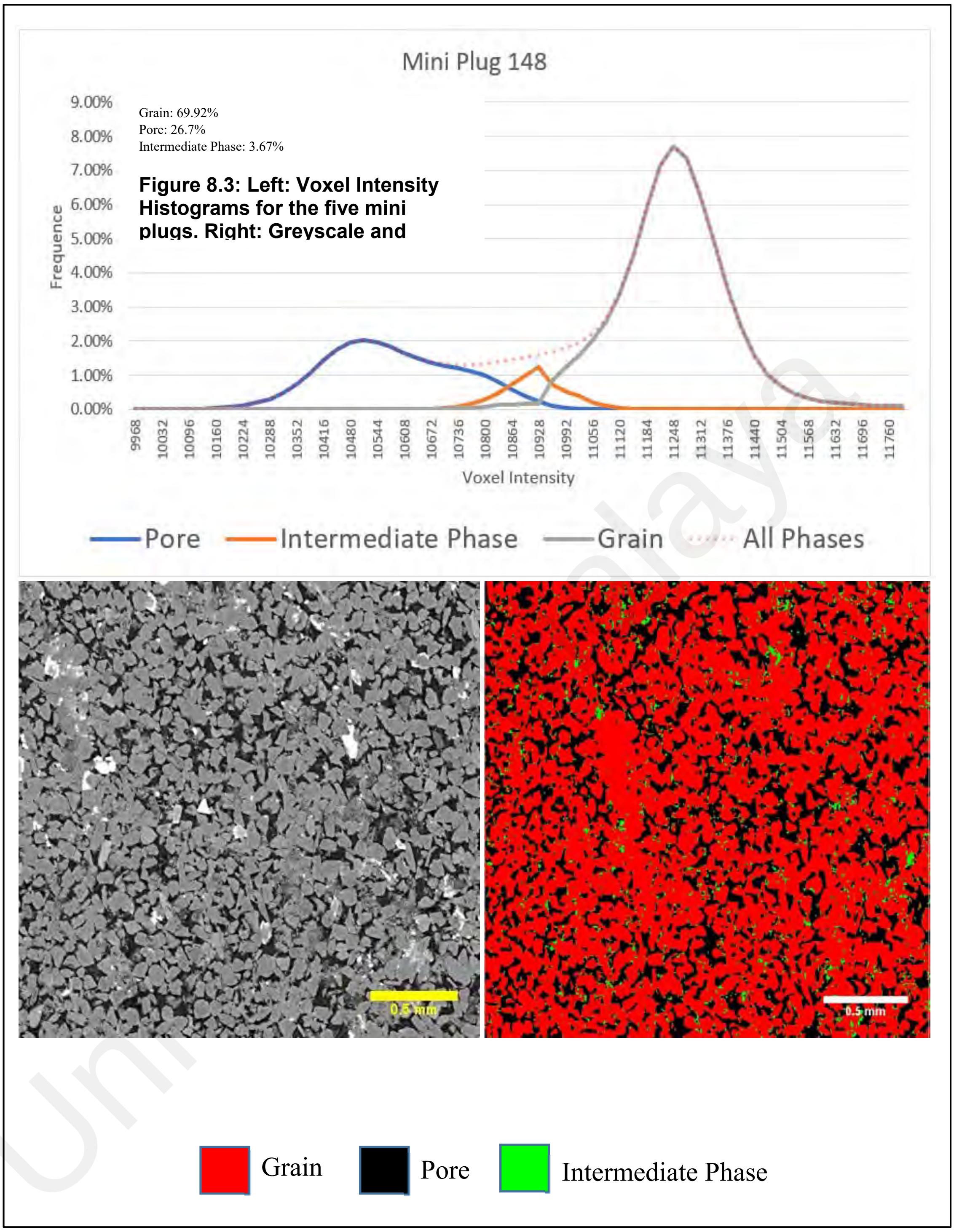

Figure 8.4: Top: Voxel Intensity Histograms of mini plug 148. Bottom: Greyscale and segmented images the mini plug 148.

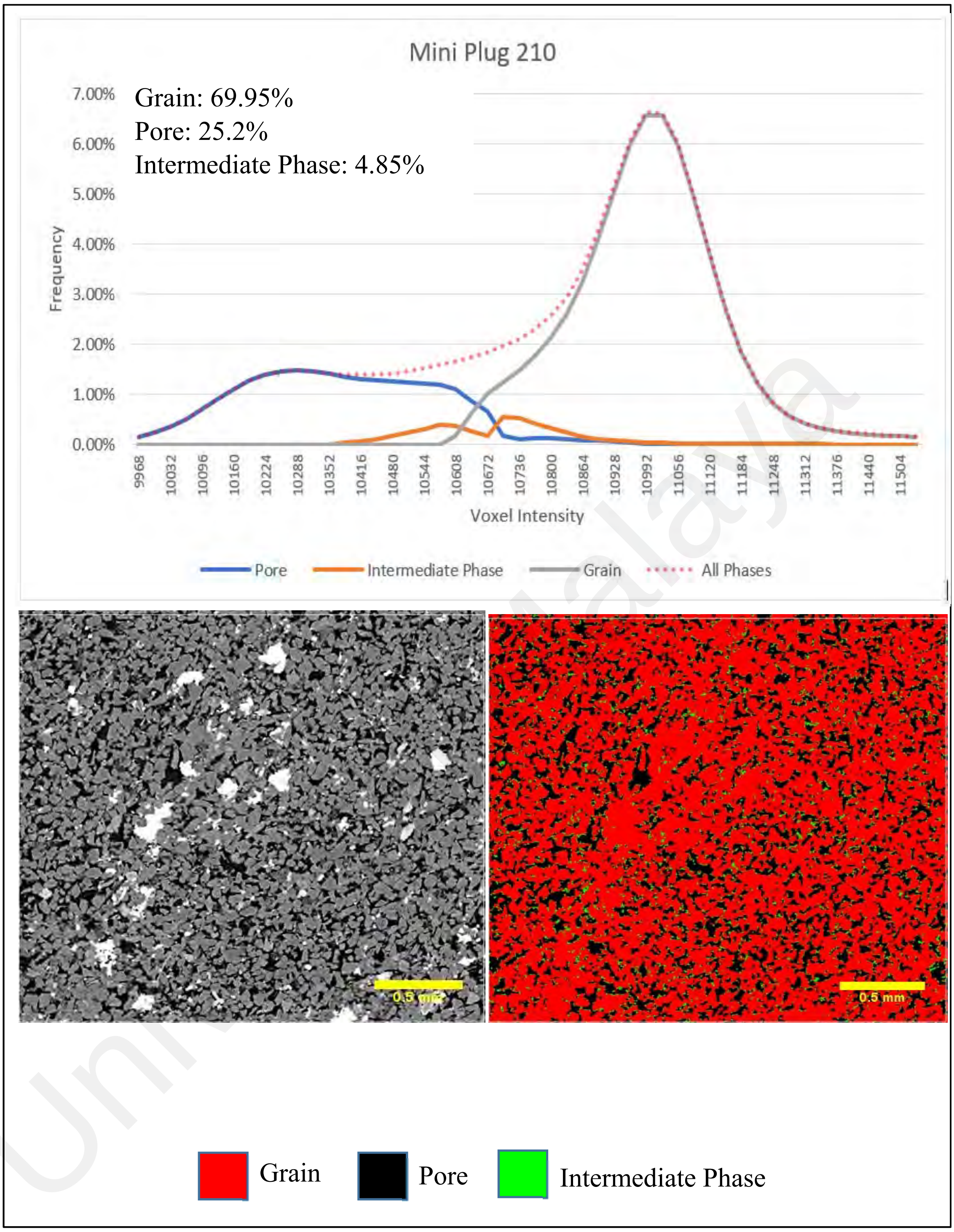

Figure 8.5: Top: Voxel Intensity Histograms of mini plug 210. Bottom: Greyscale and segmented images the mini plug 210.

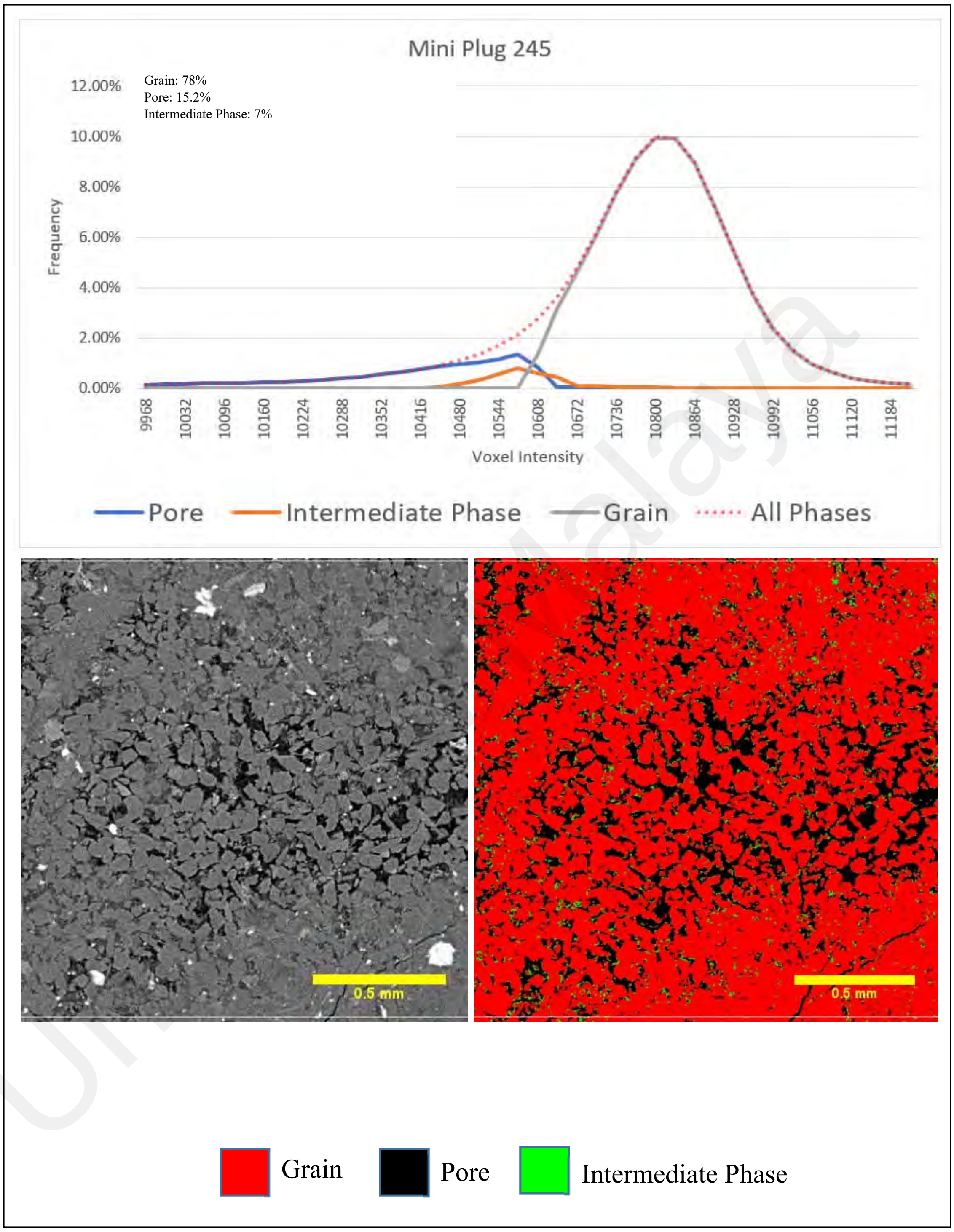

Figure 8.6: Top: Voxel Intensity Histograms of mini plug 245. Bottom: Greyscale and segmented images the mini plug 245.

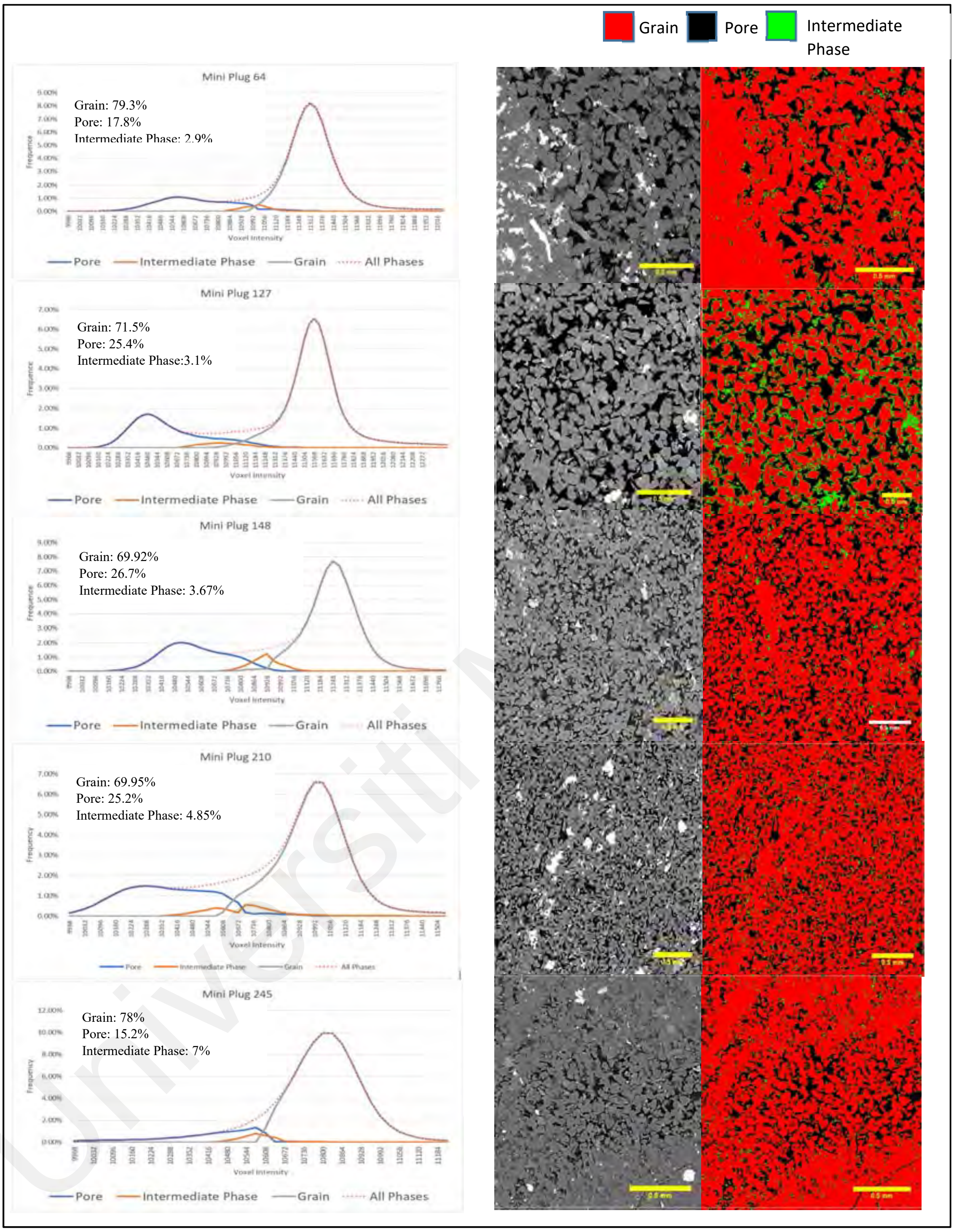

Figure 8.7: Left: Voxel Intensity Histograms for the five mini plugs. Right: Greyscale and segmented images of the mini plug.

8.1.1.2 Median Grain Size Distribution

We used MANGO to calculate the grain size distribution from the XMCT images of the five mini-plugs using the Cluster Size Distribution filter, which we summarized in Table 8.2 and Figure 8.8.

Mini plug 127 has the highest median grain diameter at 103µm followed by mini plug 148 at 92 µm, mini plug 64 at 72 µm, mini plug 210 at 36 µm and mini plug 245 at 23 µm. Although the median grain size of mini plug 64 is smaller than mini plug 127 and 148, the grain diameter profile for mini plug 64 in Figure 8.8 is closer to the two mini plugs compared to mini-plug 210 and 245. The median grain diameter in mini plug 64 is twice of that of mini plug 210 and three-time that of mini plug 245. The results for mini plug 64 suggest that its sandstone is relatively comparable to the sandstone in mini plug 127 and 148 in which are the benchmark reservoir sandstones for this thesis.

The permeability-to-median grain diameter graph in Figure 8.9 shows that permeability increases with larger grain size. Mini plug 210's lower averaged permeability compared to mini-plug 64, 127 and 148 can be correlated to its smaller median grain diameter at only 36 µm. Lastly, mini plug 245, which has the smallest median grain diameter of only 23 µm, has the lowest permeability.

Table 8.2: The measured and computed porosity, permeability and median grain size of the five mini plugs. We observed that mini-plug permeability increases with median grain diameter.

Sample	Core Plug Permeability (mD)	Mini Plug Permeability (mD)	Core Plug Porosity	Mini Plug Porosity	Mini Plug Median Grain Diameter (µm)
64	36	894	19%	17.8%	72
127	633	1358	28.9%	25.4%	103
148	394	2033	28.03%	29.8%	92
210	276	251	29.2%	25.2%	36
245	0.9	65	15.95%	15.0%	23.2

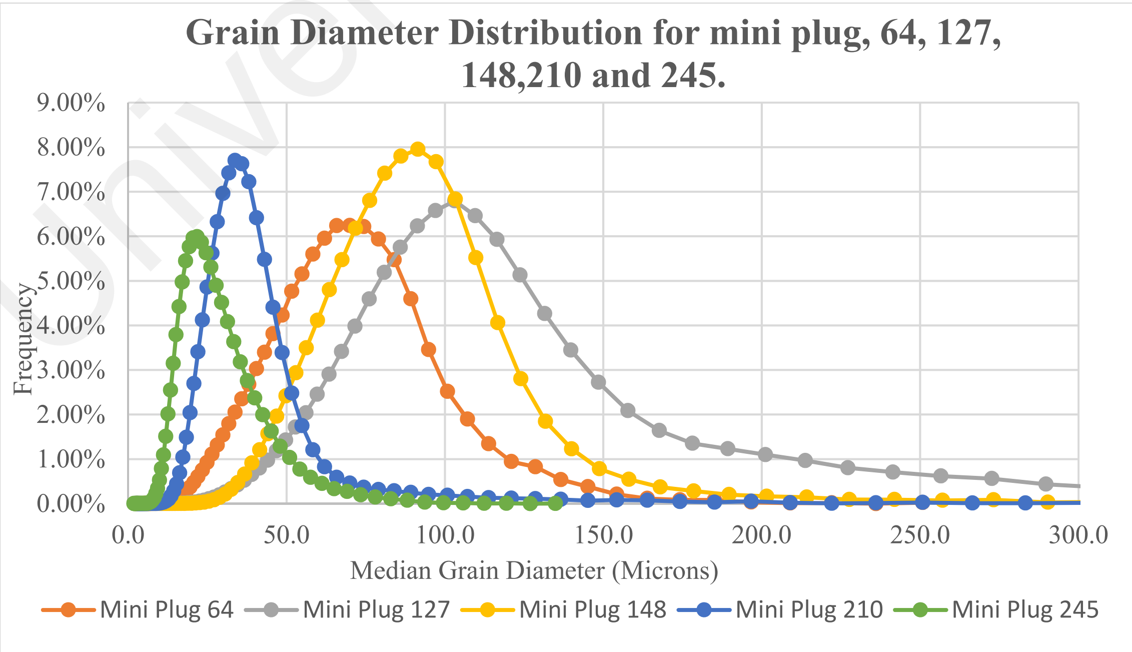

Figure 8.8: Grain size distribution calculated from the images of the mini-plugs.

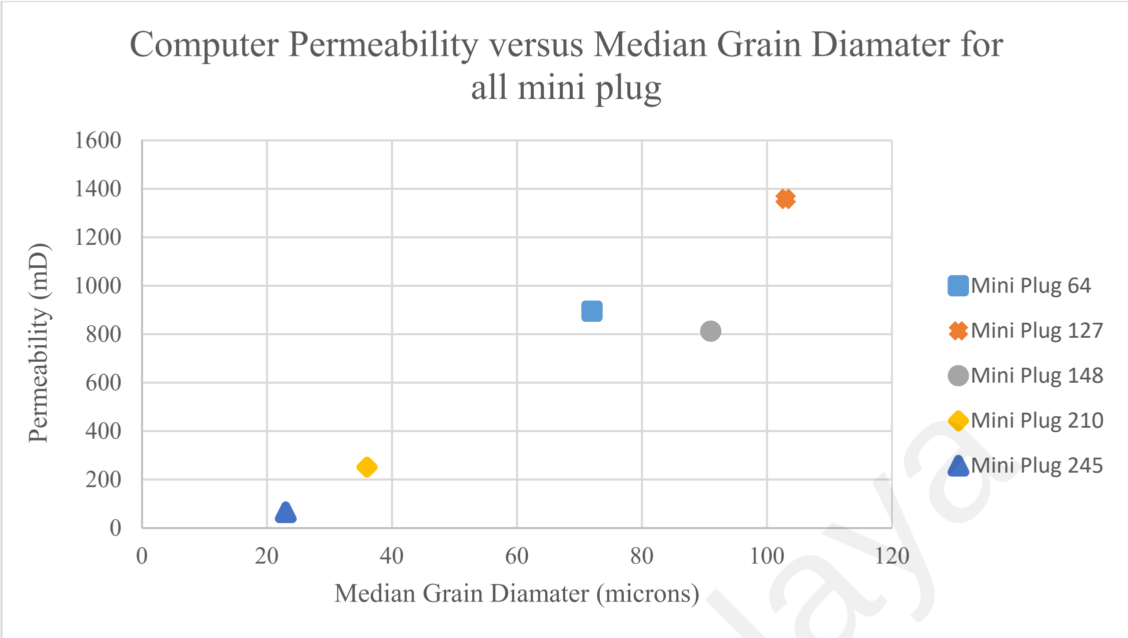

Figure 8.9: The computed permeability of the mini-plugs using digital core analysis for 300 voxels3 sub-volume sizes versus the median grain diameter of the mini-plugs. The results showed that permeability increases with median grain diameter.

8.1.1.3 Microporosity Analysis

We used MANGO to calculate the fraction of micro-porosity or pores that are below one micron of the five samples summarised in Table 8.3. This method identifies rock types affected by microporosity which causes low resistivity (Worthington, 2000). Microporosity which is associated with the clay phases causes low resistivity (Worthington, 2000). The results show that the computed microporosity of the five samples is between 0.9% to 1.5%, which meagre. Studies by Worthington (2000) show that most low resistivity reservoirs have measured microporosity of up to 50%. Therefore, the computed microporosity of the five mini-plugs is too small to be one of the leading causes of low resistivity pay.

Table 8.3: Computed Macroporosity and Microporosity of all Mini Plugs.

Mini Plug	Microporosity Analysis	
	Macroporosity (%)	Microporosity (%)
64	17.77	0.9
127	30.48	0.94
148	29.8	1.5
210	25.2	1.5
245	11.72	1.01

8.1.1.3.1 Wet Imaging Microporosity Analysis of Mini Plug 148

We used a wet-dry difference imaging technique that can resolve overlooked microporosity. We selected mini plug 148 for this procedure to determine if the sandstone rock would have any undetected microporosity. The next step involves saturating mini plug 148 with 1.5 M of Sodium Chloride (NaCl). Dr Michael Turner then scanned the mini plug at high resolution using the ANU X-Ray Micro-CT tool at 3.8 µm/voxels. The NaCl acts as a contrast agent which permeates through the sand and clay phases within the mini plug and enhance the visibility of the micropores.

In the next step, we identified an XMCT image from both the dry and NaCl saturated image that is similar. The MANGO software aligned both images and calculated the differences in intensity between the two images (Latham et al., 2008). The intensity difference is then subtracted from the dry image to remove phases that were not penetrated by the NaCl. The resultant image enables the identification of additional micropores that have absorbed the NaCl

Figure 8.10 shows the wet and dry images of mini plug 148. Image A is the original dry image of Mini Plug 148. In contrast, Image B is the mini plug saturated with a 1.5M NaCl contrasting agent that increases the voxel intensity contrast of the hidden micropores. As a result, the intensity of these two phases is higher than the grains, resulting in the pores and intermediate phases appearing brighter while the grains are dark. We inverted the Image B intensity into Image D, where the intensity profile is similar to the dry image with the grains have a higher intensity than the pore and intermediate phase.

We then applied another image registration procedure to subtract the voxel intensity of the dry image from the inverted wet image D to produce Image F. The voxel intensity difference in Image F contains the hidden micropores in mini plug 148. However, the hidden micropores are not apparent when compared to the original image. We computed the microporosity in Image F, which we segmented using the same thresholds values used for the segmentation of the dry image.

Tables 8.4 and Table 8.5 shows the computed microporosity in mini plug 148. The table shows that the pores and grains remain mostly unchanged, but the intermediate phases volume fraction increased by 18% from 3.1% t0 3.65% of the total volume. Table 8.20 shows very little change in total porosity and macroporosity of the wet image relative to the dry image. The micro-porosity, on the other hand, increases by 120% from 0.9% to 2%. The microporosity doubled after the NaCl saturation was applied. The microporosity in mini plug 148 to be too low to be a leading factor to low resistivity. Most microporous low resistivity pay has a microporosity of 50% (Worthington, 2000). The result for mini plug 148 is applicable to mini-plug 127 as the sandstone in both samples is similar. We did not apply microporosity analysis on the heterolithic samples 64 and 245 as laminated structures are the leading cause of low resistivity in these samples. The wet imaging microporosity analysis is a useful method for investigating microporosity in rock types such as carbonate in which microporosity is high.

Table 8.4: Differences in terms of phase volume percentage of the pore, grain and intermediate phases between the dry and NaCl saturated mini plug 148.

3 Phase Segmentation	Dry Image %	Wet Image %	Difference	Percentage Difference
Pore	25.4	25.09	-0.31	-1.2%
Grain	71.6	71.27	-0.33	-0.5%
Intermediate phases	3.1	3.65	+0.55	+17.7%

Table 8.5: Differences in terms of porosity, Macroporosity and microporosity between the dry and NaCl saturated mini tomogram of mini plug 148.

Micro-porosity Analysis	Dry Image %	Wet Image %	Difference (Wet-Dry)	Percentage Difference
Total Porosity	26.4	27.09	+0.7	+2.6%
Macro-porosity	25.4	25.09	-0.3	-1.2%
Micro-porosity	0.9	2.00	+1.1	+120.0%

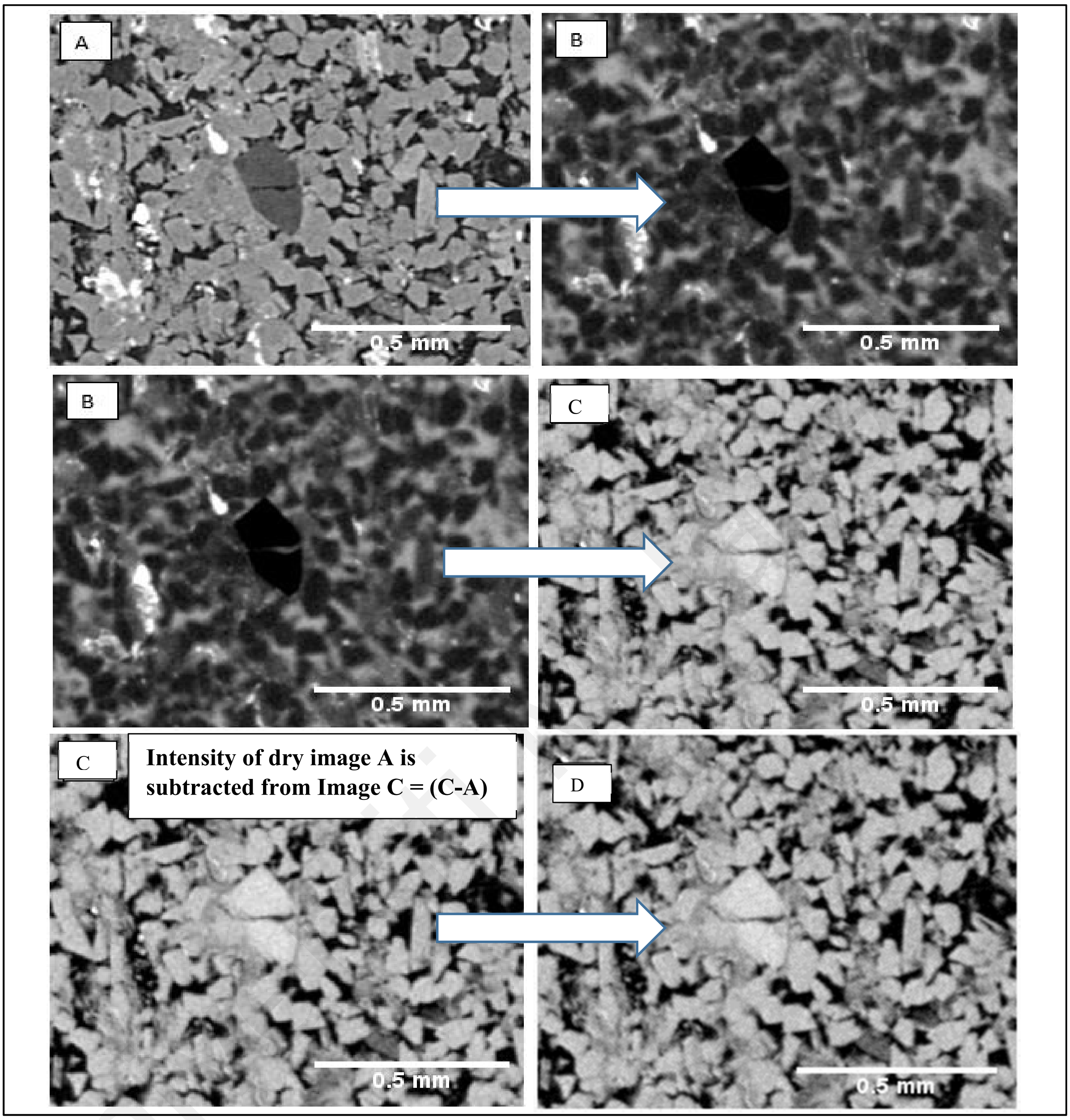

Figure 8.10: Comparison between the dry and wet images and processed images for Image Registration. Image A is the original dry image of Mini Plug 148. Image B is the tomogram of the same mini-plug saturated with 1.5M NaCl. We applied an image registration procedure on image C that subtracted the intensity of the dry image from the inverted wet image C to produce Image F. The attenuation difference between the dry (A) and wet image (C) is not apparent on image D. Therefore, we computed the porosity between the two images using the MANGO Image Analysis software and shown previously in Tables 8.5 that highlight the difference between the two images.

8.1.1.4 Image Registration of mini-plug dataset to the core plug

We performed A '3D to 3D' image registration technique using MANGO to align the mini plug dataset to its original location within the core plug. The registration technique was developed to combine XMCT images to other imaging techniques such as 2D Backscattered Scanning Electronic Microscope images that provide opportunities to examine structure at higher resolutions (Latham et al., 2008). In this thesis, this technique to align the high-resolution image of the mini plug to its original location within the low-resolution image of the core plug. This allows us to view the mini-plugs at their original location within the core plugs and allows us to confirm that the mini-plugs were extracted from the sandstone dominated region of the core plug. We compare the mini plug to the overall core plug to examine the effect of heterogeneity between these two volumes sizes on permeability. We expect that the mini-plugs with high sandstone-to-mudstone ratio extracted from the sandstone layers in the heterolithic core plugs to have a higher permeability than the experimentally measured permeability of the core plugs which have a lower sand-to-mudstone ratio.

We conducted the 3D to 3D Image Registration on mini-plugs 64 and 148, which represent heterogeneous and homogeneous core plugs respectively. Mini plug 64 comes from a heterogeneous muddy heterolithic core plug while 148 comes from a homogeneous laminated sandstone core plug. Mini plug 64 is selected due to the large difference between the permeability of its mini plug and core plug at 894mD and 36mD respectively. We used Core plug 148 as a reference to the sandstone reservoir rock as PETRONAS identified as part of the main reservoir unit.

8.1.1.4.1 3D to 3D Registration of Mini Plug 64

Firstly, we observed similar features on the mini plug dataset (2.74 microns/ voxel), and the original core plug dataset (16 microns/voxel). Once we identified these similar features, as shown in Figure 8.11, we selected 3 common locations and recorded their coordinates (x, y and z). We used the two sets of coordinates from the mini plug and core plug images to align both datasets using a Registration Transform filter on the MANGO software which aligned the two datasets onto a single coordinate system. After the transformation, the mini-plugs datasets have its coordinates virtually aligned to its original general position on the core plug. The alignment allows the 6mm diameter mini-plug to be re-sized correctly relative to the 37mm diameter core plug.

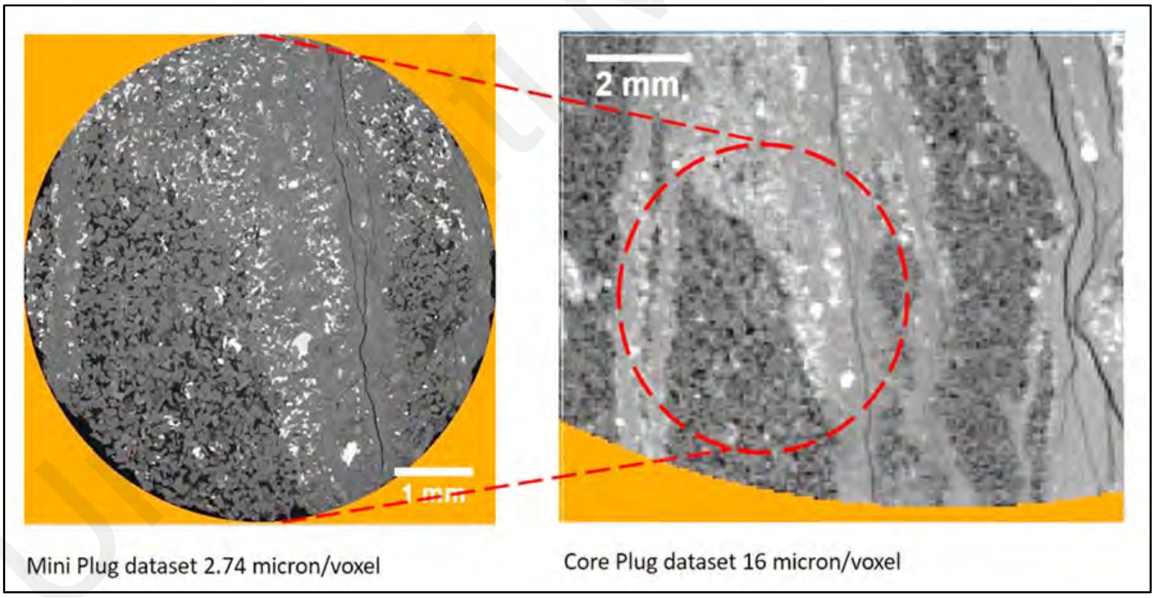

Figure 8.11: We identified **s**imilar features on the core plug (left) and mini-plug (right). Three coordinates on both features are identified and used to overlay the mini plug on the core plug using the Registration Transform function from the MANGO software (bottom images).

A 3D-to-3D volume transformation filter in MANGO matches the resolution of the mini plug to the resolution of the core plug (16 microns/voxel). It aligns the mini plug dataset to core plug dataset base on the coordinates of the similar features on the mini plug and core plug (shown previously in Figure 8.11). The resulting mini-plug dataset from this procedure will have the same resolution of the core plug dataset and aligned to approximately to its original location within the core plug. As a result, both datasets can be opened concurrently in the NCViewer slice viewer where the alignment can be inspected by toggling between two images from the same datasets. The alignment was successful as the two images from the two datasets would have a relatively good match. With features from both datasets such as cracks and grains relatively well aligned, as shown in Figure 8.12.

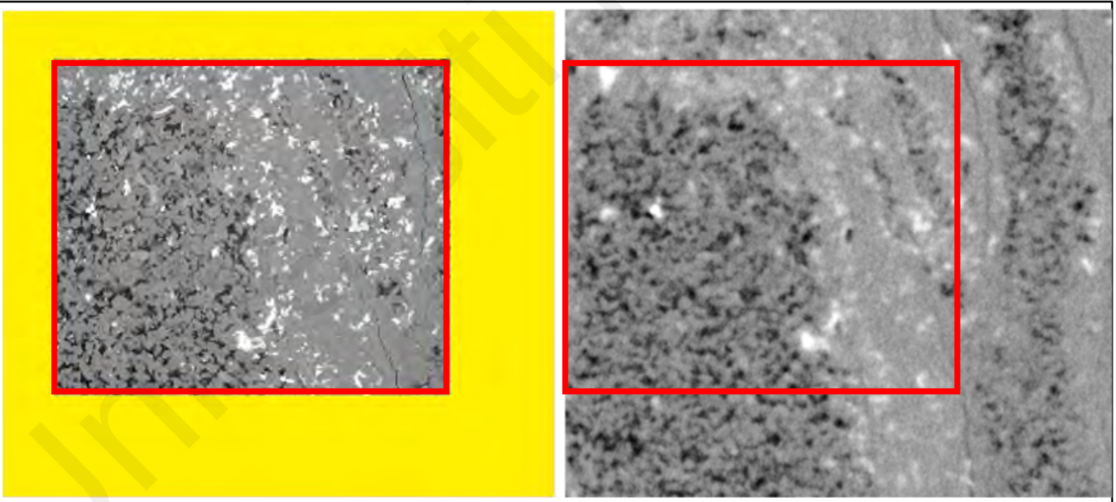

Image A: 2.74 µm/voxel **Image B: 16 µm/voxel**

Figure 8.12: Two aligned images from the mini plug (A) and core plug (B) after application of Registration 3D to 3D volume. The mini plug image resolution (left) is reduced from 2.74 microns/voxel to 16 micron/voxel. The red square in image B corresponds to image A.

8.1.1.4.1.1 Discussion

Based on the results of the Registration technique used on the mini plug and core plug 64 in Figures 8.13, 8.14, and 8.15, we show that mini plug 64 was extracted from a sandstone dominated region of the core plug which was deliberate. Figure 8.16 shows that we extracted mini plug 64 from the thick sandstone layers (circled in red) in core plug 64. As a result, the mini plug has a higher calculated permeability using DCA compared to the measured core plug permeability of 36 mD. 3D volume visualization of core plug and mini plug 64 using Drishti in Figure 8.17 validated the significant presence of sandstone within the core plug and mini plug 64. Despite the dominating presence of sandstone in mini plug 64, we observed that the sandstone thins from top to bottom with some of the bottom sandstone poorly connected. Also, within the core plug, the sandstone layers only make up 15% of the core plug volume and consist of very thin sandstone layers that have a tortuous geometry and may not be well connected and continuous in some parts. This poor connectivity and continuity of the sandstone layers result in lower effective permeability of core plug 64. Our results show that while the computed permeability of the sandstone sub-volumes is higher than the RCA measured core plug permeability, the computed results may not necessarily suggest that fluid will flow smoothly through the mini plug. In mini plug 64, the path of the fluid flow may be tortuous due to the sandstone regions being thinner at one end of the mini plug.

Similarly, the thin and tortuous sandstone layers in core plug 64 resulted in poor fluid transmissibility through the sandstone. These findings emphasize the potential impact of the connectivity and continuity of the sandstone regions in the mini plug and core plug scale that can affect effective flow properties at different scales. We discussed the impact of multi-scale heterogeneity on the permeability of Sample 64 in section 8.2.3.

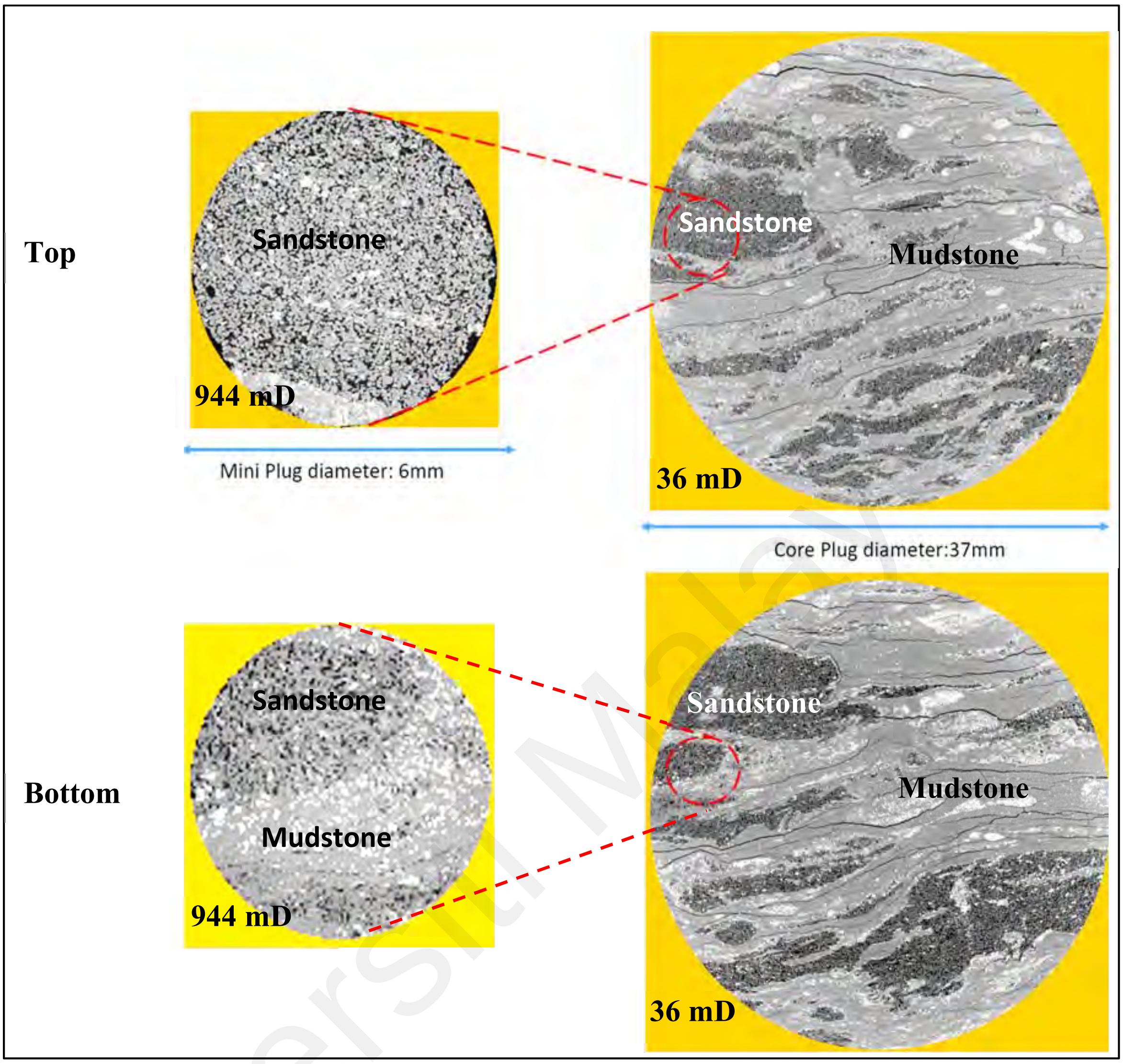

Figure 8.13: We show mini plug 64(left) relative to its original location in the core plug 64 (right). Large sections of the mini-plugs are made up of sandstone.

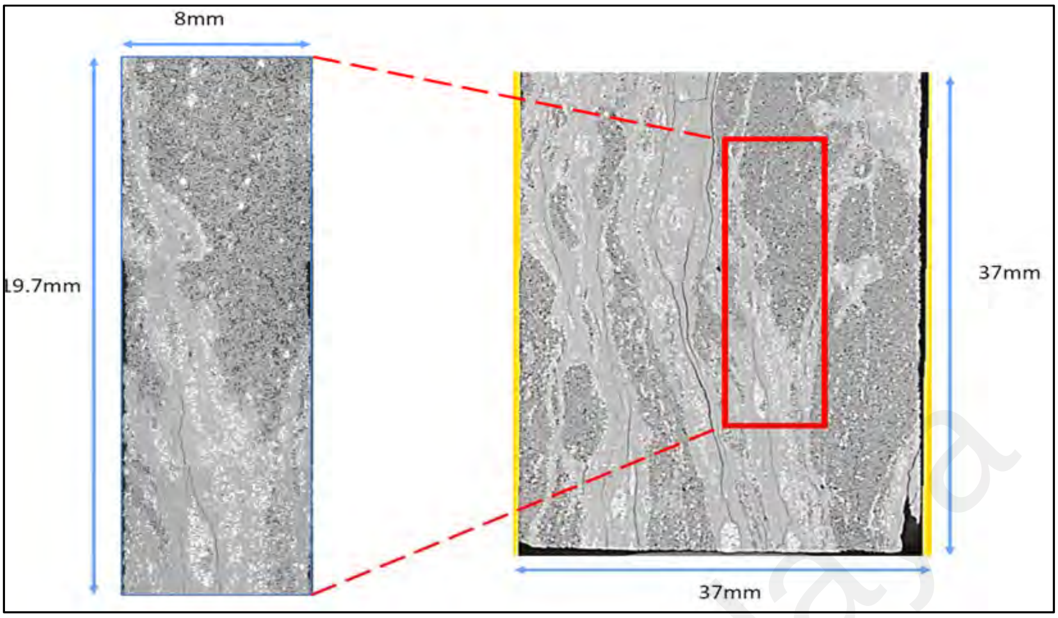

Figure 8.14: Registration of the mini plug to its original location on core plug 64. We observed that sandstone dominates a significant amount of the core plug.

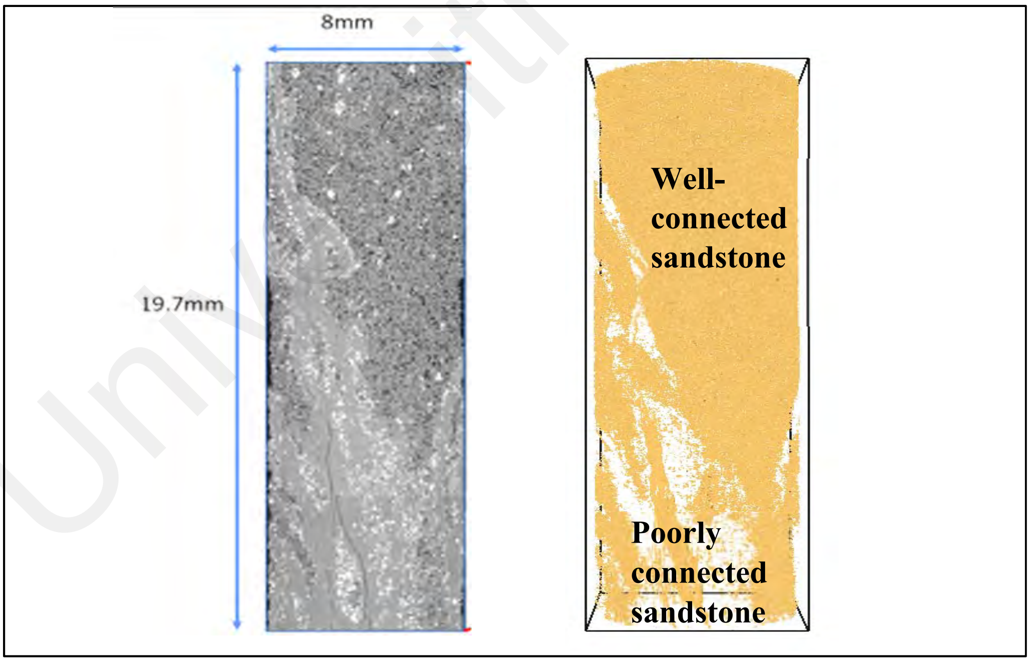

Figure 8.15: The left image is the greyscale tomogram of mini plug 64 while the right image is a corresponding Drishti rendering of the sandstone phase. We observed that the sandstone has good connectivity and span the mini plug in the axial direction but thins out at the bottom.

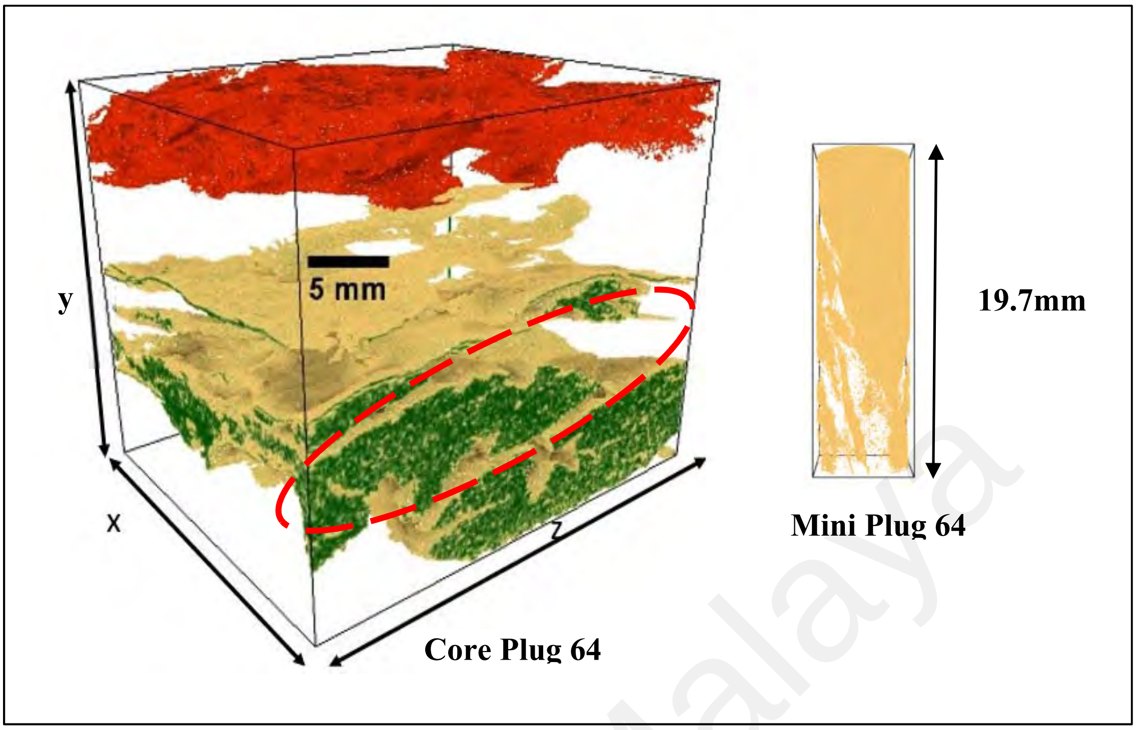

Figure 8.16: Rendered sandstone layers in core plug 64 using Drishti visualization software with the rendered mini plug 64 to the right for comparison. The green sandstone layer inside the red circle in core plug 64 is the general area from which we extracted mini plug 64.

8.1.1.4.2 3D to 3D Registration of Mini Plug 148

We initially identified similar features are on both the mini plug and core plug datasets (Figure 8.17). The coordinates of three similar features on both datasets are recorded and used in the Registration Transform to align both the datasets. We completed the alignment using a 3D to 3D Image Registration which transforms the resolution of the mini plug dataset to the resolution of the core plug (16 micron/voxel). When we opened the resultant mini-plug dataset concurrently with the core plug dataset, we positioned the mini plug within its original position in the core plug (Figure 8.18 and 8.19).

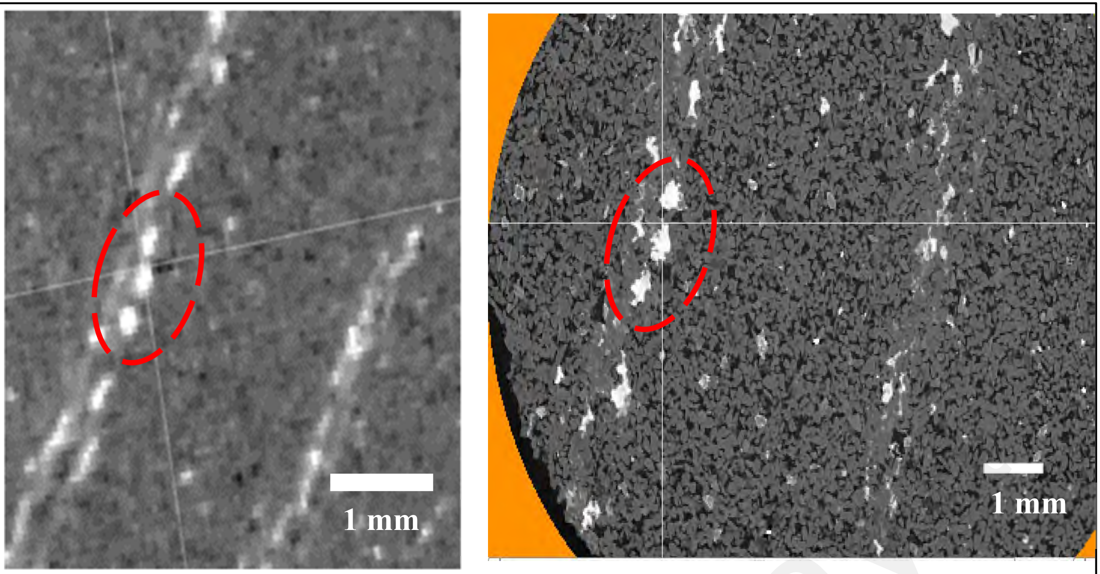

Core Plug dataset 16 micron/voxel

Mini Plug dataset 2.74 micron/voxel

Figure 8.17: We identified Similar features in the mini plug and core plug datasets (in red circles) for '3D to 3D' Image registration process.

8.1.1.4.2.1 Discussion

We see in Figures 8.18 and 8.19 that Mini plug 148 is dominated by sandstone which shows we extracted the mini plug from the sandstone region of core plug 148. These images indicate a high degree of homogeneity in mini plug 148. Despite the homogeneity, the calculated mini-plug permeability is higher than the measured core plug permeability at 812 mD versus 394 mD respectively. This discrepancy indicates that there is a difference in terms of heterogeneity at the mini plug and core plug scale that resulted in permeability difference at the core plug and mini plug scale. We discussed the impact of the heterogeneity in core plug 148 in section 8.3.1.

To sum up, the 3D-to-3D volume registration technique used on sample 64 and 148 is a useful image analysis method to view the smaller samples such as mini-plugs relative to a larger core plug from which they were extracted. The registered volume of the mini plug to the core plug allows us to compare the heterogeneity difference between the two-volume sizes. We used this method in analysing core plug 64, where which has significant multi-scale heterogeneities that caused large permeabilities difference at the core plug and mini plug scales as discussed in section 8.2.3.

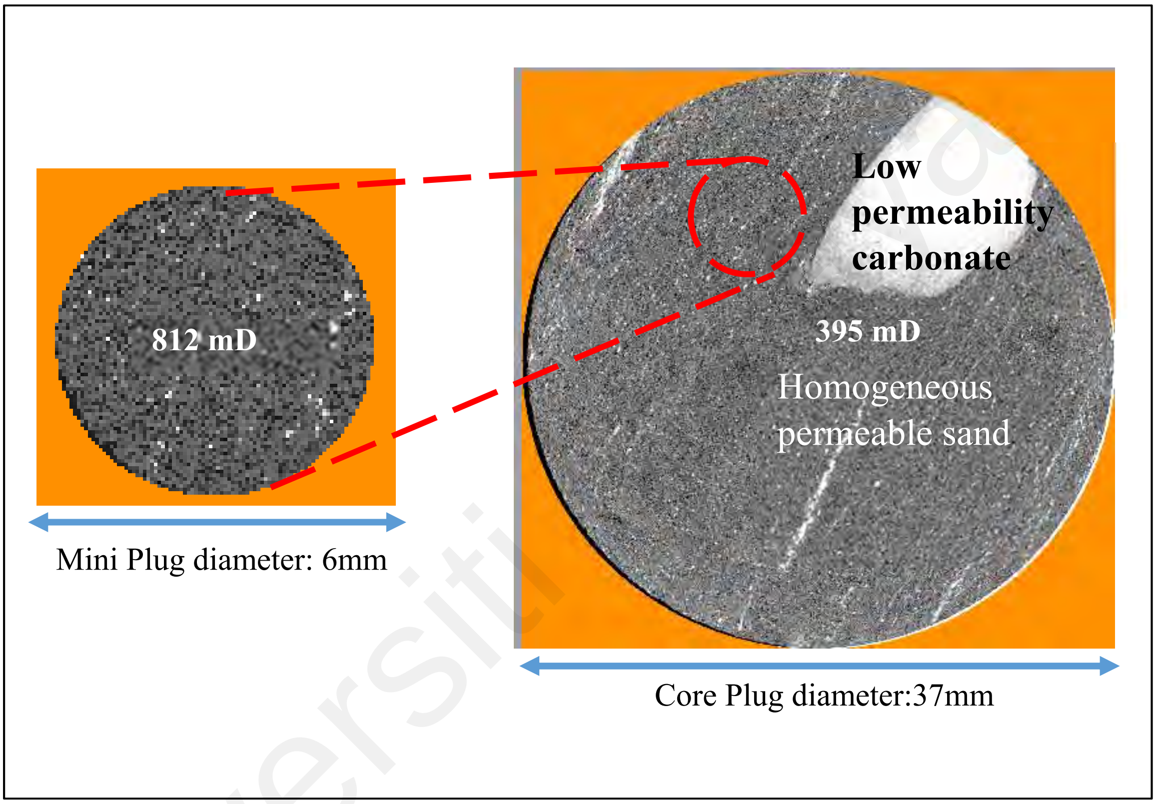

Figure 8.18: Mini plug 148(left) and its location on core plug 148 after 3D to 3D Image Registration. The mini plug is generally sandstone dominated. There is a significant presence of carbonate minerals as indicated on the image.

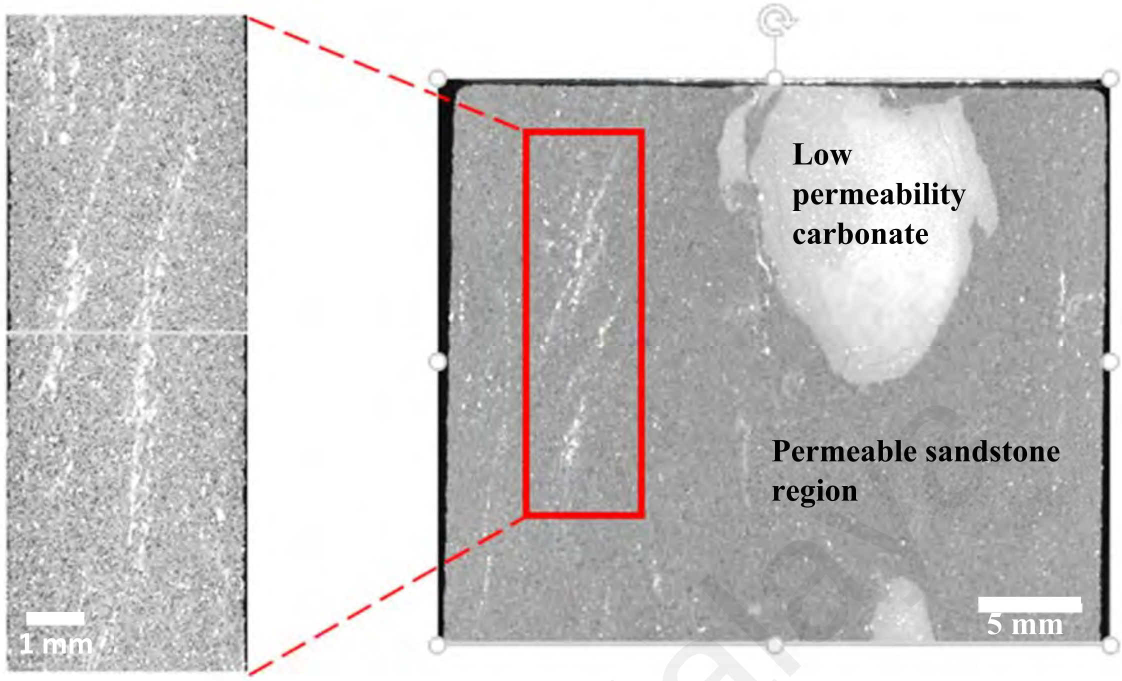

Figure 8.19: Approximated location of mini plug 148 in relative to the volume of core plug 148. We noted there is white high attenuation region that consists of carbonates that have different permeability compared to the rest of the sandstone region or act a barrier to flow, resulting in lower effective permeability of the core plug.

8.1.1.5 Spanning Cluster Analysis

Sandstone connectivity is an important aspect when evaluating the reservoir potential of heterogeneous rocks. In this section, spanning cluster filter was applied on the dataset of the five core plugs. Core plug 64 and 245 are mud dominated heterolithic rocks and contain thin sandstone layers that can be segmented. Meanwhile, in core plug 127,148 and 210, the main interests are the carbonate phase which is the dominant phase after sandstone. The MANGO filter eliminates non-connected sandstones and carbonate phases in the axial or z-direction. The connectivity in the z-direction is of interest as it is the axial direction of the cylindrical core plugs used. Core plug permeability was measured by injecting fluid through the axial direction of the core plug. We also identify connected and continuous sandstone from the 3D images by computing the amount of the sandstone phases that are connected through the z-direction by calculating the volume fraction of the sandstone phase before and after that application of the spanning cluster filter (Table 8.6). The differences represent the amount of non-connected sandstone phases in the axial direction.

Table 8.6: Sand phase volume fraction before and after the application of Spanning Cluster (SC) filter on core plug 64 and 245 dataset. We visualized the segmented sandstone layers core plug 64 and 245 using Drishti (refer to Section 8.1.1.6) In core plug 127, 148 and 210, carbonate phase is the highest occurrence phase after sandstone and are segmented and visualized using Drishti (refer to Section 8.3.4.

Core Plug	Original Sand Pay of core plug volume (%)	Sand Pay after SC (%)	Carbonate after SC (%)	Sand Pay Difference after SC (%)	% of sand that spans z-direction
64	17.54	**15.19**	N/A	-13.4	86.6
127	81.60	81.21	**16.00**	-0.48	99.5
148	83.14	83.11	**15.80**	-0.04	99.9
210	93.89	93.88	**11.00**	-0.01	99.9
245	19.85	**17.94**	N/A	-9.62	90.3

In summary, the volume fraction of the sandstone phase for core plug 64 and 245 are reduced by 9.6% and 13.4% respectively after the filter is applied as sand phases that do not span in the z-direction are removed as illustrated in Figure 8.20 and Figure 8.21 for core plug 64 and 245 respectively. On the other hand, most of the sandstone phase in core plug 127, 148 and 210 remain relatively unchanged as the sandstone in these core plugs is mostly connected. However, we noted that we might have underestimated the fraction of the sandstone in Table 8.6 as the consolidated sandstone phases may be disconnected because they were within the boundary of the core plug.

In core plug 64, sandstone makes up 15.19% of the core plug volume and 86.6% of the sandstone phase in core plug 64 spans the z-direction. These numbers are a good indication that the sandstone layers core plug 64 has good lateral connectivity. This connected sandstone in heterolithic rocks represent potentially additional net sand pay and hydrocarbon reserves heterolithic deposits. However, we should verify the reservoir potential of the additional net sand pay with additional reservoir properties. These additional petrophysical properties include irreducible water saturation, relative permeability and capillary pressure. These additional properties are essential for forecasting hydrocarbon reserves and production accurately.

Meanwhile, core plug 245, which has a sand volume fraction of 17.94% with 90% of its sand pay connected in the z-direction, which slightly higher than in core plug 64. The sand phases (red phase) in Figure 8.21 are connected in the z-direction. The images show that the sand phases in core plug 245 are thinner and narrower than the sand phases in core plug 64 and based on the very low core plug and mini plug permeability at 0.9 mD and 13 mD respectively. These low permeability numbers suggest that the sandstone in core plug 245 are poorly connected, possibly due to effects of bioturbation that reworked the sandstone layers. Discussion of the permeability results for core plug and mini plug 245 and their relationship to the connectivity of the thin sandstone layers were discussed in section 8.2.5. We show the spanning cluster images for core plug 148, 127 and 210 in section 8.2.1, 8.2.2. and 8.2.4 and their impact on core plug permeability are discussed.

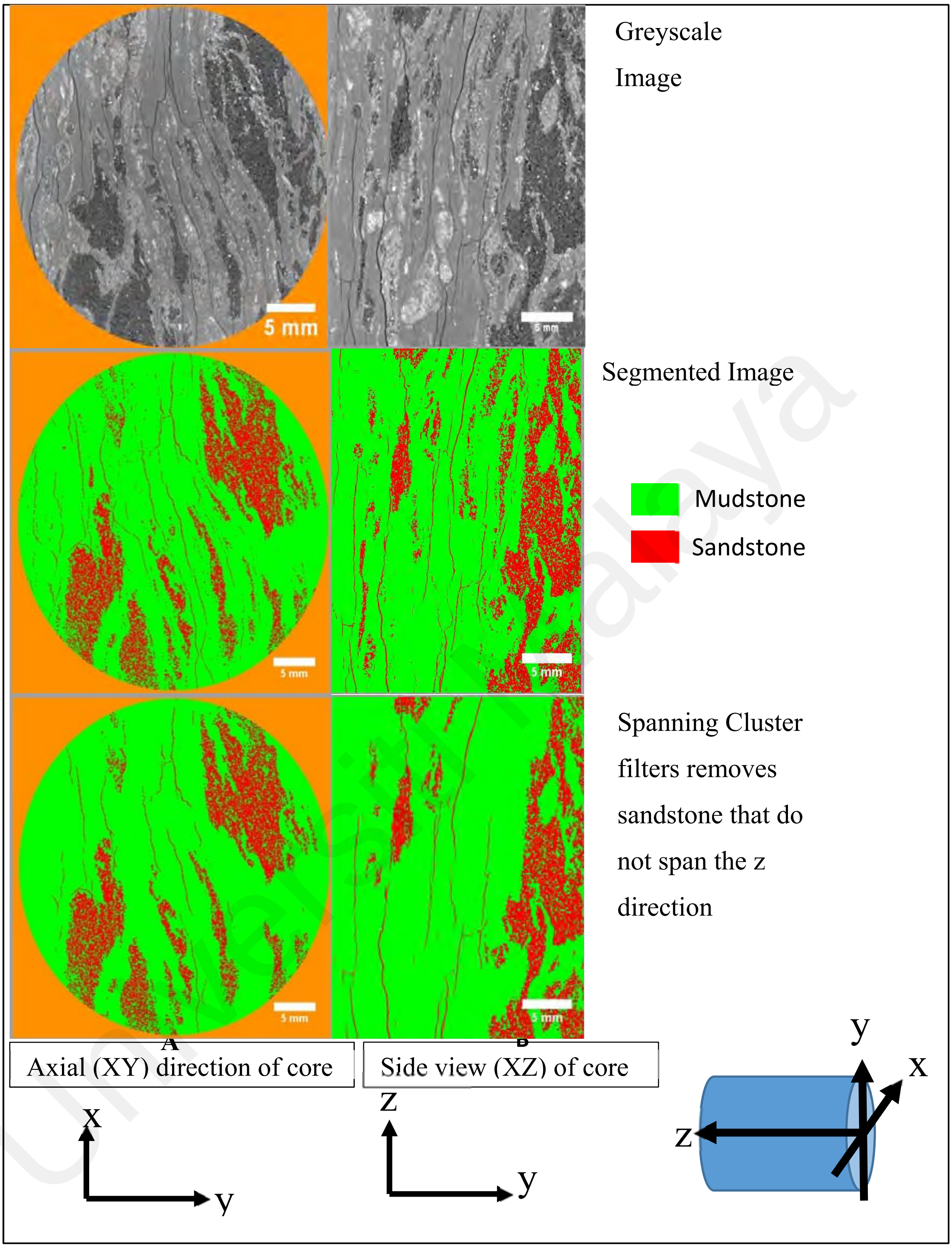

Figure 8.20: Original Image of core plug 64. B: Image of core plug 64 after application of Spanning Cluster filter. C: Diagram showing direction relative to core plug. The Spanning Cluster is applied in the z-direction. The black phase is sandstone, while the green phase is predominantly mudstone.

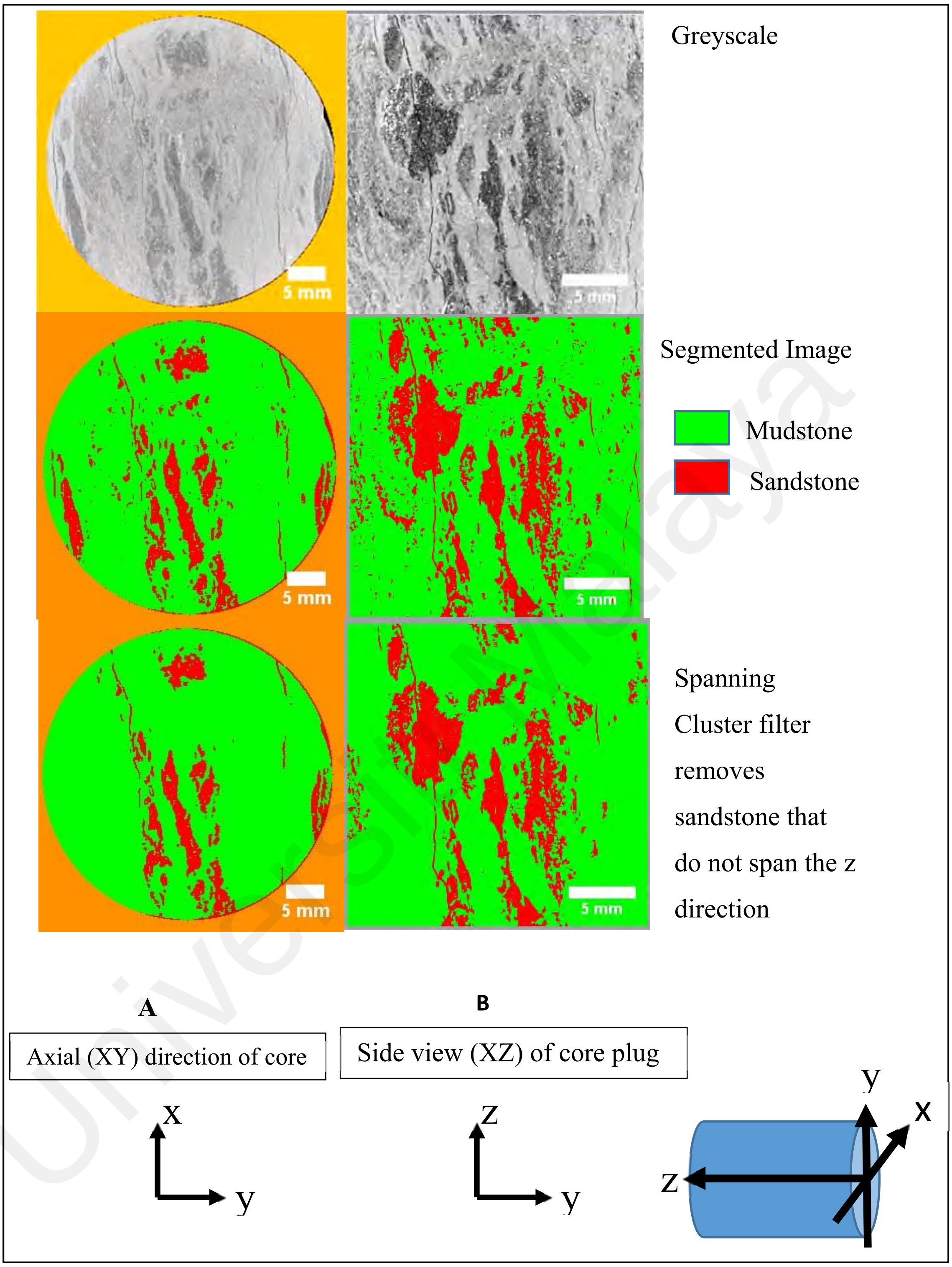

Figure 8.21: Original Image of core plug 245. B: Image of core plug 64 after application of Spanning Cluster filter. C: Diagram showing direction relative to core plug. The Spanning Cluster is applied in the z-direction. The black phase is sandstone, while the green phase is predominantly mudstone.

8.1.1.6 3D Volume Visualization

This thesis used the Drishti 3D Volume Visualization to visualize and explore volumetric 3D datasets for quantitative and qualitative analysis. Drishti was used to render the 3D volume datasets of some core plugs to render sand beddings or minerals such as carbonates which prevalent in the sandstone core plugs. The 3D visualizations allow the understanding of the connectivity of sandstone beddings in heterolithic core plugs and the impact of the geometry of carbonate minerals on the permeability in the sandstone core plugs.

3D volume view of the XMCT datasets provides information on the connectivity and continuity of the sandstone phases in the heterogeneous core plugs. The connectivity of the sandstone determines the ability of the sandstone phase to transmit fluid in the reservoir. The 2D images we show in the previous sections are useful but cannot provide information on the connectivity and continuity of the sandstone layers.

Before we rendered the 3D datasets of the core plugs, we initially segmented the datasets into the mudstone, carbonate and sandstone phases. Spanning cluster filter was applied to these datasets to eliminate unconnected phases in the axial direction

The imported the segmented datasets into Drishti Import and recompiled it in a format that can read by Drishti. In Drishti the mudstone or sandstone phases were made transparent, leaving only the sandstone phase or carbonate phase within the core plug visible. The rendered 3D image of phases of interest of each of the five core plugs is shown in Figure 8.22 to Figure 8.26.

We visualized the 3D datasets of the five core plugs using the Drishti software to characterize the geometry of the sandstone phase in core plug 64 and 245 and the carbonate minerals in core plug 127,148 and 210. The geometry of the two phases, such as the thickness, shape, connectivity and continuity are parameters that have varying impact on permeability at different scale and were discussed in section 8.3 for each sample.

8.1.1.6.1 Core Plug 64

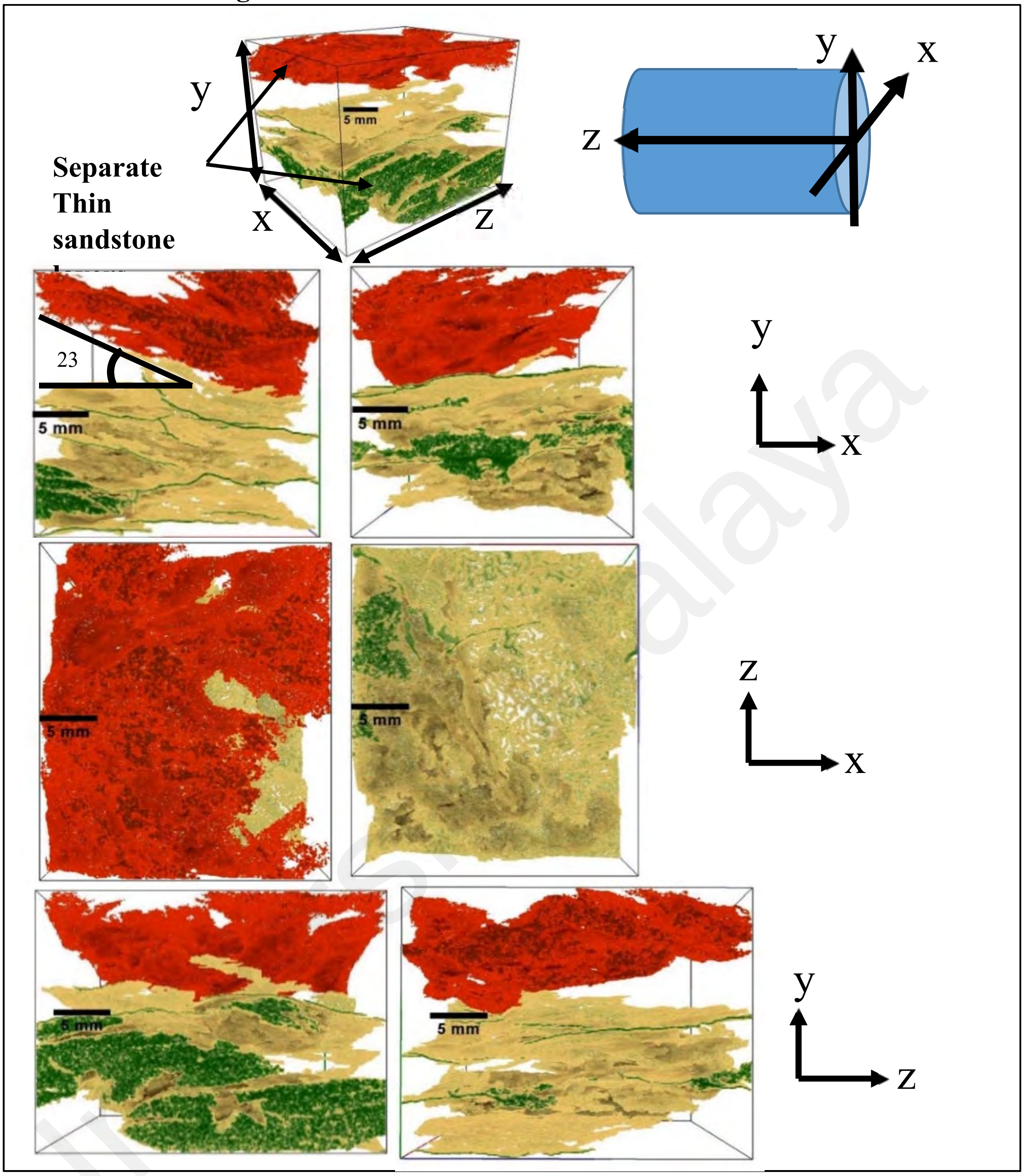

Figure 8.22: 3D volume images of core plug 64, showing two sandstone layers within the core plug. The red phase represents a very thin upper sand layer that is about 1 mm thick while the lower green phase layers consist of several 1 mm to 5 mm sandstone layers connected. The different colours of the sand layers indicate that they are not connected.

8.1.1.6.2 Core Plug 127

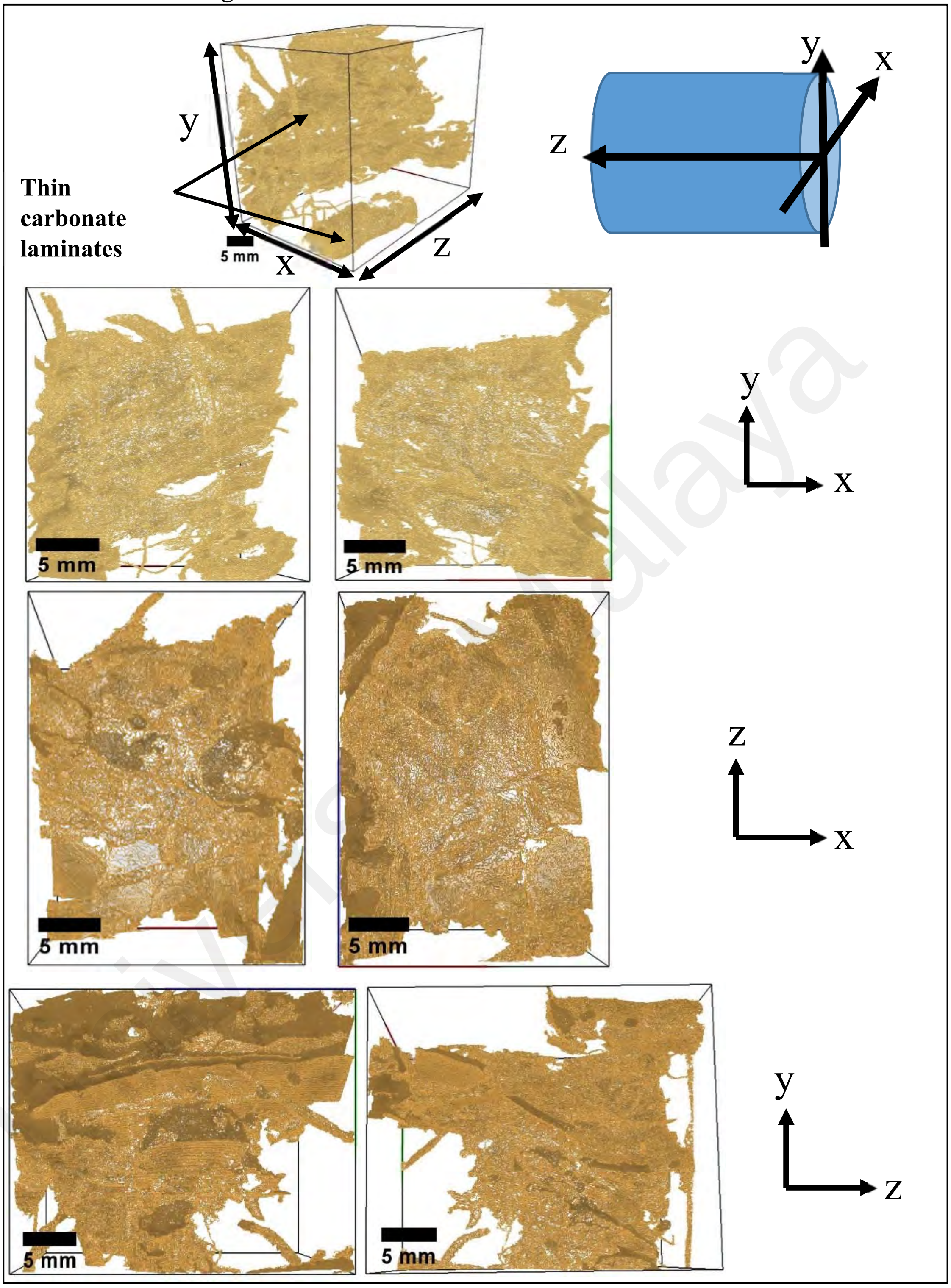

Figure 8.23: 3D volume images of core plug 127 showing the segmented carbonate laminates that could potentially block fluid flow.

8.1.1.6.3 Core Plug 148

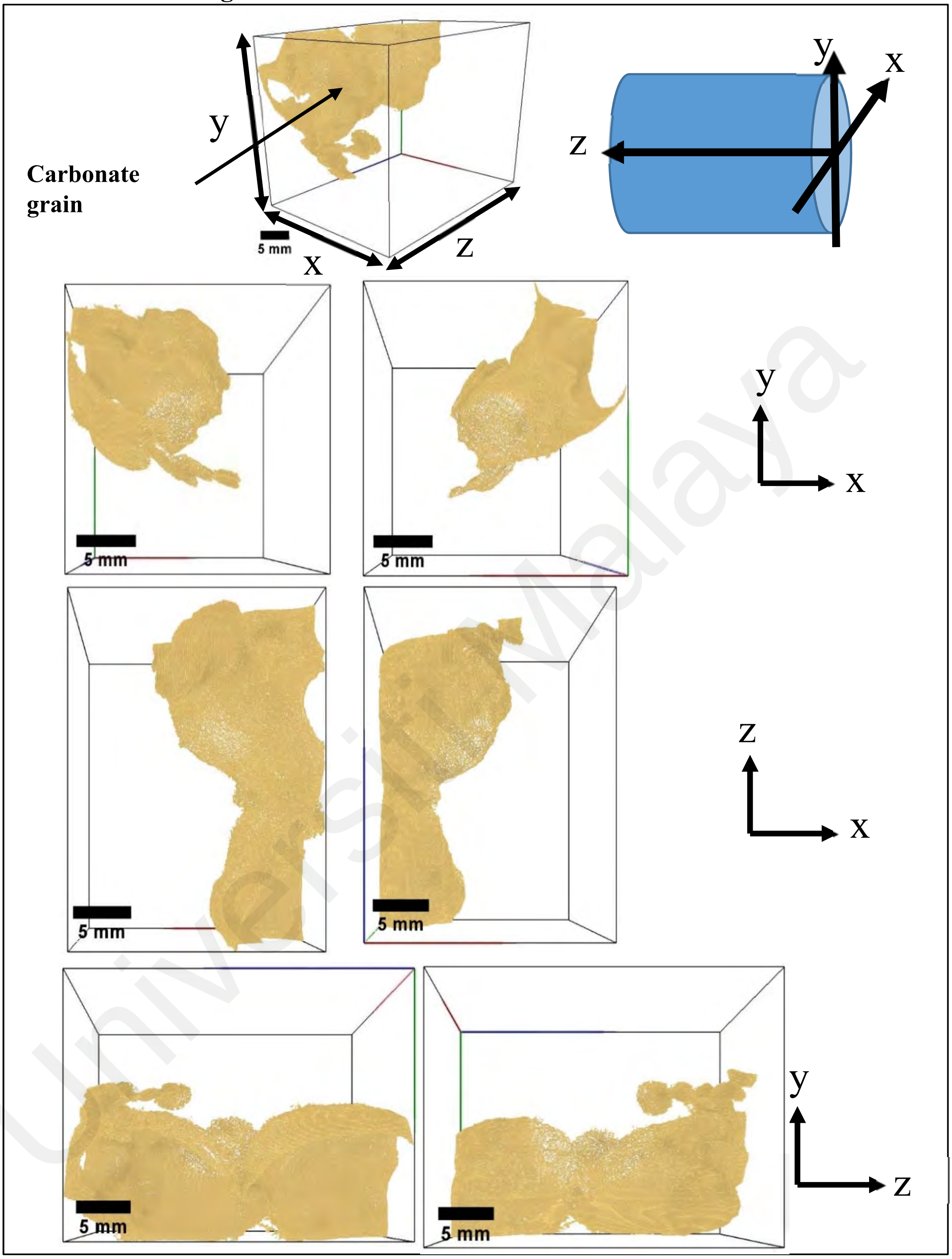

Figure 8.24: 3D volume images of core plug 148 that shows the segmented calcium carbonate that makes up 16% of the core plug volume. The calcium carbonate is a large grain that potentially blocks fluid flow that resulted in lower RCA measured permeability.

8.1.1.6.4 Core Plug 210

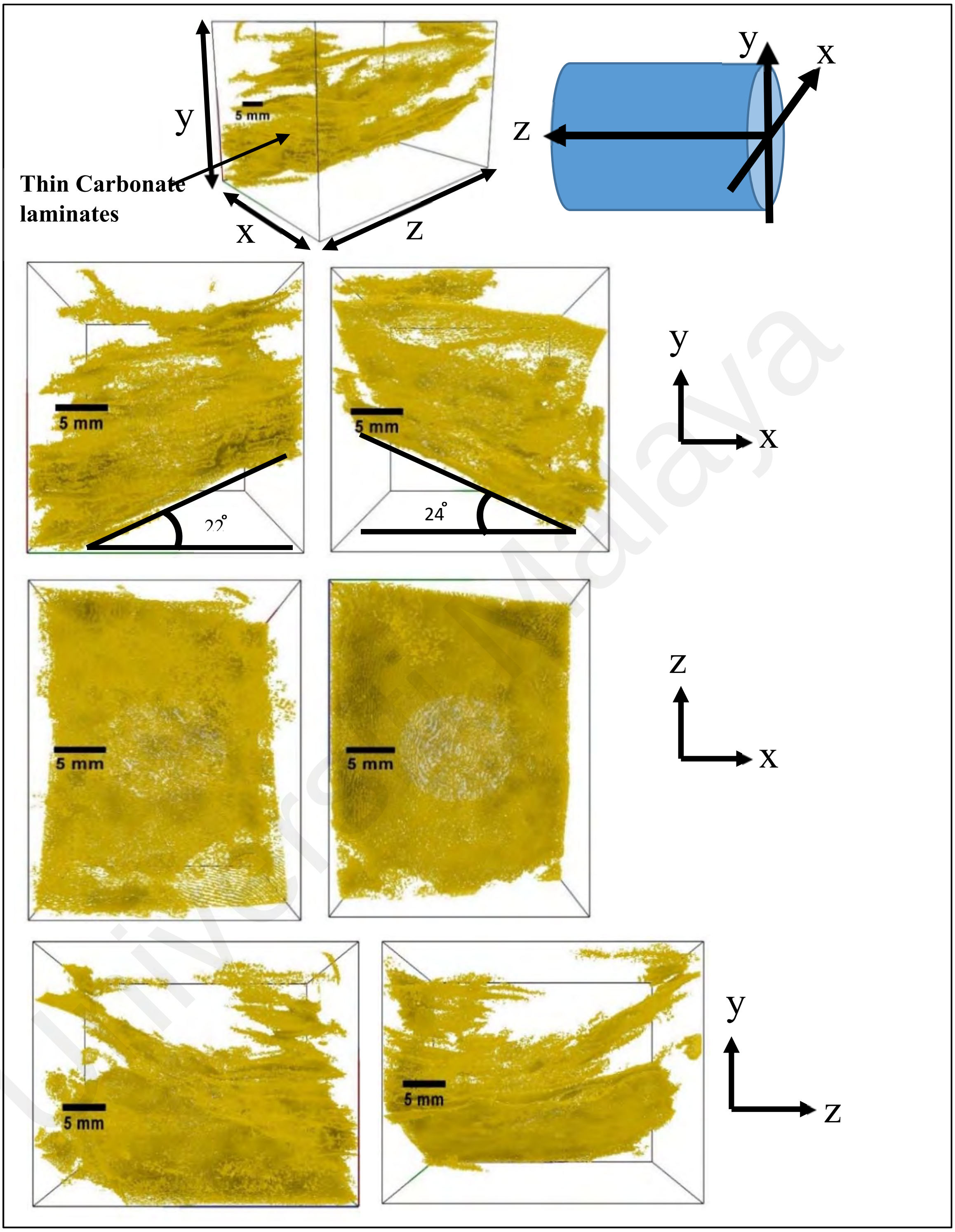

Figure 8.25: 3D volume images of Core Plug 210 showing thin carbonate laminates within the core plug.

8.1.1.6.5 Core Plug 245

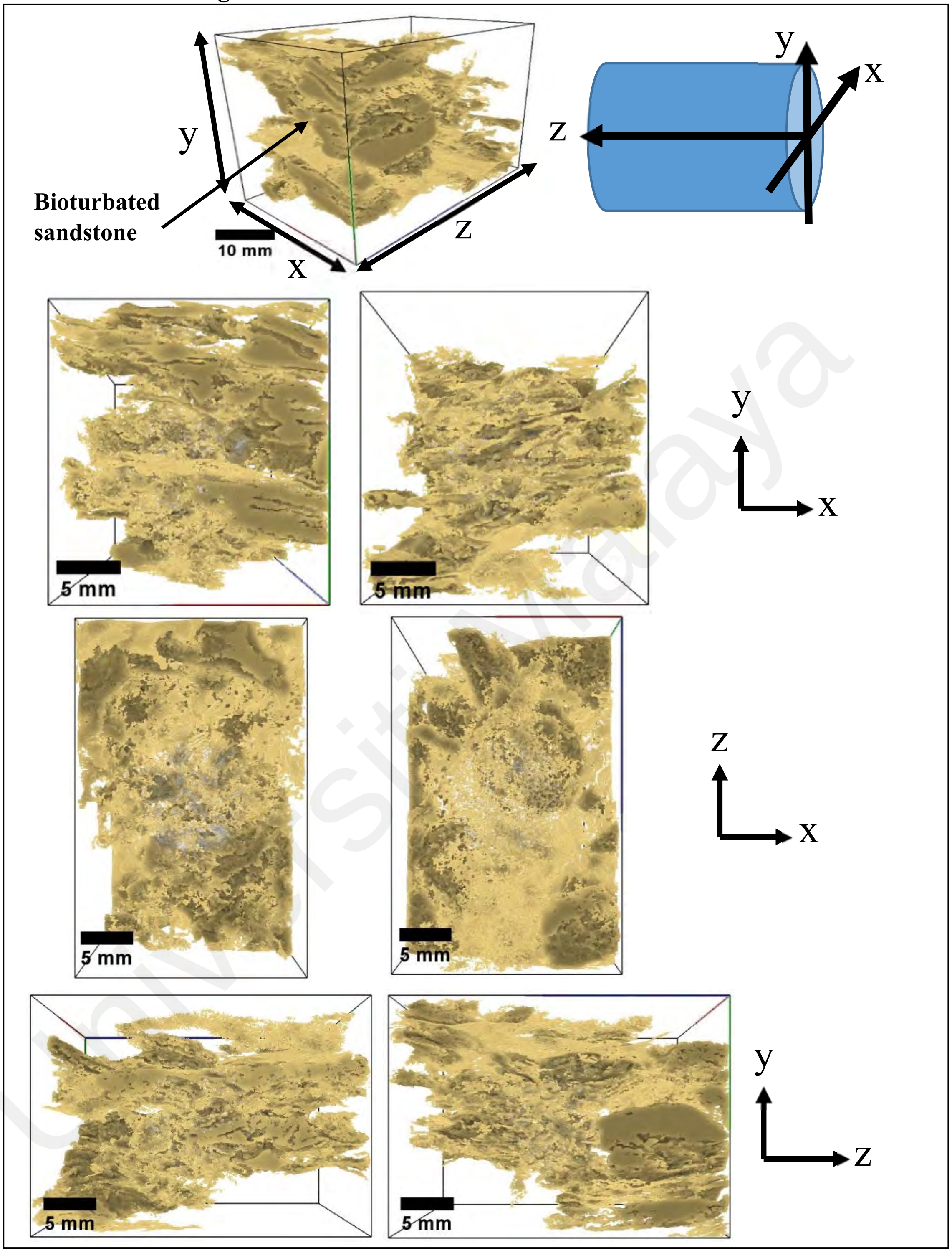

Figure 8.26: 3D Volume images of Core Plug 245, showing the sandstone phases. The bioturbated sandstone layers consist of very thin sheets that are poorly connected.

8.1.2 Computed Porosity and Permeability

The results in Table 8.7 show the computed porosity and permeability of each mini plug. The computed porosities in all the mini-plugs show some high degree of consistency with the core plug porosity measured using Routine Core Analysis which. This good correlation between computed and experimental results for porosity and other petrophysical properties has been demonstrated by previous studies where numerical measurements of flow properties and rock fabric and textures using DCA are comparable to experimental results on the same core material (Knackstedt et al., 2005; Knackstedt et al., 2007; Øren et al., 2006). We attributed this reliable porosity computation to the ability of XMCT imaging ability to resolve many of the flow limiting microstructures. However, there are issues or limitations in the calculated porosity, which is observed to be lower than the experimental results. Firstly, the segmentation process that separates the pores from the grains is subjective due to human error which may result in underestimated porosity. Secondly, XMCT imaging is still unable to completely resolve some of the micro-structures, especially in the nano-metre scale such as micropores. Therefore, we compared the computed permeability to the measured experimental results such as Routine Core Analysis and Special Core Analysis for validation. We discussed the RCA and DCA results of the five samples in section 8.2, Chapter 8.

Table 8.7: Phase volume fraction calculated after the segmentation process using the digital core analysis software, MANGO and MORPHY permeability results for 300 voxels^3 and 400 voxels^3 sub-volume sizes. The Routine Core Analysis represents the core plug while the DCA results represent the mini-plugs

Mini Plug	Routine Core Analysis		Phase Segmentation using DCA			
	Φ (%)	k (mD)	Pore (%)	Intermediate Phase (%)	300 voxels^3 (mD)	400 voxels^3 (mD)
64	18.9	35.98	17.8	2.9	894	945
127	28.0	633	25.4	3.09	1358	1384
148	27.0	394	26.7	3..67	2106	2102
210	28.0	287	25.2	4.84	251	239
245	15.7	0.9	15.0	7.%	64.7	13.6

8.1.3 NER Permeameter Measurements

Figure 8.27 to Figure 8.36 below shows the permeability map of the five core plugs, and Table 8.8 below compares the measured surface permeabilities of the core plug and the computed permeabilities of the mini plug. Each core plug consists of two permeability maps (A and B) representing one half of the core plug which we cut in two halves. The

The NER permeameter gas probe has a diameter of 4 mm and measures at an interval of 1mm which is similar to the length scale of the volume sizes of the mini plug datasets used by MORPHY (refer to section 8.2.3) to compute permeability. Hence, we used the permeameter results to validate the computed results. Also, the NER results provide permeability data of phases that are not included in the mini-plugs used this thesis. For example, the permeameter provided the permeability data for carbonate (below 100 mD) in core plug 148 because mini plug 148 does not sample any carbonate, and all the high computed permeabilities represent sandstone. The surface permeabilities provide a large amount of data that we used to determine if the permeabilities of the sandstone, mudstone and carbonate in different core plugs are statistically similar. We will discuss the comparison between the surface permeabilities and the computed permeabilities and their significance for each sample in section 8.2

Table 8.8: Comparison between computed permeabilities of the mini-plugs using digital core analysis (MORPHY and the measured surface permeabilities (NER permeability gas probe) of the core plugs. The compute computed permeabilities are of the 300 voxels3 sub-volumes.

Sample	**64**		**127**		**148**		**210**		**245**	
Methods	**DCA**	**NER**	**DCA**	**NER**	**DCA**	**NER**	**DCA**	**NER**	**DCA**	**NER**
Average (mD)	894.2	228.9	1357.9	1145.5	811.8	820.9	251.4	391.9	64.7	20.0
Max. (mD)	2300	725.6	2743.7	1994.9	1285.3	1730.8	536.4	685.6	640.8	107.0
Min. (mD)	2.4	7.5	54.9	86.7	168.8	106.8	31.2	117.3	0.1	1.3
Standard. Deviation (mD)	879.4	149.02	626.6	482.2	276.7	312.3	120.0	125.0	136.8	22.6

8.1.3.1 Core Plug 64

Core Plug 64, Side A

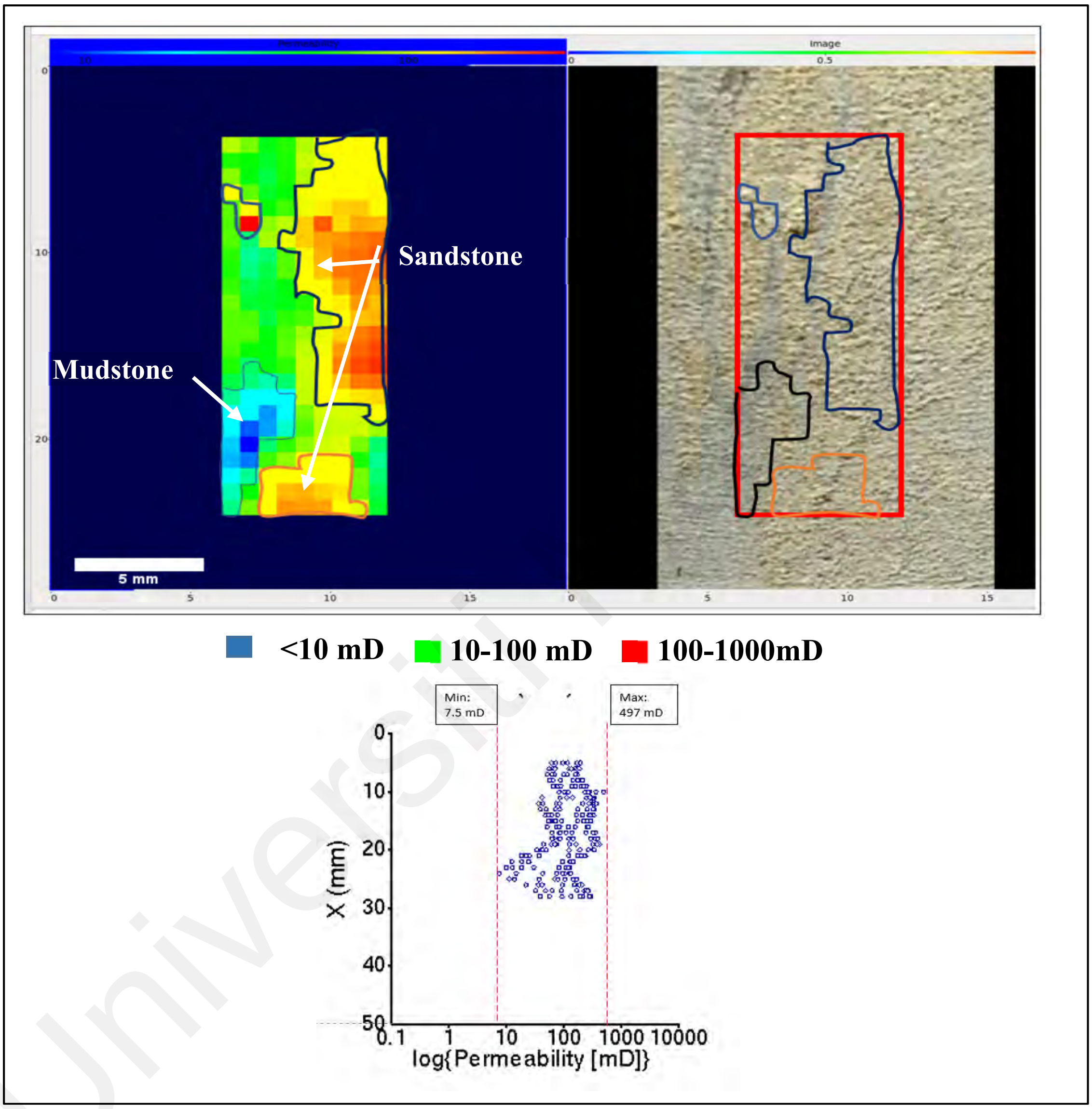

Figure 8.27: Permeability map of core plug 64, side A.

Core Plug 64, Side B

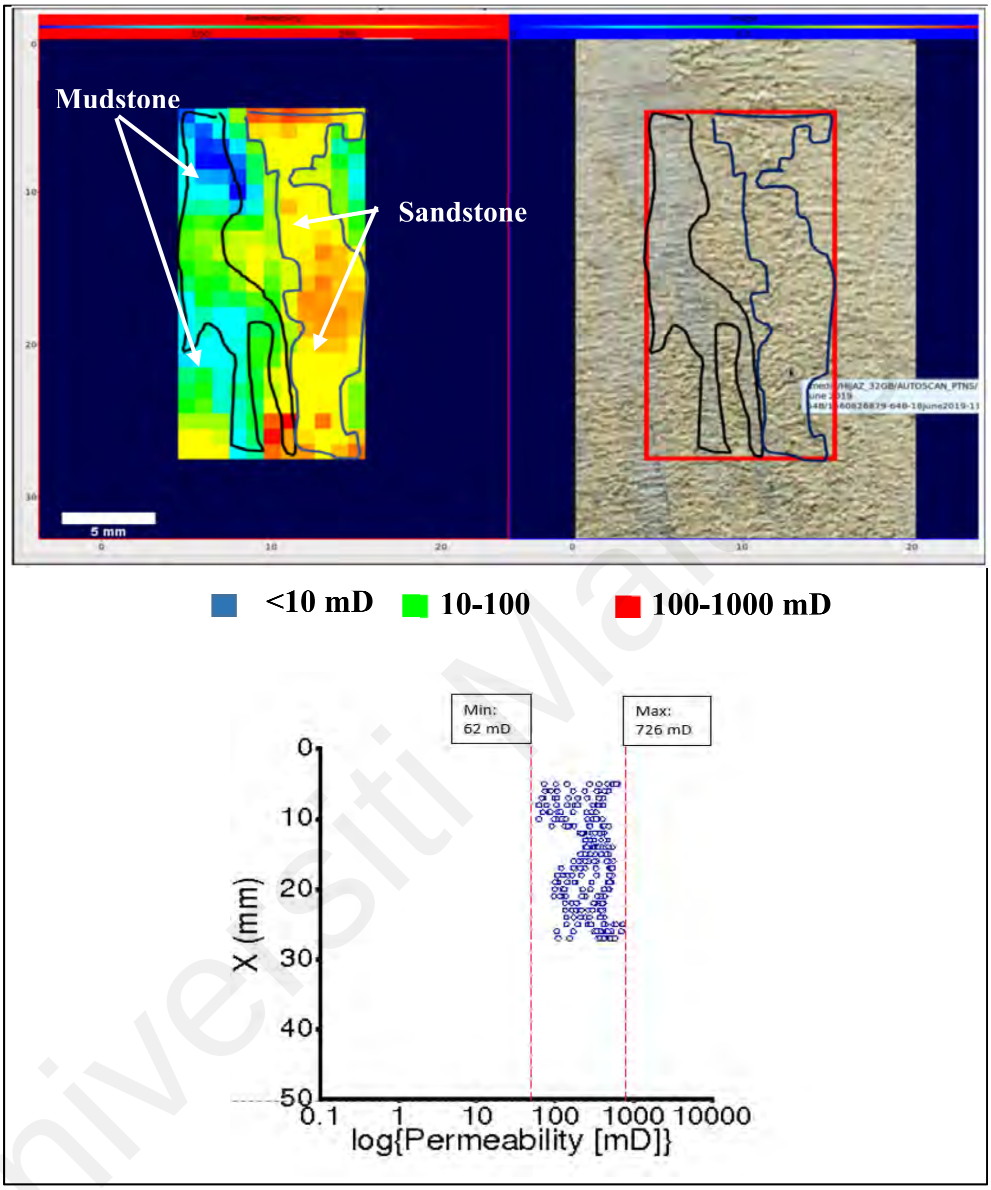

Figure 8.28: Permeability map of core plug 64, side B.

8.1.3.2 Core Plug 127

Core Plug 127, Side A

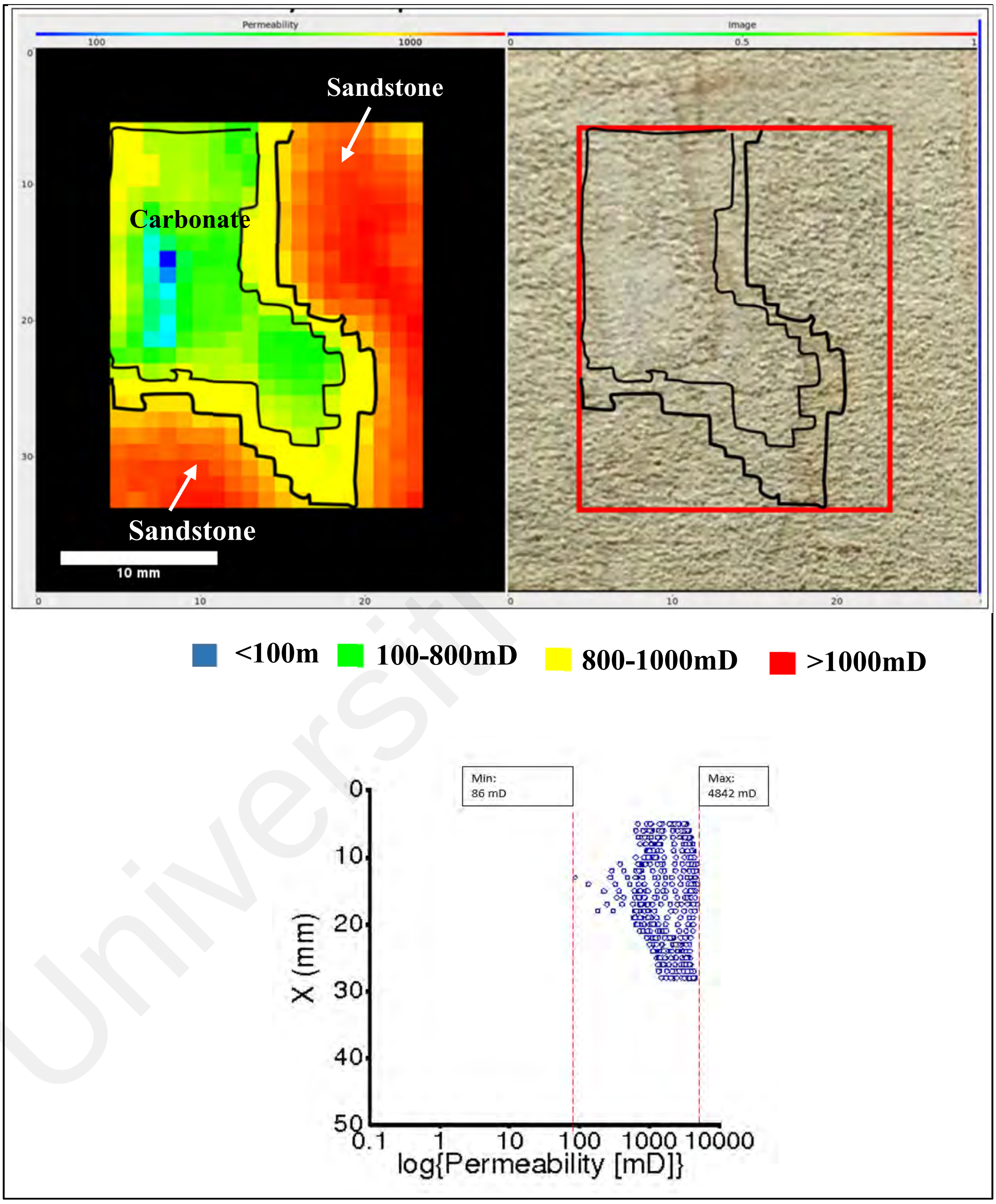

Figure 8.29: Permeability map of core plug 127, side A.

Core Plug 127, Side B

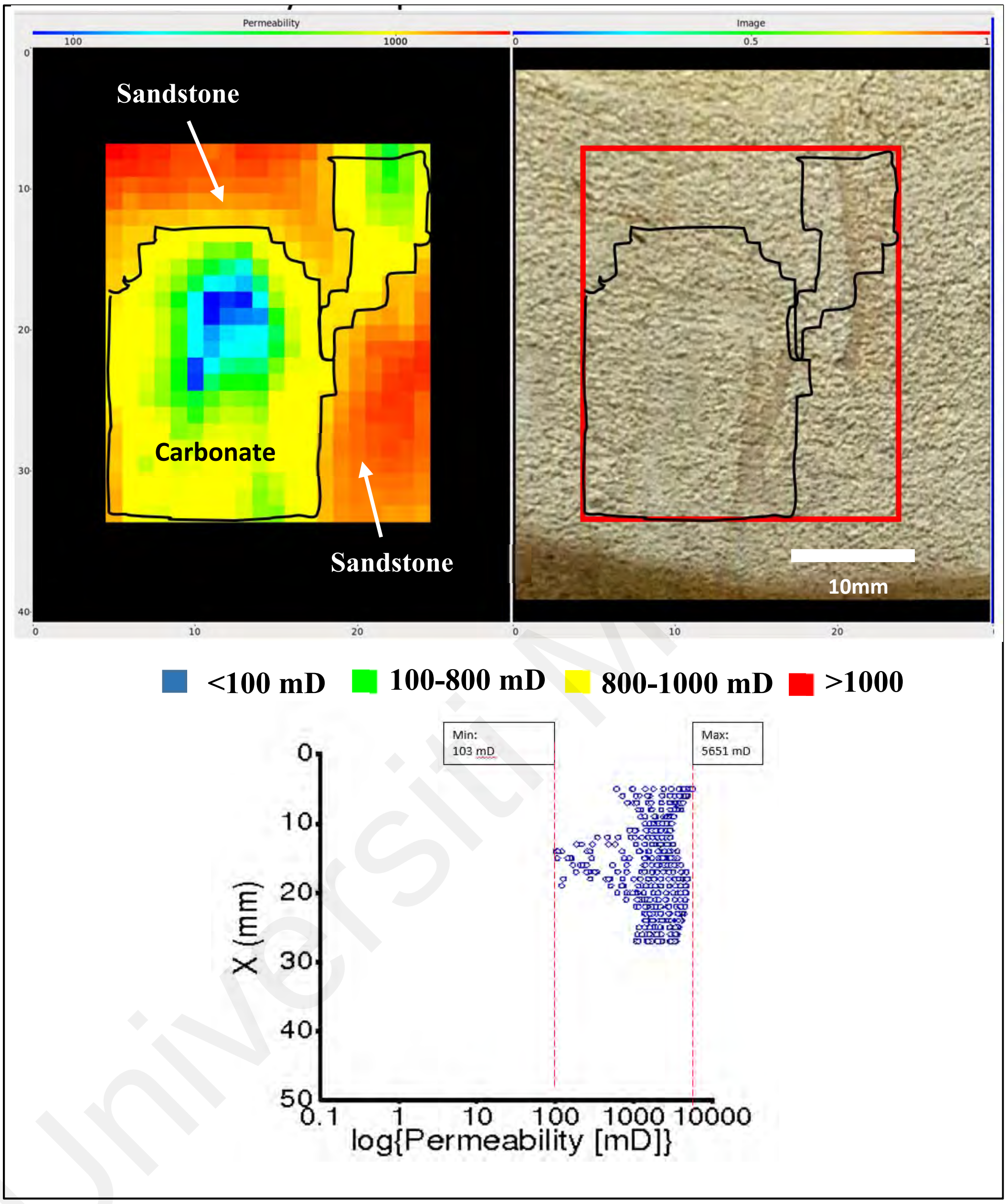

Figure 8.30: Permeability map of core plug 127, side B.

8.1.3.3 Core Plug 148

Core Plug 148, Side A

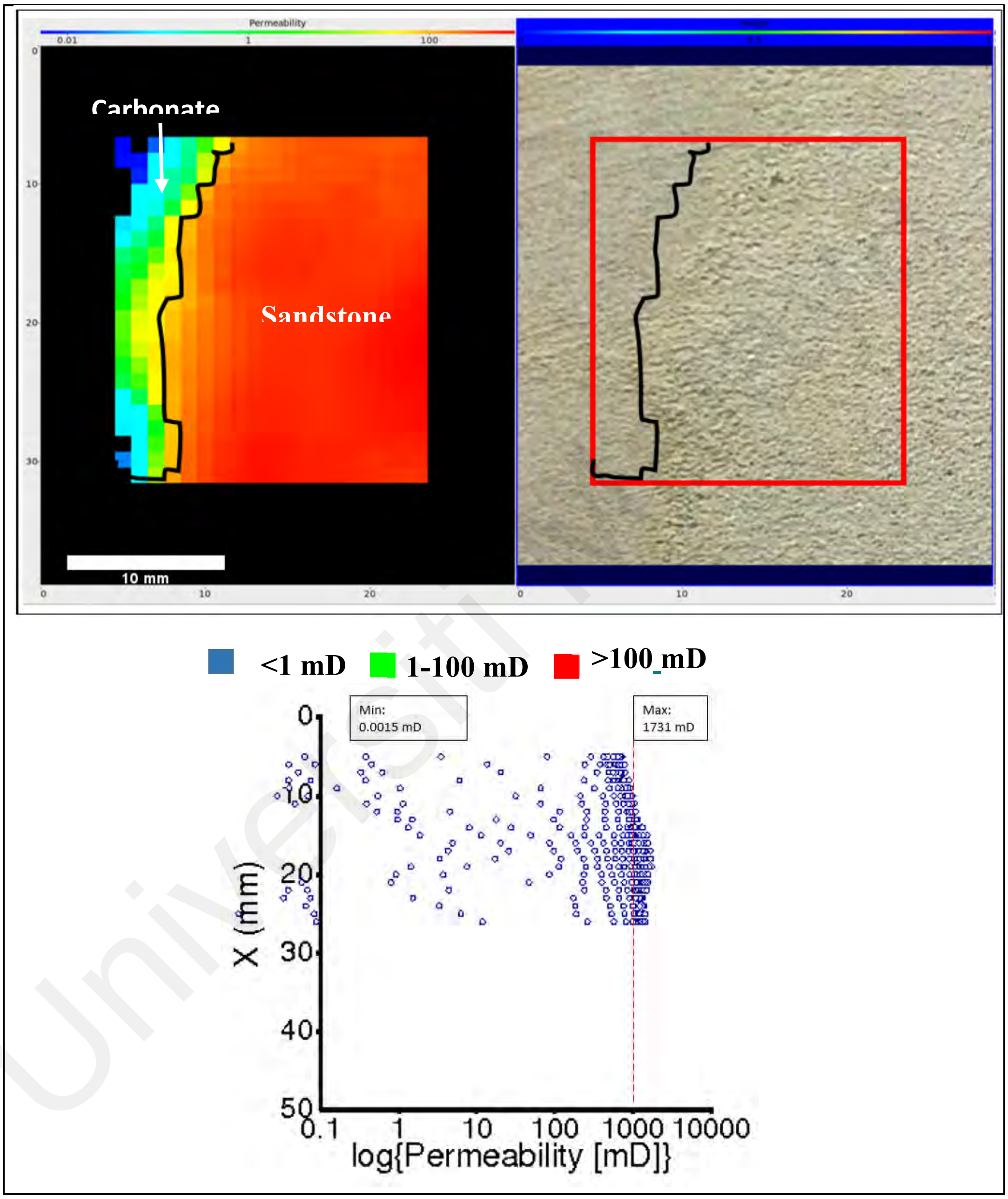

Figure 8.31: Permeability map of core plug 148, side A.

Core Plug 148, Side B

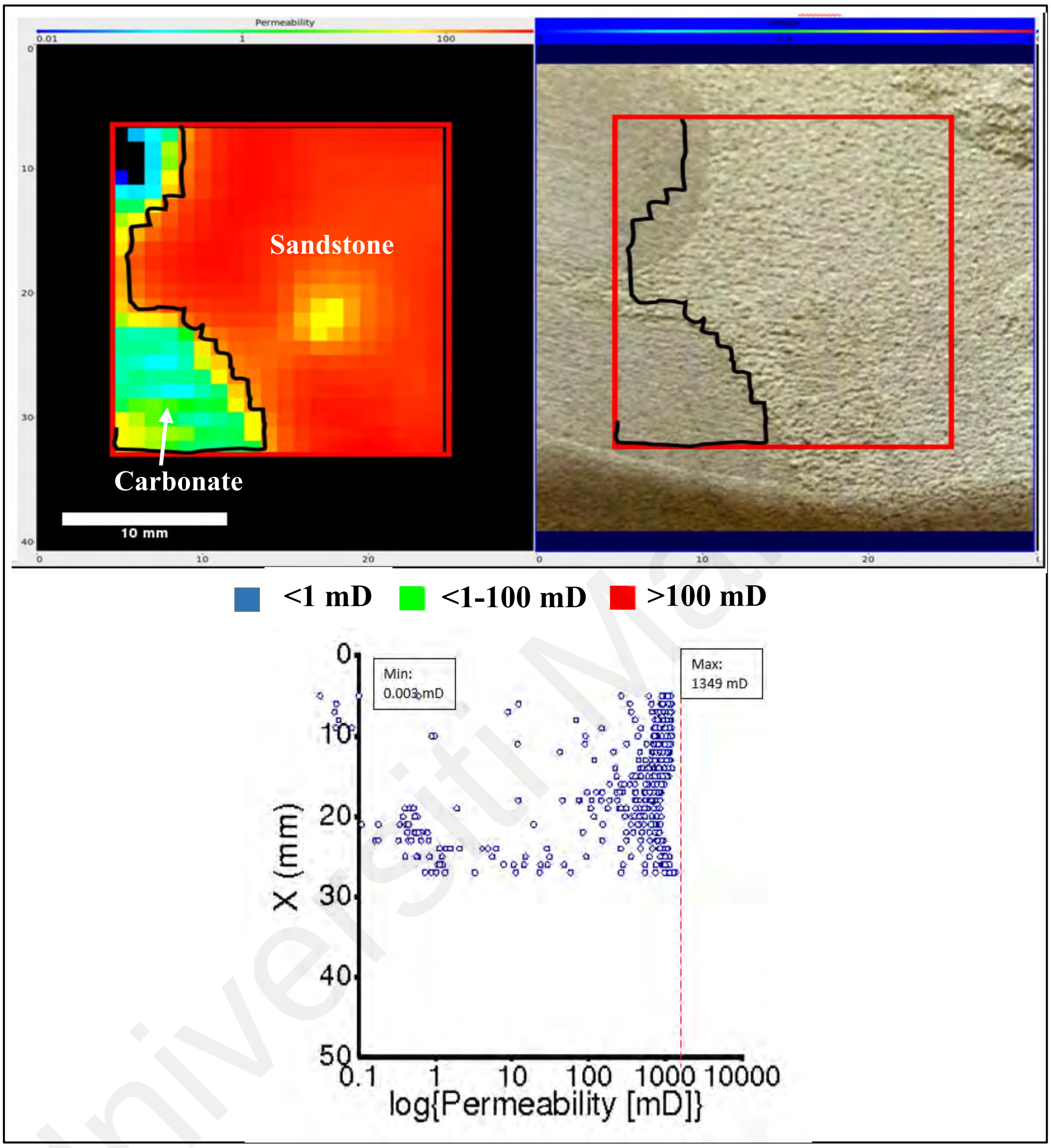

Figure 8.32: Permeability map of core plug 148, side B.

8.1.3.4 Core Plug 210

Core Plug 210, Side A

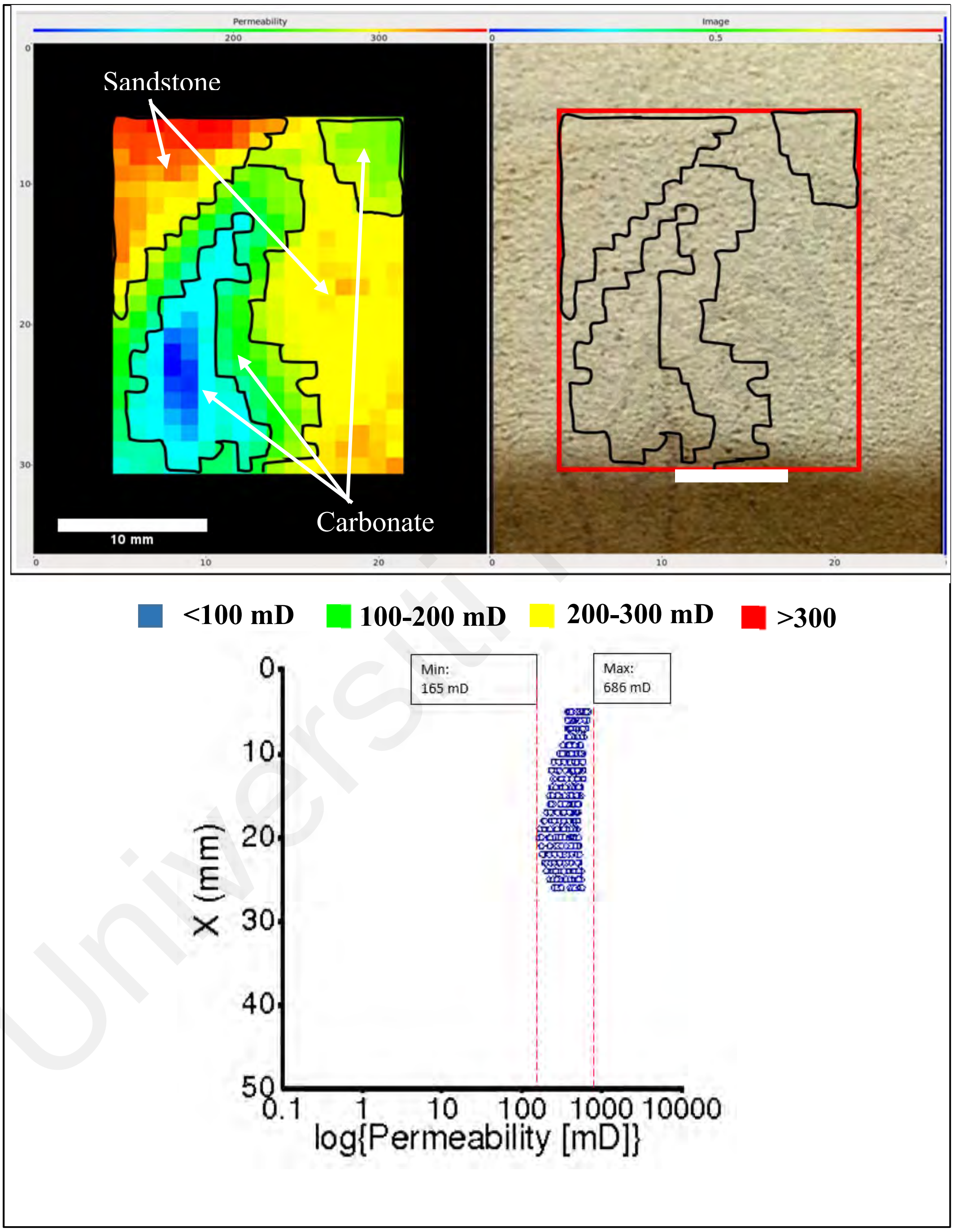

Figure 8.33: Permeability map of core plug 210, side A.

Core Plug 210, Side B

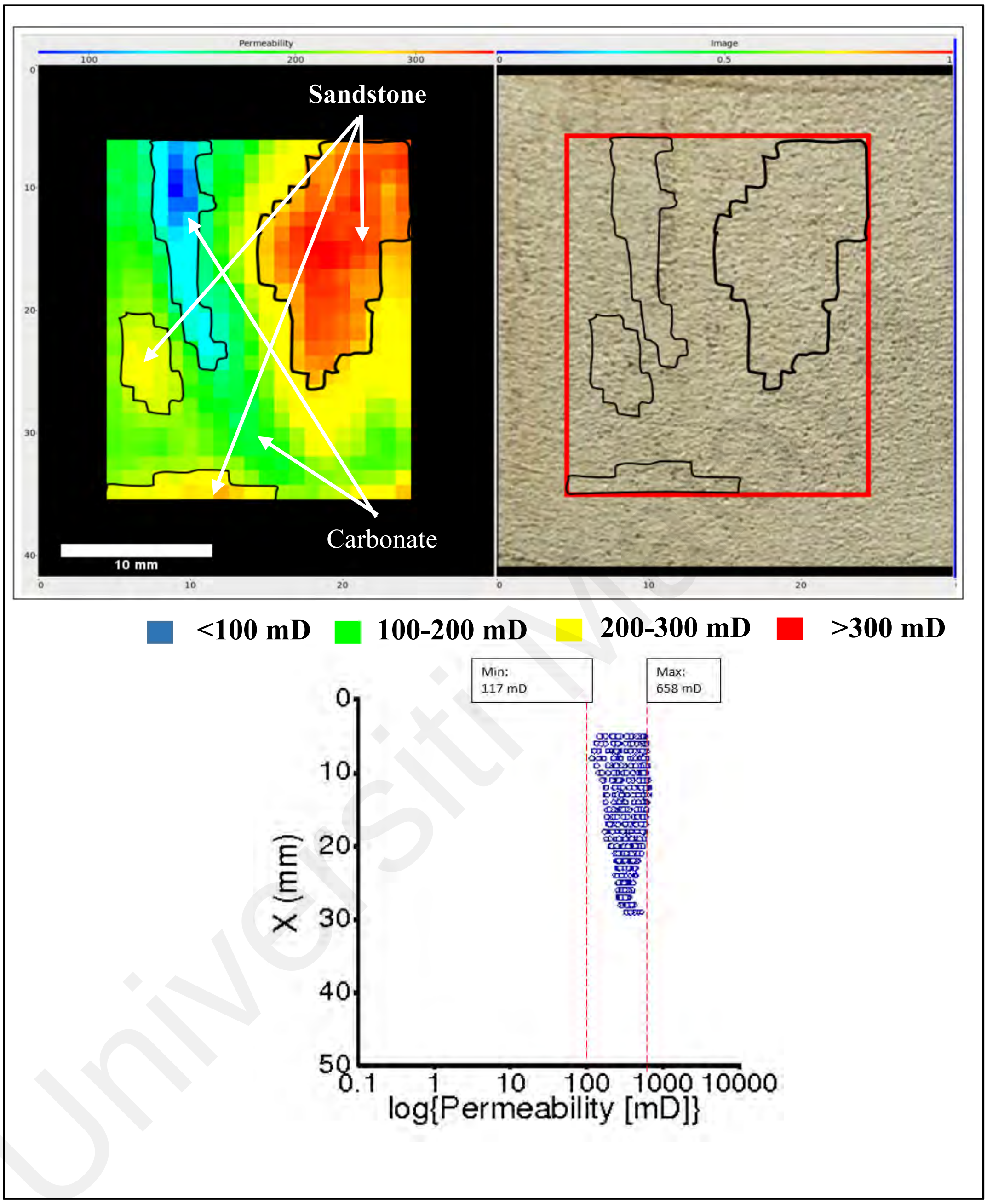

Figure 8.34: Permeability map of core plug 210, side B.

8.1.3.5 Core Plug 245

Core Plug 245, Side A

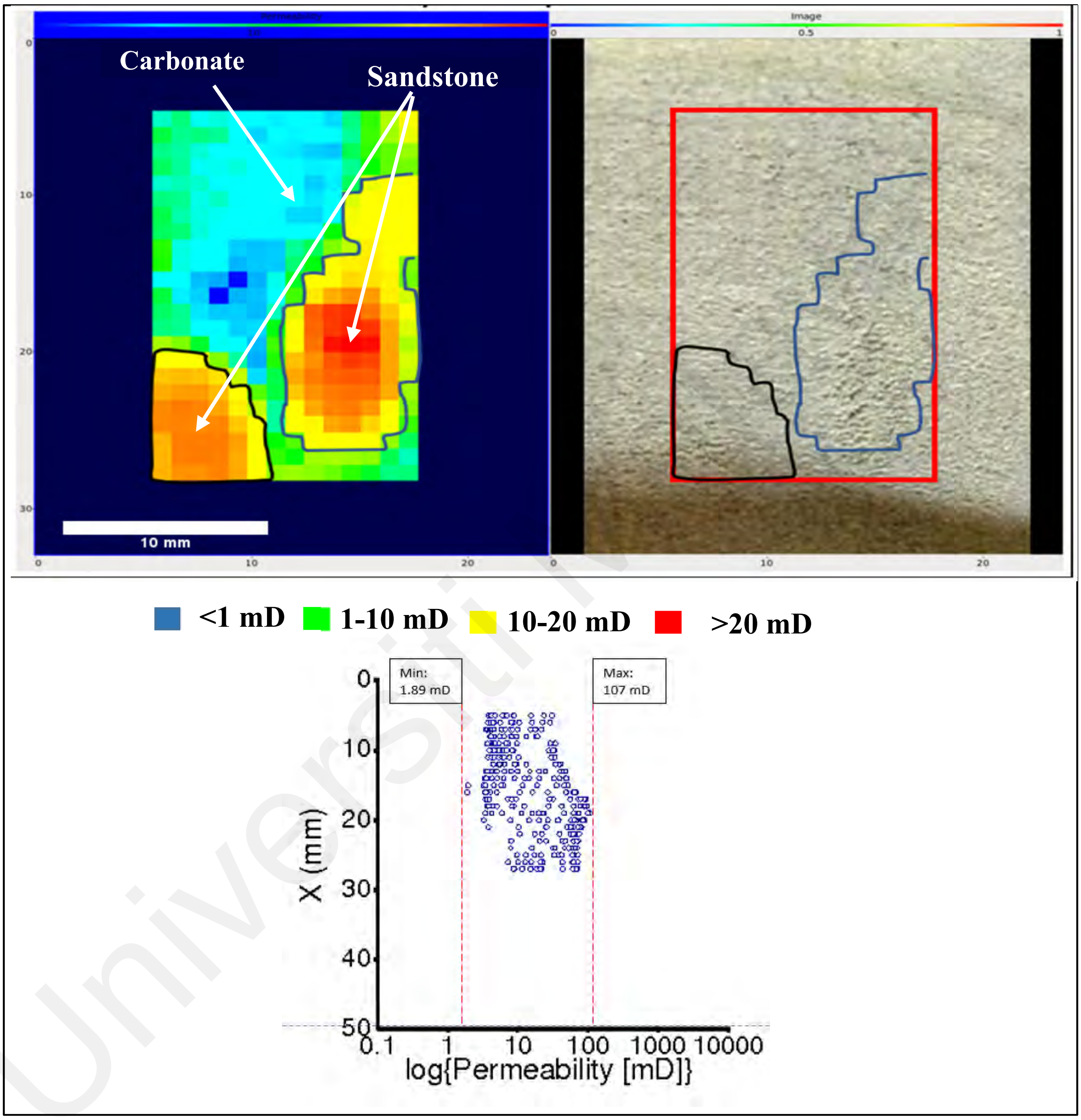

Figure 8.35: Permeability map of core plug 245, side A.

Core Plug 245, Side B

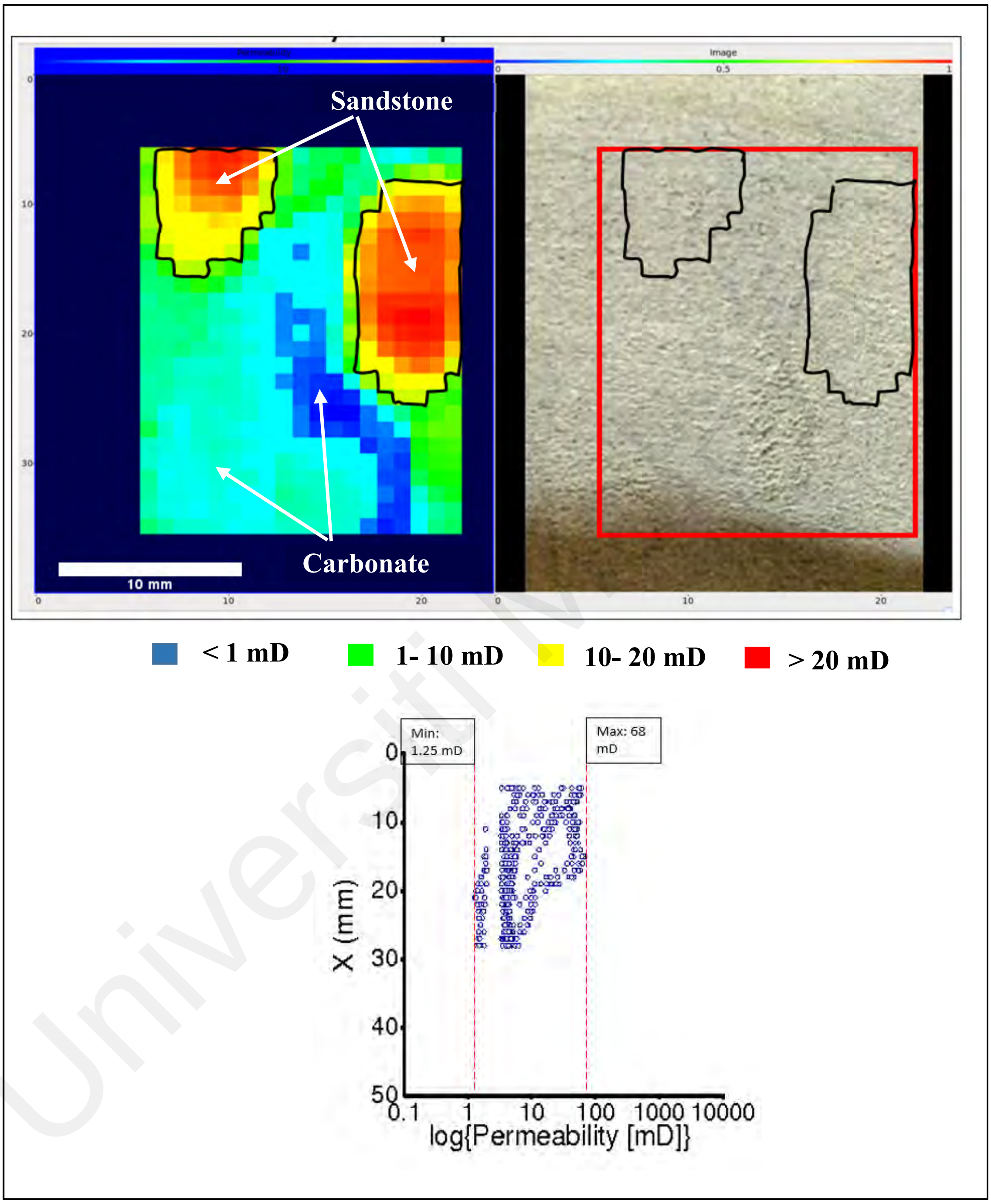

Figure 8.36: Permeability map of core plug 245, side B.

8.2 Summary and Discussion of Results by Sample

This section provides a detailed overview of the results of each of the five samples that used the XMCT imaging Analysis, Digital Core Analysis and NER permeameter methods. We present porosity and permeability results for each sample using these methods. Other results include 3D volume images of the core plugs and mini plugs rendered using the Drishti 3D visualization software, and NER generated permeability maps of the surfaces of the core plugs. Also, we discuss the porosity and permeability results at the mini plug and core plug scale for each sample and their correlation with the effects of heterogeneity observed in each sample at core plugs and mini plug scale. Also, we compare the computed permeability results to the permeameter and experimental core analysis results to discuss the similarities and differences between these results with regards to multi-scale heterogeneity and connectivity and continuity of the sandstone layers.

8.2.1 Sample 148: Laminated Sandstone

Core Plug 148 is essential as PETRONAS identified it as part of the main reservoir unit and primary reservoir rock. The core plug in Figure 8.37 consists mostly of fine-grain sandstone with a median grain diameter of 92 µm (section 8.1.1.2) with some carbonate mineral grains which are reported as common occurrences in sandstone in the reservoir.

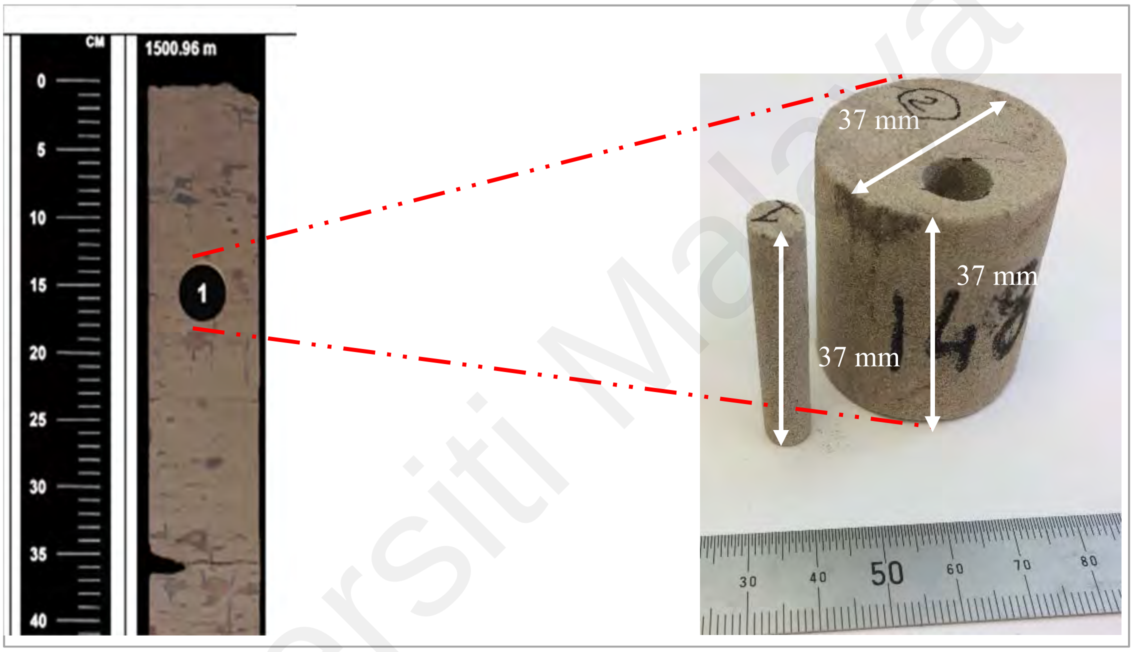

Figure 8.37: A view of core plug 148 and the core slab that indicates light-coloured sandstone.

8.2.1.1 Segmentation and 3D visualization of Sample 148

The XMCT image of the core plug in Figure 8.38 has sufficient resolution to distinguish sandstone from the mudstone and the carbonate minerals. Core plug 148 mainly consists of sandstone and carbonate mineral, as shown in Figures 8.39 and 8.40. The carbonate phase has a higher attenuation to x-ray than sandstone and appears brighter in the greyscale images. Based on the segmented dataset of core plug 148, we viewed the geometry such as the shape, thickness and connectivity of the calcium within the core plug using the Drishti 3D volume visualization software shown in Figures 8.41.

In Figure 8.43, we segmented the high-resolution images of mini plug 148 into pore, grains and intermediate phase. We could not segment the intermediate phases, which are generally clay phases into either grains or pores. The calculated porosity at 26.7% is very similar to the measured core plug porosity at 28%.

Figure 8.41 shows that carbonate phase occupies 15.8% of the core plug volume and acts as a low permeability barrier that reduced the fluid transmissibility and permeability in the core plug.

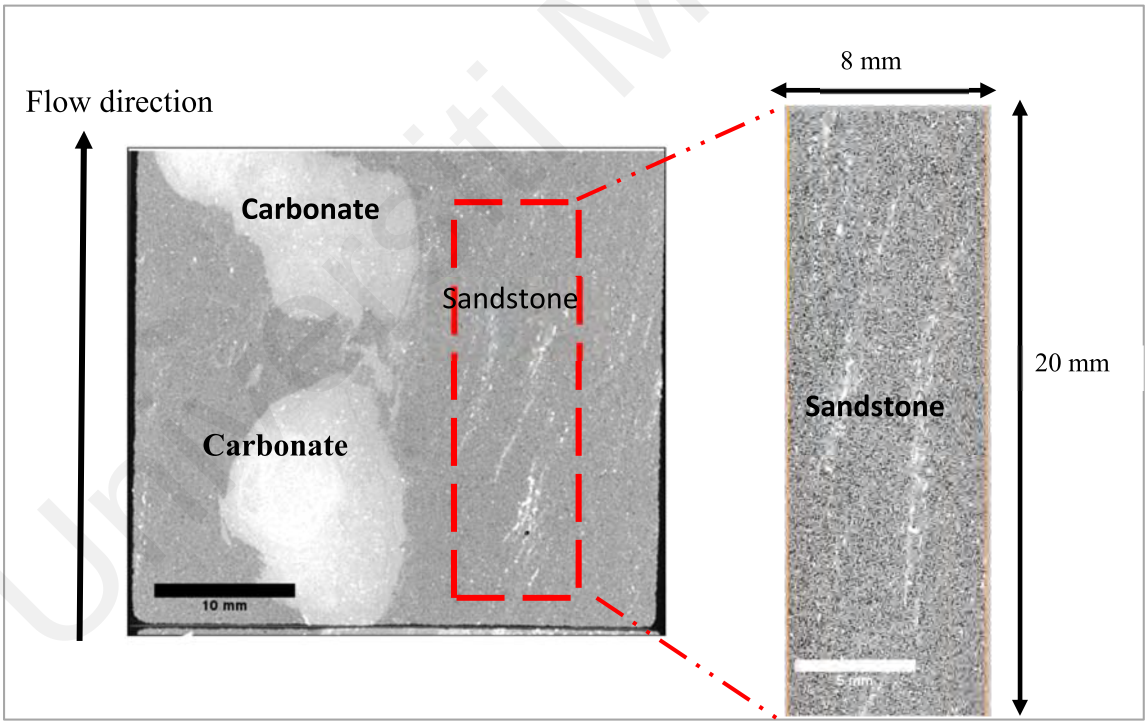

Figure 8.38: Left: Low resolution (16.3 microns/voxel) and Right: High Resolution (3.74 microns/voxel) tomograms of core plug and mini plug 148, respectively. The bright areas represent carbonate minerals. We also indicate the direction of fluid flow through the core plug and mini plug.

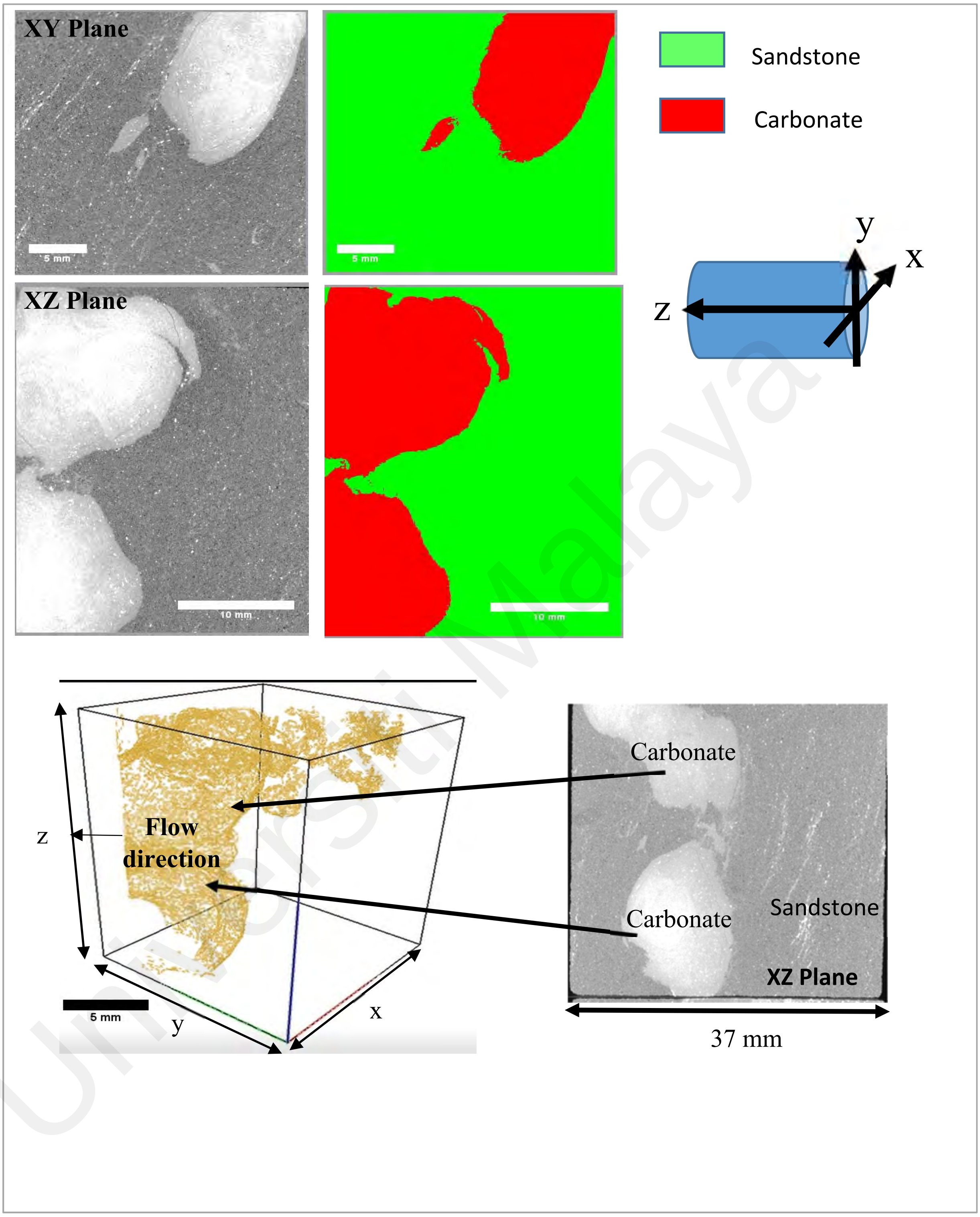

Figure 8.39: Top and Middle Images are greyscaled and segmented images of core plug 148. The left bottom image is a rendered 3D volume of core plug 148 showing the carbonate phase tagged in yellow. The segmented carbonate in core plug 148 occupies 15.8% of its volume.

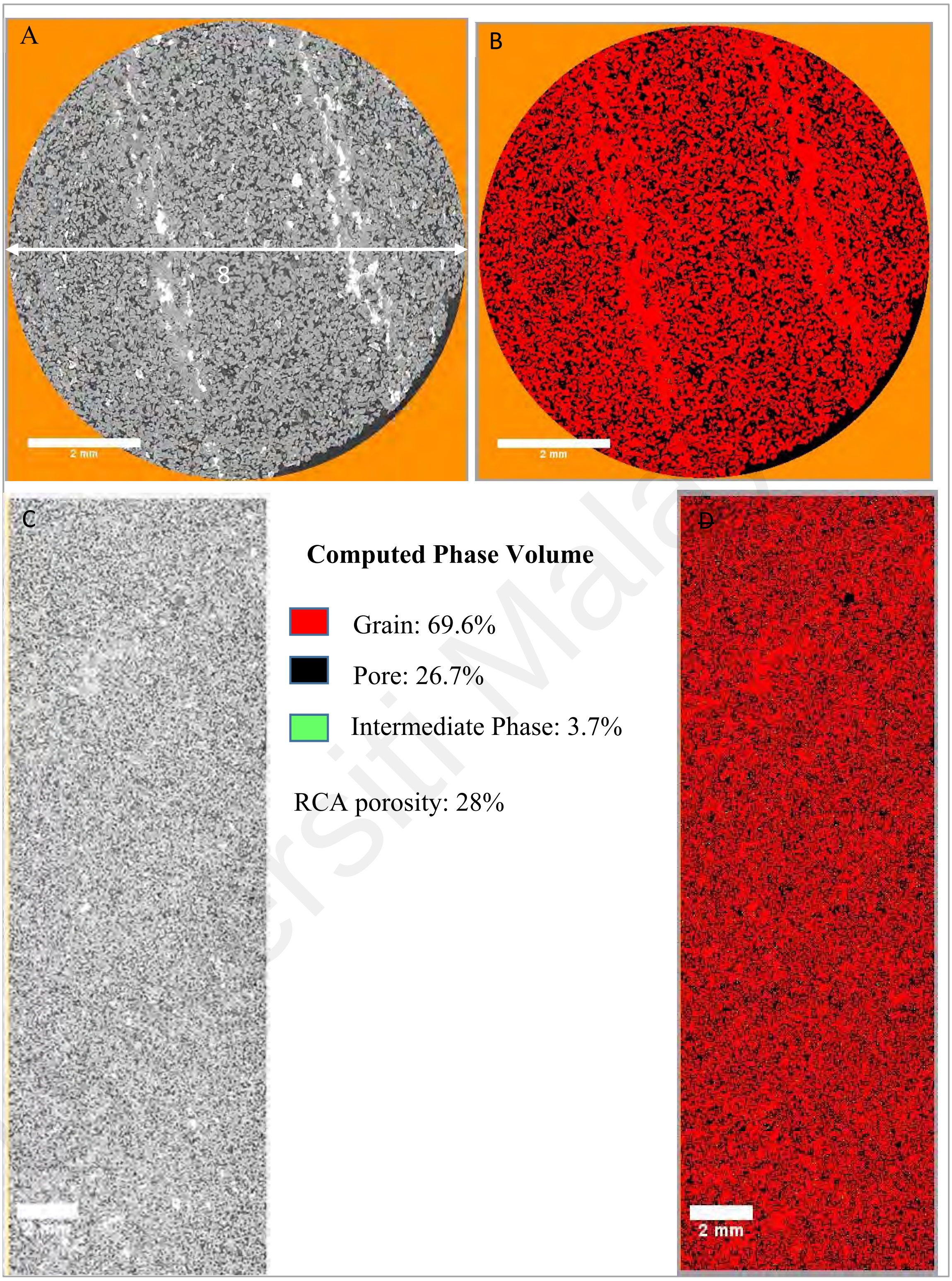

Figure 8.40: Segmented Images of Mini plug 148. A and C: Original unprocessed Greyscale tomogram, B and D: Segmented tomogram with three-segmented phases (red, green and black). The green intermediate phase is not visible due to their trace amounts in mini plug 148.

8.2.1.2 Discussion of Permeability Results for Sample 148

Table 8.9 shows there a substantial similarity between the computed porosity of mini plug 148 and the experimental porosity of the core plug 148 at 26.7% and 27% respectively. This similarity indicates that the computed porosity is reliable as the high resolution captured many of the flow limiting microstructures. We attributed the lower values in the computed porosity to several factors such as overlooked microporosity due to the segmented phases that are very subjective. The experimental porosity of core plug 148 at 27% validated the computed porosity of mini plug 148, which is 26.7%.

The permeability results in Table 8.9 also shows that the computed permeabilities at 811 mD (300 voxels^3) and 790 mD (400 voxels^3) of mini plug 148 are at least twice higher than the experimental core plug 148 permeability at 395 mD. Figure 8.41 shows that the permeabilities of the 300 voxels^3 and 400 voxels^3 sub-volume sizes are similar as shown. This excellent match between the two-volume sizes suggests that the sandstone in mini plug 148 is relatively homogeneous at these two sub-volume sizes. Due to the relative homogeneity and functional connectivity of the sandstone in mini plug 148 which do not contain any mudstone layers or carbonate laminates that can restrict fluid flow, the computed permeability of mini plug 148 is higher than the RCA result of core plug 148. The RCA measured permeability of core plug 148 is lower than the mini plug due to the flow restricting effects of the large carbonate grain shown previously in Figure 8.41 that makes up 15.8% of the core plug volume.

The NER permeameter's probe has a diameter at 4mm which is relatively similar to side lengths of the sub-volumes of mini plug 148 at 1.12 mm (300 voxels^3) and 1.50 mm (400 voxels^3) used by MORPHY to compute permeability as shown in Table 8.14. Due to the similar millimetre resolution between the two methods, we used the NER results to validate the computed results.

8.2.1.3 Comparison between MORPHY computed permeability and Gas probe measured permeability

In Table 8.11, we show that the average computed permeabilities at 812 mD (300 voxels^3) and 791 mD (400 voxels^3) are comparable to the permeameter measured surface permeability at 820 mD. We attributed this similarity to the millimetre resolution of the NER permeameter and the millimetre length scales of the sub-volumes of the mini-plugs (Table 8.10) used by MORPHY to compute permeability. Also, the average surface permeabilities in Table 8.9 represent the sandstone which is the same sandstone dominant in mini plug 148, as indicated previously in Figure 8.40. Therefore, the NER permeameter results of the sandstone of core plug 148 validated the computed permeabilities of mini plug 148. As a result, the histogram in Figure 8.42 shows that the MORPHY computed permeabilities of mini plug 148 sub-volumes and permeameter measured surface permeabilities of core plug 148 matches very well. Also, the histogram shows that both datasets have similar range and frequencies which validates the computed results.

Table 8.9: Permeability results from MORPHY calculation, Experimental Core Analysis Gas Probe measurements for Sample 148 MORPHY results represent the 8 mm diameter mini-plug while the Experimental Core Analysis and NER permeameter measurements represent the 37mm diameter core plug 148.

Method	**MORPHY (Mini Plug)**		**Experimental Core Analysis (Core Plug)**			**NER (Core Plug)**
Details	**300 voxels^3**	**400 voxels^3**	**Klinkenberg Horizontal**	**Air Horizontal**	**Routine Core Analysis**	**Gas probe**
Average	811.8 mD	790.7 mD	414.7 mD	420.3 mD	395 mD	820.9 mD
Maximum	1285.3 mD	1163.3 mD	474.0 mD	480.0 mD	N/A	1730.8 mD
Minimum	168.8 mD	259.0 mD	332.0 mD	337.0 mD	N/A	106.8 mD
Standard Deviation	276.7 mD	258.0 mD	53.7 mD	54.2 mD	N/A	312.3 mD

Table 8.10: Comparison between the two sub-volumes sizes used in MORPHY to calculate the permeability in mini plug 148.

Edge Length in voxels	**Resolution in voxel per mm**	**Side Length in mm**	**Cubic Volume in mm^3**
300	0.00374	1.122	1.41
400	0.00374	1.496	3.35

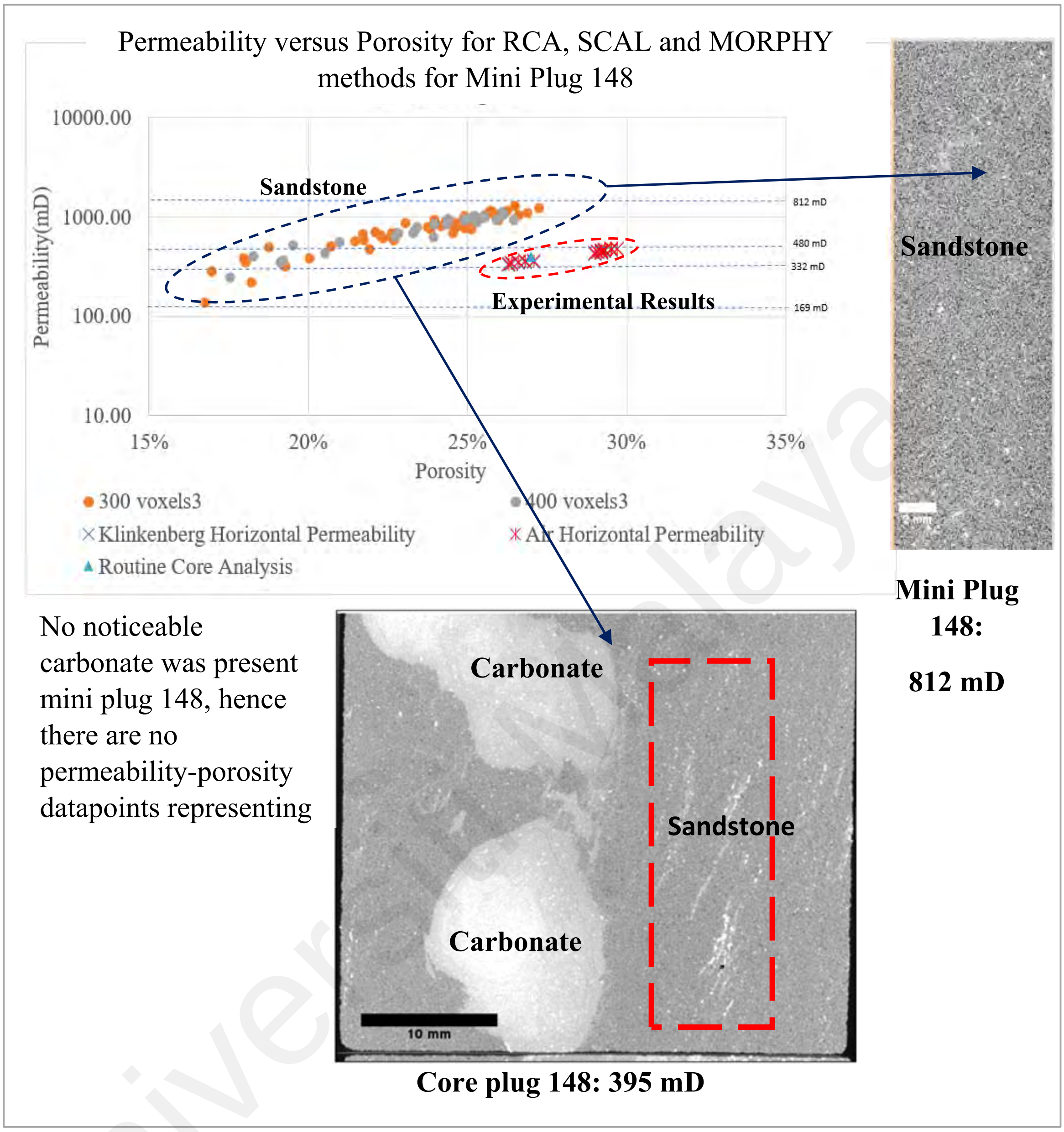

Figure 8.41: Sample 148:Permeability versus Porosity graph of Routine Core (RCA), Special Core Analysis (SCAL) and MORPHY (for 300 voxels and 400 voxels sub-volumes). The Klinkenberg horizontal permeability and horizontal air permeability are the experimental Special Core Analysis results.

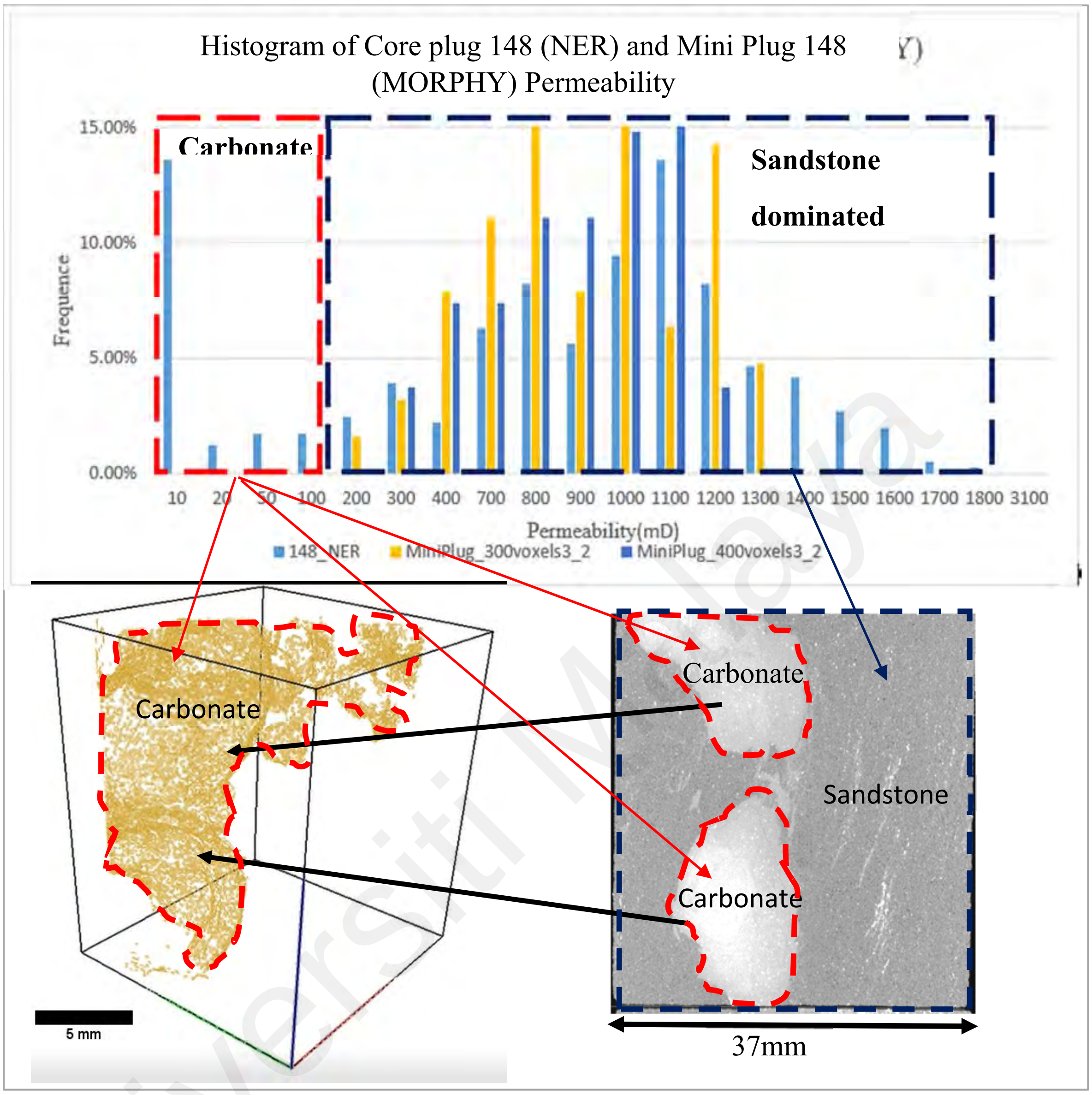

Figure 8.42: Sample 148: Histogram of Permeability results from using MORPHY and the NER Permeability Gas Probe and the 3-D image of the carbonate (bottom left) and the XMCT image (bottom right) with the dashed red and blue lines correlated to the histogram indicating the sandstone dominated matrix and carbonate permeabilities.

8.2.1.4 Conclusion

The computed high permeabilities in mini plug 148 suggest that the mini plug represent relatively clean and homogeneous sandstone in core plug 148. We attributed the significant permeability difference between the mini plug and core plug scale to the heterogeneity difference at the mini plug and core plug scale. Core plug 148 contains a large carbonate grain with low permeability (below 100 mD) that restricts fluid flow and reduces the permeability of core plug 148 to 395 mD. On the other hand, mini plug 148 mainly consists of homogeneous sandstone shown previously in Figures 8.41. As a result, the averaged computed permeability of the mini plug is higher at between 790 mD and 812 mD, which is twice the value of experimentally measured permeability of core plug 148 at 395 mD. The permeability map of core plug 148 in Figure 8.43 shows the carbonate and sandstone on the surface of core plug 148. It shows the significant permeability contrast between the permeable sandstone and less permeability carbonate phase. The permeability map of core plug 148 validates that the carbonate has lower permeability (below 100 mD) relative to the sandstone phase, which is consistent with the results of the histogram shown previously in Figure 8.42. The NER permeameter is instrumental in providing the carbonate permeability data since mini plug 148 did not sample any carbonate.

We used the permeameter results to validate the computed results due to the notable similarity between the computed permeabilities and the NER generated permeabilities, as shown previously in Figure 8.42. The NER permeameter has a measuring tip with a width of 4 mm which is similar to the edge lengths of the sub-volumes of mini plug 148 which are at 1.12 mm and 1.41 mm shown previously in Table 8.10. Also, the permeameter measures permeability at an interval of 1mm on the surface of the core plug, providing a large amount of data points that are useful for statistical analysis for comparison to the computed permeabilities as shown in the histogram in Figure 8.42. Due to the millimetre scale resolution of the NER permeameter measurement, the measured surface permeabilities validated computed permeabilities as both results show a good match, as shown previously in the histogram Figure 8.42. The surface and computed permeabilities also validated the permeability range of the sandstone, which is between 790 mD and 820 mD. Besides, the permeameter results provided the surface permeability data of carbonate on the core plug's surfaces that we did not sample in mini plug 148. There were no signs of carbonate in mini plug 148 (Figures 8.41). Therefore we used NER permeameter to measure the permeability of the carbonate on the surface of the core plug 148 in Figure 8.43, which we show are below 100 mD. The NER permeability map also shows significant permeability contrast between the high permeability sandstone regions (red regions, above 100 mD) and the low permeability carbonate regions (green and blue regions, below 100 mD). These results show that the permeability of core plug 148 is lower due to the lower permeability values of the carbonate, which can act as a barrier to fluid flow. Also, our results shown previously in Table 8.9 show that the average permeability of the reservoir sandstone in core plug 148 is at least twice higher than the measured core plug permeability. The computed permeability of mini plug 148 is a more accurate value for the sandstone in core plug 148 as the mini plug is homogeneous sandstone.

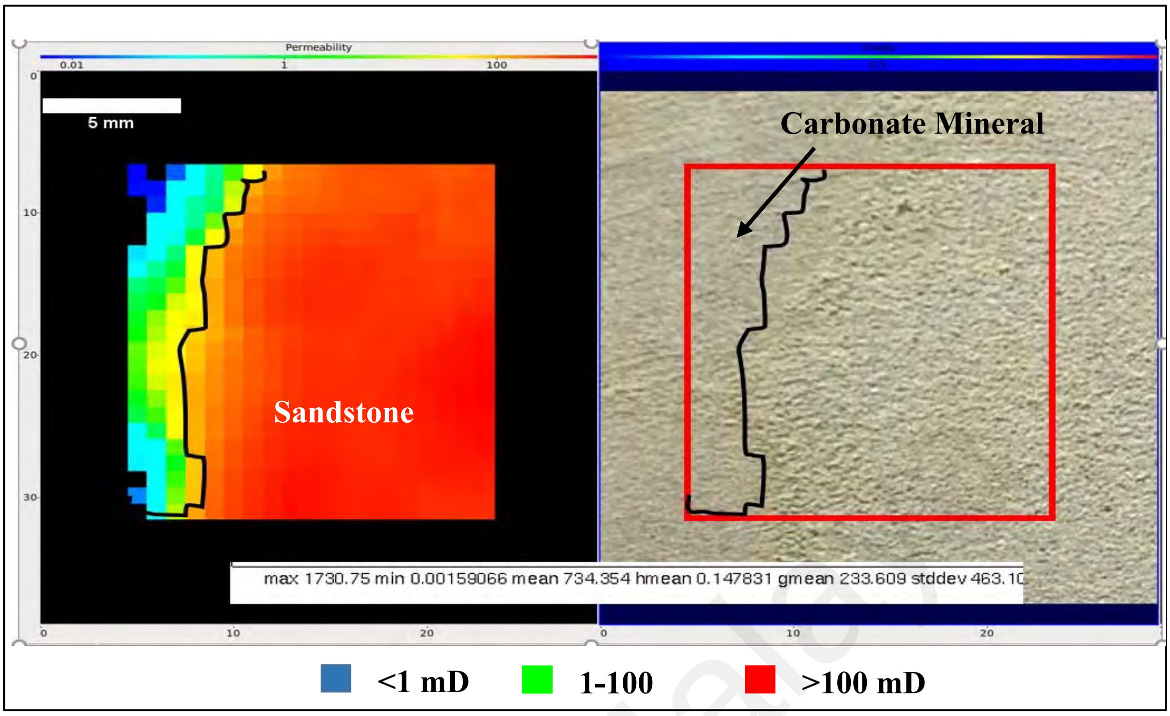

Figure 8.43: Permeability map on the surface of the core plug 148 from the NER Permeability Gas Probe. The blue areas are low permeability carbonate regions.

The results for core plug and mini plug 148 are pertinent to this thesis as they showcase the challenges in evaluating porosity and permeability of sandstone due to the impact of multi-scale heterogeneity on permeability at different length scales and volume sizes. The results from MORPHY while indicating highly permeable sub-volumes in mini plug 148, should consider the effects of heterogeneity on permeability at a larger scale. XMCT imaging shows mitigating flow carbonate in core plug 148 that causes lower core plug permeability compared to mini plug 148. XMCT imaging and DCA allows us to compute the permeability smaller and homogeneous sandstone mini-plugs from core plug 148 that is more accurate and representative of the sandstone in core plug 148. As heterogeneity affect permeability at different scales, investigating a suitable Representative Elementary Volume for sandstone is essential to accurately determine effective flow properties for use in the reservoir model. We can use XMCT imaging, and DCA computes permeability of samples smaller than a standard core plug to sample and compute permeability of different rock types within a heterogeneous core plug.

8.2.2 Sample 127: Laminated Sandstone

Core plug 127 is a laminated sandstone core plug similar to core plug 148. We extracted the core plug from a 40 cm thick sand dominated bed between mudstone dominated beds (Figure 8.44). Core plug 127 look relatively homogeneous with no signs of bioturbation (traces of plants and animal movements) on the exterior of the core plug and core slab. Sample 127 and 148 are only six meters apart. There it is likely that the sandstone in these two core plugs is a similar 3D Volume rendering of sample 127 in Figure 8.46, indicate the significant presence of thin carbonate laminates in its interior.

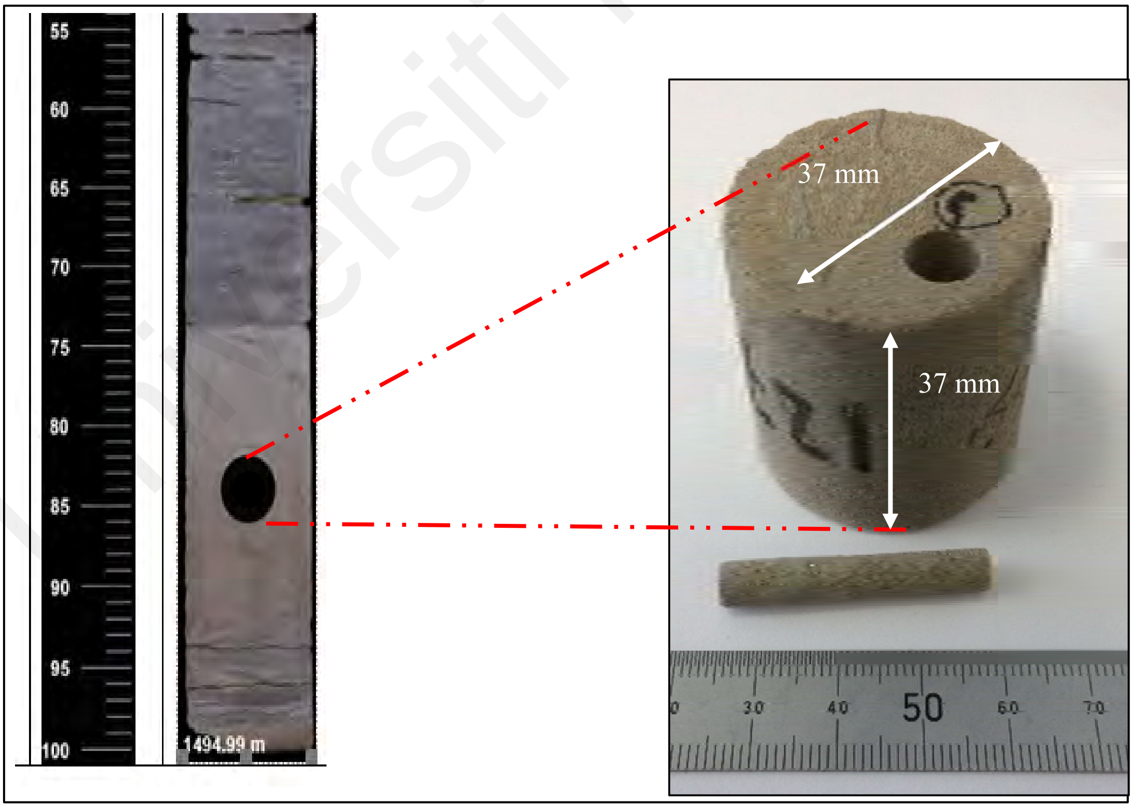

Figure 8.44: A view of the core (left) indicating distinct layers of dark coloured mudstone and light-coloured sandstone and core plug 127 (right).

8.2.2.1 Segmentation and 3D visualization of Sample 127

Similar to core plug 148, Figures 8.45 and 8.46 show there is a significant presence of carbonate minerals in core plug 127. However, unlike in core plug 148 where the carbonate is a large single grain, the carbonate minerals in core plug 127 are in the form of thin laminates (or ribbons). Similar to core plug 148, these low permeability carbonate minerals acted as a barrier to fluid flow and reduced the permeability of core plug 127. Similarly, Figure 8.47 shows that mini plug 127 is mostly homogeneous sandstone. However, there are small parts of the mini plug include some thin carbonate laminates that can potentially restrict fluid flow.

Figure 8.46 is a 3D visualization of core plug 127 that shows the presence of extensive carbonate laminates (or ribbons) throughout the core plug. The carbonate laminates are very thin, generally well connected and occupy approximately 16% of the core plug volume. There is a notable tubular structure that suggests traces of fossils within the core plug; however, we cannot yet verify this without destroying the core plug for further analysis for fossil identification. The carbonates are almost impermeable (below 100 mD) and can act as baffles to fluid flow.

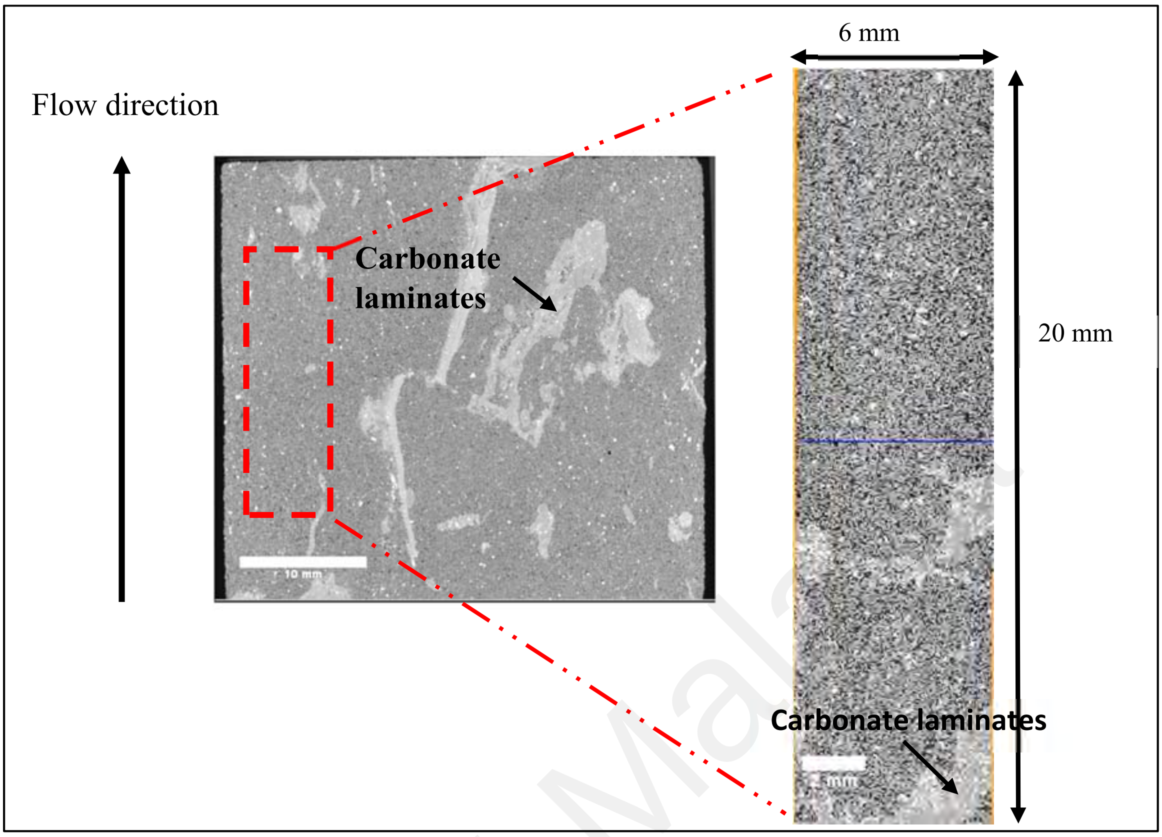

Figure 8.45: Left: Low-resolution image (37 microns/voxel) of core plug 127 and Right: High-Resolution image (3.76 microns/voxel) tomograms of mini plug 127. The location of mini-plug relative to the core plug is only an approximation.

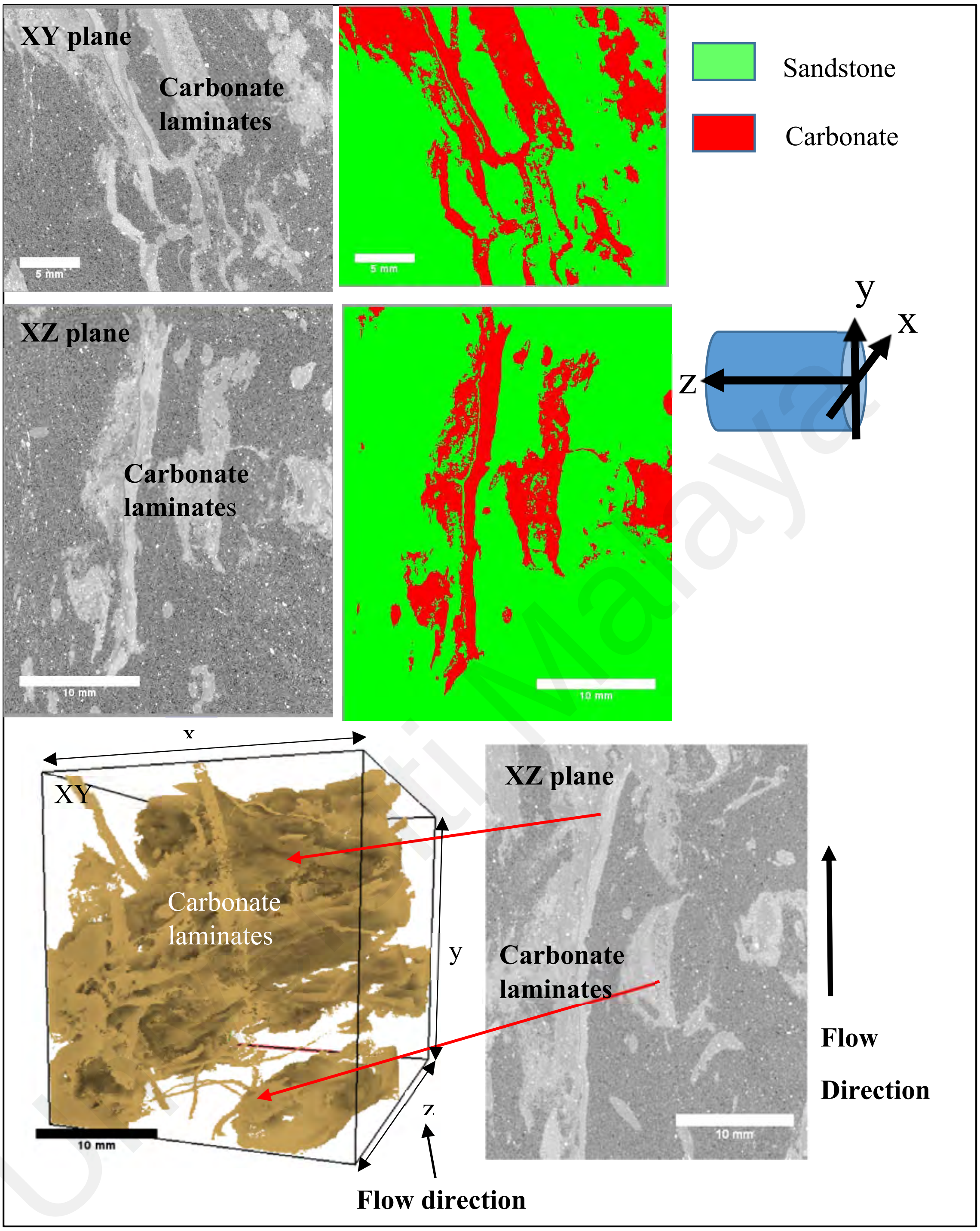

Figure 8.46: Top and Middle Images are greyscaled images and segmented images of core plug 127 The left bottom left image is a rendered 3D volume of core plug 127 showing the calcium carbonate phase tagged in yellow. The segmented calcium carbonate in core plug 127 occupies 16% of its volume. The fluid was injected in the z-direction in the experimental core plug analysis.

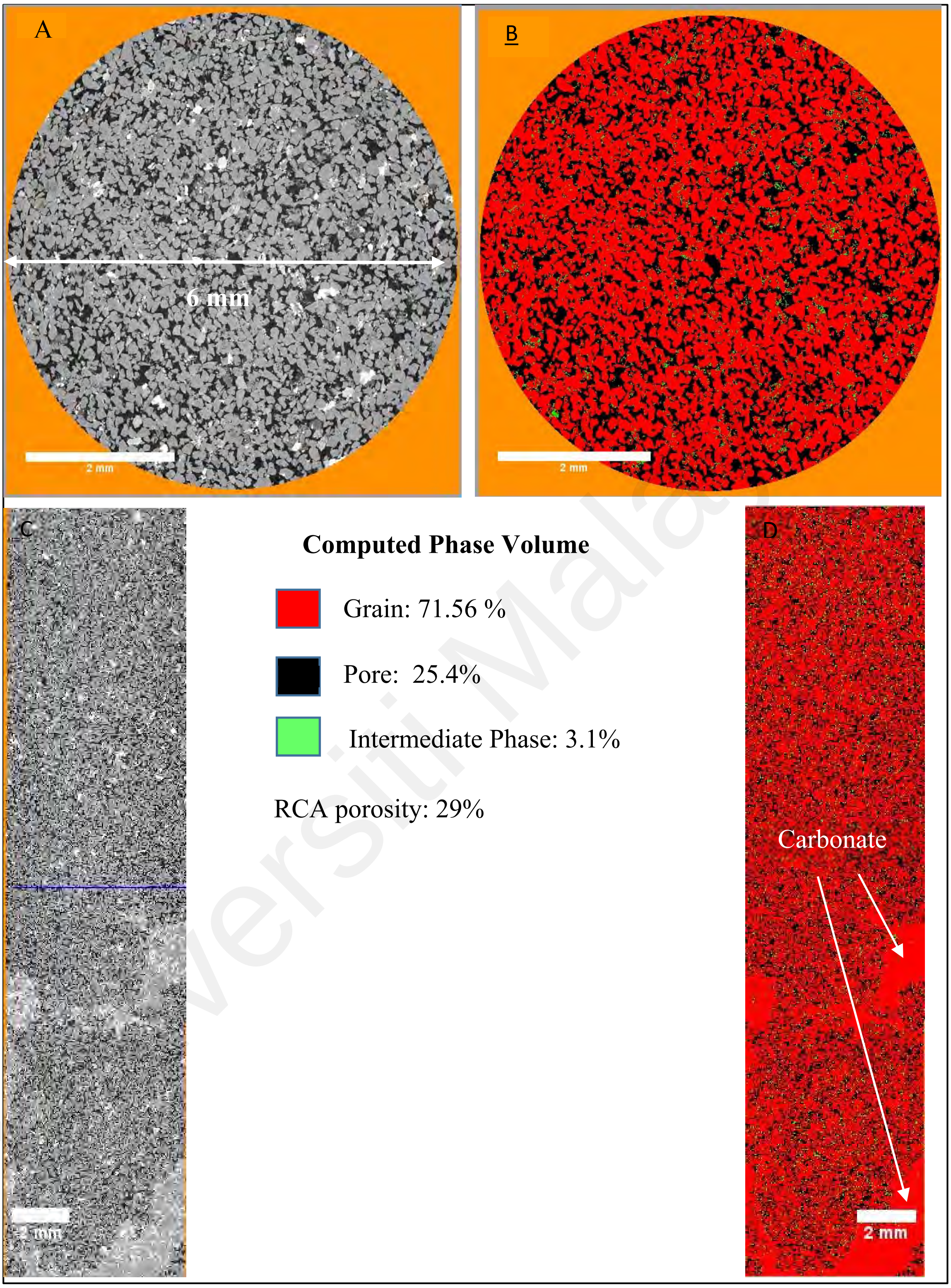

Figure 8.47: Images of Mini Plug 127. A and C: Original unprocessed Greyscale tomogram, B and D: Segmented image of mini plug 127.

8.2.2.2 Discussion of Permeability Results of Sample 127

The results in Table 8.11 shows that the computed permeabilities of mini plug 127 at 1358 mD (300 voxels^3) and 1384 mD (400 voxels$^{3)}$ are between 2-3 times higher than the experimental permeability of core plug 127 at 633 mD. Meanwhile, the averaged NER permeameter measured surface permeability is at 1145.5 mD which is 1.8 times higher than the RCA result and is at least 15% lower than the lowest computed permeability at 1358 mD (300 voxels^3) at 1358 mD. Figure 8.48 shows that the computed permeabilities at the 300 voxels^3 and 400 voxels^3 sub-volume sizes are relatively similar with only 1.9% difference. This very good match shows that the sandstone in mini plug 127 is relatively homogeneous at these two sub-volume sizes.

Comparison between sample 127 and 148 are pertinent because both samples are laminated sandstone located 6 meters apart. Core plug 148 has a core plug permeability at 395 mD, which is 60% lower than core plug 127 at 633 mD. Table 8.11 also shows that computed permeabilities of mini plug 148 at 892 mD (300 voxels^3) are 34% lower than core plug 127 at 1358 mD (300 voxels^3). The lower computed permeability for mini plug 148 compared to mini-plug 127 is attributed to the smaller average grain size of the sandstone in mini plug 148 at 92µm which is 12% lower than the average grain size in mini plug 127 at 103µm (refer to previous section 8.1.1.2). Larger average grain sizes have a linear correlation with higher permeabilities (Masch et al., 1966).

While the average permeability of sample 127 and 148 diverged at the mini plug and core scale at 812 mD versus 1358 mD respectively, Figure 8.49 shows that the porosity-to- permeability gradient of mini plug 127 and 148 are similar. This excellent match indicates that the sandstone in both mini-plugs has a similar porosity-to-permeability relationship. Similarly observed in core plug 148, the NER permeability map in Figure 8.51 shows that the carbonate minerals in core plug 127 are also below 100 mD.

The NER permeameter gas probe tip has a diameter of 4mm which is relatively similar to side lengths of the sub-volumes of mini plug 127 at 0.85 mm (300 voxels) and 1.13 mm (400 voxels) used by MORPHY to compute permeability (Table 8.12). Due to their similar resolution, we used the permeameter results to validate the computed permeabilities due to its similar resolution to the computed results using MORPHY.

Table 8.11: Permeability results from MORPHY calculation, Experimental Core Analysis Gas Probe measurements for Sample 127. MORPHY results represent the 8 mm diameter mini-plug while the Experimental Core Analysis and NER gas probe measurements represent the 37mm diameter core plug.

Method	**MORPHY (Mini Plug)**		**Experimental Core Analysis (Core Plug)**		**NER (Core Plug)**
Details	**300 voxels^3**	**400 voxels^3**	**Air Horizontal**	**Routine Core Analysis**	**Gas probe**
Average	1357.9 mD	1383.8 mD	578.6 mD	633 mD	1145.5 mD
Maximum	2743.7 mD	2431.9 mD	633.0 mD	N/A	1994.9 mD
Minimum	54.9 mD	81.8 mD	551.0 mD	N/A	86.7 mD
Standard Deviation	626.6 mD	593.8 mD	22.9 mD	N/A	482.2 mD

Table 8.12: Comparison between the two sub-volumes sizes used in MORPHY to calculate the permeability in mini plug 127.

Edge Length in voxels	**Resolution in voxel per mm**	**Side Length in mm**	**Cubic Volume in mm^3**
300	0.00282	0.846	0.61
400	0.00282	1.128	1.44

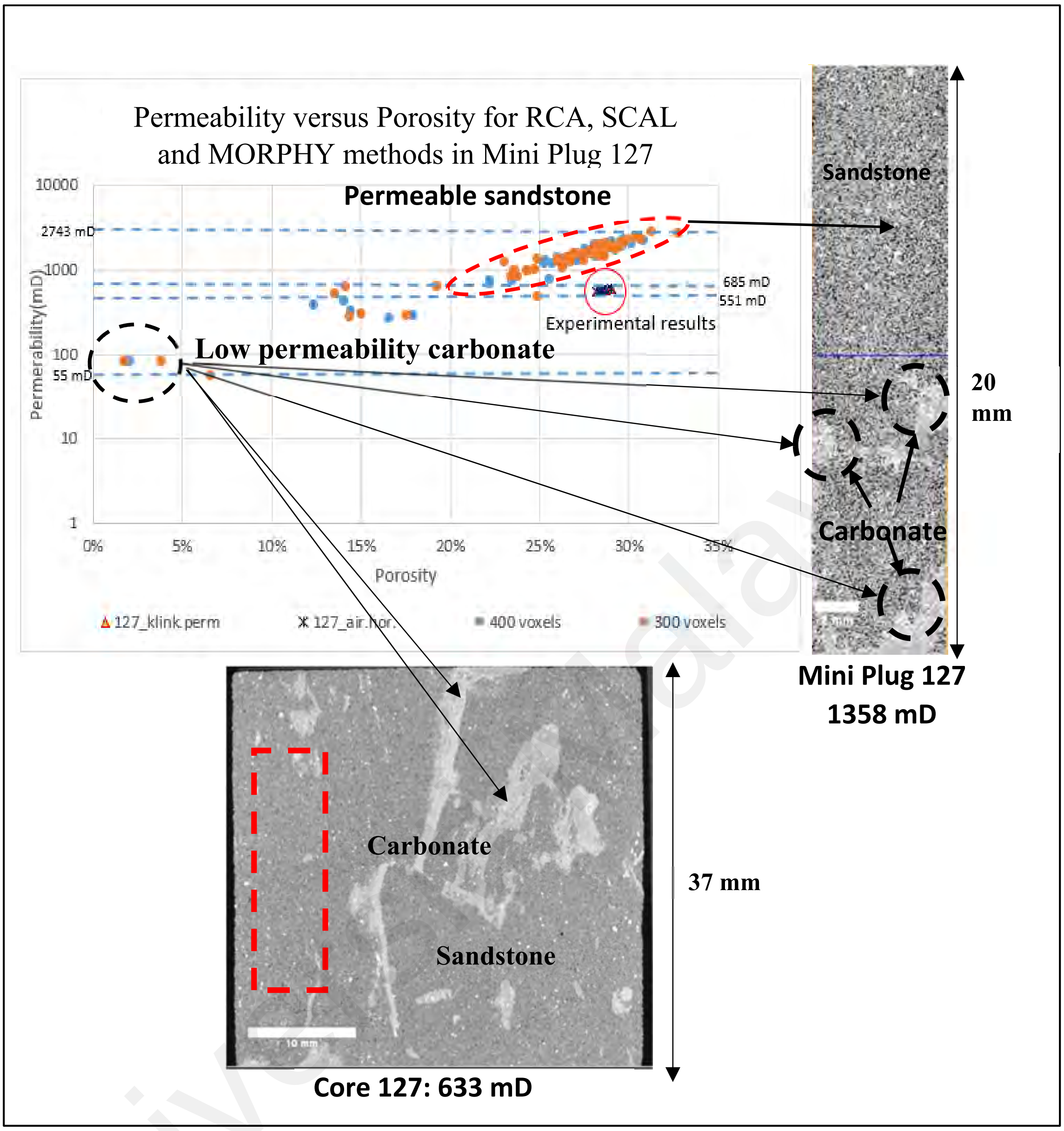

Figure 8.48: Top Left: The permeability-porosity graph of computed permeabilities and experimental permeabilities of sample 127. Top Right: XMCT image of mini plug 127 with sandstone and carbonate phase correlated to the graph to the left. Bottom Middle: XMCT image of core plug 127. We noted that the carbonate has permeability below 100 mD which was validated by the surface permeability map of core plug 127 in Figure 8.16

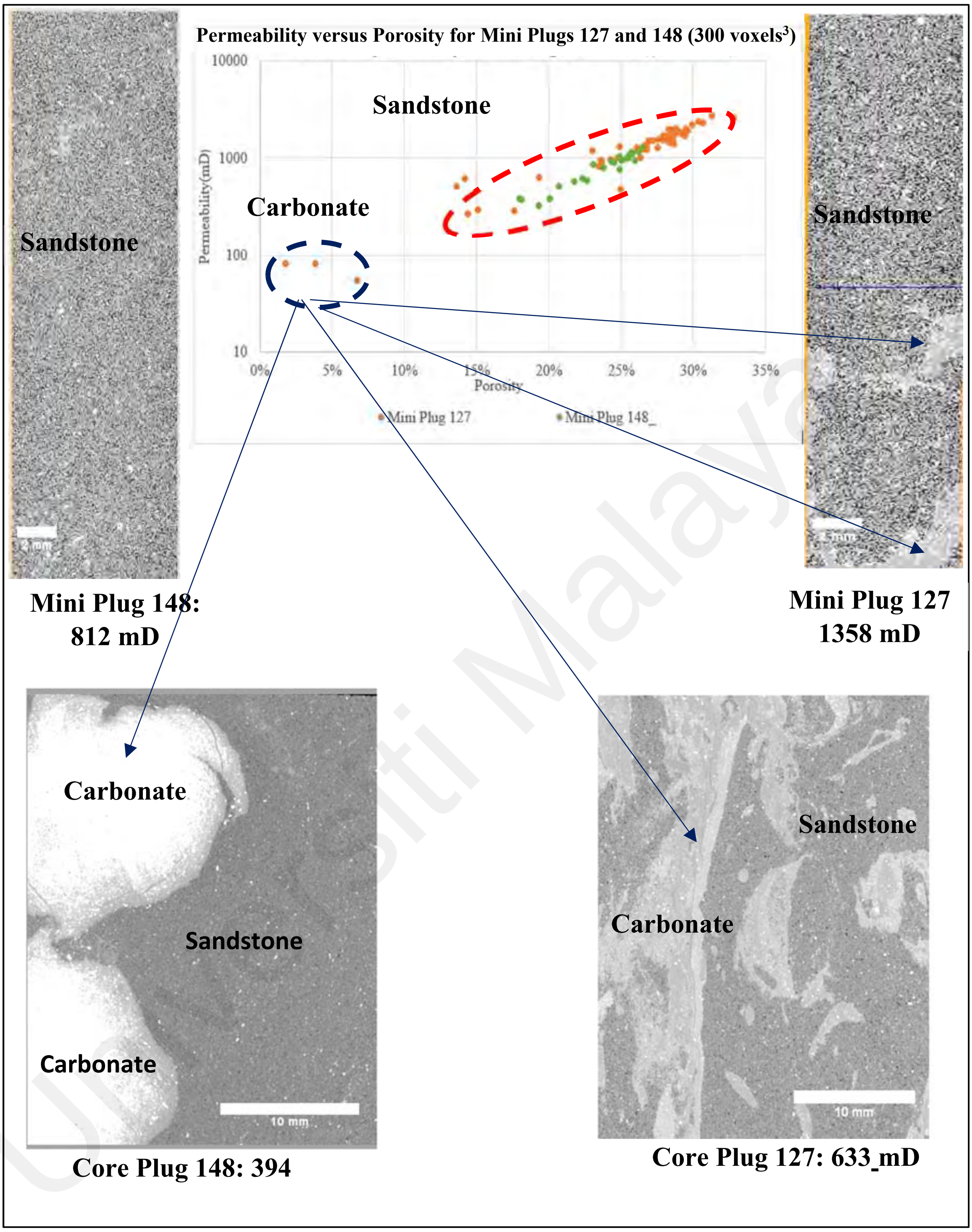

Figure 8.49: Permeability versus Porosity for mini plug 127 and 148, indicating that the gradient of the sandstone in both mini-plugs is relatively similar. With the low permeability data points below 100 mD captured in mini plug 127 representing the carbonate mineral. As sample 127 and 148 are only 6 meters apart, the carbonate in sample 127 and 148 should be similar.

8.2.2.3 Comparison between MORPHY computed permeability and Gas probe measured permeability

The histogram in Figure 8.50 shows the computed permeabilities of mini plug 127, and the NER measured surface permeabilities of core plug 127. The histogram shows that there is a good match between the histogram profiles of the two datasets which have similar permeability range and frequencies by percentage. The permeabilities below 100 mD in the histogram Figure 8.50 represent carbonate minerals measured by both digital core analysis and the NER permeability gas probe. The carbonate minerals in core plug 127 and 148 have a similar permeability range that is below 100 mD.

The permeameter results provide a large number of data points that we compared to the computed permeabilities due to similar millimetre scale resolutions used in both methods. Permeability map of the surface of core plug 127 generated by the NER measurements in Figure 8.51 shows significant permeability contrast between the red sandstone regions (above 1000 mD) and the green carbonate regions (below 100 mD). The permeability map also shows that the carbonate in sample 127 and 148 are similarly below 100 mD, indicating the carbonate and sandstone are constituent rocks in both core plugs with similar permeability ranges. The small difference of 15% between the average surface permeabilities at 1145 mD versus the computed mini permeability at 1358 mD suggests that the computed permeability of mini plug 127 is valid.

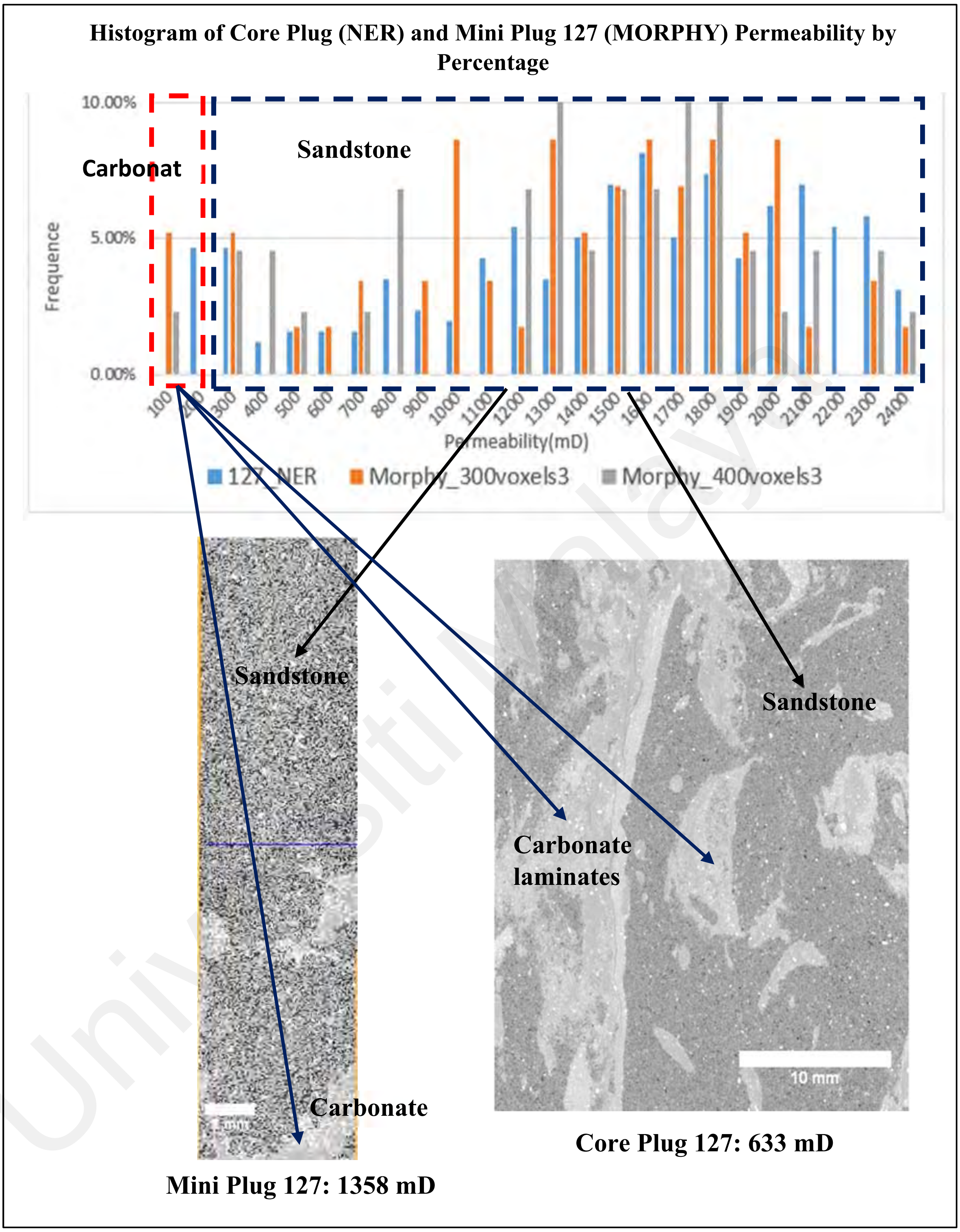

Figure 8.50: Histogram of Permeability results from using MORPHY and the NER Permeability Gas Probe. Images in the bottom are the XMCT images of mini plug 127 and core plug 127. We correlated the low permeability results on the histogram below 100 mD to the carbonate minerals in core plug 127.

8.2.2.4 Conclusion for Sample 127

The computed permeability of mini plug 127 at 1358 mD is higher than the RCA measured core plug permeability at 633 mD by a factor 2. We attributed the divergence between the two-scale to the different level of heterogeneity at the two-volume sizes. Mini plug 127 is more homogeneous than core plug 127 and show similar permeability results at the 300 $voxels^3$ and 400 $voxels^3$ sub-volume sizes. Hence it is strongly suggested that mini plug 127 represent the relatively homogeneous sandstone in core plug 127. On the other hand, Core plug 127 includes 16.7% carbonate laminates that restrict fluid flow, resulting in a lower core plug permeability at 633 mD compared to the more homogeneous mini plug 127 which is at least 1358 mD.

Figure 8.50 shows that the NER permeability map of core plug 127 validated the computed permeabilities of mini plug 127 as the permeabilities of both results match very well. Besides, the NER permeameter results in sample 127, and 148 verify that the carbonate minerals are below 100 mD. These results show that the constituent rocks in both samples, sandstone (above 100 mD) and carbonate (below 100 mD) can be distinguished based on their distinct permeability ranges and limits.

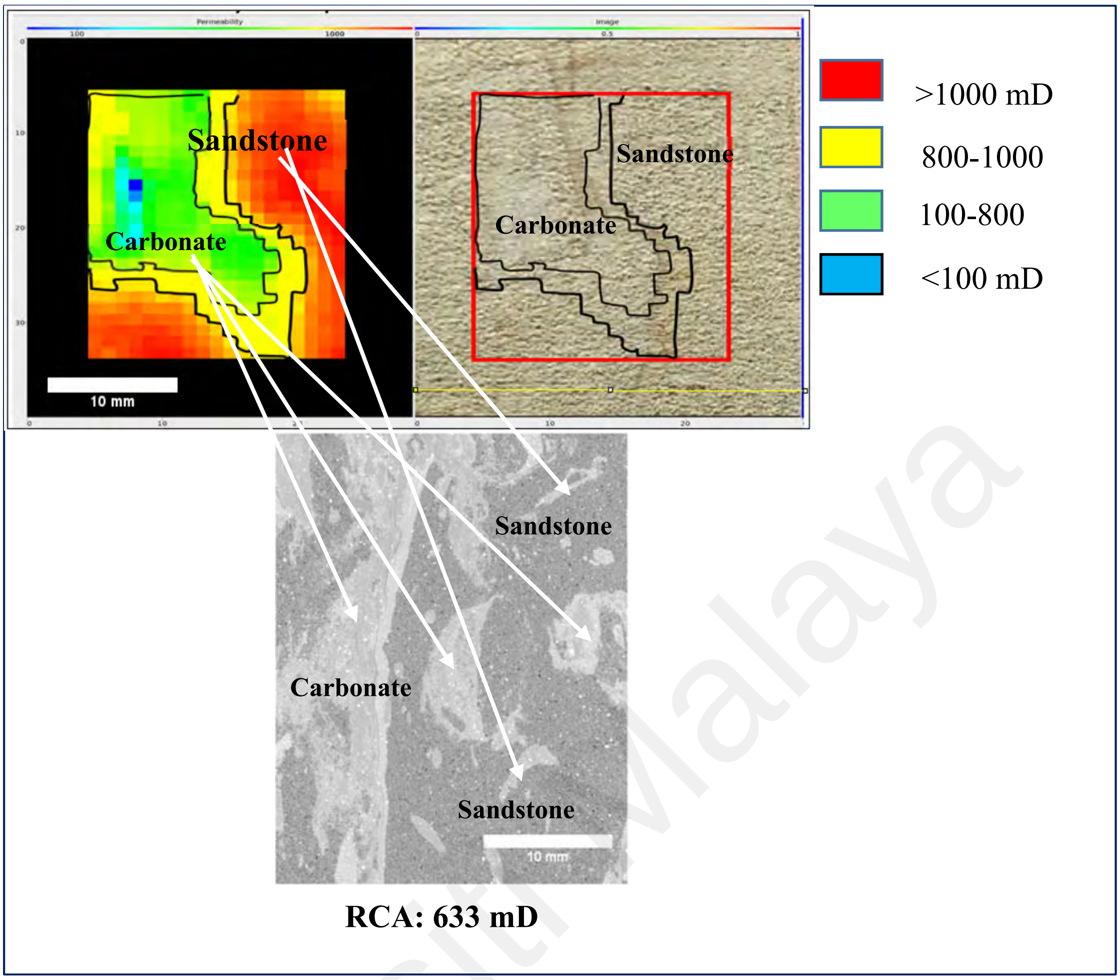

Figure 8.51: Top image: Permeability map on the surface of the core plug 127 from the NER permeameter. The red regions are high permeability sandstone while the green, yellow and blue regions are carbonate minerals with permeability below 1000 mD. Bottom image: XMCT image of core plug 127 with carbonate laminated correlated to the low permeability regions on the permeability map.

The RCA measured and computed permeability of core plug, and mini plug 127 respectively are higher than core plug and mini plug 148. Table 8.13 shows that the ratio between the RCA and computed permeabilities from both samples are relatively similar at between 1.52 to 1.74. The average grain size of mini plug 127 at 103 μm is 13% higher than mini plug 148 at 92 μm. The results suggest that the permeability difference between the two samples are related to the average grain sizes difference and not due to the shape or geometry of the carbonate minerals. However, we believe that the geometry, orientation and positioning of the carbonate laminates could affect permeability in a different direction which we could consider for future work.

Table 8.13 shows a significant difference between the RCA and computed permeabilities between Samples 127 and 148, despite both samples categorized as laminated sandstone with 15% to 17% carbonate minerals. The carbonate in core plug 148 is a large thick carbonate grain that reduced the axial (z-direction) cross-section of core plug 148 and restricts fluid flow. This restriction most likely causes lower permeability of core plug 148 at 395 mD, which is 106% lower than the average computed permeability of mini plug 148 at 812 mD (300 voxels^3). Similarly, despite the carbonate in core plug 127 taking the form of thin laminates, its core plug permeability at 633 mD is 114% lower than computed core plug permeability at 1358 mD. The permeability of both samples reduces by the same factor between mini and core plug volumes sizes, although the carbonate in both samples has different shapes and geometry. This result seems to suggest that carbonate may not be the leading factor that causes permeability difference between sample 127 and 148. The carbonate minerals only affect the permeability difference between the core plug and mini plug of both samples, which shows the effect of heterogeneity on permeability at different volume sizes.

Also, Table 8.13 shows that the median grain size in mini plug 127 is 11 μm bigger than mini plug 148. The table shows the permeability ratio of sample 127 to 148 (or 127/148) are similar at 1.6 for RCA permeability and 1.52 (300 voxels^3) and 1.74(400 voxels^3) for computed permeabilities. This strong correlation verifies that median grain size is a leading factor to the permeability difference sample 127 and 148. Sample 127 has a higher RCA and computed permeabilities because of its larger median grain size than sample 148.

To sum up, the permeability difference observed at the mini plug, and core plug scale of Sample 127 and 148 are strongly correlated to the carbonate minerals within the core plugs that resulted in lower core plug permeabilities compared to their mini plugs. However, the shape of the carbonate minerals is not the leading factor in the permeability difference between sample 127 and 148. Instead, we show that the permeability difference between Sample 127 and 148 are strongly correlated to the median grain size of the sandstone in the two samples.

Table 8.13: Measured and computed permeability of core plug 127 and 148. The RCA permeability of core plug 127 is 61% higher than core plug 148. Inversely, the computed permeability of mini plug 148 is 55% higher than mini plug 127.

Mini Plug	Routine Core Analysis		Phase Segmentation using DCA					
	Φ (%)	k (mD)	Pore (%)	Intermediate Phase (%)	Carbonate (% of core plug volume)	k_300 voxels^3 (mD)	k_400 voxels^3 (mD)	Median Grain Diameter (µm)
127	29	633	25.4	3.09	15.8	1358	1384	103
148	28.0	395	26.7	3.67	16.0	892	791	92
127/148	-	1.60	N/A	N/A-	N/A	1.52	1.74	1.13

8.2.3 Sample 64: Muddy Heterolithic

Sample 64 is a muddy heterolithic rock type which we considered as a non-reservoir rock due to a high mud content of at least 50%. Also, the high content of mud and laminated structure resulted in low resistivity reaction in the well logs, suggesting high water saturation which is not accurate. Core plug 64 is of significant interest as heterolithic rocks make up 60% of the interval in well X-4 from which core plug 64 originated. Heterolithic deposits in other reservoirs the same basin as 'Well X-4' has been shown to produce a considerable amount of hydrocarbon despite interpreted high water saturation and can potentially contain tens of millions of barrels of hydrocarbon (Kantaatmadja et al., 2014). However, the effective flow properties in heterolithic intervals cannot be determined accurately from the well logs due to resolution limits that cannot resolve thin beds. Overlooked thin sandstone layers can be part of additional net sand pay that potentially holds hydrocarbon. Also, experimental core plug data analysis is unable to measure the permeability of sandstone layers that is smaller than a standard core plug (Passey et al., 2006).

Figure 8.52 shows that externally, core plug 64 consists of alternating layers of sandstone and mudstone with the darker coloured mudstone r dominating most of the core plug external surfaces. We estimated that sandstone makes up a significant part of the core plug volume; however, quantifying the fraction of the sandstone is difficult. 3D images in Figure 8.56 also shows the significant presence of lighter coloured sandstone beddings intercalated between mudstone beddings. The average grain size of sediments in sample 64 is 72 µm which is the third-largest after Sample 127 (103 µm) and Sample 148 (92 µm).

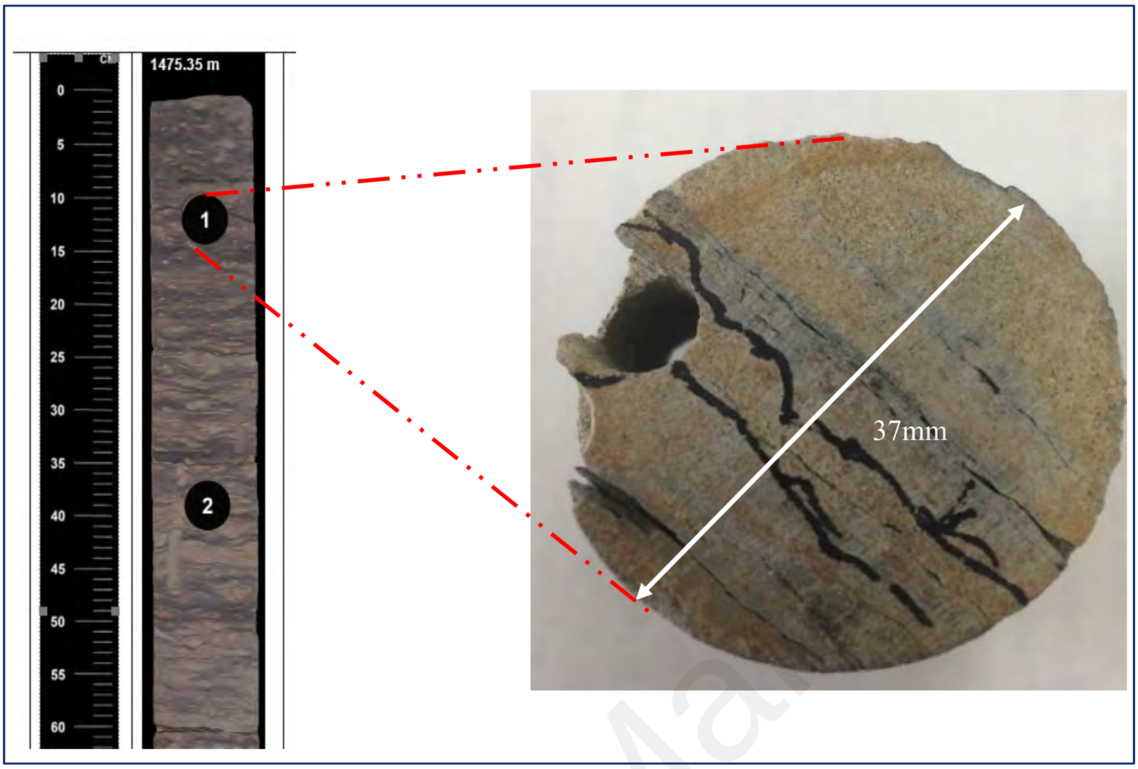

Figure 8.52: A view of one of the faces of core plug 64 (right), indicating distinct layers of dark coloured mudstone and light-coloured sandstone. The numbers in the core slab on the left indicate the order of the core plug. The hole on the core plug in the location from where we extracted a 6 mm mini-plug.

8.2.3.1 Segmentation and 3D visualization of Sample 64

Figures 8.53, 8.54 and 8.55 show we extracted mini plug 64 from a generally sand dominated region in core plug 64. Core plug 64 is affected by a high degree of heterogeneity with sandstone regions surrounded by a mudstone dominated matrix. Besides, the sandstone and mudstone layers are not continuous and are intercalated into each other. As a result, mini plug 64 incorporates a significant amount of low permeability mudstone.

In Figure 8.54, we segmented the XMCT dataset of core plug 64 XMCT datasets into two-phase, sandstone and mudstone. The mudstone phase may include other non-sandstone phases such as minerals and clay. In Figure 8.54, 3D visualization of the sandstone phase in core plug 64 reveals two separate millimetre scale sandstone beddings within the mudstone matrix. These sandstone layers occupy 15% of the core plug volume and are connected in the axial direction (z-direction in Figure 8.54) of the core plug. This notable observation suggests that many of the millimetre-to-centimetre thick sandstone layers in some muddy heterolithic deposits are connected and continuous in the lateral direction, which is the plane of deposition.

Figure 8.55 shows the segmented images of mini plug 64, which have a porosity of 17%, which is 10% lower than the core plug porosity at 18.9%. The slightly lower porosity can be attributed to the pore filling mudstone in mini plug 64 that reduced the porosity. The small difference is considered acceptable and validated the calculated porosity, which we may have overestimated or underestimated due to the subjective nature of the segmentation process. However, the small difference of 10% between the computed and RCA results are deemed acceptable.

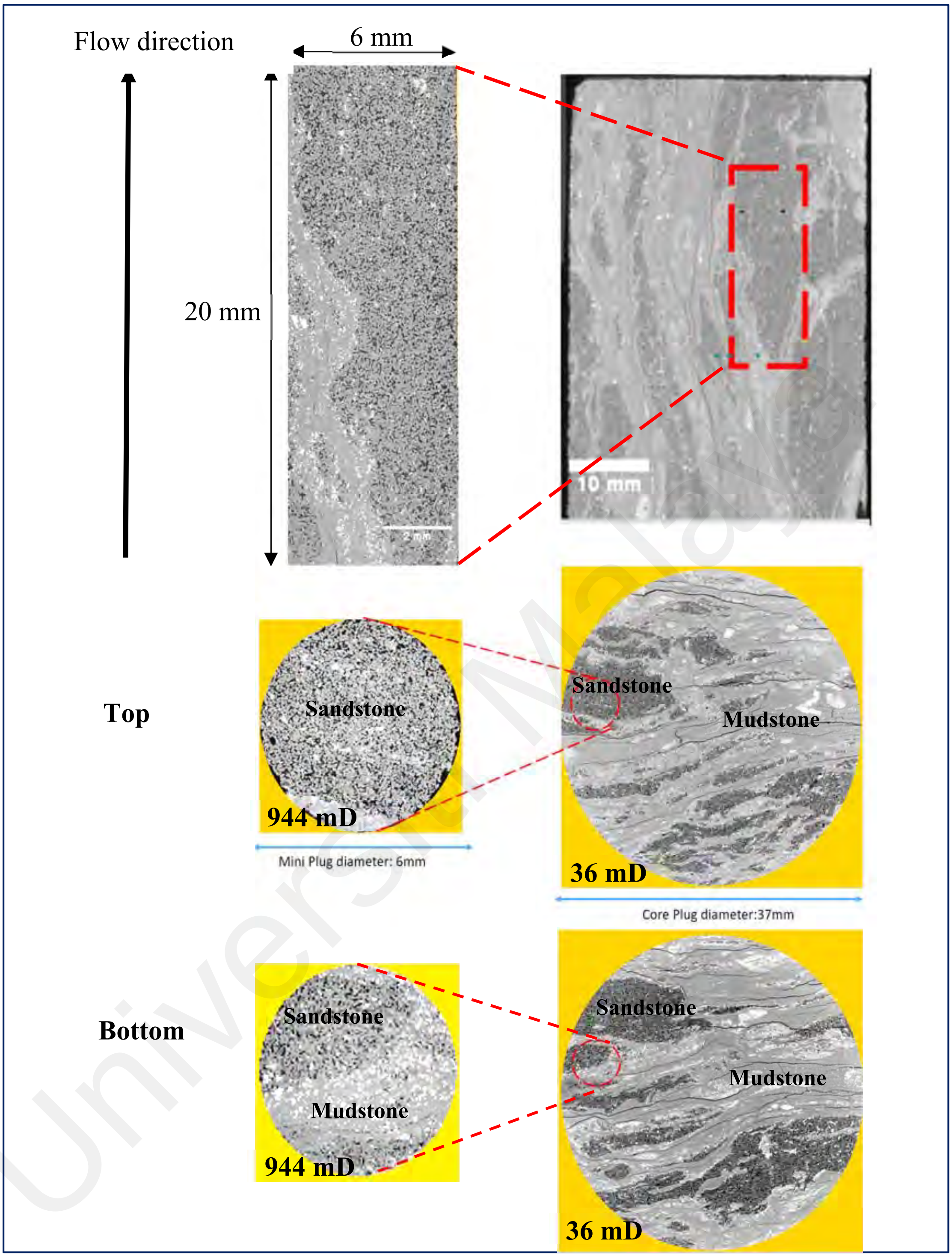

Figure 8.53: Left: High resolution (2.74 microns/voxel) and Right: Low Resolution (16.3 microns/voxel) tomograms of Sample 64 indicating the location of mini plug 64 in core plug 64.

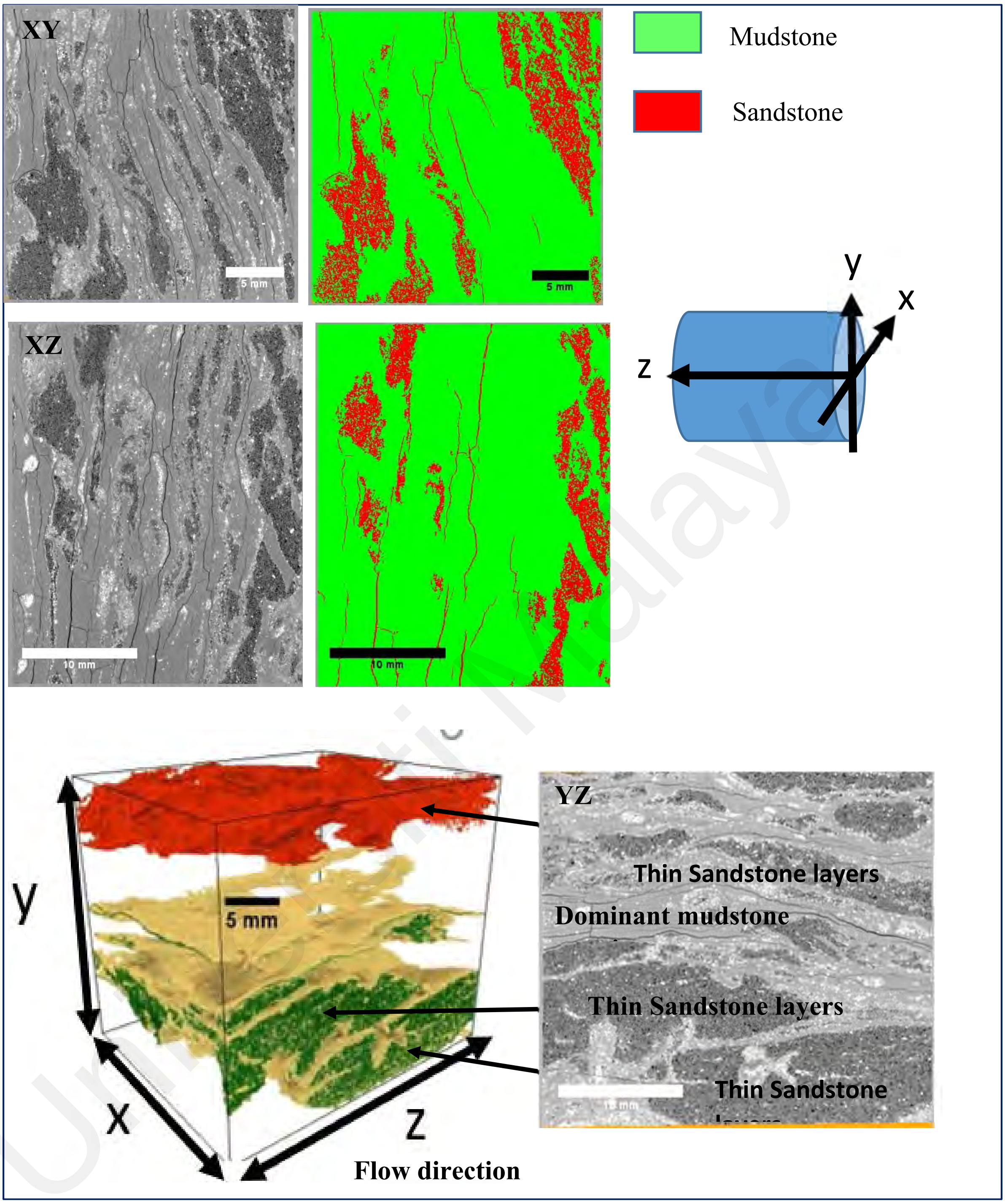

Figure 8.54: Top and Middle Images are greyscaled images and segmented images of core plug64. The left bottom left image is a rendered 3D volume of core plug 64 showing the sandstone phase tagged in red and yellow. The different colours indicate that the sand layers are not connected. The segmented sandstone in core plug 64 occupies 15% of its volume.

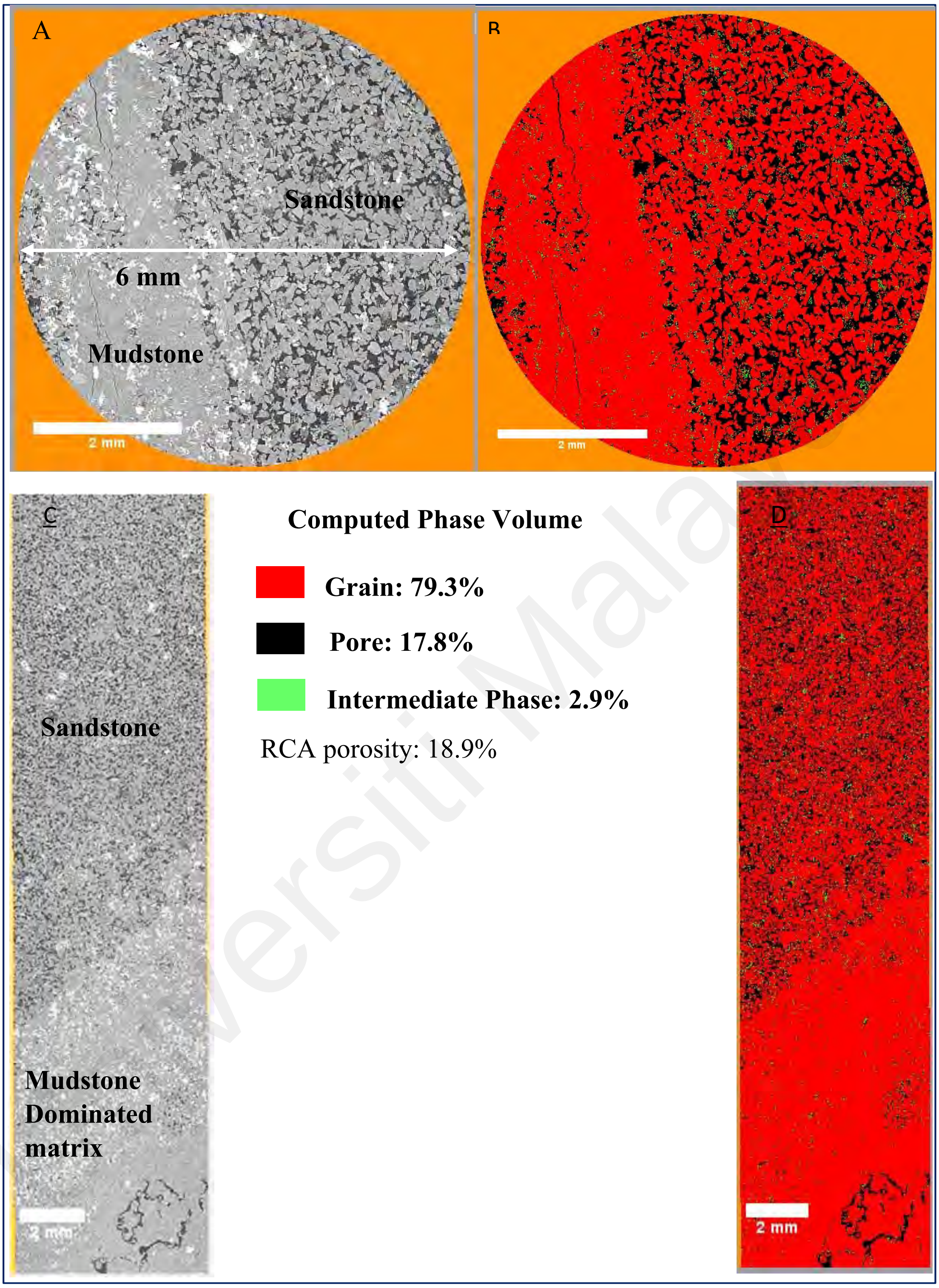

Figure 8.55: Images of mini plug 64. Greyscale and segmented images of Mini Plug 64. Image A and D: Greyscale. Image B and D: Segmented images of Mini Plug 64.

8.2.3.2 Discussion of Permeability Results for Mini Plug 64

Table 8.14 shows the permeability results from MORPHY, Routine Core Analysis and NER permeability gas probe for Sample 64. There is no reference Klinkenberg horizontal and Air Horizontal results for core plug 64 as muddy heterolithic core samples represented by core plug 64 were considered non-reservoir and were not selected to undergo Special Core Analysis. There is a 50 mD or 6% difference between the permeability of the 300 voxels^3 and 400 voxels^3 side length which is 894 mD and 944 mD respectively. This significant difference between the two sub-volumes sizes not observed in samples 127 and 128 is correlated to the higher level of heterogeneity in sample plug 64. While we extracted mini plug 64 from a relatively sandstone dominated region of the core plug, we see previously in Figure 8.55 that the mini plug still includes many mudstones that span the length of the mini plug. As a result, the 300 voxels^3 sub-volumes incorporate more mudstone than the 400 voxels^3 sub-volumes, resulting in the 50 mD between the two sub-volume sizes results.

Figure 8.56 shows that the sub-volumes in mini plug 64 can be divided into sandstone that has the increasing trendline and the flat trendline that represent mudstone. A notable result in Figure 8.59 shows that the permeability and porosity of the sandstone sub-volumes in mini plug 64 matches well with the data points in mini plug 127 and 148. This trend suggests that many of the data points in mini plug 64 are part of the thin sandstone layers in core plug 64 that are similar to the reservoir sandstone in mini plug 127 and 148 (Figure 8.59). This similarity validates the presence of overlooked thin permeable sandstone layers in heterolithic core plug 64 that has similar permeability-to-porosity behaviour as the reference reservoir sandstone in core plug 127 and 148.

The NER permeameter probe has a diameter of 4mm which is relatively similar to the side lengths of the sub-volumes of mini plug 64 at 0.86 mm (300 voxels) and 1.15 mm (400 voxels used by MORPHY to compute permeability as shown in Table 8.15. Due to their similar resolution, the NER results validated the computed permeability results.

Table 8.14: Permeability results from MORPHY calculation, Experimental Core Analysis Gas Probe measurements. MORPHY results represent the 6 mm diameter mini-plug while the Experimental Core Analysis and NER gas probe measurements represent the 37mm core plug

Method	**Digital Core Analysis: MORPHY**		**Experimental Core Analysis**	**NER**
Details	**300 voxels^3**	**400 voxels^3**	**Routine Core Analysis**	**Gas probe**
Average	894.2 mD	944.7 mD	35.98 mD	228.9 mD
Maximum	2297.5 mD	2571.0mD	N/A	725.6 mD
Minimum	2.4 mD	7.5 mD	N/A	7.5 mD
Standard Deviation	879.4 mD	975.3 mD	N/A	149.0 mD

Table 8.15: The two sub-volumes sizes used in MORPHY to calculate the permeability in mini plug 64.

Edge Length in voxels	**Resolution in voxel per mm**	**Side Length in mm**	**Cubic Volume in mm^3**
300	0.00287	0.861	0.64
400	0.00287	1.148	1.51

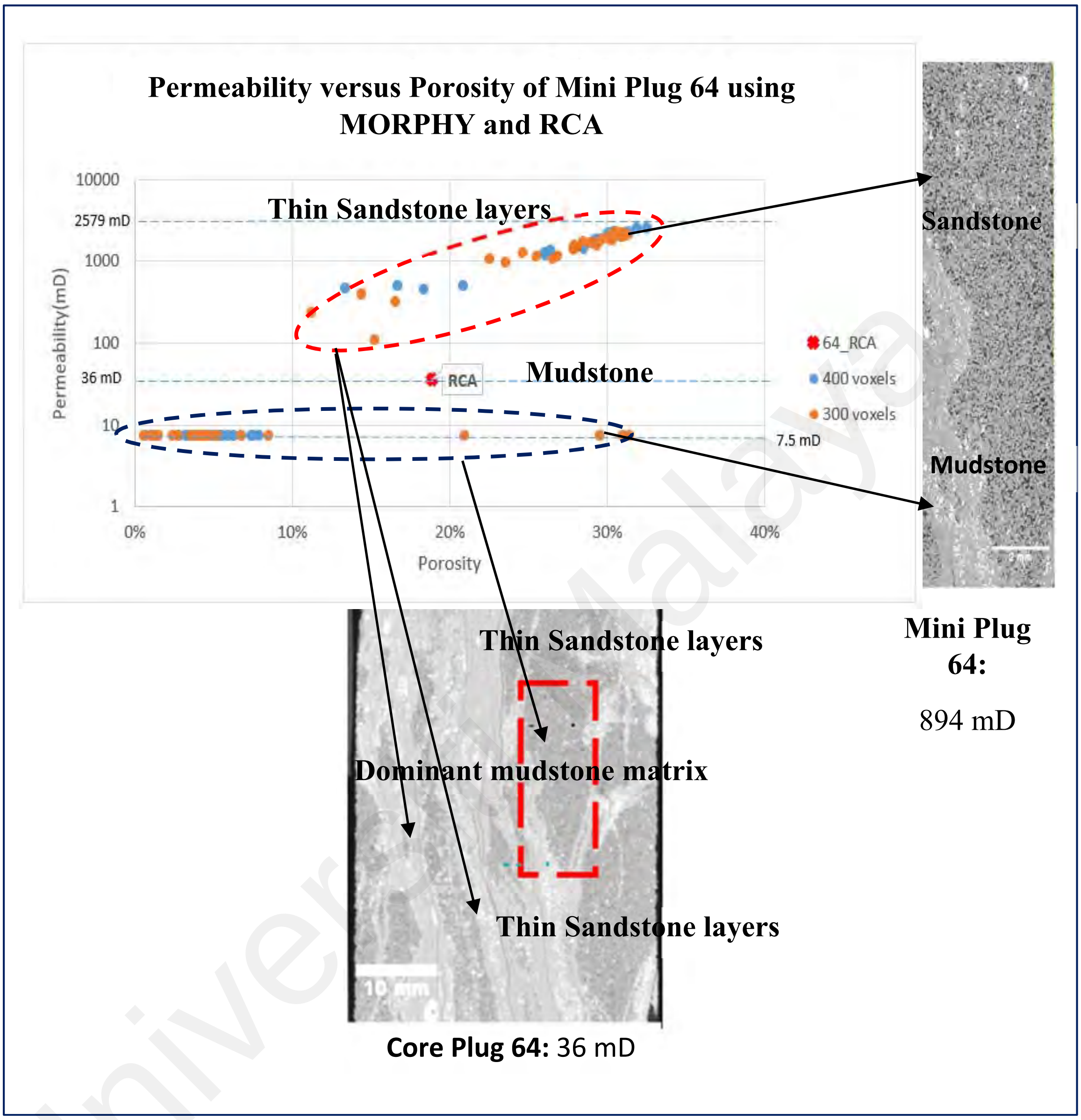

Figure 8.56: The porosity versus permeability of Mini Plug 64 from MORPHY and RCA results. The computed permeabilities in mini plug 64 represent the sandstone and mudstone in core plug 64.

8.2.3.3 Comparison between MORPHY computed permeability and Gas probe measured permeability

The histogram in Figure 8.57 shows the computed permeabilities of mini plug 64, and the NER measured surface permeabilities. Also, the histogram shows that the range of the measured permeabilities on the surface plug 64 is below 1000 mD at between 10 mD to 800 mD with an average surface permeability of 229 mD. On the other hand, the computed permeability of the sub-volumes in mini plug 64 has a range between 10 mD to 2700 mD with no permeability values making up more than 10% of frequency. However, many of the permeabilities of the 300 voxels^3 and 400 voxels^3 sub-volumes are above 1000 mD, resulting in higher average computed permeability of mini plug 64 at 894 mD (300 voxels^3) and 944 mD (400 voxels^3). These values are at least four times the average surface permeability at 229 mD. The average computed permeability at 894 mD (300 voxels^3) and surface permeability ay 229 mD is at least 26 times and 6 times higher compared to the RCA measured core plug permeability at 36 mD. This divergence between the three datasets is due to mini-plug 64 has a higher sandstone content by volume percentage than the core plug, which is dominated by mudstone.

Similarly, the computed permeability of mini plug 64 is also higher than the surface permeabilities of core plug 64 by 3.9 times due to higher sandstone content samples by mini plug 64 compared to core plug 64. The NER permeameter measures the permeability of sandstone and mudstone on the surface of core plug 64. The results show that at least half of its datapoint at equal to or below 200 mD, resulting in a lower average surface permeability compared to the computed permeability of the mini plug which has a higher number sandstone sub-volumes than mudstone sub-volumes.

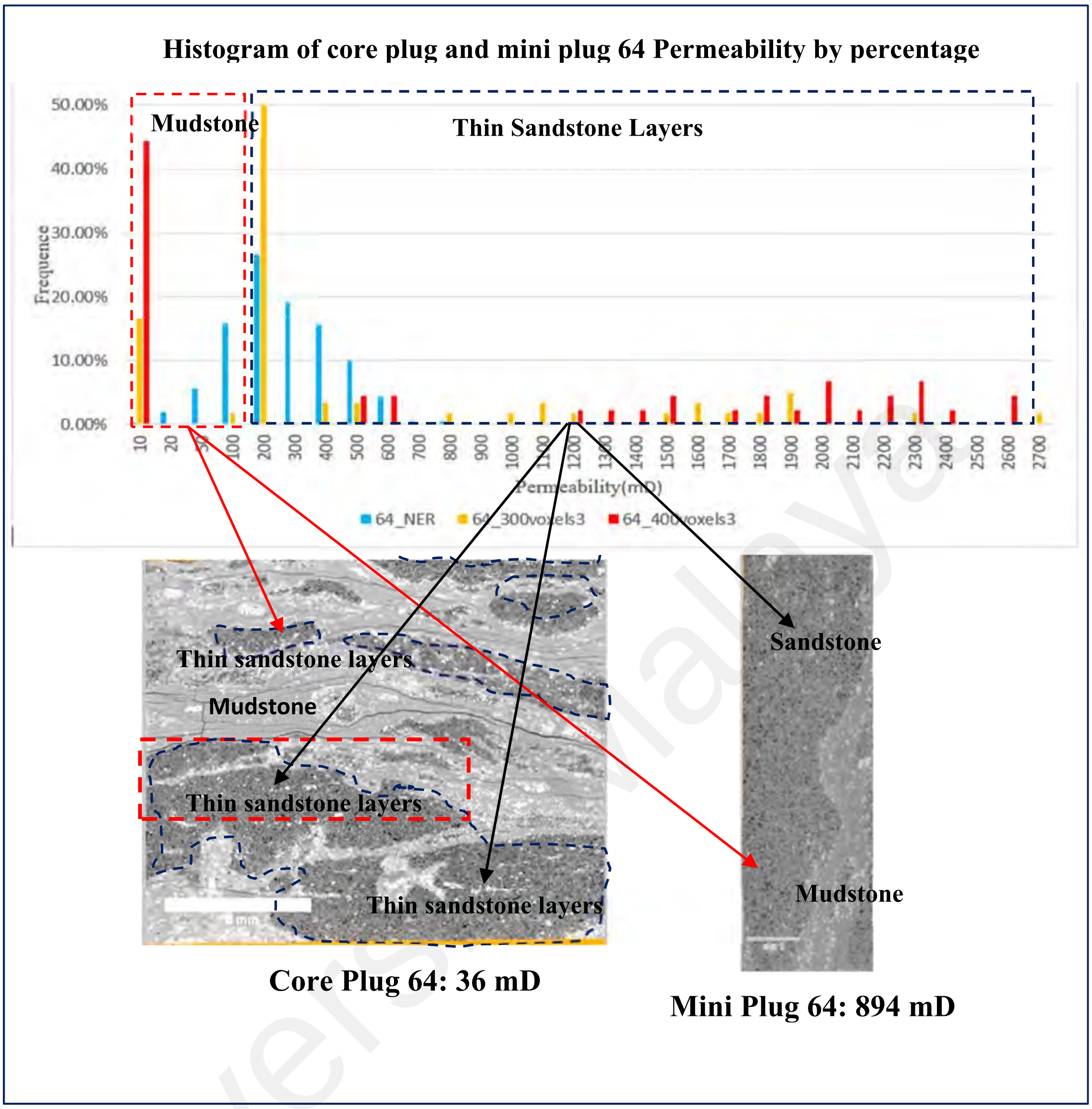

Figure 8.57: Histogram of Permeability results from using MORPHY and the NER Gas Probe. The MORPHY results represent mini plug 64 while the NER results are from core plug 64.

Figure 8.58 shows the permeability map of core plug 64 surfaces. There is a significant permeability contrast between the sandstone regions (yellow/red) and the mudstone that are below 10 mD (blue). Some areas are between 10 to 100 mD (green), which are the intermediate areas between the sandstone and mudstone regions. This intermediate region occurs because the NER permeameter averages the permeability of the sandstone and mudstone within these intermediate regions. As a. result of the mudstone, these regions are lower than the sandstone but higher than the mudstone.

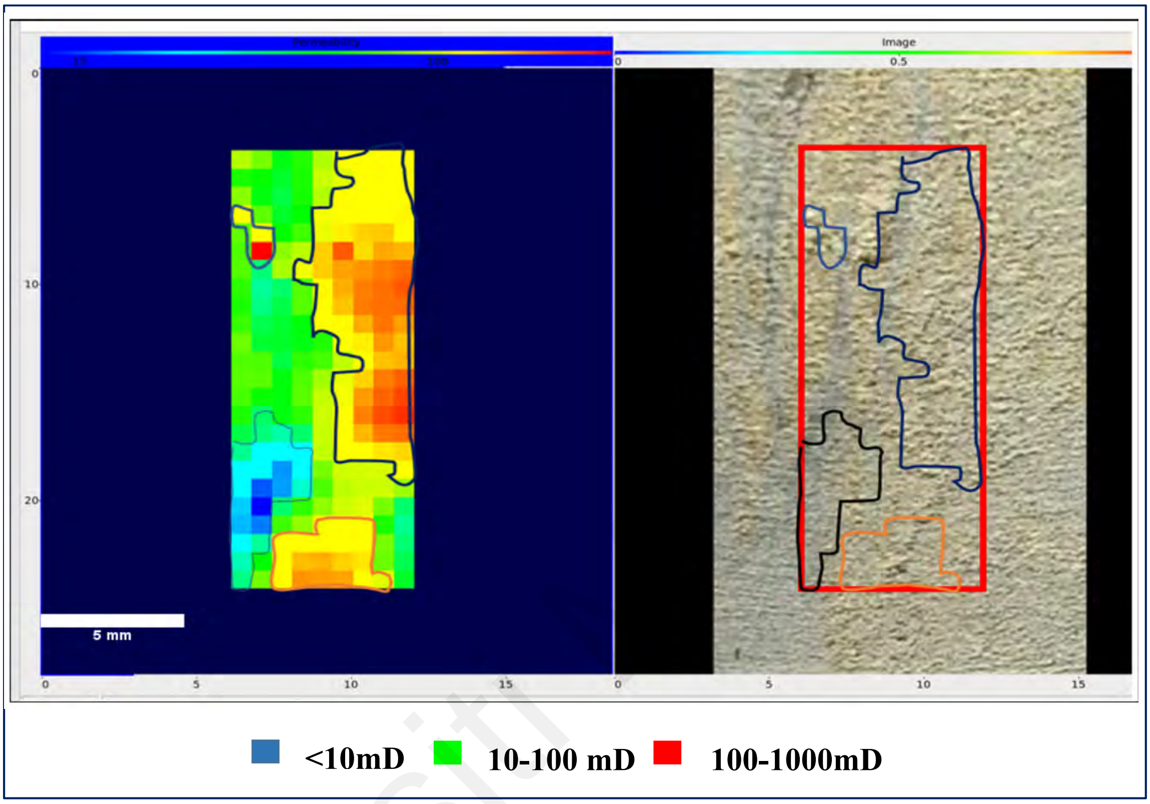

Figure 8.58: Permeability on the surface of the core plug 64 from the NER Gas Probe. The blue/green areas are low permeability mudstone dominated regions that are below 100 mD while the yellow/orange areas and permeable sandstone regions that are between 100-1000 mD.

8.2.3.4 Conclusion for Sample 64.

3D visualization of core plug 64 shown previously in Figure 8.54 revealed thin sandstone layers make up 15 % of the core plug volume. The thin sandstone layers in core plug 64 have millimetre scale thickness and seem to be laterally and well-connected and continuous. Mini plug 64, which we extracted from these sandstone layers is heterogeneous, consisting of mudstone and sandstone. However, the sandstone to mudstone ratio of mini plug 64 is higher than core plug 64. As a result, the average permeability of the mini plug is dominated by the permeable sandstone phase. Also, the average grain size of mini plug 64 is 72 µm which is smaller than the average grain sizes in sample 127 (103 µm) and 148 (92 µm). The smaller median grain size of the sandstone in core plug 64 is a factor to its lower measured and computed permeability compared to sample 127 and 148.

. Figure 8.59 shows that the permeability-to-porosity gradient of mini plug 64 is similar to mini-plug 127 and 148. This excellent match confirmed that the sandstone in sample 64 is mainly similar to the reference reservoir sandstone in sample 127 and 148. Also, this result validated the presence of thin permeable sandstone in heterolithic rocks that often overlooked. These thin sandstone layers represent potential additional net sand pay and hydrocarbon reserves in heterolithic deposits at the larger reservoir scale. We have shown previously the abundance of heterolithic rocks that make up 60% of well X-4 from where the samples come. The additional gas produced from well X-4 was most likely produced from the connected and continuous sandstone layers within the heterolithic intervals.

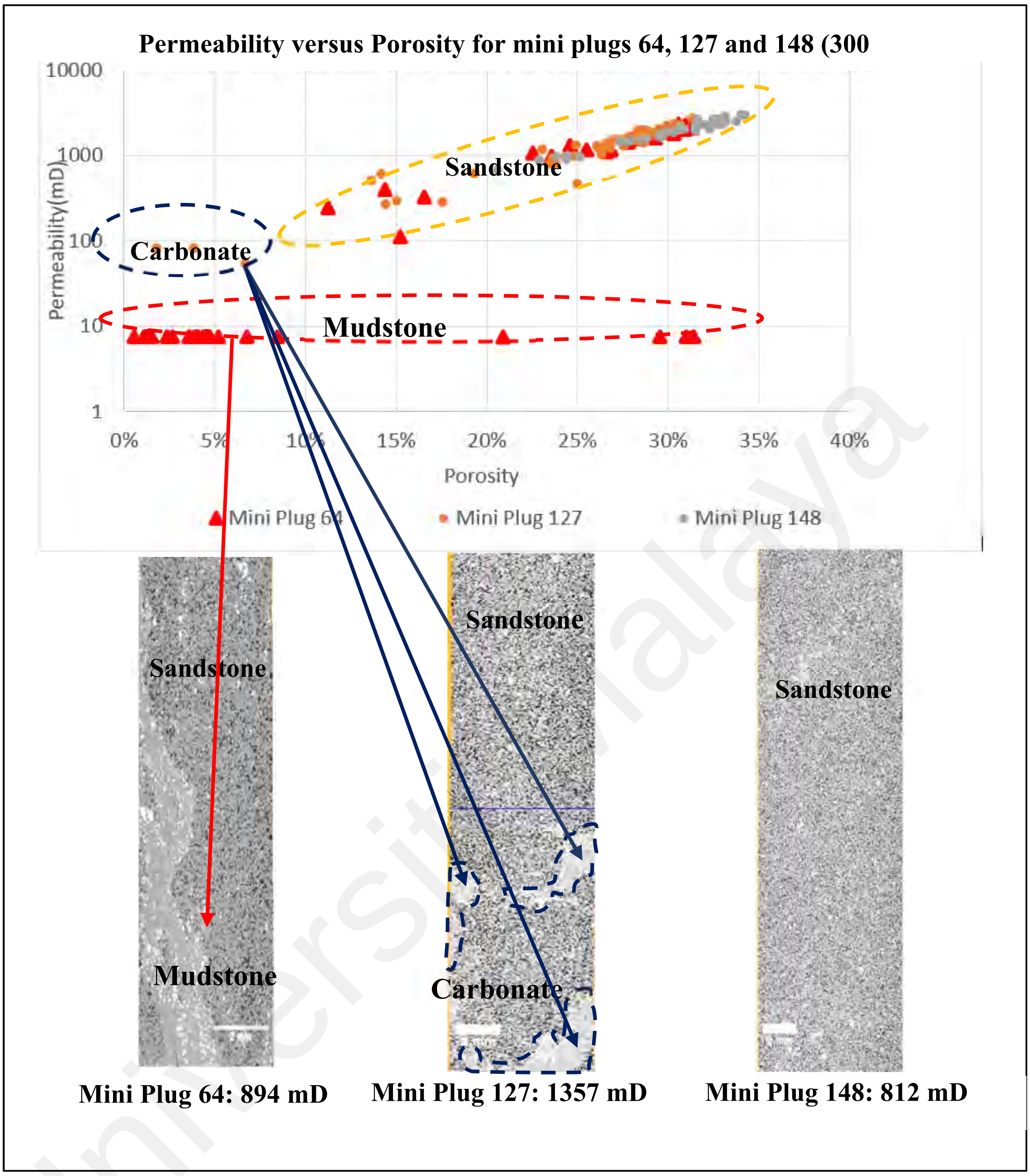

Figure 8.59: Porosity versus Permeability chart of mini plug 64 and mini plug 127 and 148. The sandstone of the three mini-plugs is statistically consistent with similar porosity-permeability gradients.

The average permeameter measured permeabilities of core plug 64 are smaller than computed permeabilities at 229 mD compared to at least 894 mD (300 voxels^3) for the computed results using MORPHY. However, the histogram of the permeabilities of both results shows some good match within the 20 mD to 600 mD range. Hence, the NER permeameter results validate the computed permeabilities of mini plug 64. The divergence between the two results is due many sub-volumes in mini plug 64 having permeabilities equal or above 1000 mD while the permeameter measured more mudstone than sandstone on the surface of core plug 64.

Figure 8.60 highlights the challenge of measuring surface permeability in heterogeneous rock samples, such as in core plug 64. Heterolithic core plugs contain low permeability layers that change the trajectory of injected gas from the NER permeameter. This effect causes measured surface permeabilities with high variations compared to homogeneous samples such as core plugs 148 and 127. Despite this discrepancy, there is sufficient similarity between the computed and mini-permeameter measured results for core plug 64 that validated the computed results, as shown previously in the histogram in Figure 8.60. These results show that we can use the NER permeameter to validate the accuracy and reliability of the Lattice-Boltzmann solver permeability results we used in this thesis.

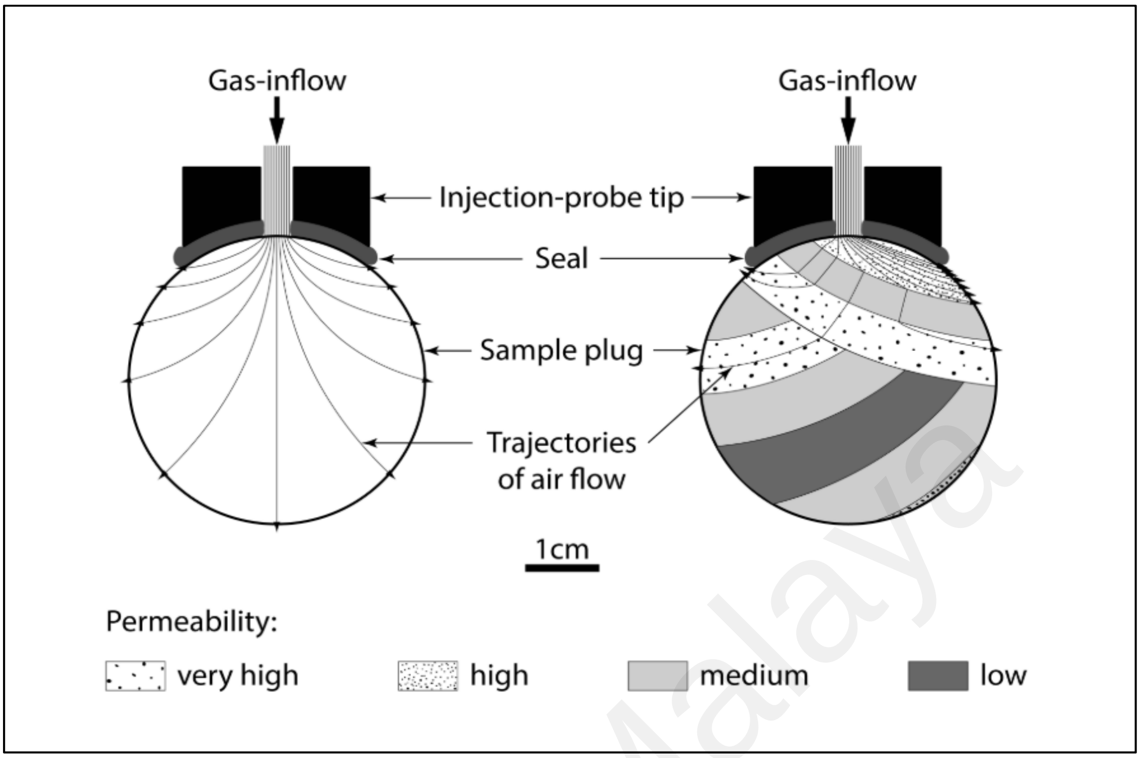

Figure 8.60: Gas-flow trajectories for (a) homogeneous samples and (b) heterogeneous samples. Such structures strongly affect flow geometry by inducing preferential flow, which creates issues in determining volume and area represented by surface permeability measurements.

8.2.4 Sample 210: Sandy Heterolithic

Sample 210, a sandy heterolithic rock type, is different than sample 127 and 148 despite being a sandstone dominated sample because of its lower measured and computed permeabilities. This sample is located 18 m below sample 148 and was extracted from a sandstone region that is sandwiched between two thin mudstone layers (Figure 8.61). The sandstone in sample 210 has a smaller median grain diameter at 68 μm compared to core plug 127 and 148, which have median grain sizes of 103 μm and 92 μm respectively.

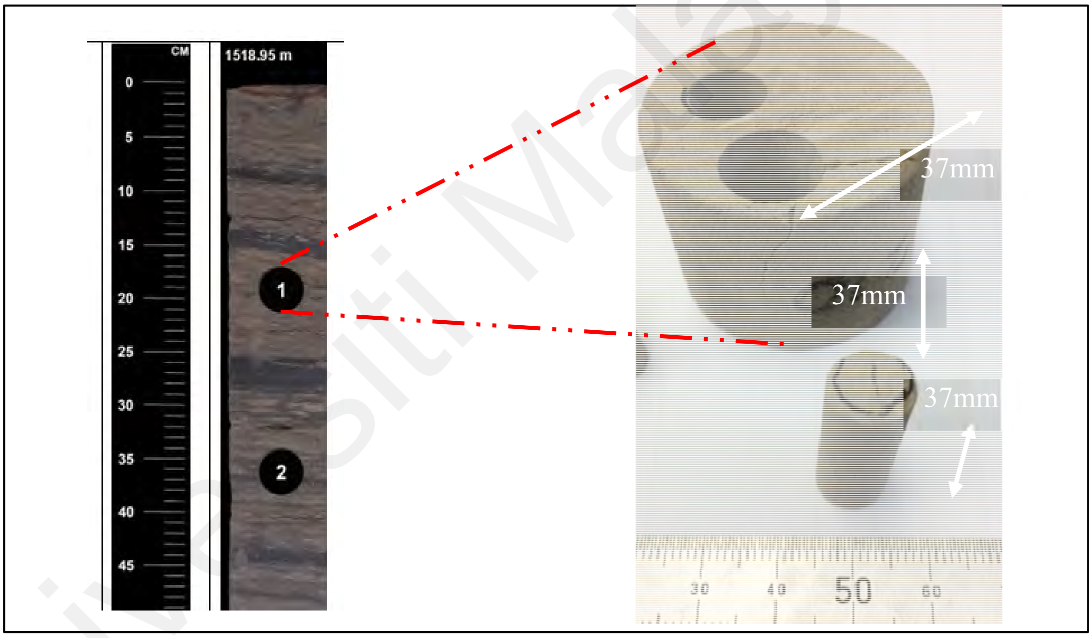

Figure 8.61: A view of core plug 210 and the core slab that indicates light-coloured sandstone with interbedded mudstone and siltstone layers.

8.2.4.1 Segmentation and 3D visualization of Sample 210

The XMCT images of core plug 210 in Figure 8.62 indicate a sandstone dominated core plug sparsely interbedded with very thin carbonate laminates. Core plug 210 was segmented into sandstone and carbonate phases in Figure 8.63 and rendered into a 3D volume using Drishti. The carbonate in core plug 210 makes up 11% of the total volume of the core plug and consist of very thin laminates (or ribbons) that are at least 1 mm thick and concentrated in the middle region of the core plugs as shown in Figure 8.63. These thin carbonate laminates are deposited at an angle of about 23 degrees angle in the x-direction. The thickness, continuity and angle of these thin sheets could have an impact on the permeability of the core plug and mini plug as previously observed in core plug 127.

The segmented images of mini plug 210 in Figure 8.64 has a computed porosity of 25.2%, which is 10% lower than the RCA measured core plug porosity of 28%. We attributed the lower computed porosity to the carbonate laminates in mini plug 210 or subjective segmentation process that may have underestimated the porosity. However, the computed porosity is acceptable due to the small 10% difference compared to the RCA measured porosity of core plug 210.

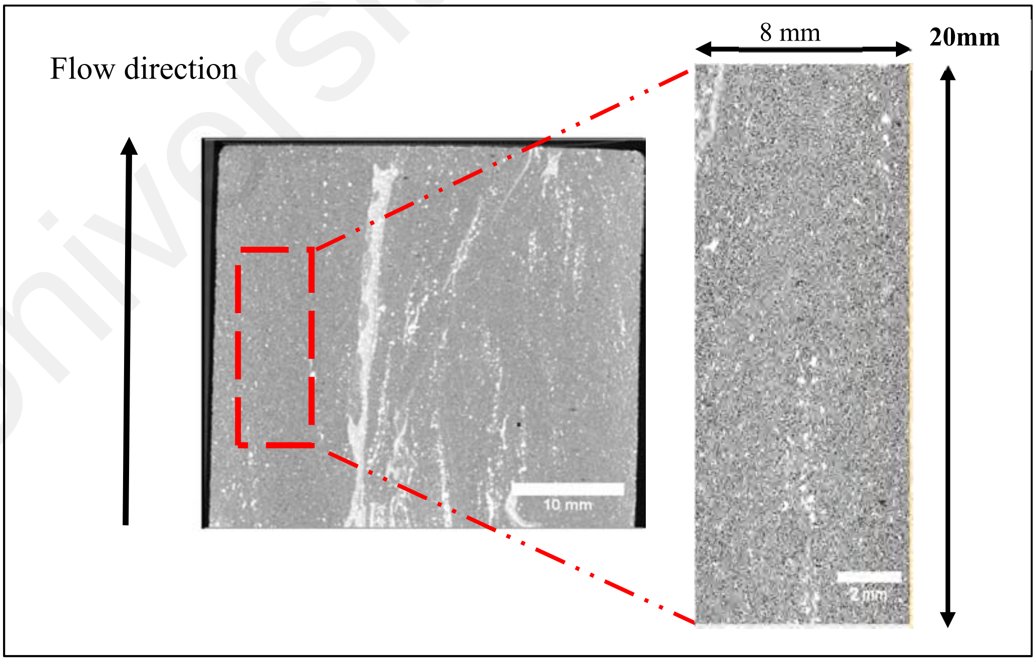

Figure 8.62: Left: Low-resolution image (37 microns/voxel) and Right: High-Resolution image (3.76 microns/voxel) tomograms of Sample 210. The location of mini-plug relative to the core plug is an approximation.

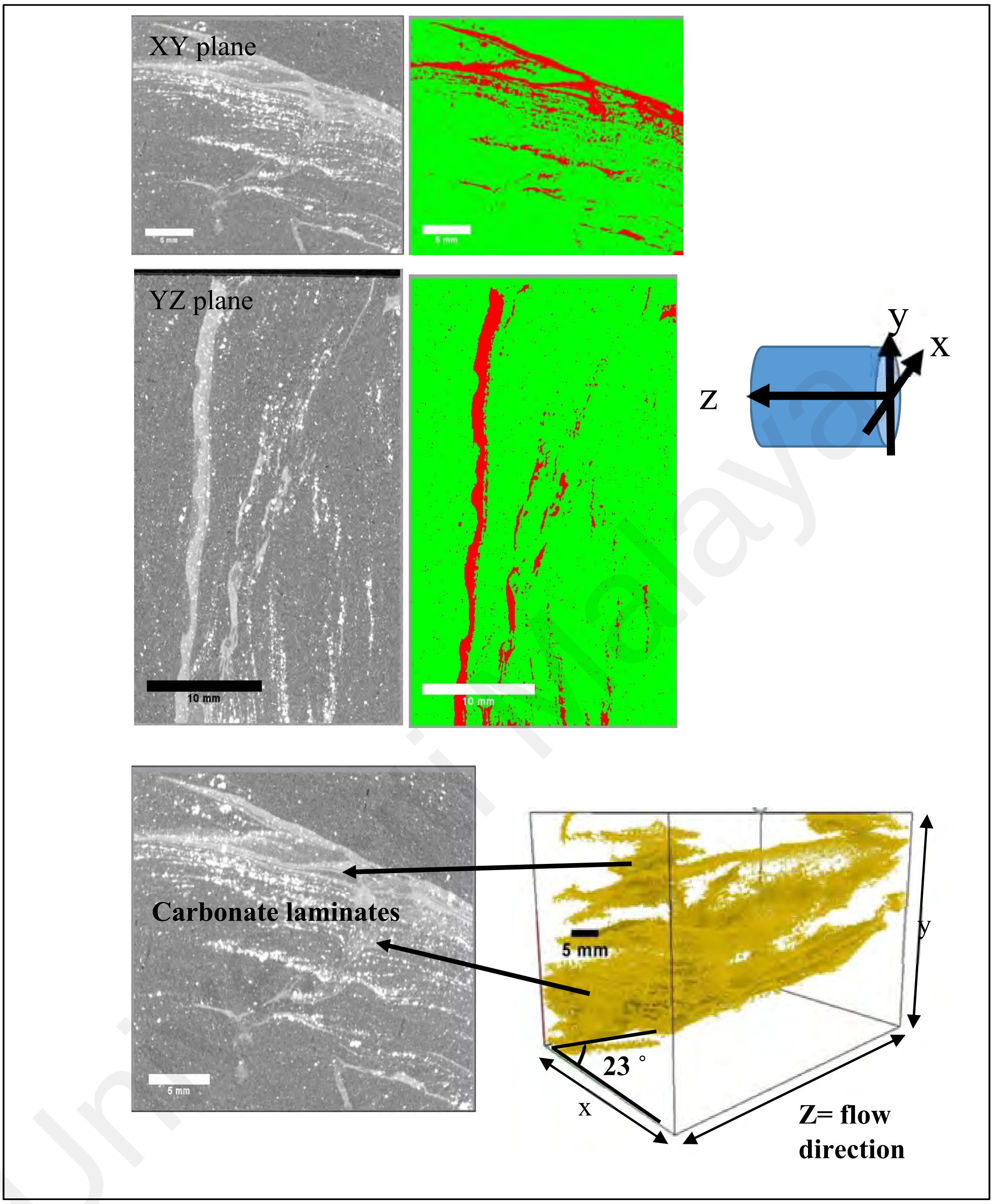

Figure 8.63: Top and Middle Images are greyscaled images and segmented images of core plug 210. The left bottom left image is a rendered 3D volume of core plug 210 showing the calcium carbonate phase tagged in yellow. The segmented calcium carbonate in core plug 148 occupies 11% of its volume.

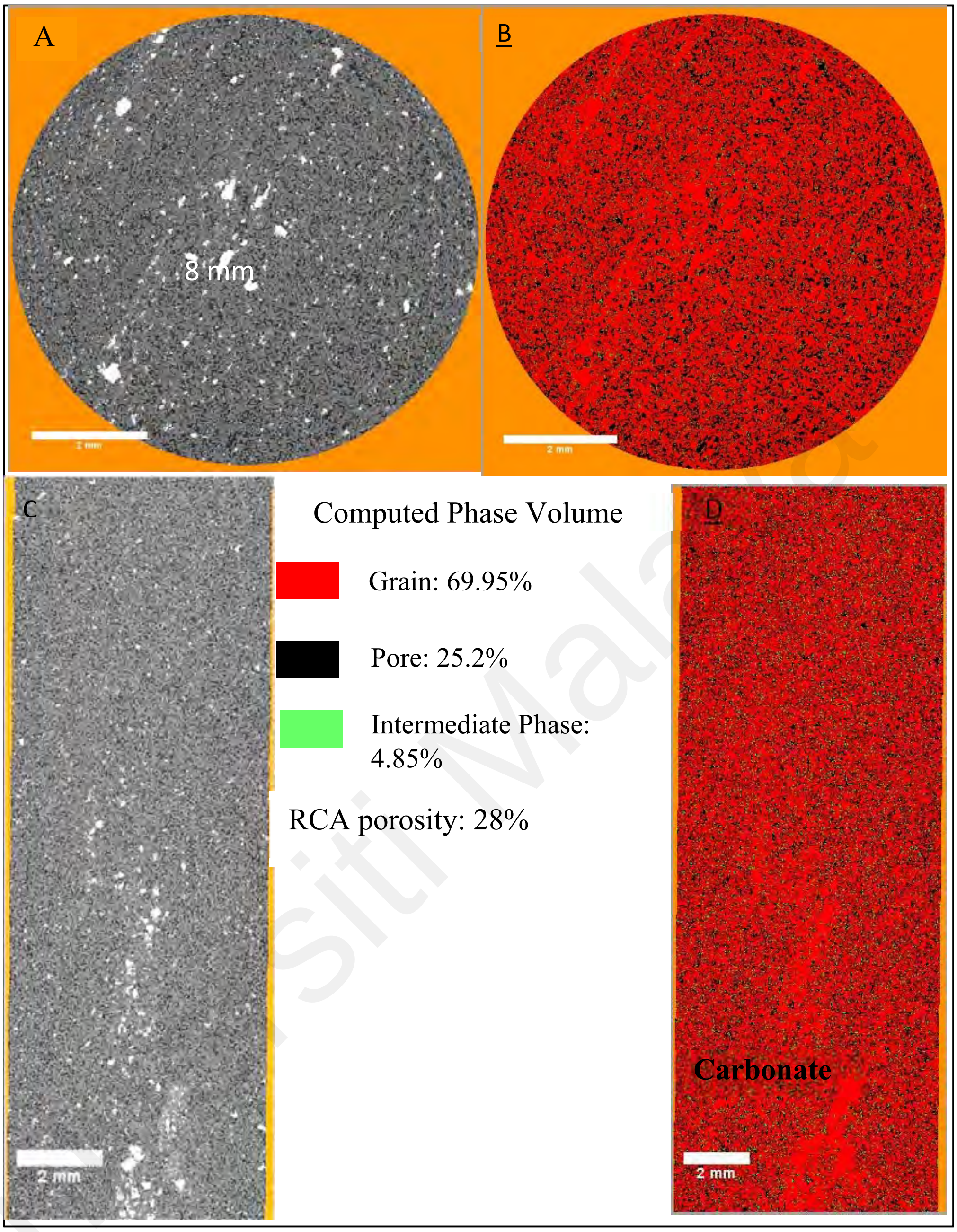

Figure 8.64: Image A and C: Greyscale image of Mini Plug 210. Image B and D: Segmented images of Mini Plug 210. The sandstone grains in mini plug 210 are very fine and well connected with little signs of heterogeneity.

8.2.4.2 Discussion of Permeability Results of Sample 210

Table 8.16 summarises the computed and measured permeability results for sample 210. Firstly, Figure 8.65 shows that the computed average permeability of mini plug 210 at 251 mD (300 voxels^3) and 239 mD (400 voxels^3) are relatively similar to the RCA core plug permeability at 287 mD with 12% and 16% differences respectively. The substantial similarity between the computed and RCA results suggests that Sample 210 is relatively homogeneous at the core plug and mini plug scale.

Compared to sample 127 and 148, the average core plug and mini plug permeability of sample 210 are substantially lower. Core plug 210 permeability at 287 mD sizes is 54% lower than core plug 127 (633 mD) and 27% lower than core plug 148 (395 mD) for 300 voxels^3 sub-volume. Meanwhile, the computed permeability at 300 voxels sub-volumes of mini plug 210 at 251 mD is 81% lower compared to mini-plug 127 at 1358 mD and 69% lower compared to mini-plug 148 at 812 mD. This difference can be correlated mainly to the smaller median grain diameter of the sandstone in sample 210 which at 36 mD is at least 2.5 times smaller than the median grain diameter of the sandstone in sample 127 and 148 at 103 µm and 92 µm respectively. Figure 8.66 shows the impact of median grain size differences on the permeability of sample 127, 148 and 210. The figure shows that the sandstone in mini-plugs 127 and 148 have significantly larger median grain sizes and higher permeability than mini plug 210. This trend shows that grain size is a leading factor in the lower permeability of the sandstone in mini plug 210 when compared to mini-plugs 127 and 148.

Despite the presence of 11% carbonate laminates in core plug 210, the thin laminates do not seem to cause significant impact on the permeability of mini plug and core plug 210. Table 8.16 shows that the computed permeabilities of core plug 210 differ by 12%

(300 voxels^3) and 16% (400 voxels^3) when compared to the RCA measured permeability of core plug 210. This relatively small difference suggests that the thin carbonate laminates do not affect fluid flow at both scales. Hence permeability is consistent. This result also suggests for largely homogeneous sandstone; the RCA results should be a good reference.

The NER permeameter probe diameter at 4mm is relatively similar to side lengths of the sub-volumes of mini plug 127 at 1.16 mm (300 voxels^3) and 1.55 mm (400 voxels^3) used by MORPHY to compute permeability as shown in Table 8.17. Due to their similar resolution, we used the NER results to validate the computed permeability results of mini plug 210.

Table 8.16: Permeability results from MORPHY calculation, Experimental Core Analysis Gas Probe measurements. MORPHY results represent the 8 mm diameter mini-plug while the Experimental Core Analysis and NER gas probe measurements represent the 37mm diameter core plug.

Method	**MORPHY (Mini Plug)**		**Experimental Core Analysis (Core Plug)**			**NER (Core Plug)**
Details	**300 voxels^3**	**400 voxels^3**	**Klinkenberg Horizontal (**	**Air Horizontal**	**Routine Core Analysis**	**NER Gas probe**
Average	251.4 mD	239.1 mD	253.8 mD	254.6 mD	287 mD	391.9 mD
Maximum	536.4 mD	493.7 mD	262.0 mD	262.0 mD	N/A	685.6 mD
Minimum	31.2 mD	55.0 mD	246 mD	250 mD	N/A	117.3 mD
Standard Deviation	210.0 mD	210.7 mD	6.18 mD	5.08 mD	N/A	125.0 mD

Table 8.17: Comparison between the two sub-volumes sizes used in MORPHY to calculate the permeability in mini plug 210.

Edge Length in voxels	Resolution in voxel per mm	Side Length in mm	Cubic Volume in mm^3
300	0.00387	1.161	1.56
400	0.00387	1.548	3.71

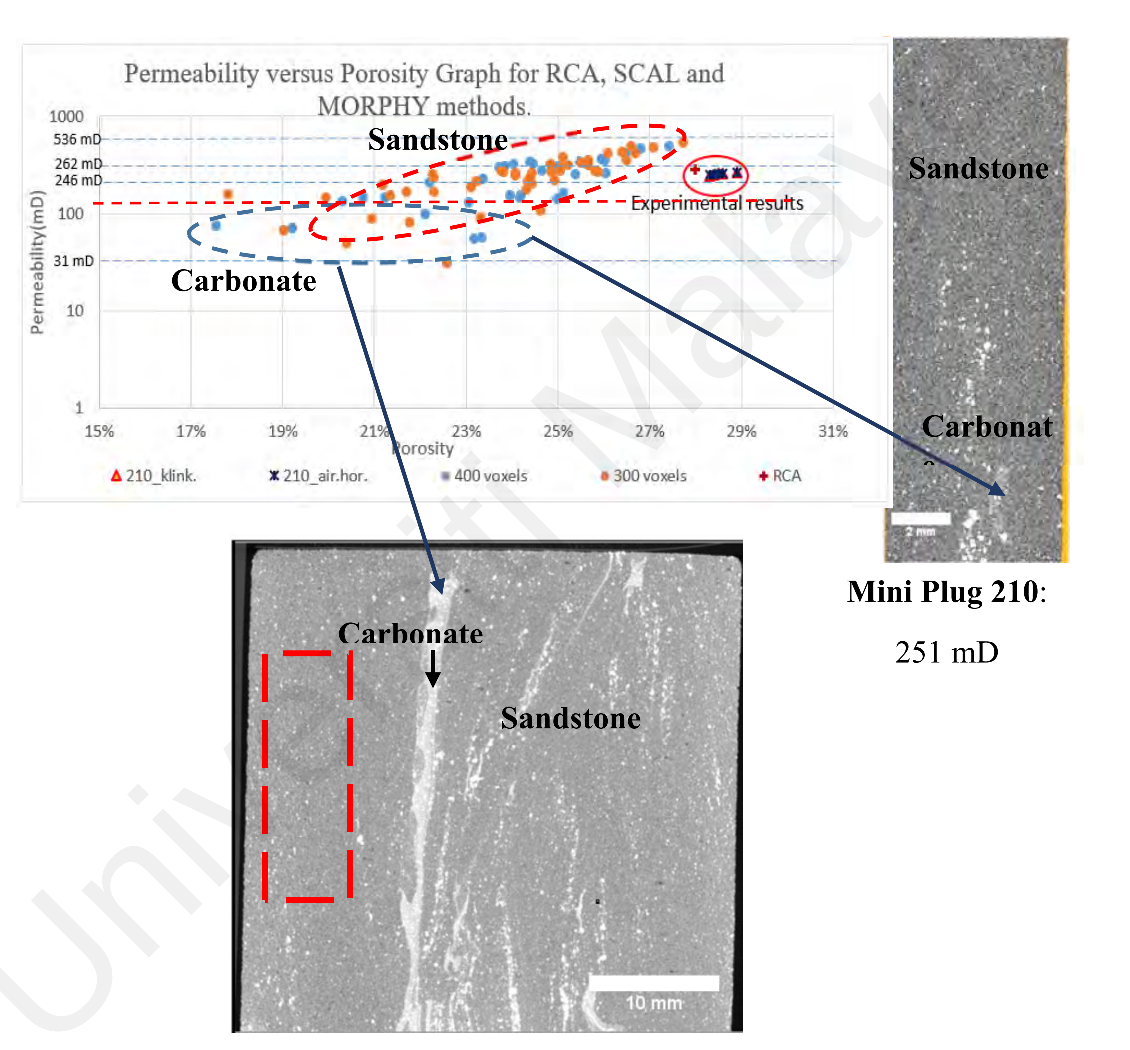

Core Plug 210: 287 mD

Figure 8.65: Permeability versus Porosity graph of Routine Core (RCA), Special Core Analysis (SCAL) and MORPHY (for 300 voxels and 400 voxels sub-volumes). The Klinkenberg horizontal permeability and horizontal air permeability are the experimental

Special Core Analysis results with a range between 253 mD to 287 mD while average computed permeabilities range is from 239 mD to 251 mD.

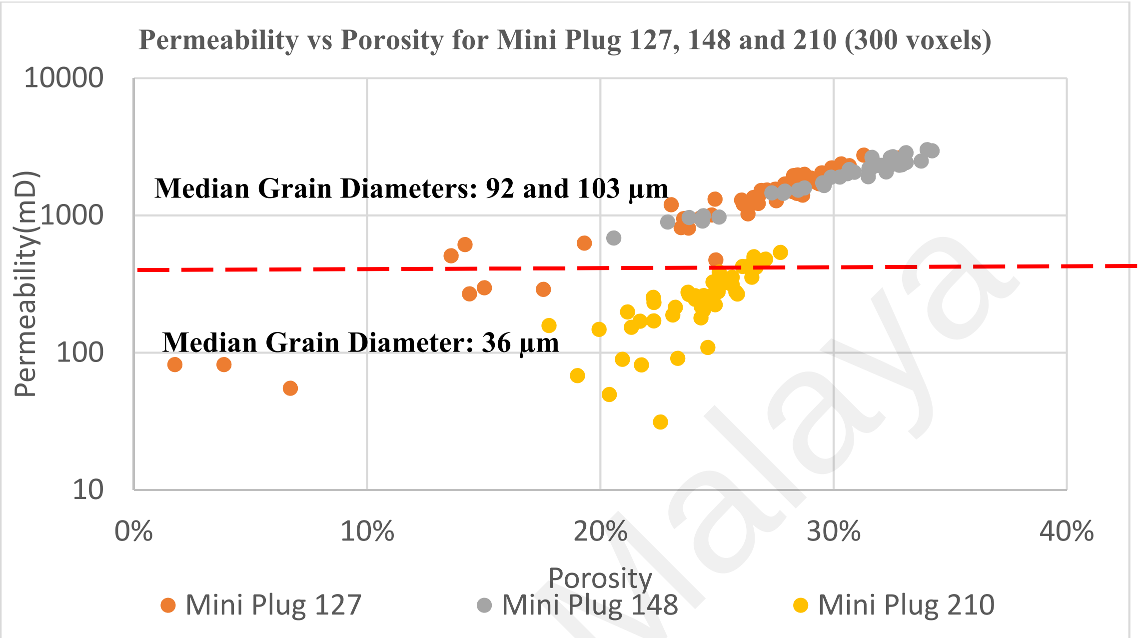

Figure 8.66: The porosity and permeability distribution of mini plug 127, 148 and 210. The results show that the permeability datapoints of mini plug 210 are lower than the other mini plugs. The grain size in mini plug 210 is smaller than in the other mini-plugs by at least 2.5 times that contributed to the lower permeability of mini plug 210.

8.2.4.3 Comparison between MORPHY computed permeability and Gas probe measured permeability

The histogram in Figure 8.67 shows the computed permeabilities, and the NER measured surface permeabilities. The histogram suggests an excellent match between both results. However, the average surface permeability at 392 mD is 56% and 64% higher than the computed mini-plug permeability at 251 mD (300 voxels^3) and 239 mD (400 voxels^3) respectively. However, the histogram in Figure 8.67 still shows an excellent match and similarity between the two results that share similar permeability ranges and frequency. The excellent match and similarity between the surface permeability, computed permeability and RCA measured permeability is attributed to the relatively high level of homogeneity in sample 210 at the mini plug and core plug scale compared to the other samples examined in this thesis.

The permeability map of core plug 210 in Figure 8.68 shows some contrast between the highly permeable red sandstone regions (above 300 mD) and the low permeability green regions (below 100 mD) which represent some of the carbonate laminates. We noted that carbonate in sample 210 has permeability below 100 mD similar to the carbonate in sample 127 and 148. Our results for sample 127, 148 and 210 show that the DCA method and permeameter measurements are useful for differentiating sandstone from carbonate, which has distinct permeability ranges.

In Figure 8.67, the measured surface permeability datapoints on core plug 210 are dominated by data points that are above 400 mD with a total frequency of about 70%, resulting in a high averaged surface permeability at 409 mD. On the other hand, in mini plug 210, less than 30% of its data points are above 400 mD. This lower value occurs because the NER permeameter measured the surface permeability over a larger surface area. In contrast, the permeability datasets of mini plug 64 are represented by a smaller number of sub-volumes. Therefore, the larger surface area of core plug 210 provides more permeameter data points compared to the smaller number sub-volumes in mini plug 210 used by MORPHY to compute permeability. This difference may have resulted in statistical bias between the permeability results of MORPHY and the NER permeameter.

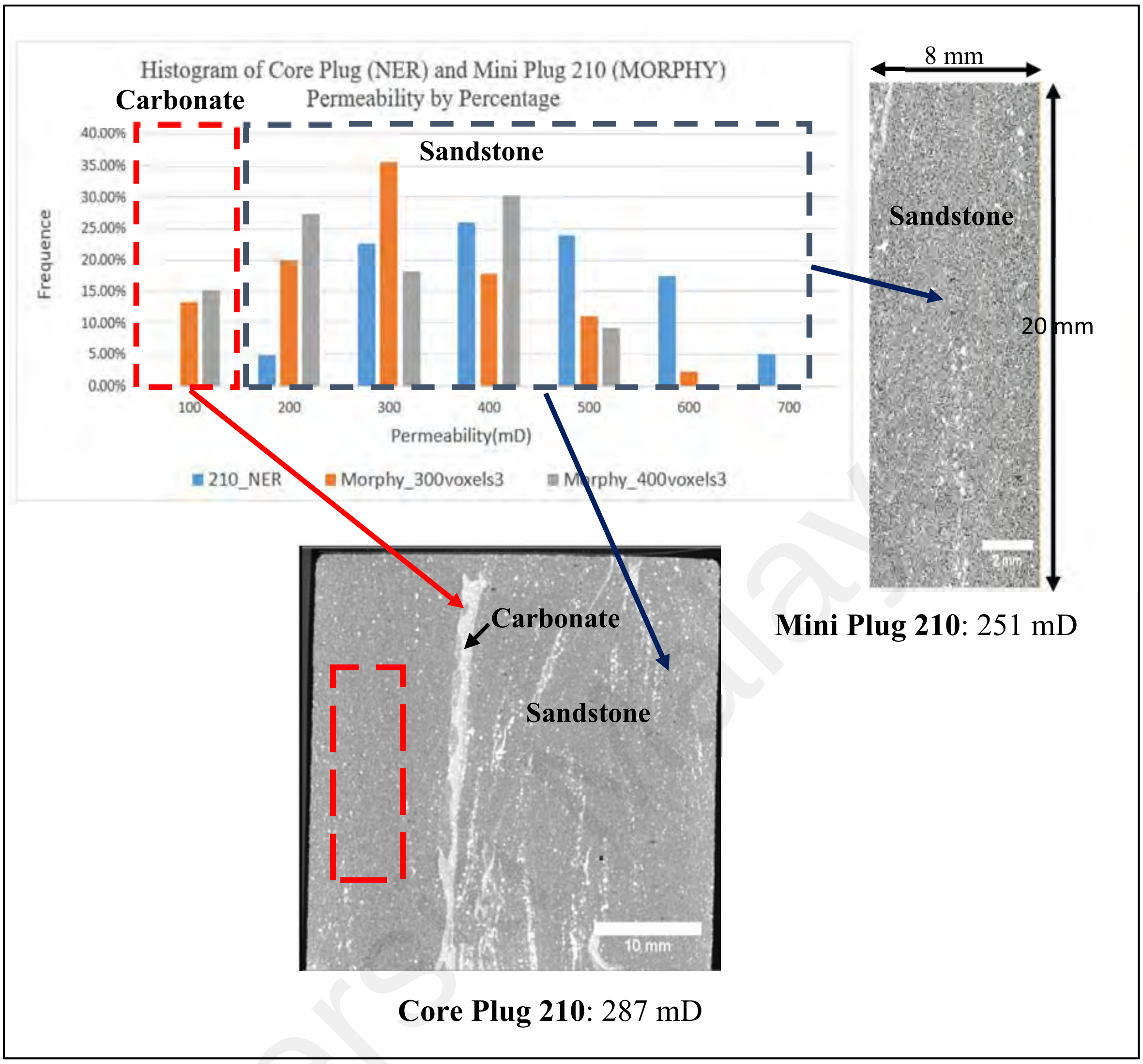

Figure 8.67: Histogram of Permeability results from using MORPHY and the NER Gas Probe of Sample 210. There is some degree inconsistency between the MORPHY computed permeabilities and the NER gas probe measured permeabilities though many of the NER gas probe results are on the higher side. The NER gas probe averaged permeability is at least 60% higher than the averaged computed permeability.

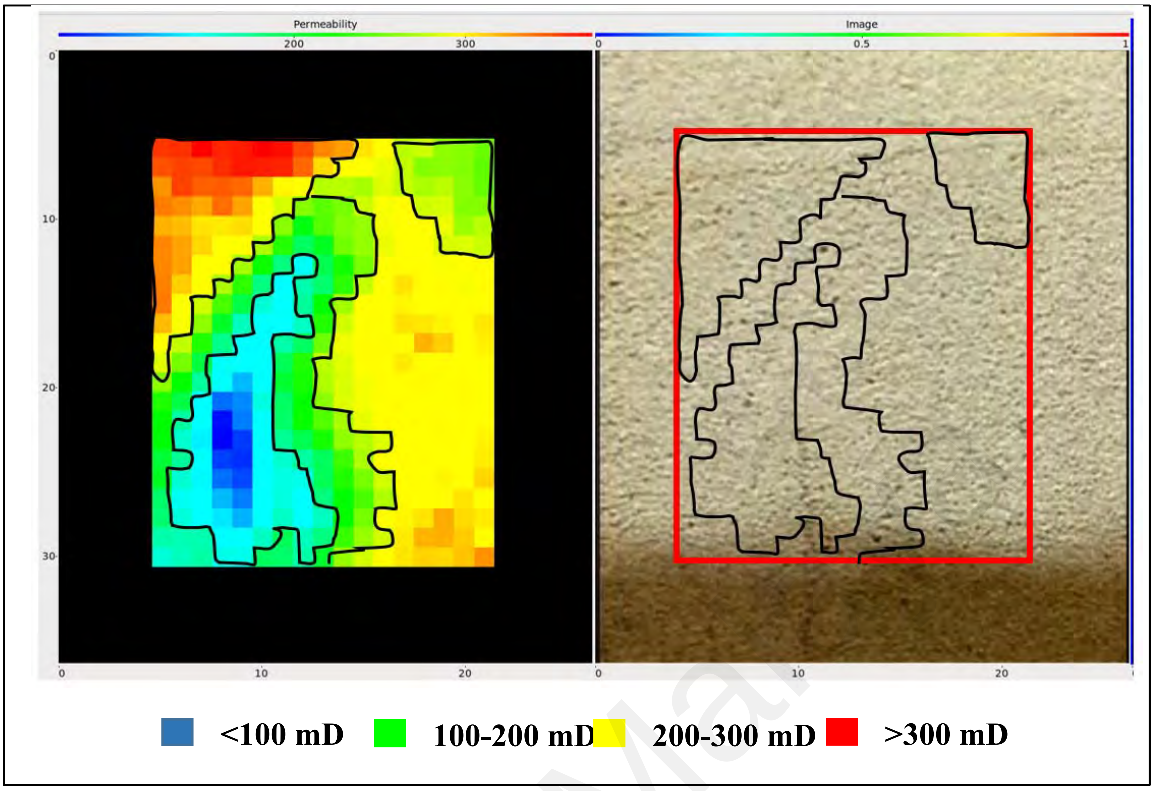

Figure 8.68: Permeability on the surface of the core plug 210 from the NER permeameter. The blue/green areas are low permeability mudstone dominated regions that are below 100 mD while the yellow/green/red areas are permeable sandstone regions that are above 100 mD.

8.2.4.4 Conclusion for Sample 210

Sample 210 exhibit consistent permeability at the core plug and mini plug scales, which suggests that core plug 210 is a relatively homogeneous sandstone but with a smaller median grain size of 36 µm when compared to the other sandstone core plugs 127 and 148. Also, XMCT imaging and 3D visualization reveal the presence of thin carbonate laminates concentrated in the middle of the core plug. Despite the presence of heterogeneity, the sandstone in core plug 210 is well connected and continuous while the carbonate laminates location does not seem to restrict fluid flow. This correlation is shown by consistent permeability at the mini plug and core plug scale.

The computed permeabilities identified two constituent rocks, sandstone and carbonate in sample 210 with distinct permeability ranges. The carbonate in sample 210 is similar to sample 127 and 148, with its average permeability below 100 mD compared to sandstone which is above 100 mD.

The smaller permeability of Sample 210 compared to Sample 127 and 148 are correlated to its smaller median grain size at 36 µm compared to 103 µm and 92 µm for Sample 127 and 148 respectively. Smaller grains sizes result in lower permeability due to the linear relationship between these two parameters (Masch et al., 1966).

Permeameter measured permeabilities from the surfaces of core plug 210 have higher average permeability than computed results due to higher frequency of datapoints above 400 mD at 70% in the NER dataset compared to less than 30% for the computed results dataset. However, the histogram of the two results shows a relatively good correlation in terms of permeability range and frequency. However, the more substantial amount of surface permeability data points higher than 400 mD causes a higher average surface permeability due to statistical bias. To reduce this bias, it may be ideal to compute permeability of a volume of rock samples that have a similar number of sub-volumes as the number of data points collected by the permeameter.

8.2.5 Sample 245: Muddy Heterolithic

Sample 245 is a muddy heterolithic rock which is the same type of rock as sample 64. However, this sample is 54 meters below sample 64. Figures 8.69 and 8.70 show that core plug 245 is dominated by mudstone with little sandstone layers that we can observe on its surface. We estimated that that mudstone makes up more than 50% of the core plug volume. The thin sandstone and mudstone layers are also not continuous. They are intercalated into one another with creates poor contrast between the sandstone and mudstone layers, making it difficult to estimate the sand-to-mud ratio. There is also some degree of bioturbation observed within the structure of the beddings that altered the structure, connectivity and distribution of the thin sandstone and mudstone layers within the core plug. The average grain size in Sample 245 is 23 μm which is the smallest among the five samples.

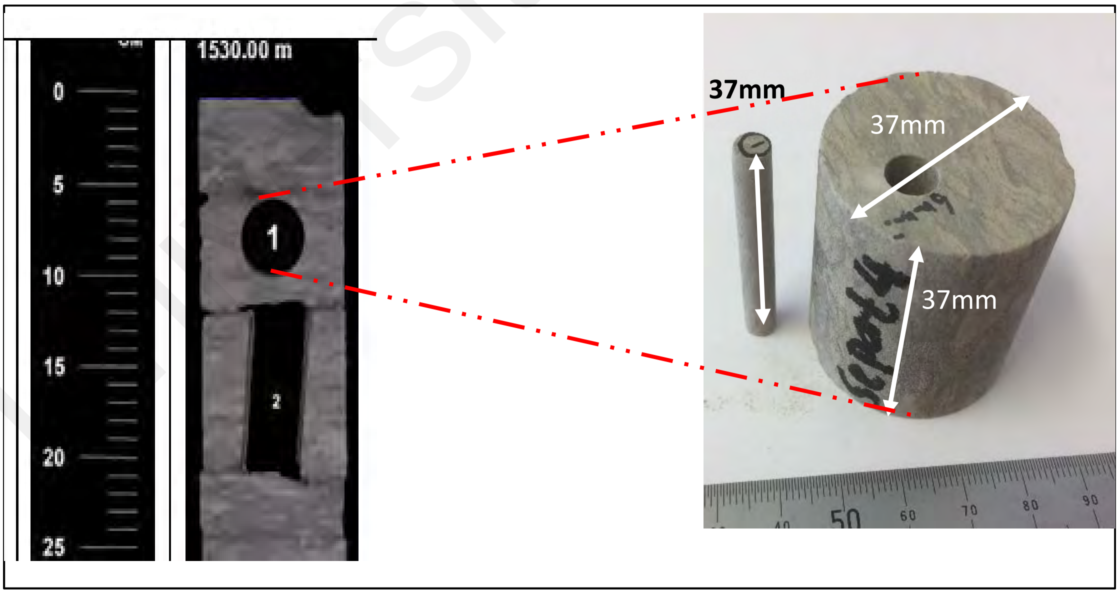

Figure 8.69: A view of core plug 245 and the core slab that indicates dark-coloured mudstone with intercalated with thin streaky layers of light-coloured sandstone.

8.2.5.1 Segmentation and 3D Visualization of Sample 245

In Figure 8.71, we segmented core plug 245 into mudstone and sandstone which shows that the disconnected sandstone phase makes up 17.94% of the core plug volume which is comparable to the sandstone content in sample 127 and 148 at between 15 and 16% respectively. The segmented image and 3D visualization of core plug 245 in Figure 8.71 reveal that the sandstone phase consists of tiny pockets of thin sandstone layers within a tight mudstone matrix. These thin sandstone layers in core plug 245 seem to be poorly connected and not continuous. In contrast, we observed that the sandstone layers in core plug 64 are well connected and continuous.

Figure 8.72 shows that the segmented image of mini plug 245 has a computed porosity of 15%, which matches the RCA core plug porosity at 15%. We attributed this excellent match to the uniform distribution of the sandstone and mudstone in core plug 245.

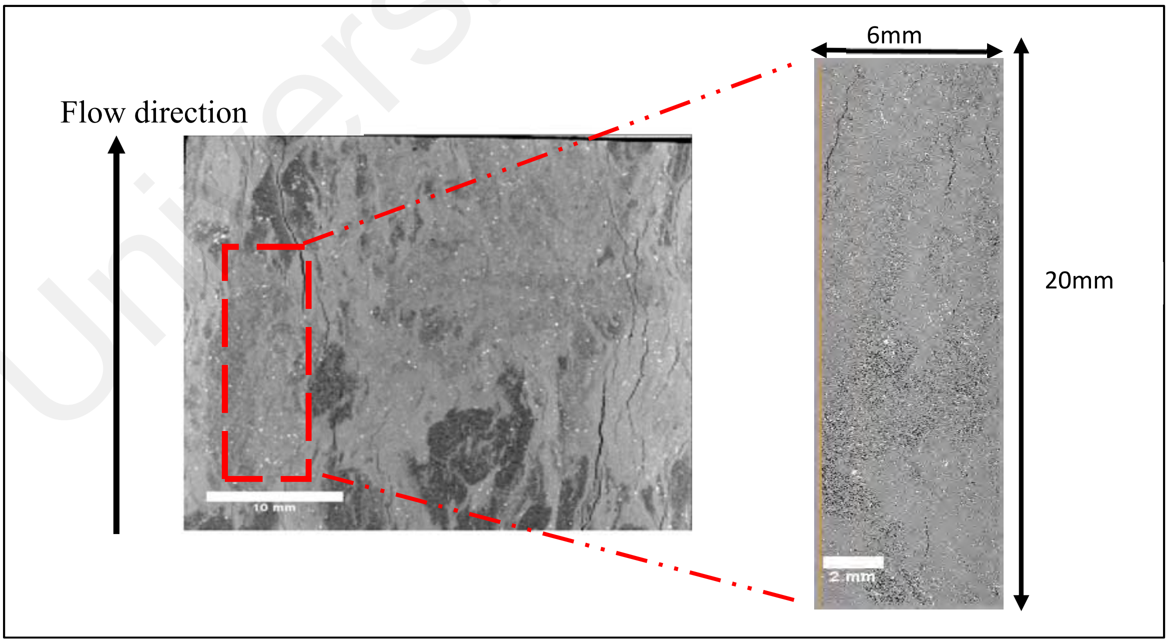

Figure 8.70: Left: Low-resolution image (37 microns/voxel) and Right: High-Resolution image (3.76 microns/voxel) tomograms of Sample 245.

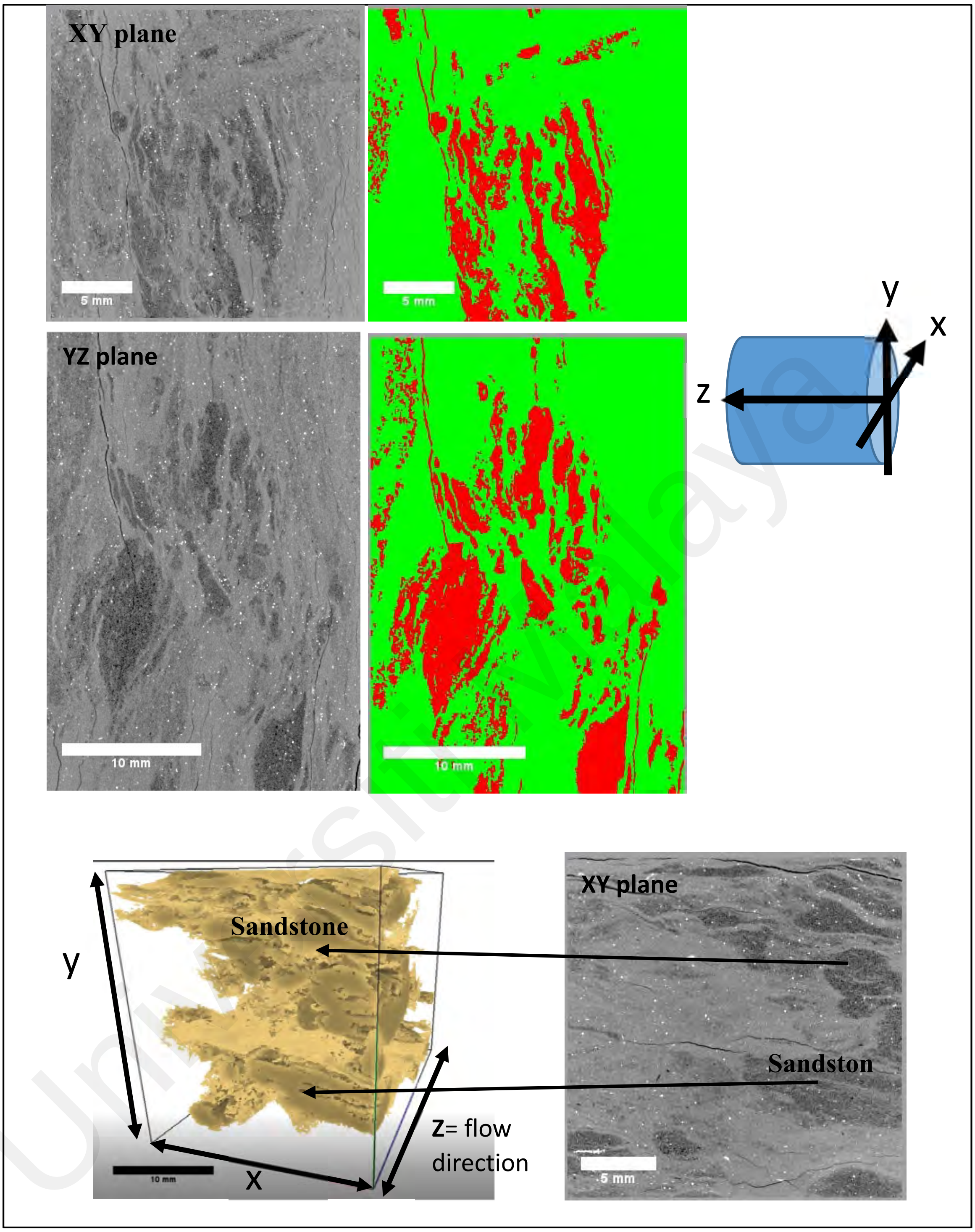

Figure 8.71: Top and Middle Images are greyscaled images and segmented images of core plug 245. The left bottom left image is a rendered 3D volume of core plug 245 showing the sandstone phase tagged in yellow. The segmented mudstone in core plug 245 occupies 17.9% of its volume.

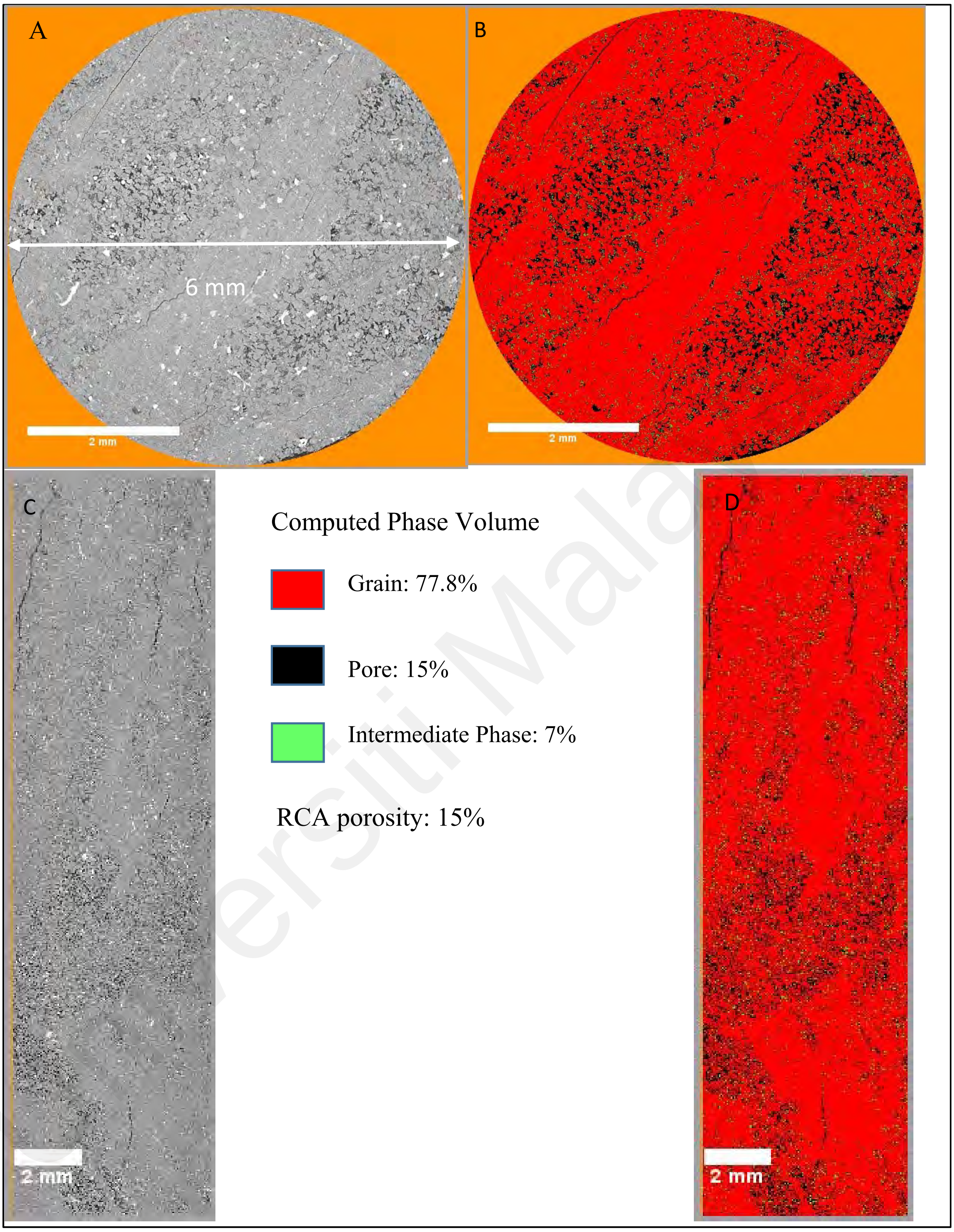

Figure 8.72: Greyscale and segmented images of Mini Plug 245. Image A and C: Greyscale images. Image B and D: Segmented Image and C. It is noted that pores in mini plug 245 are poorly connected and separated by mudstone grains with almost no porosity.

8.2.5.2 Discussion of Permeability Results of Sample 245

Table 8.18 shows the computed permeabilities for mini plug 245 are 64.7 mD (300 voxels^3) and 13.6 mD (400 voxels^3) compared to the RCA core plug permeability 0.9 mD. We attributed this considerable divergence to a high level of multi-scale heterogeneity in sample 245, as different volume sizes of the same sample exhibit different permeabilities. As a result, the RCA measured core plug permeability, which is only 0.9 mD is at least 15 times lower compared to the computed permeability of mini plug 245 at 13.6 mD (300 voxels^3). Most importantly, the computed and measured permeabilities of sample 245 are consistently very low (below 100 mD), which suggests that the permeabilities of sample 245 are generally very low at all length scales and volume sizes.

In Figure 8.75, a majority of the permeability data points from MORPHY and NER permeameter results in mini plug 245 are below 10 mD, indicating a primarily impermeable mudstone matrix. Also, Figure 8.76 shows the permeability-to-porosity data points of mini plug 245 do not match with any of the data points of other mini plugs. Only three data points in mini plug 245 correlate with the data points in mini plug 210 indicating the sandstone in mini plug 245 is very fine-grained. The average grain size in Sample 245 is 23 µm, which is only 7 µm higher than Sample 210. Also, both sample 210 and 245 are 10 meters apart. Hence the sandstone in both samples should be relatively similar as they should have the same sediment source.

The NER permeameter probe has a diameter of 4mm which is relatively similar to side lengths of the sub-volumes of mini plug 127 at 0.85 mm (300 voxels^3) and 1.13 mm (400 voxels^3) used by MORPHY to compute permeability as shown in Table 8.19. Due to their similar resolution, we used the NER permeameter results to validate the computed permeabilities of mini plug 245.

Table 8.18: Permeability results from MORPHY calculation, Experimental Core Analysis Gas Probe measurements. MORPHY results represent the 6 mm diameter mini-plug while the Experimental Core Analysis and NER gas probe measurements represent the 37mm diameter core plug.

Sample 64	MORPHY (Mini Plug)		Experimental Core Analysis (Core Plug)	NER (Core Plug)
Details	**300 voxels^3**	**400 voxels^3**	**Routine Core Analysis**	**Gas probe**
Average	64.7 mD	13.6 mD	0.9 mD	28.4 mD
Maximum	640.8 mD	332.7 mD	N/A	107.0 mD
Minimum	0.1 mD	1.3 mD	N/A	1.9 mD
Standard Deviation	136.8 mD	53.7 mD	N/A	26.7 mD

Table 8.19: Comparison between the two sub-volumes sizes used in MORPHY to calculate the permeability in mini plug 245.

Edge Length in voxels	Resolution in voxel per mm	Side Length in mm	Cubic Volume in mm^3
300	0.00282	0.846	0.61
400	0.00282	1.128	1.44

8.2.5.3 Comparison between MORPHY computed permeability and Gas probe measured permeability

The histogram in Figure 8.73 compares the computed permeabilities of mini plug 245, to the NER permeameter measured surface permeabilities of core plug 245. The histogram shows an excellent match between both datasets. The histogram shows that two datasets show that more than 50% of the sub-volumes and the surface permeabilities of mini plug and core plug 245 respectively are below 10 mD. As a result, low permeability mudstone dominated the permeability of the mini plug and core plug.

Figure 8.74 shows the NER permeability map of core plug 245 that illustrates the low permeability contrast between the sandstone and mudstone on the surface of the core plug 245. This low contrast shows that there is a minimal gap between the permeability of the sandstone and mudstone in core plug 245. The permeability contrast between the adjacent two rock types is the lowers compared to the other core plugs. We attributed this poor permeability contrast between the sandstone and mudstone as a result of bioturbation that caused mudstone and sandstone to intermix. The intermixing between the sandstone and mudstones causes the sandstone to incorporate fine-grain mudstone that caused the sandstone to have smaller average grain size and lower permeability than the cleaner sandstone in other core plugs.

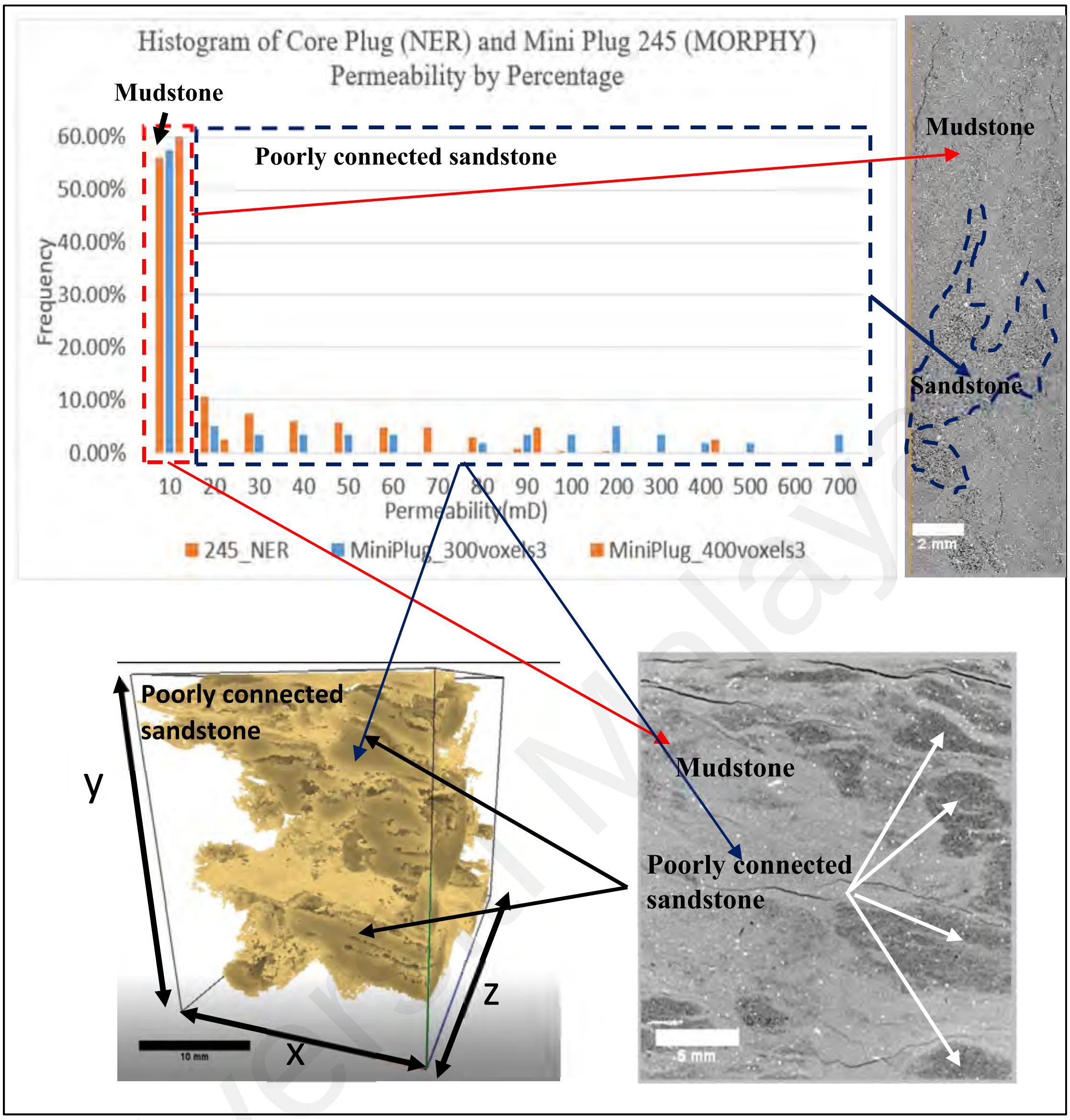

Figure 8.73: Histogram of Permeability results from using MORPHY and the NER Gas Probe. There is a reasonable degree of consistency between the two datasets.

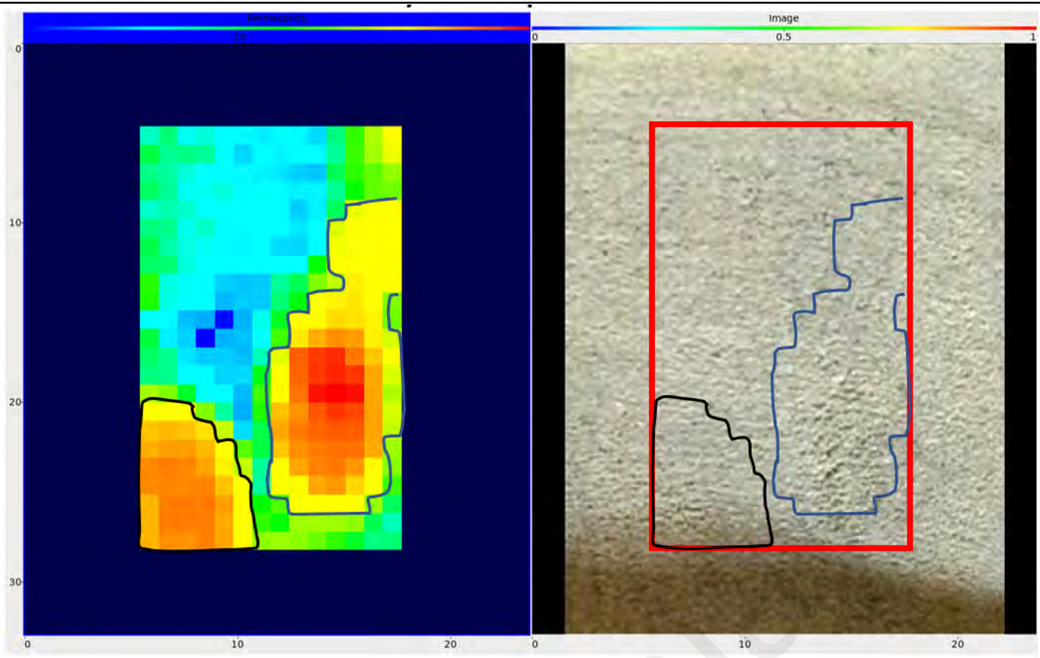

Figure 8.74: Permeability map of the surfaces of core plug 245 showing permeability contrast between sandstone (yellow and red) and the tight mudstone matrix (green and blue)

8.2.5.4 Conclusion for Sample 245

XMCT imaging and 3D volume visualization of mini plug and core plug 245 indicate a heterogeneous rock that is uniformly distributed in core plug 245. Core plug 245 is dominated by mudstone with some sparsely disconnected sandstone regions. XMCT imaging and 3D visualization show that sandstone makes up 17.9% of the core plug volume. However, due to the poor connectivity and continuity of the sandstone in core plug 245, its permeability is only 0.9 mD.

Computed permeabilities of mini plug 245 at the 300 voxels^3 and 400 voxels^3 are 64.7 mD and 13.7 mD respectively, which are very low compared to the mini-plugs of from the other core plugs. The substantial divergence between two sub-volumes suggests a high level of heterogeneity within mini plug 245. The 300 voxels^3 sub-volumes most likely sampled more sandstone than the 400 voxels^3 sub-volumes which suggests that the sandstone in core plug 245 are not uniformly distributed as previously suggested. As a result, different length scale and volume sizes have different permeability values. The average computed permeabilities of mini plug 245 are at least 15 times larger than the RCA measured core plug permeability, which is only 0.9 mD However, the mini plug permeabilities are still too low when benchmarked to the reference reservoir sandstone in mini-plugs 64, 127 and 148. As a result, we validated Sample 245 as non-reservoir heterolithic rock which is unlikely to contain any hydrocarbon.

The NER measured permeabilities shown previously in Figure 8.73 match very well with the computed permeabilities. 50% of the permeabilities of both datasets are below 10 mD. We attribute this low permeability to the impermeable mudstone matrix with poorly connected and discontinuous sandstone layers.

We attributed the poor connectivity and continuity of the sandstone layers in core plug 245 to a post-deposition disturbance called bioturbation. Bioturbation is caused by the movement of living organisms in the sediment, which destroyed the connectivity and continuity of the sandstone layers. The destruction of the sandstone layers reduced the effective porosity and permeability of the rock (Tonkin et al., 2010) as fluid cannot flow through the poorly connected sandstone phases. The action of bioturbation also reduces the quality of the sandstone by mixing the sandstone the fine-grained mudstone and silt, which reduces the average grain size, effective porosity and permeability. Also, bioturbated laminated structures in heterolithic beddings in Malaysia where core plug 245 comes from cause uncertainty in measuring reservoir properties such as permeability accurately across different scale lengths and volume sizes (Ben-Awuah et al., 2015; Carney et al., 2008; Heavysege, 2002).

To sum up, bioturbation destroyed the connectivity of the sandstone layers in poor quality heterolithic rocks. It reduced the quality of the sandstone through intermixing with mudstone, resulting in bioturbated heterolithic rocks in core plug 245 with poor reservoir quality. Also, the tiny average grain sizes in Sample 245 contribute to its very low permeability. We can use XMCT imaging to identify non-reservoir rocks in low resistivity heterolithic intervals such as in well X-4. 3D visualization of sample 64 and 245 differentiates reservoir from non-heterolithic rocks based on the continuity of the sandstone layers from the 3D images of sandstone layers in heterolithic rocks.

8.2.6 Summary and Conclusion

This section shows that the permeabilities at different scales vary due to the effects of multi-scale heterogeneity. Also, we show that median grain size is a leading factor to the difference in permeability between samples of similar rock types. Figure 8.75 shows that the heterogeneity manifests in the core plug and mini plug of each sample in the form of a variety of rocks, minerals and bioturbated structures adjacent to each other.. Core plug 127 and 148 represent laminated sandstone and sandy heterolithic rock types that consist of 15-16% carbonate minerals. The carbonate in core plug 148 is a large thick grain while the carbonate in core plug 127 is thin laminates. The computed permeabilities of the mini plug and RCA measured permeability of core plug of Sample 127 and 148 differ by a factor of 1.5 to 1.7 respectively. Despite the different geometries of the carbonates in these two samples, the permeability ratio between the core plug and mini plug of both samples are remarkably similar. The similar magnitude of reduction suggests that the shape and thickness of the carbonates are not a significant factor to the permeability difference between two volume sizes of the two samples. The leading factor that contributes to the permeability difference at the core plug and mini plug scale of samples 127 and 148 is the difference in median grain size. The median grain size of mini plug 127 is 11 μm larger than mini plug 148 has computed permeabilities that are 52% (300 voxels^3) and 74% (400 voxels^3) higher than mini plug 148.

Also, the results for sample 148 and 127 that represent the same reservoir sandstone show that core plug permeability can be affected by overlooked heterogeneity. XMCT imaging of core plug 148 shows that carbonate minerals make up 15% of the core plug and is the leading factor of its lower measured core plug permeability compared to core plug 127. Despite core plug 127's relative homogeneity, we find a significant difference between the computed permeability of mini plug 127 and measured permeability core plug 127. This divergence highlights that permeability within core plug 127 may be affected by thin carbonate laminates affect fluid flow within the core plug. The permeability difference between mini-plugs and core plugs of sample 127 and 148 shows the challenges in determining a Representative Elementary Volume (REV) even for sandstone due to small scales heterogeneities such as carbonate minerals that affect fluid flow. These carbonate minerals also take different shapes that may affect fluid flow differently at different volume sizes. XMCT imaging techniques and DCA are useful for computing permeability samples smaller than a standard core plug that allows for multi-scale REV analysis of sandstone and other rock types.

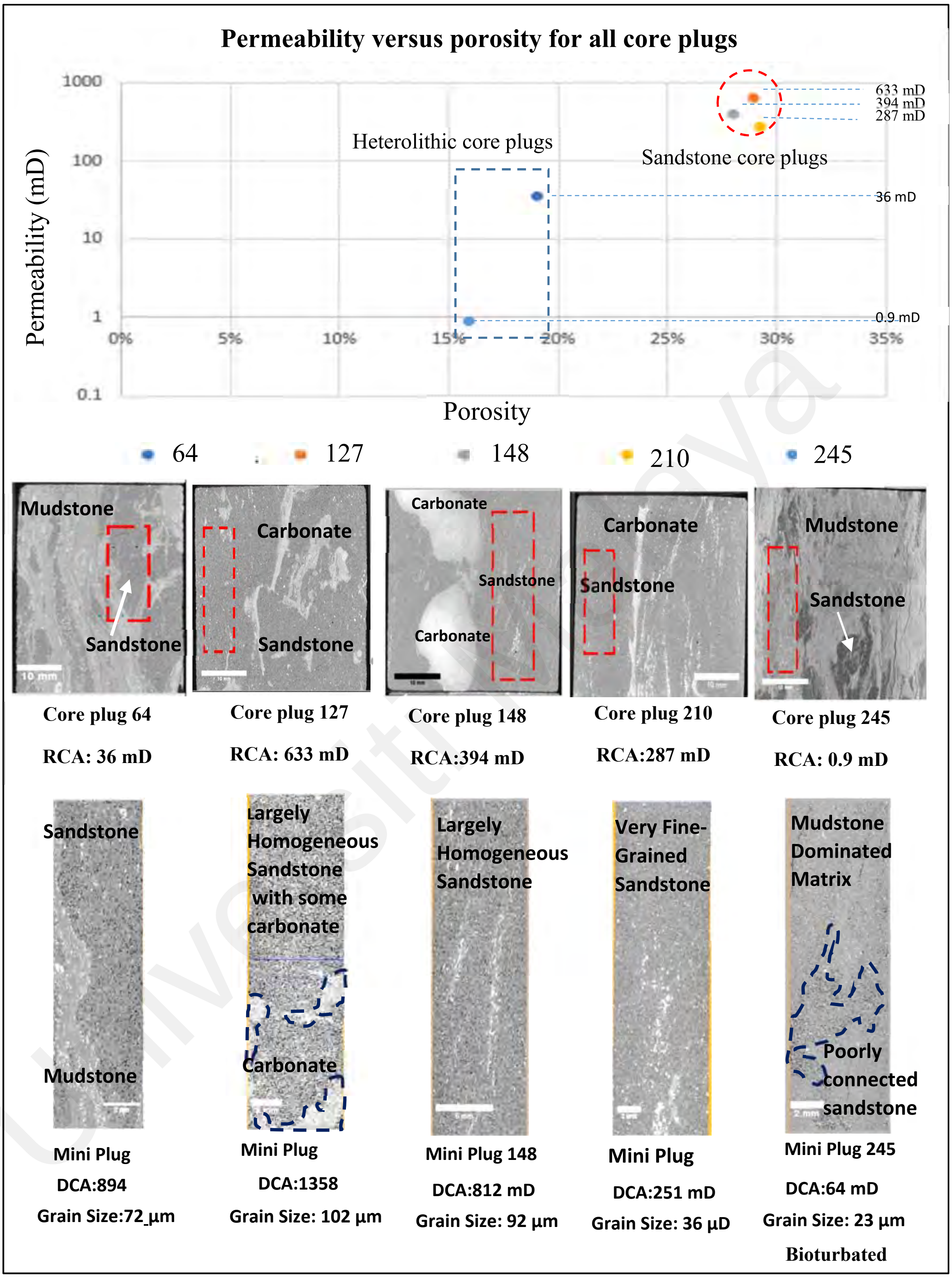

Figure 8.75: Permeability vs Porosity graph for the five core plugs followed by images of the core plugs and mini plugs indicating the different levels of heterogeneity that affect the measured (RCA) and computed permeabilities(DCA).

Meanwhile, sample 210, a relatively homogeneous sandy heterolithic rock has a significantly lower permeability compared to sample 127 and 148 due to its smaller average grain size of 36 µm compared to Sample 148 (92 µm) and 127 (103 µm.). Despite the presence of thin carbonate laminates, the computed and measured permeabilities of mini plug and core plug 210 are similar. The similar permeability at the two-volume sizes shows that core plug 210 is mostly homogeneous. 3D visualization suggests that the concentration of the thin laminates in the middle of the core plug do not restrict fluid flow which can bypass or flow between the thin carbonate laminates. This finding also suggests that the location of carbonate minerals within a volume of rock is a factor in their impact on fluid flow.

Our results show that the low RCA measured and computed permeabilities of sample 210 compared to sample 127 and 148 are directly correlated to its smaller average grain sizes. The result for sample 210 also shows that for largely homogeneous sandstone core plug samples, the experimentally measure core plug permeability may be accurate, and DCA results may not be necessary. In contrast, core plugs 127, 148, 64 and 245 consists of different rock types and minerals. For heterogeneous rocks, we recommend XMCT imaging and DCA analysis to characterize the permeabilities of the different rock types that make up the heterogeneous core plug.

In sample 64, the thin sandstone layers in the muddy heterolithic rock have computed porosity and permeability similar to the sandstone in sample 127 and 148. This similarity validates the presence of thin reservoir sandstone layers in some heterolithic rocks. These permeable sandstone layers represent additional hydrocarbon reserves potential in heterolithic deposits that cannot be resolved and measured by well logs. In contrast, 3D visualization of core plug 245 indicates that thin sandstone layers that are poorly connected and not continuous result in a lower permeability at a wide range of scales. To sum up, we can use XMCT imaging and 3D Visualization to resolve and characterize the connectivity and continuity of the thin sandstone layers in low net to gross heterolithic rocks. Our methods can improve the identification of reservoir heterolithic pay that represent additional hydrocarbon reserves in thin-bed and LRLC reservoirs. Well X-4 in Malaysia demonstrates that a low net to gross well dominated by low resistivity heterolithic rocks can be a productive gas well despite interpreted high water saturation from well logs. Our results show that the connectivity and continuity if sandstone layers are a leading factor to improved hydrocarbon reserves and production forecasts in heterolithic rocks (Massart et al., 2016) that make up thin-bed and LRLC reservoirs.

Lastly, our results show that bioturbation reworked the sandstone layers in sample 245 into disconnected and discontinuous sandstone layers and causes the sandstone and mudstone to intermix. As a result of these changes, bioturbated sample 245 has a lower median grain size, porosity and permeability that characteristically non-reservoir. We have shown that XMCT imaging and 3D visualization is useful for identifying bioturbated heterolithic rocks that do not need DCA analysis for further analysis.

The computed permeabilities and porosity in Figure 8.76 shows that the constituent rock types in the five core plugs which are reservoir sandstone, fine-grained sandstone, carbonate and mudstone generally have distinct porosity and permeability trends or gradients. We noted that the permeability-to-porosity trends of the reservoir sandstone in sample 64, 127, and 148 are very similar. The sandstone in sample 210 has a lower permeability value than the reservoir sandstone in sample 64, 127 and 148 due to its smaller grain sizes. Meanwhile, the carbonate in sample 127, 148 and 210 are consistently below 100 mD. These carbonate minerals are the leading cause of the lower measured core plug permeability in core plugs 127 and 148. Lastly, impermeable mudstones that are below 10 mD are present in core plugs 64 and 245.

We show that our DCA results are a useful reference for the permeability of constituent rock types in heterolithic rocks that consist of different rock types. Also, DCA provides computed reservoir properties such as permeability of small volume sizes at the millimetre-to-centimetre scale. Reservoir properties at these scales are vital in characterizing heterolithic rocks that consist of thin beds that have a thickness in the millimetre-to0centimetre scale. As a result, these computed small-scale reservoir properties are more accurate than core plug data that cannot measure properties of samples that are smaller than a standard core plug. As a result, experimental core plug permeability datasets have a broad range of values due to the spatial distribution of the constituent rock that causes permeability variations at different length scales (Ringrose et al., 2014).

Also, we can integrate reservoir properties at the millimetre-to-centimetre scale from DCA into a multiscale workflow for modelling heterogeneous reservoirs. This multiscale approach integrates fine-scale properties into coarse simulation grids while preserving key rock properties at all scales (Hurley et al., 2012). Multi-scale and fine-scale reservoir models can improve the predictions of hydrocarbon reserves and production in complex and heterogeneous reservoirs such as thin-bed and LRLC reservoirs (Elfenbein et al., 2005).

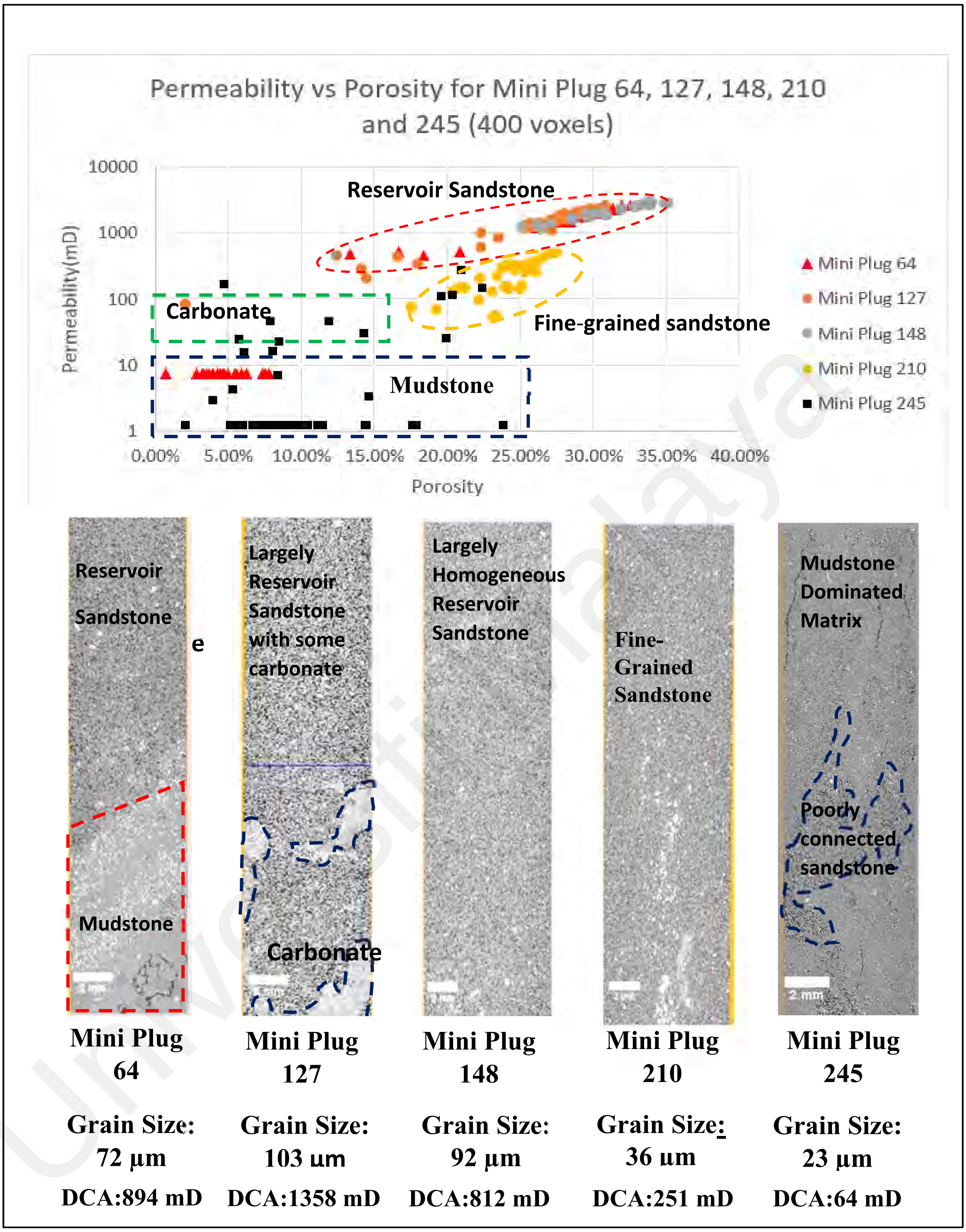

Figure 8.76: Permeability vs Porosity graph for the five mini plugs. The heterogeneity and median grain size of contributed to varying mini-plug permeability.

CHAPTER 9 : DISCUSSION AND CONCLUSION

This thesis highlights the potential of heterolithic deposits in a thin-bed LRLC reservoir in Malaysia as a commercially viable hydrocarbon reserve. Sedimentology studies show that heterolithic deposits are abundant in shallow marine environments and potentially represent a large volume of net sand pay that could contain additional hydrocarbon reserves. We used 3D volume visualization of core plugs' XMCT images to resolve the connectivity and continuity of thin sandstone layers that are a leading factor to permeability potential in heterolithic rocks. Also, we used XMCT imaging and DCA to compute the permeability of constituent rocks that make up the core plugs examined in this thesis that are more accurate than core plug data.

In Chapter 6, we show that heterolithic deposits in a Malaysian thin bed LRLC reservoir show promising potential as a source of hydrocarbon due to its sizeable volumetric abundance. The heterolithic deposits studied in this thesis are interpreted as a part of progradational tidal bar deposits with reasonable areal extent and connectivity, suggesting potential large volumes of heterolithic deposits. Characterizing the net sand pay and effective flow properties of heterolithic deposits could uncover a substantial amount of hydrocarbon reserves. However, the stacking patterns of the tidal bars may cause the heterolithic deposits to be poorly connected, causing production problem such as requiring secondary recovery programs such as production from multiple intervals or drilling additional wells.

In Chapter 7, mineralogical analysis on a laminated sandstone and a sandy heterolithic sample show an insignificant amount of clay that can cause low resistivity. These results verify that thin bed structure is the leading cause of the low resistivity pay in the Malaysian thin bed LRLC reservoir.

In Chapter 8, XMCT Imaging and DCA to characterized the porosity, permeability and geometry thin sandstone layers in heterolithic rocks. Our results confirm the presence of permeable reservoir sandstone in heterolithic rocks. These thin sandstone layers in low net to gross heterolithic rocks are essential to improved hydrocarbon reserves and production hydrocarbon in thin-bed and LRLC reservoirs where well logs and core analysis indicating high water saturation and low permeability (Kantaatmadja et al., 2014). These thin sandstone layers represent potentially overlooked hydrocarbon reserves in thin-bed LRLC reservoirs. Also, our results that geometrical parameters such as shape, thickness, continuity and locations of thin sandstone beddings and carbonate laminates could have varying impact on effective permeabilities at a larger scale. For example, the effective permeability of heterolithic core plugs is low due to the poor fluid transmissibility of the thin sandstone layers while carbonate laminates in laminated sandstone act as baffles that reduce permeability. However, smaller samples from the sandstone dominated regions with little heterogeneity show large effective permeabilities, suggesting permeability variation at different length scales for heterogeneous rocks and some sandstones. These results highlight the multi-scale effects of small-scale heterogeneities on effective flow properties that are overlooked in most reservoir models, resulting in a weak correlation between estimated reserves and actual reserves (Elfenbein et al., 2005). This thesis provides opportunities to investigate the effects of small-scale heterogeneities and their impact on a larger scale. However, these finds would be more meaningful if the small-scale properties can be upscaled and integrated into a fine-scale reservoir model to determine their impact on effective properties and reserve estimates at a larger scale.

XMCT Imaging and Digital Core Analysis resolved thin sandstone beddings in heterolithic that exhibit similar permeabilities as reservoir sandstone. NER permeability gas probe also resolved high permeability sandstone layers on the surface of a heterolithic rock sample, validating the computed results. Mineralogical analyses of the reservoir sandstones show a low amount of clay and conductive minerals content that can cause low resistivity. Besides, 3D Visualization of a heterolithic sample reveals laterally connected thin sandstone beds between mudstone layers. However, these thin sand layers are very thin with complex geometries that may create tortuous paths to fluid flow, reducing the effective permeability at a larger scale. Characterization of another heterolithic sample with very low computed and measured permeabilities indicate that poorly connected sandstones with very thin geometries resulted in very low effective permeabilities. To sum up, we show that very thin sandstone beddings in heterolithic rocks have permeabilities similar to reservoir sandstone. However, their potential as productive net sand pay depends on their geometry parameters such as thickness, shape and connectivity.

9.1 Future Work

This thesis demonstrates that XMCT Image Analysis, Digital Core Analysis, and 3D Visualization can describe the flow properties and geometries of thin sandstone layers in heterolithic rocks that present opportunities to uncover hydrocarbon reserves in heterogeneous reservoirs. Also, characterizing the geometry parameters of carbonate laminates and their impact on the permeabilities in laminated sandstone could improve the characterization of effective permeabilities in heterogeneous reservoirs. However, we can integrate and upscale the properties of these small-scale heterogeneities into larger-scale models to investigate their impact on effective flow properties and hydrocarbon reserves forecasts in low resistivity heterolithic deposits.

In Figure 9.1, we show that reservoir properties at millimetre-to-centimetre scales can be upscaled and integrated into a multi-scale workflow for reservoir simulation (Hurley et al., 2012). A multi-scale workflow integrates properties at the pore-scale (micron-to-millimetre), borehole-scale (millimetre-to-meter), inter-well scale (10's to 100s of meters) and reservoir scale (kilometres). Also, the multi-scale model incorporates sedimentary structures observed at the pore scale (mud drapes and laminates) up to the reservoir scale (faults and stratigraphic traps). These features affect fluid flow and are essential for improved effective reservoir properties and hydrocarbon reserves forecasts.

Results from this thesis are a starting point for characterizing permeability of millimetre-to-centimetre scale sandstone properties in heterolithic rocks. Hence the next ideal step would be to upscale the flow properties of the thin sandstone layers to the borehole and inter-well scale using a multiscale workflow as to investigate their impact on effective flow properties subsequently on the next adjacent scale.

Another potential future work that spins off from this thesis is the characterization of the varying geometry of carbonate layers in laminated sandstone in thin-bed LRLC reservoirs and their impact on effective permeabilities at a different scale. This work would be concurrent to efforts to characterize the impact of mud drapes in cross-bedded sandstone on effective flow properties in heterolithic sandstone (Massart et al., 2016; Massart, et al., 2016).

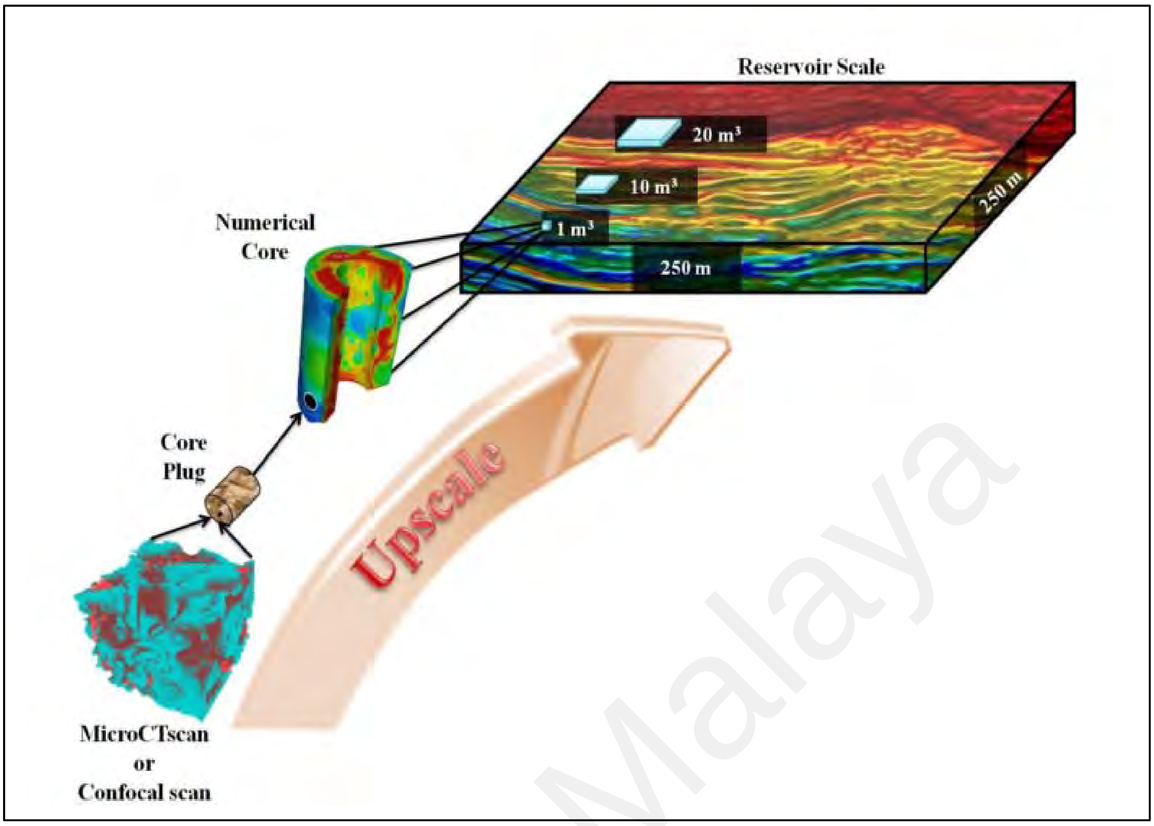

Figure 9.1: Upscaling workflow diagram in heterogeneous rocks. A grid block used in a reservoir simulator is 250 x 250 x 1m in size (right). Borehole-scale numerical cores represent rock volumes on the cubic-meter scale (centre). Core plugs, X-Ray Micro-CT scans, and confocal scans represent even smaller volumes (left). The question is, how representative are these small volumes when compared to coarse grid blocks, or full fields? (Hurley et al., 2012)

Also, there are currently efforts to develop larger and more powerful X-Ray Micro-CT scanners that can image larger samples such as one-inch core plugs and entire core with a diameter of 30 to 40 mm at high resolution. This progress could potentially provide computed petrophysical properties of whole core plugs that could then be compared to experimental data. This is important as currently we compared computed results of small samples (sub-plugs and mini plugs with 5 to 10 mm diameters) to the experimental results of standard one-inch core plugs which may not be appropriate due to significant difference between the two-volume sizes. Also, this new capability could potentially allow us to image a larger heterolithic core plug and core sample and directly compute effective permeability at centimetre-to-meter scale.

REFERENCES

Aksu, I., Bazilevskaya, E., & Karpyn, Z. T. (2015). Swelling of clay minerals in unconsolidated porous media and its impact on permeability. *GeoResJ, 7*, 1-13.

Al-Raoush, R. I., & Willson, C. S. (2005a). Extraction of physically realistic pore network properties from three-dimensional synchrotron X-ray microtomography images of unconsolidated porous media systems. *Journal of Hydrology, 300*(1–4), 44-64.

Al-Raoush, R. I., & Willson, C. S. (2005b). A pore-scale investigation of a multiphase porous media system. *Journal of Contaminant Hydrology, 77*(1–2), 67-89.

Alam, M. (2012). *Estimation of Reservoir Heterogeneity from the Depositional Environment in Reservoir Characterization of a CHOPS Field.* (Degree of Master of Science Master Theses). University of Calgary, Calgary, Alberta, Canada.

Alam, M., Ibna-Hamid, L., Embleton, J., & Lines, L. (2014). *Synthetic core from conventional logs: A new method of interpretation for identification of key reservoir properties* (Vol. 3).

Alyafei, N., McKay, T. J., & Solling, T. I. (2016). Characterization of petrophysical properties using pore-network and lattice-Boltzmann modelling: Choice of method and image sub-volume size. *Journal of Petroleum Science and Engineering, 145*, 256-265.

Andrä, H., Combaret, N., Dvorkin, J., Glatt, E., Han, J., Kabel, M., . . . Zhan, X. (2013). Digital rock physics benchmarks—Part I: Imaging and segmentation. *Computers & Geosciences, 50*, 25-32.

Anyiam, O. A., Aghara, K. I., Mode, A. W., & Okene, A. (2016). Hydrocarbon volume optimization using improved net-to-gross estimates through core-log calibration of the “Akar field,” Niger Delta. *Arabian Journal of Geosciences, 9*(9), 547-558.

Arns, C., A. Knackstedt, M., Pinczewski, V., & S. Martys, N. (2004). *Virtual permeametry on microtomographic images* (Vol. 45).

Arns, C. H., Bauget, F., Sakellariou, A., Senden, T. J., Sheppard, A. P., Sok, R. M., . . . Kelly, J. C. (2005). Digital Core Laboratory: Petrophysical Analysis from 3D Imaging of Reservoir Core Fragments.

Arns, C. H., Knackstedt, M. A., Pinczewski, W. V., & Martys, N. S. (2004). Virtual permeametry on microtomographic images. *Journal of Petroleum Science and Engineering, 45*(1–2), 41-46.

Arns, J.-Y., Arns, C. H., Sheppard, A. P., Sok, R. M., Knackstedt, M. A., & Val Pinczewski, W. (2003). Relative permeability from tomographic images; effect of correlated heterogeneity. *Journal of Petroleum Science and Engineering, 39*(3–4), 247-259.

Arrufat, T., Bondino, I., Zaleski, S., Lagree, B., & Keskes, N. (2014). *Developments on Relative Permeability Computation in 3D Rock Images*. Paper presented at the Abu Dhabi International Petroleum Exhibition and Conference, Abu Dhabi, UAE.

Baptist, C. O., & Sweeney, A. S. (1954). *The Effect of Clays on the Permeability of Reservoir Sands to Waters of Different Saline Contents* (Vol. 3).

Bastia, R. N., Tyagi, A. K., Saxena, K., Klimentos, T., Altman, R. M., Alderman, S., & Bahuguna, S. (2007). *Evaluation of Low-Resistivity-Pay Deepwater Turbidites Using Constrained Thin-Bed Petrophysical Analysis*.

Bates, R. L., Jackson, J. A., & Institute, A. G. (1984). *Dictionary of Geological Terms*: Anchor Press/Doubleday.

Bellile, T. (2003). Tidal Deposits. *Sedimentology and Stratigraphy.* 23rd March 2017 from http://www4.uwm.edu/course/geosci697/sed-seminar.html

Ben-Awuah, J., & Eswaran, P. (2015). Effect of bioturbation on reservoir rock quality of sandstones: A case from the Baram Delta, offshore Sarawak, Malaysia. *Petroleum Exploration and Development, 42*(2), 223-231.

Bentley, M. (2015). Modelling for comfort? *Petroleum Geoscience, Vol. 22*(petgeo2014-089), 3–10.

Bernaschi, M., Fatica, M., Melchionna, S., Succi, S., & Kaxiras, E. (2009). A flexible high-performance Lattice Boltzmann GPU code for the simulations of fluid flows in complex geometries. *Concurrency and Computation: Practice and Experience, 22*(1), 1-14.

Botha, P. (2017). *Predicting Permeability and Capillary Pressure in Low-Resolution Micro-CT Images of Heterogeneous Laminated Sandstones.* (PhD). Australian National University, Canberra, Australia.

Boyd, R., Dalrymple, R., & Zaitlin, B. A. (1992). Classification of clastic coastal depositional environments. *Sedimentary Geology, 80*(3), 139-150.

Brandsæter, I., Wist, H. T., Næss, A., Lia, O., Arntzen, O. J., Ringrose, P. S., . . . Lerdahl, T. R. (2001). Ranking of stochastic realizations of complex tidal reservoirs using streamline simulation criteria. *Petroleum Geoscience, 7*(S), S53-S63.

Bultreys, T., Van Hoorebeke, L., & Cnudde, V. (2015). Multi-scale, micro-computed tomography-based pore network models to simulate drainage in heterogeneous rocks. *Advances in Water Resources, 78*, 36-49.

Campbell, C. V. (1967). Lamina, laminasets, bed and bedset. *Sedimentology, 8*(1), 7-26.

CariGali, P. (2008). *Well Proposal Open Area Block XXX Peninsular Malaysia*. Retrieved from Malaysia:

Carney, S., Barr, D. C., Chai, S. N., Leal, L. A., & Abu Bakar, M. F. (2008). *Reservoir Characterisation of the Mid Miocene Reservoirs of the North Malay Basin, Joint Malaysian Thailand Development Area (MTJDA).*

Cerepi, A., Durand, C., & Brosse, E. (2002). Pore microgeometry analysis in low-resistivity sandstone reservoirs. *Journal of Petroleum Science and Engineering, 35*(3–4), 205-232.

Chai, S. N., Carney, S., Leal, L. A., Boardman, D., & Shepstone, K. (2008, May 2008). *Low Resistivity Low Contrast Pay in Complex Miocene Reservoirs of the Malaysia Thailand Joint Development Area.* Paper presented at the Indoneian Petroleum Association 32nd Annual Convention and Exhibition, Indonesia.

Chen, L., Zou, C., Wang, Z., Liu, H., Yao, S., & Chen, D. (2009). Logging evaluation method of low resistivity reservoir—A case study of well block DX12 in Junggar basin. *Journal of Earth Science, 20*(6), 1003-1011.

Cnudde, V., & Boone, M. N. (2013). High-resolution X-ray computed tomography in geosciences: A review of the current technology and applications. *Earth-Science Reviews, 123*, 1-17.

Daidu, F., Yuan, W., & Min, L. (2013). Classifications, sedimentary features and facies associations of tidal flats. *Journal of Palaeogeography, 2*(1), 66-80.

Dalrymple, R. W., & James, N. P. (2010). *Facies models 4* (Vol. 6.). St. John's, Nfld: Geological Association of Canada.

Droser, M. L., & Bottjer, D. J. (1986, 14th March 2986). *A Semiquantitative Field Classification of Ichnofabric*. Manuscript. Research Methods Paper, (90089-0741). Department of Geological Sciences, University of Southern California, Los Angelesm California.

Elfenbein, C., Husby, Ø., & Ringrose, P. (2015). *Geologically based estimation of kv/kh ratios: an example from the Garn Formation, Tyrihans Field, Mid-Norway.* Paper presented at the 6th Petroleum Geology Conference, London.

Elfenbein, C., Ringrose, P., & Christie, M. (2005). Small-scale reservoir modeling tool optimizes recovery offshore Norway. *World Oil*(October 2005), 45-50.

Eshimokhai, S., Akhirevbulu, O. E., & Osueni, L. (2011). Evaluation of Thin Bed using Resistivity Borehole and NMR Imaging Techniques. *Ethiopian Journal of Environmental Studies and Management, 4*(4), 96-102.

Evans, P. D., Morrison, O., Senden, T. J., Vollmer, S., Roberts, R. J., Limaye, A., . . . Knackstedt, M. A. (2010). Visualization and numerical analysis of adhesive distribution in particleboard using X-ray micro-computed tomography. *International Journal of Adhesion and Adhesives, 30*(8), 754-762.

Golab, A., Romeyn, R., Averdunk, H., Knackstedt, M., & Senden, T. J. (2013). 3D characterisation of potential CO2 reservoir and seal rocks. *Australian Journal of Earth Sciences, 60*(1), 111-123.

Grader, A., Kalam, M. Z., Toelke, J., Mu, Y., Derzhi, N., Baldwin, C., . . . Stenger, B. (2010). *A Comparative Study of Digital Rock Physics and Laboratory SCAL Evaluations of Carbonate Cores*. Paper presented at the Internatinal Symposium of the Society of Core Analyst, Halifax Canada. Conference Paper

Grover, D., Savidge, C. R., Townsend, L., Rosario, O., Hu, L.-B., Rizzo, D. M., & Dewoolkar, M. M. (2016). Surface permeability of natural and engineered porous building materials. *Construction and Building Materials, 112*, 1088-1100.

Gupta, R., & Johnson, H. D. (2001). Characterization of Heterolithic Deposits using Electrofacies Analysis in the tide dominated Lower Jurassic Cook Formation (Gullfaks Field, Offshore Norway). *Petroleum Geoscience, 7*(3), 321-331.

Hansen, L. A. S., Callow, R. H. T., Kane, I. A., Gamberi, F., Rovere, M., Cronin, B. T., & Kneller, B. C. (2015). Genesis and character of thin-bedded turbidites associated with submarine channels. *Marine and Petroleum Geology, 67*, 852-879.

Hassan, S. M. (2013). *Sequence Stratigraphy of the Lower Miocene Moghra Formation in the Qattara Depression, North Western Desert, Egypt*: Springer International Publishing.

Heavysege, R. G. (2002). *Formation Evaluation Of Fresh Water Shaly Sands Of The Malay Basin, Offshore Malaysia*. Paper presented at the SPWLA 43rd Annual Logging Symposium, 2-5 June, Oiso, Japan.

Hommel, J., Coltman, E., & Class, H. (2018). Porosity–Permeability Relations for Evolving Pore Space: A Review with a Focus on (Bio-)geochemically Altered Porous Media. *Transport in Porous Media, 124*(2), 589-629.

Hurley, N. F., Zhao, W., & Zhang, T. (2012). *Multiscale Workflow For Reservoir Simulation*. Paper presented at the SPWLA 53rd Annual Logging Symposium, Cartagena, Colombia.

Jackson, M. D., Yoshida, S., Johnson, H. D., & Muggerdige, A. H. (1999). *Three-Dimensional Reconstruction, Flow Simulation, and Upscaling of Complex Bedform-Scale Sedimentary Structures Within Tidal Sandstone Reservoirs*. Paper presented at the 19th Annual Research Conference Advanced Reservoir Characterization, December, Houston, Texas, United States. Conference Paper

Jones, A., Doyle, J., Jacobsen, T., & Kjønsvik, D. (1995). Which sub-seismic heterogeneities influence waterflood performance? A case study of a low net-to-gross fluvial reservoir. *Geological Society, London, Special Publications, 84*(1), 5-18.

Jouini, M. S., Vega, S., & Al-Ratrout, A. (2015). Numerical estimation of carbonate rock properties using multiscale images. *Geophysical Prospecting, 63*(2), 405-421.

Kalam, Z., & Gomes, J. S. E. (2012). Digital Rock Physics for Fast and Accurate Special Core Analysis in Carbonates. *New Technologies in the Oil and Gas Industry (Book)*, 26.

Kantaatmadja, B. P., Nurhono, A. A., Majid, R. B. A., Mohamad, N. Y. B., & Amdan, A. B. (2014). *Unlock hydrocarbon volumetric potential of LRLC clastic reservoirs in Malaysian Basins*. Paper presented at the Society of Petroleum Engineers - International Petroleum Technology Conference 2014, IPTC 2014 - Innovation and Collaboration: Keys to Affordable Energy.

Karoteev, D., Dinariev, O., Klemin, D., Nadeev, A., Safonov, S., Gurpinar, O., . . . de Jong, H. (2014). Direct Hydrodynamic Simulation of Multiphase Flow in Porous Rock. *Petrophysics, 55*(3), 273-356.

Ketcham, R. A., & Carlson, W. D. (2001). Acquisition, optimization and interpretation of x-ray computed tomographic imagery: Applications to the geosciences. *Computers and Geosciences, 27*(4), 381-400.

Ketcham, R. A., & Hanna, R. D. (2014). Beam hardening correction for X-ray computed tomography of heterogeneous natural materials. *Computers & Geosciences, 67*, 49-61.

Knackstedt, M., Kelly, J., Saadatfar, M., Senden, T., & Sok, R. (2005). *Rock fabric and texture from Digital Core Analysis*. Paper presented at the SPWLA 46th Annual Logging Symposium, New Orleans, Louisiana.

Knackstedt, M. A., Arns, C., Ghous, A., Sakellariou, A., Senden, T., Sheppard, A. P., . . . Pinczewski, V. (2006). 3D imaging and characterization of the pore space of carbonate core; implications to single and two phase flow properties. *Annual Logging Symposium of the Society of Petrophysicists & Well Log Analysts (SPWLA 2006)*.

Knackstedt, M. A., Arns, C. H., Sakellariou, A., Senden, T. J., Sheppard, A. P., & Sok, R. M. (2007). *X‐Ray Micro‐Tomography Applications Of Relevance To The Petroleum Industry*. Paper presented at the AIP Conference Proceedings.

Knackstedt, M. A., Latham, S., Madadi, M., Sheppard, A. P., Varslot, T., & Arns, C. H. (2009). Digital rock physics: 3D imaging of core material and correlations to acoustic and flow properties. *The Leading Edge, Special Edition*, 6.

Krakowska, P., Dohnalik, M., Jarzyna, J., & Wawrzyniak-Guz, K. (2016). Computed X-ray microtomography as the useful tool in petrophysics: A case study of tight carbonates Modryn formation from Poland. *Journal of Natural Gas Science and Engineering, 31*, 67-75.

Krassakopoulos, G. (2013). *Petrophysical Characterization of Gas Reservoir Rock Samples using High Resolution Micro-CT Images.* (Masters Degree Masters Degree). TU Delft, Netherlands, TU Delft, Netherlands.

Kumar, M., Lebedeva, E., Melean, Y., Madadi, M., Sheppard, A. P., Varslot, T. K., . . . Knackstedt, M. A. (2013). Micro-Petrophysical Experiments Via Tomography and Simulation. In *Advances in Computed Tomography for Geomaterials* (pp. 238-253): John Wiley & Sons, Inc.

Kumar, M., Sok, R., Knackstedt, M. A., Latham, S., Senden, T. J., Sheppard, A. P., . . . Arns, C. (2010). Mapping 3D Pore Scale Fluid Distributions: How Rock Resistivity is Influenced By Wettability And Saturation History.

Kyle, J. R., & Ketcham, R. A. (2015). Application of high resolution X-ray computed tomography to mineral deposit origin, evaluation, and processing. *Ore Geology Reviews, 65, Part 4*, 821-839.

Latham, S., Varslot, T., & Sheppard, A. (2008). *Image registration: enhancing and calibrating X-ray micro-CT imaging*. Paper presented at the International Symposium of the Society of Core Analysts, Abu Dhabi.

Limaye, A. (2012). *Drishti: a volume exploration and presentation tool* (Vol. 8506): SPIE.

Long, H., Swennen, R., Foubert, A., Dierick, M., & Jacobs, P. (2009). 3D quantification of mineral components and porosity distribution in Westphalian C sandstone by microfocus X-ray computed tomography. *Sedimentary Geology, 220*(1–2), 116-125.

Lopez, O., Mock, A., Skretting, J., Peterson Jr, E. B., Øren, P., & Rustad, A. B. (2010). Investigation into the Reliability of Predictive Pore-Scale Modeling for Siliciclastic Reservoir Rocks. *International Symposium of the Society of Core Analyssts, Halifax, Nova Scotia,Canada*, 12.

Madon, M., Abolins, P., Hoesni, J., & Ahmad, M. (1999). *The Petroleum Geology and Resources of Malaysia: Malay Basin*. Malaysian: Petroliam Nasional Berhad.

Manescu, A., Kho, S., & Ha, K. (2010). Petrophysical Evaluation of Low-Contrast Low-Resistivity Thin-Bedded Shale and Sand Beds. *SPE NEWS, Society of Petroleum Engineers*(March 2011), 6.

Martinius, A. W., Ringrose, P. S., Brostrøm, C., Elfenbein, C., Næss, A., & Ringås, J. E. (2005). Reservoir Challenges of Heterolithic Tidal Sandstone Reservoirs in the Halten Terrace, mid-Norway. *Petroleum Geoscience, 11*(2005), 3-17.

Masch, F. D., & Denny, K. (1966). *Grain Size Distribution and Its Effect on The Permeability of Unconsolidated Sands* (Vol. 2).

Massart, B., Jackson, M., Hampson, G., Johnson, H., Legler, B., & Jackson, C. (2016). *Effective flow properties heterolithic, cross-bedded tidal sandstones: Part 1. Surface-based modeling* (Vol. 100).

Massart, B. Y. G., Jackson, M. D., Hampson, G. J., & Jackson, H. D. (2016). Effective flow properties of heterolithic, cross-bedded tidal sandstones: Part 2. Flow simulation. *AAPG Bulletin, 100*(5), 723-743.

McLean, A. Q., & Wilson, B. (2016). Recognizing seasonal fluvial influence in ancient tidal deposits. *Geological Society, London, Special Publications, 444*.

Meakin, P., & Tartakovsky, A. M. (2009). Modeling and simulation of pore-scale multiphase fluid flow and reactive transport in fractured and porous media. *Reviews of Geophysics, 47*(3), 1-47.

Mode, A. W., Anyiam, O. A., & Aghara, I. K. (2015). Identification and petrophysical evaluation of thinly bedded low-resistivity pay reservoir in the Niger Delta. *Arabian Journal of Geosciences, 8*(4), 2217-2225.

Mokso, R., Quaroni, L., Marone, F., Irvine, S., Vila-Comamala, J., Blanke, A., & Stampanoni, M. (2012). X-ray mosaic nanotomography of large microorganisms. *Journal of Structural Biology, 177*(2), 233-238.

Munawar, M. J., Lin, C., Cnudde, V., Bultreys, T., Dong, C., Zhang, X., . . . Wu, Y. (2018). Petrographic characterization to build an accurate rock model using micro-CT: Case study on low-permeable to tight turbidite sandstone from Eocene Shahejie Formation. *Micron, 109*, 22-33.

Nadeau, P. H. (1998). An experimental study of the effects of diagenetic clay minerals on reservoir sands. *Clays and Clay Minerals, 46*(1), 18-26.

Nordahl, K. (2004). *A petrophysical evaluation of tidal heterolithic deposits.Application of a near wellboremodel for reconciliation of scale dependent well data.* (Degree of Doktor Ingeniør Doctoral Thesis). Norwegian University of Science and Technology, Trondheim, Norway.

Oifoghe, S. (2014). *Challenges in identifying and quantifying hydrocarbons in thinly bedded, laminated, and low-resistivity pay zones.* Paper presented at the Proceedings of the Annual Offshore Technology Conference.

Øren, P., Bakke, S., & Rueslåtten, H. G. (2006). Digital Core Laboratory: Rock and Flow Properties Derived from Computer Generated Rocks. *International Symposium of the Society of Core Analysts, Trondheim*, 12.

Passey, Q. R., Dahlberg, K. E., Sullivan, K. B., Yin, H., Brackett, R. A., Xiao, Y. H., & Guzmán-Garcia, A. G. (2006). Characterizing Thinly Bedded Reservoirs with Core Data. *AAPG Archie Series, 1*(1), 73-88.

Pratama, E., Suhaili Ismail, M., & Ridha, S. (2017). An integrated workflow to characterize and evaluate low resistivity pay and its phenomenon in a sandstone reservoir. *Journal of Geophysics and Engineering, 14*(3), 513-519.

Reineck, H.-E., & Singh, I. B. (1980). Depositional Sedimentary Environments with reference to terrigeneous clastics(Vol. 2nd, rev. and updat). Berlin: Springer Verlag.

Reineck, H.-E., & Wunderlich, F. (1968). Classification and origin of flaser and lenticular bedding. *Sedimentology, 11*(1-2), 99-104.

Riepe, L., Suhaimi, M. H., Kumar, M., & Knackstedt, M. A. (2011). *Application of High Resolution Micro-CT-Imaging and Pore Network Modeling (PNM) for the Petrophysical Characterization of Tight Gas Reservoirs- A Case History from a Deep Clastic Tight Gas Reservoir in Oman*. Paper presented at the SPE Middle East Unconventional Gas Conference and Exhibition, Muscat,Oman. Journal Article

Ringrose, P., & Bentley, M. (2014). *Reservoir Model Design: A Practioner's Guide*: Springer.

Ringrose, P., Martinius, A., & Alvestad, J. (2008). *Multiscale geological reservoir modelling in practice* (Vol. 309).

Ringrose, P., Nordahl, K., & Wen, R. (2005). Vertical permeability estimation in heterolithic tidal deltaic sandstones. *Petroleum Geoscience, 11*(2005), 29-36.

Ringrose, P., Skjetne, E., & Elfenbein, C. (2005). *Permeability Estimation Functions Based on Forward Modeling of Sedimentary Heterogeneity*.

Ringrose, P. S., Sorbie, K. S., Corbett, P. W. M., & Jensen, J. L. (1993). Immiscible flow behaviour in laminated and cross-bedded sandstones. *Journal of Petroleum Science and Engineering, 9*(2), 103-124.

Rink, M., & Schopper, J. R. (1974). *Interface Conductivity And Its Implications To Electric Logging*. Paper presented at the SPWLA 15th Annual Logging Symposium, McAllen, Texas.

Saadatfar, M., Sheppard, A. P., Senden, T. J., & Kabla, A. J. (2012). Mapping forces in a 3D elastic assembly of grains. *Journal of the Mechanics and Physics of Solids, 60*(1), 55-66.

Sakellariou, A., Arns, C. H., Sheppard, A. P., Sok, R. M., Averdunk, H., Limaye, A., . . . Knackstedt, M. A. (2007). Developing a virtual materials laboratory. *Materials Today, 10*(12), 44-51.

Schepp, L. L., Ahrens, B., Balcewicz, M., Duda, M., Nehler, M., Osorno, M., . . . Saenger, E. H. (2020). Digital rock physics and laboratory considerations on a high-porosity volcanic rock. *Scientific Reports, 10*(1), 1-16.

Sheppard, A., Latham, S., Middleton, J., Kingston, A., Myers, G., Varslot, T., . . . Senden, T. (2014). Techniques in helical scanning, dynamic imaging and image segmentation for improved quantitative analysis with X-ray micro-CT. *Nuclear Instruments and Methods in Physics Research Section B: Beam Interactions with Materials and Atoms, 324*, 49-56.

Sheppard, A., Sok, R., & Averdunk, H. (2004). Techniques for image enhancement and segmentation of tomographic images of porous materials. *Physica A: Statistical Mechanics and its Applications, 339*(1), 145-151.

Sheppard, A. P., Arns, C. H., Sakellariou, A., Senden, T. J., Sok, R. M., Averdunk, H., . . . Knackstedt, M. (2006). Quantitative Properties of Complex Porous Materials Calculated from X-ray μCT Images. *Society of Photographic Instrumentation Engineers, 6318*, 1-15.

Snyder, C. J., Khan, S. D., Bhattacharya, J. P., Glennie, C., & Seepersad, D. (2016). Thin-bedded reservoir analogs in an ancient delta using terrestrial laser scanner and high-resolution ground-based hyperspectral cameras. *Sedimentary Geology, 342*, 154-164.

Sun, H., Vega, S., & Tao, G. (2017). Analysis of heterogeneity and permeability anisotropy in carbonate rock samples using digital rock physics. *Journal of Petroleum Science and Engineering, 156*, 419-429.

Sun, J., Zhao, J., Liu, X., Hui, C., Jiang, L. M., & Zhang, J. Y. (2014). Pore-scale analysis of electrical properties in thinly bedded rock using digital rock physics. *Journal of Geophysics and Engineering, 11*, 1-8.

Tang, X., Jiang, Z., Jiang, S., & Li, Z. (2016). Heterogeneous nanoporosity of the Silurian Longmaxi Formation shale gas reservoir in the Sichuan Basin using the QEMSCAN, FIB-SEM, and nano-CT methods. *Marine and Petroleum Geology, 78*(Supplement C), 99-109.

Theting, G. T., Rustad, A. B., Lerdahl, T. R., Stensen, J. A., Øren, P., Bakke, S., & Ringrose, P. (2005). *Pore-to-field multi-phase upscaling for a depressurization process*. Paper presented at the 13th European Symposium on Improved Oil Recovery.

Tiab, D., & Donaldson, E. C. (2012). Petrophysics: Theory and Practice of Measuring Rock and Fluid Transport Properties. In *Petrophysics (Third Edition)* (Vol. Third Edition). Boston: Gulf Professional Publishing.

Tonkin, N. S., McIlroy, D., Meyer, R., & Moore-Turpin, A. (2010). Bioturbation influence on reservoir quality: A case study from the Cretaceous Ben Nevis Formation, Jeanne d'Arc Basin, offshore Newfoundland, Canada. *AAPG Bulletin, 94*(7), 1059-1078.

Turner, M. L., Knüfing, L., Arns, C. H., Sakellariou, A., Senden, T. J., Sheppard, A. P., . . . Knackstedt, M. A. (2004). Three-dimensional imaging of multiphase flow in porous media. *Physica A: Statistical Mechanics and its Applications, 339*(1–2), 166-172.

Tyagi, A. K., Bastia, R., & Das, M. (2008). *Identification and Evaluation of the Thin Bedded Reservoir Potential in the East Coast Deep Water Basins of India*. Paper presented at the 7th International Conference and Exposition on Petroleum Geophysics, Hyderabad, India. Conference Paper

Vajnar, E. A., Kidwell, C. M., & Haley, R. A. (1977). *Surprising Productivity From Low-Resistivity Sands*. Paper presented at the SPWLA 18th Annual Logging Symposium, Houston, Texas.

Van Wagoner, J. C. (1990). *Siliciclastic sequence stratigraphy in well logs, cores, and outcrops* (Vol. 7.). Tulsa, Ok., USA American Association of Petroleum Geologists.

Watney, W., & Doveton, J. (May 13, 2004). Geo-Engineering Modeling through internet informatics (GEMINI). 10th July 2019 from https://digital.library.unt.edu/ark:/67531/metadc781056/

Wen, R., Martinius, A. W., & Ringrose, P. (1998). *Three-dimensional simulation of small-scale heterogeneity in tidal deposits - A process-based stochastic simulation method*. Paper presented at the Internation Association of Mathematical Geoscience, Isola d'Ischia, Naples, Italy.

Wildenschild, D., & Sheppard, A. P. (2013). X-ray imaging and analysis techniques for quantifying pore-scale structure and processes in subsurface porous medium systems. *Advances in Water Resources, 51*, 217-246.

Williams, G. E., Gostin, V. A., McKirdy, D. M., & Preiss, W. V. (2008). The Elatina glaciation, late Cryogenian (Marinoan Epoch), South Australia: Sedimentary facies and palaeoenvironments. *Precambrian Research, 163*(3–4), 307-331.

Wood, L. (2004). *Predicting Tidal Sand Reservoir Architecture Using Data from Modern and Ancient Depositional Systems* (Vol. 80).

Worthington, P. F. (2000). Recognition and evaluation of low-resistivity pay. *Petroleum Geoscience, 6*(1), 77-92.

Yun, T. S., Jeong, Y. J., Kim, K. Y., & Min, K.-B. (2013). Evaluation of rock anisotropy using 3D X-ray computed tomography. *Engineering Geology, 163*, 11-19.